UNIVERSITY OF LEEDS

Limit to the Ultra-High Energy Gamma-Ray Flux Using Data from the Surface Detectors of the Pierre Auger Observatory.

Heather Louise Cook

University of Leeds

School of Physics and Astronomy

Submitted in accordance with the requirements for the degree of

Master of Philosophy

April 2012

Abstract

Cosmic-rays are highly energetic particles originating from outer space. Ultra-high energy cosmic-rays (UHECRs) are defined as those above 10^{18} eV. The Pierre Auger Observatory is a hybrid detector comprising a surface array of over 1660 water-Cherenkov detectors and 27 nitrogen-fluorescence detectors, the data from which can be studied separately or combined in hybrid mode. Data-taking began in 2004, with construction of the array completed in 2008.

The mass-composition of UHECR, in particular the flux of photons, is currently unknown. UHECR photons are expected from the interaction of protons with energies greater than $\sim 3 \times 10^{19}$ eV with the cosmic microwave background. Previous limits on the fraction of UHECR photons from surface array data are of the order of a few % above 10^{19} eV.

Surface array data have been used to update and improve a mass-sensitive shower-timing parameter, $\langle\Delta\rangle$, derived from the signal risetimes of individual detectors. A complete overhaul of this method has been performed, providing a more robust parameter sensitive to the mass-composition of UHECR. The change of $\langle\Delta\rangle$ with energy has been investigated and a correlation between $\langle\Delta\rangle$ and another mass-sensitive parameter - the depth of maximum, X_{max}, has been found. A study of the mass-sensitivity of $\langle\Delta\rangle$ has been made by comparison to photon and hadronic simulations. From this comparison it is found that the composition of UHECRs, on average, tends towards heavier primaries with increasing energy.

Ten events have been identified as potential photon-initiated air showers. Conservative integral upper limits to the flux of UHE photons have been computed at 8.7×10^{-3}, 4.7×10^{-3}, 2.8×10^{-3} and $2.3 \times 10^{-3}\,\mathrm{km^{-2}\,sr^{-1}\,yr^{-1}}$ above 10, 20, 30 and 40 EeV respectively. Integral upper limits to the fraction of photons have also been found at 1.5%, 3.2%, 4.9% and 9.1% above these energies. These new limits improve upon previous works and exclude all 'top-down' models for photon

production except the Z-burst model, which is strongly disfavoured. These limits do not yet probe the GZK region.

The arrival directions of these photon-candidates have been compared to the positions of nearby AGN from the VCV and Swift-BAT catalogues. No obvious sources have been found for these events and none of the photon-candidate arrival directions lie close to Cen A.

The differences between those events above 5×10^{19} eV that correlate with AGN from the VCV catalogue, or originate from within 18° angular separation of Centaurus A, to those that do not, have been studied using the $\langle\Delta\rangle$ parameter. No significant differences in their average $\langle\Delta\rangle$ have been found, nor is a systematic change in $\langle\Delta\rangle$ observed as a function of angular distance from Cen A.

Finally, the azimuthal asymmetry on the risetimes has been reviewed as a potential mass-sensitive parameter in relation to previous works. A possible alternative method for determining the dependence of the asymmetry on the energy has been explored with limited success. This new method is in the early stages of development and further study is required.

Declaration

The candidate confirms that the work submitted is her own and that appropriate credit has been given where reference has been made to the work of others.

Contents

List of Figures

List of Tables

Abbreviations

AERA	Auger Engineering Radio Array
AGASA	Akeno Giant Air Shower Array
AGN	Active Galactic Nucleus / Nuclei
AMIGA	Auger Muon Infill Ground Array
CDAS	Central Data Acquisition System
CLF	Central Laser Facility
CMB	Cosmic Microwave Background
CORSIKA	COsmic Ray SImulations for KAscade
CR	Cosmic Ray
EAS	Extensive Air Shower(s)
EeV	10^{18} eV
FADC	Flash Analogue to Digital Converter
FD	Fluorescence Detector
Fermi-LAT	Fermi Large Area Telescope
GDA	Gold Deconvolution Algorithm
GRB	Gamma Ray Burst
GZK	Greisen, Zatsepin and Kuzmin
HEAT	High Elevation Auger Telescope
H.E.S.S.	High Energy Stereoscopic System
LDF	Lateral Distribution Function
LEP	Large Electron-Positron Collider
LHC	Large Hadron Collider
LHCf	LHC-forward
LIDAR	LIght Detection And Ranging
LPM	Landau, Pomeranchuk & Migdal

MC	Monte-Carlo
MIT	Massachusetts Institute of Technology
NGC	New Galactic Catalogue
NKG	Nishimura-Kamata-Greisen
PeV	10^{15} eV
PMT	Photomultiplier Tube
QED	Quantum Electro-Dynamics
SD	Surface Detector
SHDM	Super Heavy Dark Matter
SPR	Single Particle Response
STC	Single Trigger Condition
Swift-BAT	Swift Burst Alert Telescope
TeV	10^{12} eV
TD	Topological Defect
ToT	Time over Threshold
VEM	Vertical Equivalent Muon
VCV	Veron-Cetty-Veron
VHE	Very High Energy ($10^{12} \leq \mathrm{E} \leq 10^{18}$ eV)
UHE	Ultra High Energy ($\mathrm{E} \geq 10^{18}$ eV)
2MRS	Two Micron (All-Sky) Redshift Survey

Personal Contributions

In chapter 3 of this thesis I describe my update and rigorous re-analysis of the risetime $\langle\Delta\rangle$-method for identifying candidate ultra-high energy gamma-rays. This update incorporated the new stop-times method introduced by my colleague, Dr. Ronald Bruijn. Section 3.1.2 of this thesis provides the first detailed description of Ronald's work on the stop-times and baselines of surface detector FADC traces, which I subsequently found has a significant impact on the results of the $\langle\Delta\rangle$-method. This is the first time the 'new stop-times' have been implemented in the analysis of data from the Pierre Auger Observatory. The rest of the thesis describes an overview of my key contributions to the improvement of the $\langle\Delta\rangle$-method and new limits to the flux and fraction of UHE gamma-rays using data from the surface array of the Pierre Auger Observatory. An overview of the results given in this thesis have been presented on my behalf at a recent Pierre Auger Collaboration meeting (2012). I also describe some of my additional work on a potential alternative mass-sensitive parameter.

It is anticipated that this thesis will be submitted to the Pierre Auger Collaboration as an internal 'GAP-note'. It is also hoped that the updated method and results from this work will be included in future Pierre Auger Observatory journal publications on photon limits.

In addition to the work described in this thesis, I took part in a three-week 'FD shift' on-site in Malargüe during November 2009, involving the collection of data using the fluorescence detectors and a variety of atmospheric monitoring equipment. Following this shift, I became a named Pierre Auger Collaboration author on 16 full-author-list papers from January 2010 to July 2012.

Acknowledgements

Firstly I would like to thank my supervisors, Dr. Johannes Knapp and Professor Alan Watson, for the opportunity to do this research and for their continued help and support. I would like to thank the Pierre Auger Collaboration, without whose tireless work there would be no data and no project. I would particularly like to thank the observatory staff and my 'co-shifters' for making my time on the FD shift so enjoyable. Thanks also go to STFC for funding my work and to Professor David Fegan and Dr. Stella Bradbury for agreeing to be my examiners.

Next I would like to thank the Leeds high-energy group both past and present - to the post-docs Ronald, Rebecca, Carla and Ines for their help, advice, company and much needed assistance with programming; to Jo, Dan, Lu, Paul and Mo for being great office-mates, for enjoyable discussions and for providing a listening ear to occasional rants and far-fetched theories. A big thank you goes to the Leeds 'low-energy' group for company at coffee and keeping me sane (a hard challenge). I would also like to thank Cameron for helping me organise the IOP Astroparticle physics group student meeting in Leeds during my time as postgraduate representative. Finally I would like to thank the Leeds University Scottish Dance Society, and the RSCDS Leeds branch for providing a pleasant distraction every week and proving that there's more to life than work.

Chapter 1

Cosmic-Ray Astrophysics

1.1 Introduction

It has been a century since Victor Hess first discovered cosmic-rays. Since then, there has been an abundance of discoveries in particle physics and cosmic-ray astrophysics. Yet there are still many unanswered questions surrounding the enigma of cosmic-rays, including the ultimate: where do cosmic-rays come from? The main science goals of the Pierre Auger Observatory are to determine the origins, propagation, composition and energy spectrum of ultra-high energy cosmic-rays (UHECR) with energies greater than $10^{18}\,\mathrm{eV}$. The flux of UHECR is extremely low ($\sim 1\,\mathrm{km}^{-2}\,\mathrm{year}^{-1}$ above $10^{18}\,\mathrm{eV}$); therefore the construction of a cosmic-ray observatory roughly twice the size of Greater London has been necessary to detect a sufficiently large number of showers that the highest energy cosmic-rays might be probed. Located in Malargüe, Argentina, the Pierre Auger Observatory is a hybrid detector comprising 24 nitrogen fluorescence detectors and over 1600 water-Cherenkov detectors covering an area of $3000\,\mathrm{km}^2$, and has been collecting data since the beginning of January 2004.

1.2 Thesis Outline

The work presented in this thesis utilises the data recorded by the surface array of the Pierre Auger Observatory to determine a new and more stringent limit on

both the flux and the fraction of UHECR photons above 10^{19} eV. Presented in this chapter is an introduction to the field of cosmic-ray astrophysics, including a brief overview of the most important historic discoveries, the propagation of cosmic-rays through galactic and intergalactic space, and potential sources. Primarily the discussion will focus on ultra-high energy cosmic-rays.

Chapter 2 gives a technical description of the Pierre Auger Observatory and the reconstruction techniques employed to determine key shower parameters such as the energy, arrival direction, depth of maximum development and shower timing parameters. A brief review of the major results published by the collaboration will also be given.

Chapter 3 describes the re-analysis of a method that uses the time-spread of shower particles at ground as a mass composition indicator. This includes several substantial changes to the method. Pierre Auger Observatory data from January 2004 to December 2010 has been analysed with this new method. Chapter 4 outlines the application of the updated method described in chapter 3 to photon, proton and iron simulations. New, more stringent limits to the fraction and flux of UHECR photons are also presented.

Chapter 5 uses the method and results from chapters 3 and 4 to analyse the timing information of the highest energy events detected by the Pierre Auger Observatory in relation to their proximity to AGN from the Veron-Cetty-Veron catalogue and to Centaurus A. The positions of potential photon-candidate events in relation to astrophysical objects are also remarked upon. In chapter 6, the potential for two new mass-sensitive variables to be created from the asymmetry in the timing information are investigated. Concluding remarks are given in chapter 7.

1.3 A Century of Cosmic-Ray Astrophysics

In 1912 Victor Hess flew in a balloon to a height of over 16,000 feet (5 km). The experiment on board the balloon was designed to measure the rate of discharge of an electroscope with increasing altitude. At the time it was believed that most of

the natural background radiation that caused electroscopes to discharge was from radioactive elements in the ground (1). Therefore Hess expected that the rate of discharge would decrease with increasing altitude. However, Hess found that above a height of 1 km the rate of discharge of the electroscope increased with altitude. Hess concluded that the source of the radiation that caused electroscopes to discharge came from outside the Earth's atmosphere.

With this discovery and its publication by Hess (2), the field of cosmic-ray astrophysics was created. However, the term 'cosmic-ray' was not used until 1925 after Millikan's series of experiments in Lakes Muir and Arrowhead in Southern California which measured the rate of discharge of electroscopes at increasing depths (1). As the most penetrating form of radiation known at the time was Gamma-radiation from radioactive substances, the assumption was made that cosmic-rays were merely far more energetic Gamma-rays, hence the misnomer.

In 1929 Bothe and Kolhörster used newly invented Geiger counters to 'count' individual cosmic-rays. They noticed that two Geiger counters placed one above the other a short distance apart would discharge simultaneously. Such coincidences must be due to a charged particle passing through both Geiger counters as coincidence measurements were unlikely to come from multiple Compton collisions of a single photon traversing both detectors. This lead to the hypothesis that, at sea level, cosmic-rays were primarily a combination of photons and electrons, possibly from higher energy photons that had interacted with the atmosphere (1).

Compton and Alvarez, and Johnson (in 1933) independently observed an increased flux of particles ($\simeq 10\%$) from the west compared to the east - the 'East-West' effect (3). Two years later, Clay demonstrated that the flux of cosmic-rays decreased by 15% between Amsterdam and the equator (4), (5). These two experiments showed that a significant component of positively charged particles existed in the cosmic-ray flux.

In 1935 Compton and Getting predicted the increase in energy and intensity of cosmic-rays detected on Earth due to the motion of the Earth around the

Sun and of the solar system in the galaxy, thus generating a small anisotropy in cosmic-ray arrival directions (6). Firm detection of this effect at all energies has yet to be made. Compton and Bennet also predicted variations to the cosmic-ray flux from the Earth's rotation on its axis (7).

The measurement of a larger than expected number of simultaneous detections (coincidences) in detectors separated by up to 300 m was made by Pierre Auger et. al. in 1938. This led to the concept of extensive air showers (EAS) and hence the discovery of primary cosmic-rays of energy greater than 10^{15} eV, then seen as inconceivably energetic particles (8). The development of a photon-initiated air shower in the atmosphere was first described in a theoretical paper by Bhabha and Heitler in the same year (9). Hadrons from protons to iron nuclei were also identified as components of the cosmic-ray flux. During the late 1940s and 1950s a wealth of new particles, for example pions, muons and kaons, were identified. These discoveries allowed the bones of cascade theory to be fleshed out.

The discovery of the cosmic microwave background (CMB) by Penzias and Wilson in 1965 (10) prompted Zatespin and Kuzmin, and independently Greisen, to predict the interaction of the highest energy cosmic-rays with the CMB, now known as the 'GZK effect'. This placed limits on the propagation distance of cosmic-rays and predicted a sharp steepening of the cosmic-ray flux spectrum above $\simeq 3 \times 10^{19}$ eV, and thus an end to the energy spectrum (11). At the time, the highest energy cosmic-ray, recorded at Volcano Ranch four years previously, had an energy of 10^{20} eV. Further detections of events above 3×10^{19} eV, including seven events above 10^{20} eV by AGASA in the 1990s, cast doubts on the existence of the GZK cut-off (12).

Since the 1960s many instruments have been built to try and answer fundamental questions about both Very- and Ultra-High Energy Cosmic-Rays, for example the mass composition and flux spectrum. These experiments have exploited a variety of detection techniques, for example using water-Cherenkov, Scintillation and Fluorescence detectors, to increase our understanding of the finer details of air shower physics. The Pierre Auger Observatory is the largest

and most recent observatory constructed to investigate cosmic-rays above 10^{18} eV. As the study of cosmic-rays reaches its 100^{th} birthday, the wealth of information gathered has been vast and the techniques used diverse. As far as the highest energy cosmic-rays are concerned, our increasing knowledge of the mass-composition of UHECR and confirmation of the GZK steepening will take us ever closer to the ultimate goal: the discovery of the sources of the highest energy cosmic-rays.

1.4 The Energy Spectrum of Cosmic-Rays

The cosmic-ray energy spectrum extends over 12 orders of magnitude, from below 10^9 eV to beyond 10^{20} eV. Below 10^{10} eV cosmic-rays are modulated by the solar wind. Above 10^{10} eV, the flux follows an almost continuous power law spectrum with only a few changes in the slope (figure 1.1) (13). The cosmic-ray spectrum is described by:

$$\frac{dN}{dE} = kE^{-\alpha} \tag{1.1}$$

where k is a constant and α describes the slope of the spectrum. A change in the slope occurs at $\simeq 3 \times 10^{15}$ eV from $\alpha \simeq 2.7$ to $\alpha \simeq 3.0$ - called the 'knee'. The flux at the knee is $\simeq 1\,\text{m}^{-2}\,\text{yr}^{-1}$. Another change in slope is apparent at 3×10^{18} eV, called the 'ankle', where the slope changes from $\alpha \simeq 3.0$ to $\alpha \simeq 2.5$ (and the flux is $\simeq 1\,\text{km}^{-2}\,\text{yr}^{-1}$). The origin of the knee and ankle are not yet settled. Changes in source acceleration mechanisms, source type, interaction and propagation mechanisms have all been considered. Cosmic-rays with energies below the knee are predominantly protons and light nuclei accelerated by diffusive shock acceleration in supernovae within the Milky Way Galaxy (14), (15). Other elements are represented in the composition of cosmic-rays, which roughly follows solar system abundances (except for lithium, beryllium and boron due to spallation).

Due to deflections by galactic magnetic fields, galactic cosmic-rays with TeV to PeV energies become trapped within the galaxy for many thousands of years. Thus it is possible (in terms of the observed flux) for galactic supernovae that

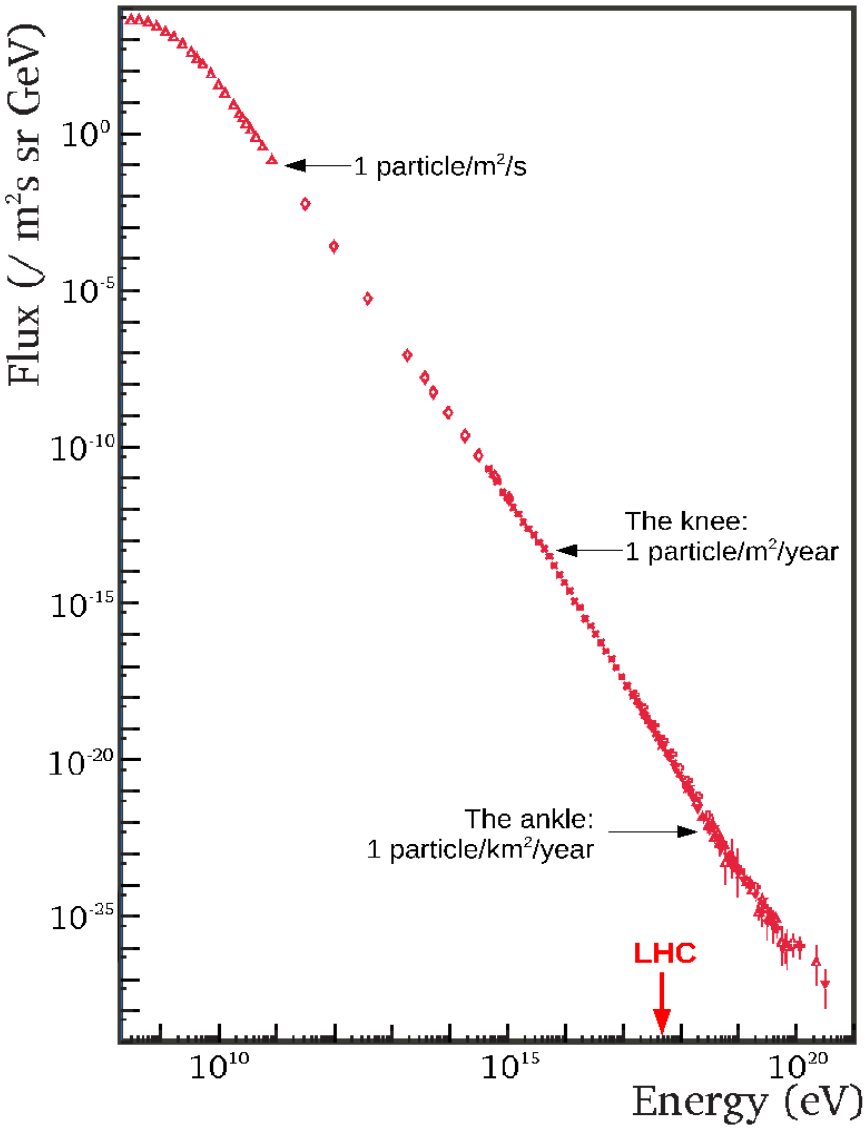

Figure 1.1: Observed spectrum of cosmic-rays. This spectrum follows a power law with small deviations at the points labelled 'knee' and 'ankle' (13). The equivalent centre-of-mass energy for proton-proton collisions at the LHC is also shown.

exploded thousands of years ago to be the sources of cosmic-rays (16). The flux of cosmic-rays that escape from the galaxy can then easily be replenished by new supernova explosions, of which 3 ten-solar-mass supernovae occur per century on

average. Scattering by the galactic magnetic field makes it impossible to trace lower energy cosmic-rays back to their specific sources. There is evidence for a gradual change in the composition of cosmic-rays around the knee to heavier nuclei, probably due to lighter elements reaching the required rigidity to allow their escape from the galaxy (17).

The ankle could represent a transition between galactic and extragalactic sources, or occur due to pair production as a result of the interaction of protons with the CMB (18), (19):

$$p + \gamma \rightarrow p + e^{+} + e^{-} \tag{1.2}$$

Observation of the mass composition of cosmic-rays around the ankle will help determine the correct interpretation of the spectral features and, ultimately, the source model. If the cosmic-rays at energies below the ankle are predominantly iron then galactic to extragalactic source transition models are favoured. However, a proton dominated composition below the ankle favours the pair-production scenario.

At energies above the ankle observations of cosmic-rays become very difficult due to their small fluxes (less than $1\,\mathrm{km}^{-2}\,\mathrm{century}^{-1}$ above $10^{19}\,\mathrm{eV}$), necessitating detectors spanning several km^2 such as the Pierre Auger Observatory. The sources of these cosmic-rays must be some of the most active and turbulent places in the universe (20). Objects such as the cores, jets and hot-spots of active galactic nuclei (AGN) (21), and gamma-ray bursts (GRBs) (22) are being discussed as possible sources. Figure 1.2 shows the differential flux spectrum (multiplied by E^{-3}) for data from the Pierre Auger Observatory (23). This highlights the change in the slope of the flux spectrum at the 'ankle' and indicates a significant downturn in the spectrum at $3 \times 10^{19}\,\mathrm{eV}$, where the index α becomes $\simeq 4.0$. This steepening of the spectrum is widely believed to be due to the GZK effect - i.e. the interaction of UHECR with the CMB - although it could simply be the energy above which sources are no longer able to accelerate cosmic-ray particles. Experimental evidence supporting any of the above theories is still inconclusive.

1.5 Sources of Cosmic-Rays

The exact mechanisms that accelerate cosmic-rays are still uncertain. For cosmic-rays in the region of tens to hundreds of TeV, diffusive shock acceleration in supernova shocks is a likely candidate as a spectrum with index $\alpha \simeq 2 - 2.5$ can be produced. Diffusive shock acceleration is also a plausible acceleration mechanism for much higher energy cosmic-rays, provided the size of the acceleration region and associated magnetic fields are large enough. Particles are swept up by a passing shock front, deflect off magnetic field irregularities within the shock, and ricochet back across the shock front. The number of crossings is proportional to the energy of the shock. After a large number of crossings, the accelerated particle will escape via the trailing edge of the shock having been significantly boosted in energy (25). This mechanism appears to be efficient at accelerating particles to high energies with up to 10% of the shock energy transferred to the

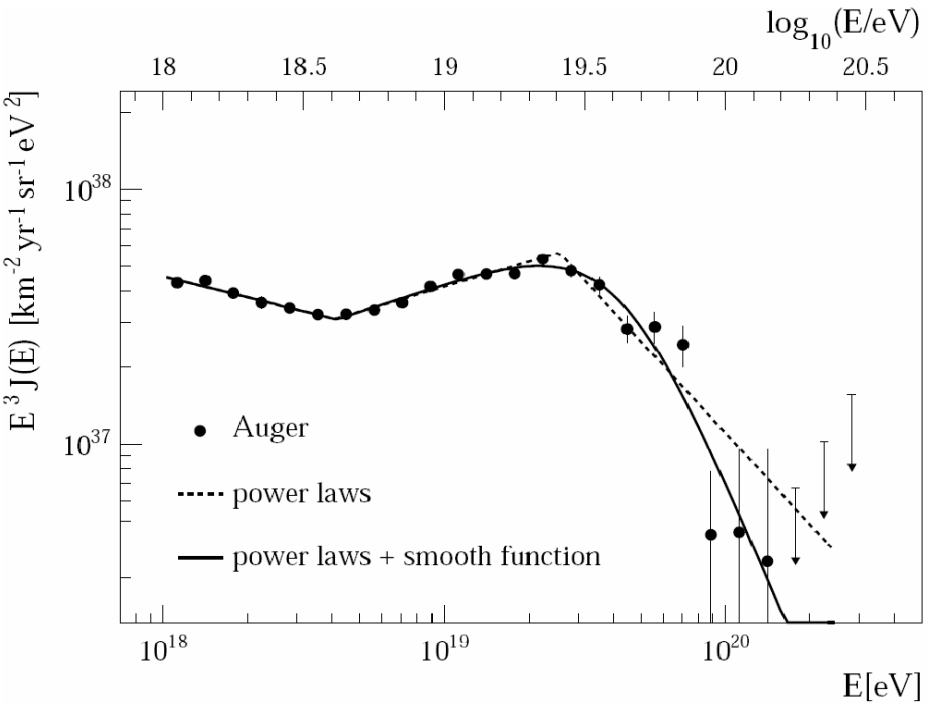

Figure 1.2: Differential flux spectrum (multiplied by E^{-3}) of cosmic-rays above 10^{18} eV as detected by the Pierre Auger Observatory (24).

particles. If the magnetic fields in the shock front have been driven into tight spirals by stellar winds then the amount of particle acceleration will be larger (26). The maximum energy a particle can take from the shock is given by:

$$E_{max} = kZeB\beta_s R \tag{1.3}$$

where β_s is the shock velocity, B the magnetic field strength, R the size of the shock region, Z the atomic number of the particle being accelerated and e the charge on an electron.

Few sources are capable of accelerating cosmic-rays to the highest energies observed. The criteria laid down by Hillas in 1984 describe the size and strength of the magnetic field required to accelerate cosmic-rays by Fermi acceleration processes to a given energy (27). The average size and magnetic field of some potential sources are shown in figure 1.3. The minimum diameter of the acceleration region is given by twice the Larmor radius of a particle of charge Z and energy E in a magnetic field B (27). Particles with a Larmor radius greater than the size of the acceleration region will be able to escape the source. Protons are less easy to accelerate than iron nuclei due to their charge. Figure 1.3 illustrates a large difference between proton and iron requirements (dashed and dot-dashed lines) assuming a shock speed $\beta_s = 1$. For slower shock speeds the requirements are larger. Determination of the cosmic-ray composition will thus enable the range of required source sizes and magnetic fields to be constrained.

At the highest energies the most extreme environments are required for such acceleration to occur. Active galactic nuclei and associated radio jets, galaxy clusters, magnetars, gamma-ray bursts and various 'top-down' mechanisms have all been suggested as sources of UHECR. It is likely that a combination of such sources could contribute to the total flux above 10^{18} eV. However, even the most optimistic model predictions of currently known astrophysical objects have not been able to explain the origin of the highest energy cosmic-rays known (those above $\simeq 10^{20}$ eV).

One object of particular interest is the radio galaxy Centaurus A (Cen A or NGC 5128, figure 1.4) as this is the closest radio galaxy potentially capable of

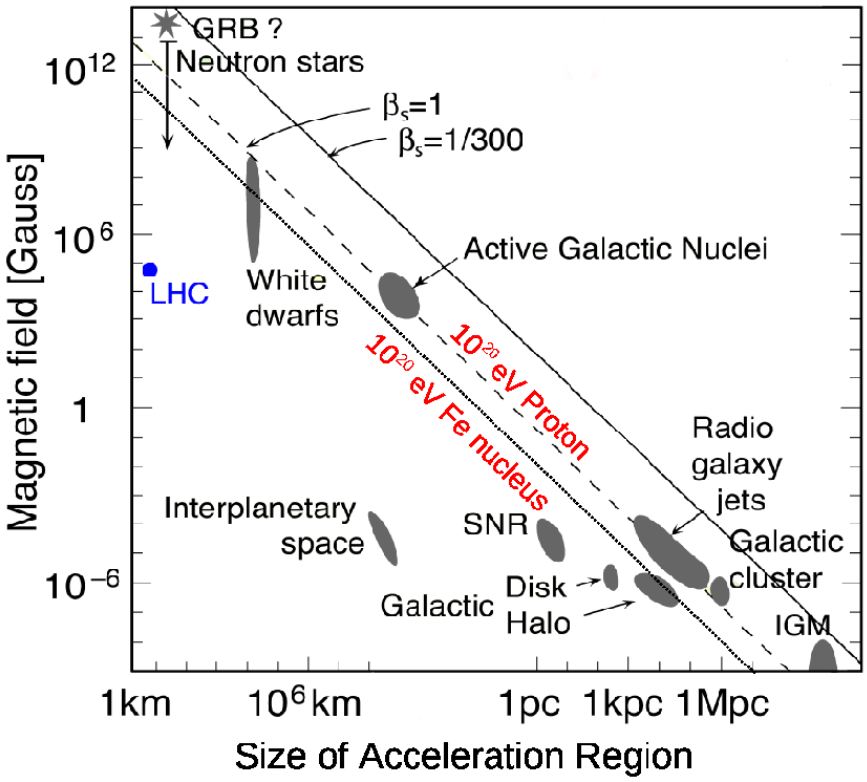

Figure 1.3: The Hillas plot showing the magnetic field strength of some astrophysical objects as a function of their size. The diagonal lines represent the range of minimum magnetic fields and source radii required to accelerate a cosmic-ray proton (solid and dashed lines) and iron nuclei (dot-dashed line) to 10^{20} eV. The equivalent position of the LHC is also shown. Adapted from (27) and (28).

accelerating UHECRs and is within the field of view of the Pierre Auger Observatory. Cen A contains a $(0.5-1.2)\times10^8$ solar-mass black hole at its centre and has two radio lobes spanning 10° in a North-South orientation (29). At 3.7 Mpc away in the southern sky, Cen A is well within the GZK horizon - a limit to the maximum distance a cosmic-ray can travel due to the GZK effect. Estimated at $50-100$ Mpc for cosmic-rays above 3×10^{19} eV the GZK horizon severely reduces the number of possible UHECR sources. Deflections of cosmic-rays from Cen A in intergalactic magnetic fields are expected to be small ($\leq 6°$ for protons) compared to those from more distant sources.

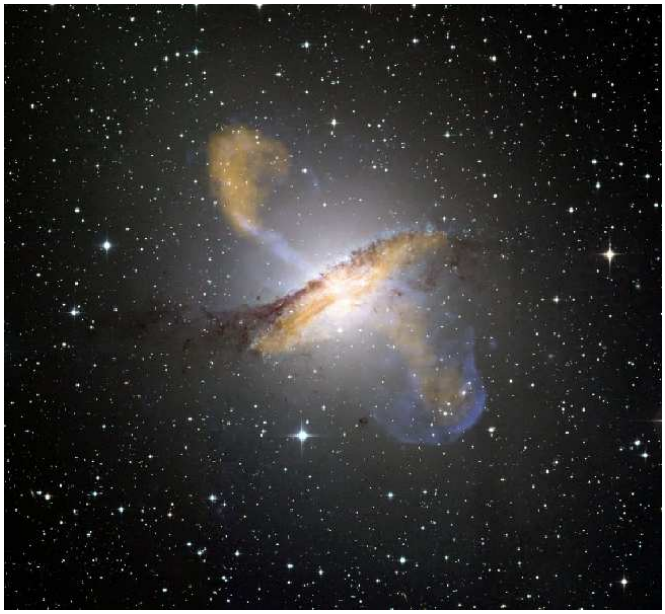

Figure 1.4: Centaurus A in the optical, sub-millimetre and X-ray. Credit: ESO/WFI (Optical); MPIfR/ESO/APEX/A.Weiss et al. (Sub-millimetre); NASA/CXC/CfA/R.Kraft et al. (X-ray). The radio jets span $\simeq 10°$.

Recent attempts have been made by the Pierre Auger Collaboration to determine the flux and composition of cosmic-rays above 55 EeV coming from the vicinity of Cen A (30). Two UHECR events above 57 EeV have been observed to come from within 3° of Cen A (30). However, no definite conclusion has yet been made whether these events originate from Cen A or from the Centaurus cluster behind (at $\simeq 45\,\mathrm{Mpc}$).

Many models have been created to determine whether Cen A is capable of accelerating cosmic-rays to ultra-high energies (21), (31). Scepticism remains as to whether protons could be accelerated to more than $10^{19}\,\mathrm{eV}$ in the jets of radio galaxies (29). In the context of a multi-wavelength approach, Cen A has been observed by a multitude of instruments across all wavelengths, most recently by the Fermi-LAT at GeV energies (32) and by H.E.S.S. in the TeV γ-ray regime (29). Comparison of these observations to model predictions (normalised to the Pierre Auger Observatory results) have led to the hypothesis by Kachelriess et

al. that the region around the core of Cen A and the inner radio lobes form the acceleration region, if any, for UHECR (33). However, this hypothesis relies heavily on many assumptions concerning the acceleration model and injection spectrum. It remains possible that cosmic-rays from the direction of Cen A originate from an unknown source behind Cen A or, if they are iron nuclei, have been subjected to greater deflections by galactic magnetic fields and therefore come from other nearby sources. In the northern sky the Virgo super-cluster has also been suggested as a potential source of UHECR.

Gamma-Ray Bursts (GRBs) have been suggested as another potential source of UHECR. Despite their numerous detections, relatively little is known about GRBs. The 'Fireball Model' may describe the acceleration of particles within GRBs. In this model a compact source releases energy over a short timescale creating a series of relativistic shock fronts and producing beamed emission. The out-flowing material in internal shock fronts have different Γ-factors whilst the external shock is due to collisions with the surrounding medium. It is proposed that UHECR could be accelerated first by the external shock and then by the internal shocks through some Fermi acceleration mechanism (22). Such a model appears to favour mixed compositions (34), although some authors (e.g. (35)) disagree. If GRBs are sources of UHECR this could explain the low observed anisotropy and imply a mixture of galactic and extragalactic cosmic-rays incident upon Earth.

1.6 The Propagation of Cosmic-Rays

1.6.1 Deflection by Magnetic Fields

To reach Earth, cosmic-rays must travel through the galactic magnetic field and, if from an extragalactic source, through extragalactic magnetic fields. The amount a charged particle is deflected by is dependent on its charge, energy, magnetic field strength and angle to the magnetic field. Lower energy cosmic-rays are deflected more than higher energy cosmic-rays. Likewise, heavier nuclei are deflected more

than lighter nuclei due to their greater charges. Photons are not deflected by magnetic fields.

To calculate the magnitude of the deflection and so attempt to track a cosmic-ray back to its source region, the strength, direction and coherence length - the scale over which the magnetic field strength and direction are the same - of the relevant field must be known. Unfortunately, relatively little is known about the detailed magnetic field structure in our galaxy and even less about extragalactic magnetic fields.

The nearby large scale structure of the magnetic field within the disk has been probed using the rotation measures of pulsars and by observing the Zeeman splitting of the 21 cm line in neutral hydrogen (HI regions). If the magnetic field is parallel to the observer's line of sight, the Zeeman effect is observed as two circularly polarized components of the spectral line. In the case of neutral hydrogen these components are separated by $\simeq 28\,\mathrm{GHz\,T^{-1}}$.

Magnetic field lines in the Milky Way roughly follow the optical spiral arms and are believed to reverse direction between them (36). This is known as the Bi-symmetric spiral model and is illustrated in figure 1.5. The magnetic field strength is thought to average $3\,\mu$G and is stronger in localised areas such as star forming regions. The coherence length of the galactic magnetic field is believed to be of the order of $\simeq 1\,\mathrm{kpc}$. The coherence length and the strengths of small scale fields are the main source of uncertainty when mapping the galactic magnetic field. The magnetic field strength in the galactic halo is more difficult to observe. However, it is believed to be approximately $\frac{1}{10}$ of that in the disk and has an orientation analogous to the magnetic field of a bar magnet placed at the galactic centre, perpendicular to the galactic disk (36).

The gyro-radius of a charged particle of energy E, mass m and charge q in a magnetic field B is given by:

$$r = \frac{E}{qv \times B} \tag{1.4}$$

Using current estimates for the galactic magnetic field strength a $10^{19}\,\mathrm{eV}$ proton travelling in the galactic disk will have a gyro-radius of approximately 10

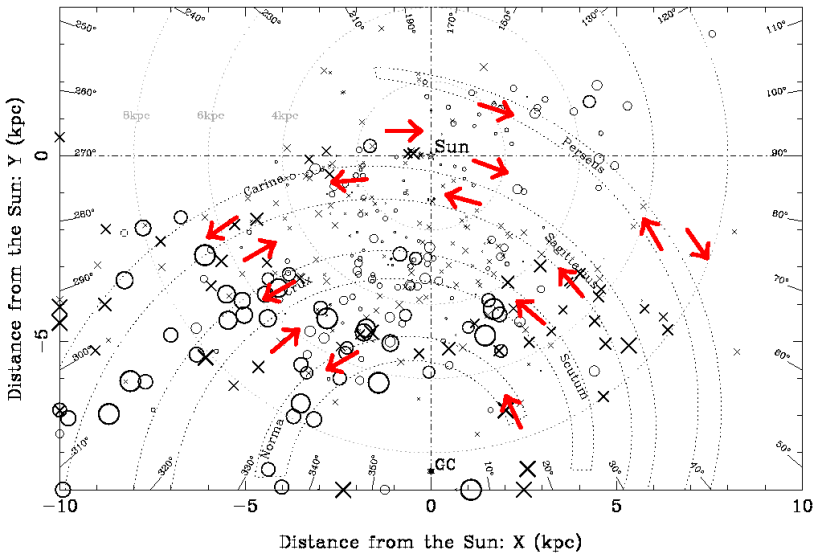

Figure 1.5: An illustration of the magnetic field lines in the disk of the Milky Way Galaxy. The magnetic field lines (red arrows) roughly follow the spiral arms (dotted lines) and reverse direction between them. Crosses represent positive rotation measures, open circles represent negative rotation measures. Figure from (36).

kpc, much greater than the disk thickness (100 pc), and suffers minimal deflections ($\simeq 1^\circ$ over the thickness of the galactic disk). In contrast, a proton of energy 10^{15} eV will have a gyro-radius of $\simeq 1$ pc - much less than the disk thickness. Hence cosmic-rays with gyro-radii smaller than the size of the galactic disk cannot be tracked back to their source region. Deflections of cosmic-rays in the galactic halo are expected to be of the same order as those in the galactic disk for the same energy.

Cosmic-rays from extragalactic sources will be affected by extragalactic magnetic fields. The extragalactic magnetic field strength has been estimated at $\simeq 1$ nG over a coherence length of $1 - 10$ Mpc (37), providing significant deflections for cosmic-rays. A 10^{19} eV cosmic-ray proton propagating to Earth from a distance of 3.8 Mpc (the distance to Cen A) is expected to be deflected by $\lesssim 6^\circ$ assuming a magnetic field perpendicular to the line of sight.

1.6.2 The GZK Effect

The GZK effect is the interaction of cosmic-rays of energy greater than $\simeq 5 \times 10^{19}$ eV with cosmic microwave background (CMB) photons and predicts the existence of UHECR photons and a steepening in the cosmic-ray spectrum (38). The original model predicted a sharp cut-off in the spectrum, however it is now believed to merely cause a steepening of the cosmic-ray spectrum (11). There are several possible interactions involved in the GZK mechanism which depend upon the specific cosmic-ray source composition. If the cosmic-rays at the source are protons then interaction with the CMB will result in a Δ^+ resonance that decays after a mean rest frame lifetime of 10^{-23} s to a proton and a neutral pion:

$$p + \gamma_{\mathrm{CMB}} \rightarrow \Delta^+ \rightarrow p + \pi^0 \tag{1.5}$$

After an average lifetime of 8.4×10^{-17} s, times the Lorentz factor Γ, the resulting pion decays to two photons with a combined energy of $\simeq \frac{1}{6}$ that of the primary cosmic-ray proton.

The GZK mechanism also predicts the production of neutrons and charged pions from the interaction of protons with the CMB, and the creation of neutrons or protons and lighter nuclei from the photo-disintegration of heavier nuclei by CMB photons (38):

$$\begin{aligned} p + \gamma_{\mathrm{CMB}} &\rightarrow \Delta^+ \rightarrow n + \pi^+ \\ A + \gamma_{\mathrm{CMB}} &\rightarrow (A-1) + n \end{aligned} \tag{1.6}$$

Importantly, neither of these two interactions produce photons. Therefore the only channel by which photons can be directly produced is the decay of the π^0 in equation 1.5. Theoretically it is possible that a proton from the decay of a neutron produced by either channel in equation 1.6 could have sufficient energy to interact again with the CMB (as in equation 1.5), thereby producing photons. However, the likelihood of this is small. The GZK effect is predicted to occur for cosmic-rays above a threshold energy of $\simeq 5 \times 10^{19}$ eV, assuming a CMB photon energy of 10^{-4} eV.

Many factors involved in the calculation of the flux of photons from the GZK model are uncertain. First, the energy of the cosmic-rays at their source is unknown and dependent upon the power of the source and the acceleration mechanisms involved (38). Second, the exact shape of the proton spectrum at the source is uncertain. Third, the propagation distances of photons from the source to the Earth vary due to further (energy dependent) interaction with the CMB and radio background; the latter of which is also uncertain (38). Finally the mass composition is unknown and likely to be a mixture of many different types of nuclei, as implied by e.g. (39). Further, the CMB is a black-body spectrum at 2.7 K. This implies the possibility for the interaction of lower energy cosmic rays (down to $\simeq 3 \times 10^{19}\,\mathrm{eV}$) with the high-frequency tail of the CMB spectrum (11).

The observed steepening of the flux spectrum at $3 \times 10^{19}\,\mathrm{eV}$ is believed to be evidence of the GZK effect (see figure 1.2). It could, however, simply be an indication of a lack of sources capable of accelerating particles to higher energies. The detection of photons above the GZK threshold would imply a proton component in the source spectrum, thus constraining the fraction of cosmic-ray protons and the required size and magnetic field strengths of sources. Accurate determination of the photon component of UHECRs would therefore provide an indication of the nature of underlying acceleration mechanisms and improve our understanding of potential sources.

The GZK horizon can be calculated as a function of energy for hadronic primaries, thus limiting the range of possible source locations. A proton with energy $\geq 3 \times 10^{19}\,\mathrm{eV}$ detected at Earth cannot have travelled more than $\simeq 100\,\mathrm{Mpc}$, otherwise interaction with the CMB would have occurred (11), (34). For an iron nucleus this distance is approximately the same. The products of the GZK mechanism are able to further interact with the CMB and other background radiation fields, provided their energy is still sufficient to do so. The interaction of a photon with a background radiation field creates electron-positron pairs. These are free to interact again with background radiation fields, initiating an electromagnetic cascade which propagates for several Mpc through the intergalactic medium.

Figure 1.6 shows the propagation distance of UHECR photons as a function of energy. The propagation distance of photons that interact with the optical, UV and cosmic microwave background fields are relatively well quantified (40). Less certain is the distance travelled by photons that interact with the radio background. To be observed on Earth, 10^{19} eV photons must therefore originate from protons from sources much closer than $50 - 100$ Mpc (40). The nearest radio galaxies potentially capable of accelerating protons to energies above 10^{19} eV are a few Mpc from Earth, of which Cen A is one of the closest.

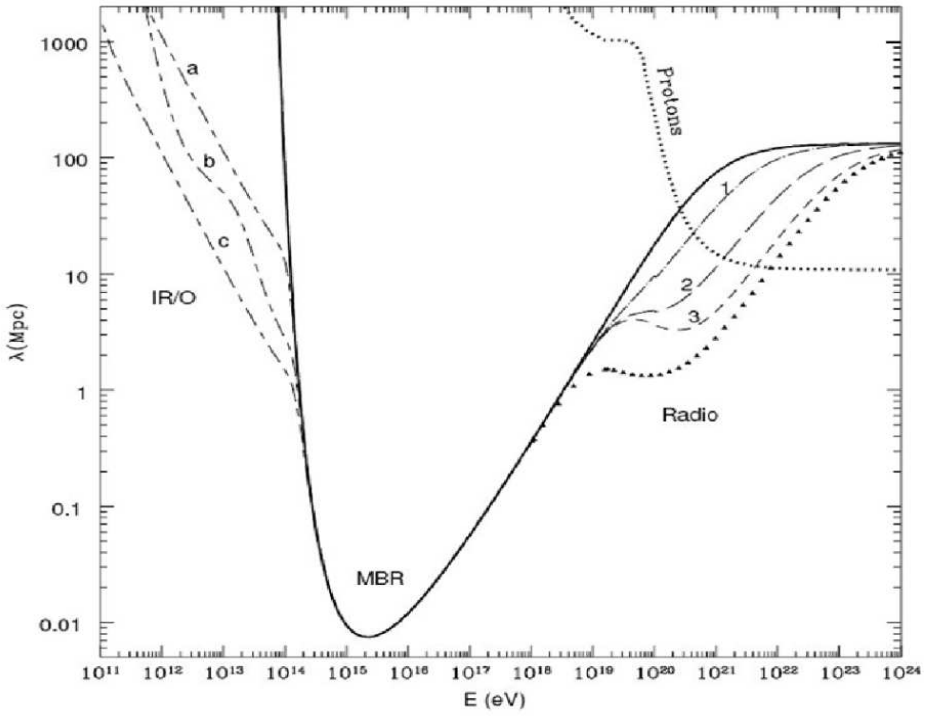

Figure 1.6: The mean free path of UHE photons and protons as a function of energy due to their interaction with background radiation fields (40). Dot-dashed lines a, b, c and dashed lines 1, 2, 3 indicate predictions from different IR and radio background models respectively.

UHE neutrinos are also expected to be created if the product of a GZK interaction of a proton with the CMB involves a charged pion (equation 1.5). The pion will subsequently decay to a muon and a muon neutrino. Further decay of

the muon to an electron would produce two further UHE neutrinos:

$$\pi^{\pm} \rightarrow \mu^{\pm} + \nu_{\mu}(\bar{\nu_{\mu}}) \rightarrow e^{\pm} + \nu_{e}(\bar{\nu_{e}}) + \nu_{\mu}(\bar{\nu_{\mu}}) \tag{1.7}$$

The interaction of a neutron with the CMB would also yield electron neutrinos via similar particle cascades (41). No UHE neutrinos have been observed to date. Upper limits to the UHE neutrino flux have been imposed using data from the Pierre Auger Observatory (42).

1.6.3 Top-Down Models

Many theories involving 'new' physics, popular when AGASA was in operation, were created to explain the lack of a downturn in the cosmic-ray spectrum reported by AGASA (43). These models avoid the difficulties encountered in 'bottom-up' acceleration models where the size of the acceleration region, the magnetic field strength and energy losses experienced by the propagation of cosmic-rays place serious constraints on the maximum attainable cosmic-ray energy and fail to explain the most energetic cosmic-rays. Top-down models include relic particle decays from super-heavy dark-matter (SHDM), topological defects and the Z-burst model (44). A common theme is the decay or annihilation of super-heavy ($\geq 10^{22}\,\mathrm{eV/c^2}$) hypothetical particles to produce large fractions of photons and neutrinos above $10^{18}\,\mathrm{eV}$ from nearby sources (e.g. $\geq 40\%$ at $3 \times 10^{19}\,\mathrm{eV}$ for SHDM) (45). As a result, top-down models predict a much flatter spectrum and different particle composition above a few times $10^{19}\,\mathrm{eV}$ compared to the GZK mechanism (46).

Recent strong evidence ($\geq 20\sigma$) of the steepening of the flux spectrum above $10^{19}\,\mathrm{eV}$, combined with current constraints on the UHECR photon flux (47), (48) makes the majority of top-down models unlikely at best, with only the Z-burst model not yet excluded by limits to the flux and photon fraction. The Z-burst model predicts photons from the interaction of UHECR neutrinos with the massive ($\simeq 0.1\,\mathrm{eV}$) relic neutrino background. Z-bursts are predicted close to large concentrations of matter due to their gravitational attraction. Gamma-ray photons are subsequently emitted from the decay of the Z^0 particle (which

has a lifetime of 10^{-25} s) creating relativistic beamed particles; a 'Z-burst' (49). However, the necessary fluxes of ultra high energy neutrinos given in this model are improbable given constraints from lower energy measurements with the LEP (44).

Thus far no UHECR photons have been detected. Improved limits from the accumulation of new data and the refinement of existing parameters capable of distinguishing photon from hadron-initiated air showers will, in the near future, begin to extend down into the predicted GZK-region and detections of photons may be possible.

1.7 Physics of Air Showers

When an ultra high energy cosmic-ray impacts the Earth's atmosphere it interacts with atmospheric molecules creating particle cascades or 'extensive air showers' (EAS) which spread laterally over several square kilometres as they evolve. The size of these particle cascades are dependent upon the energy and type of incident primary particle. Cosmic-ray primaries with energy greater than 100 TeV are able to produce cascades which penetrate down to sea level and thus can be observed by ground based arrays. Due to the attenuation of particles in the atmosphere, lower energy air showers do not reach ground level.

Key to the determination of the incoming primary particle type is the measurement of observables that describe the significant differences between photon and hadron-initiated air showers. These include: the depth of shower maximum, the time spread of the shower, the shape of the shower front, muon content, and the lateral spread of the shower. It is the aim of mass-composition studies, including photon limit work, to distinguish different primary types using a variety of different techniques. This is most easily done between hadrons and photons where the differences are greatest. Thus far such differences have only been determined on an average basis, not on an event-by-event basis (47). The development of photon and hadron-initiated air showers are described in the following sections.

1.7.1 Photon Primaries

UHECR photons interact with the Earth's atmosphere to form an electromagnetic cascade. An electron-positron pair is created from the interaction of the primary photon with electric fields in atmospheric nuclei after a mean free path length $\lambda = 37\,\mathrm{g\,cm^{-2}}$ has been traversed (9). The electron (or positron) will travel an average distance $d = X_0 ln2$ ($\mathrm{g\,cm^{-2}}$), where $X_0 = 9/7\lambda$ is the radiation length, before emitting photons via bremsstrahlung radiation. Bremsstrahlung photons produced in air showers can, after travelling a further mean free path length λ, produce electron-positron pairs which may in turn interact with nuclear electric fields, emitting more bremsstrahlung radiation. This is illustrated in figure 1.7.

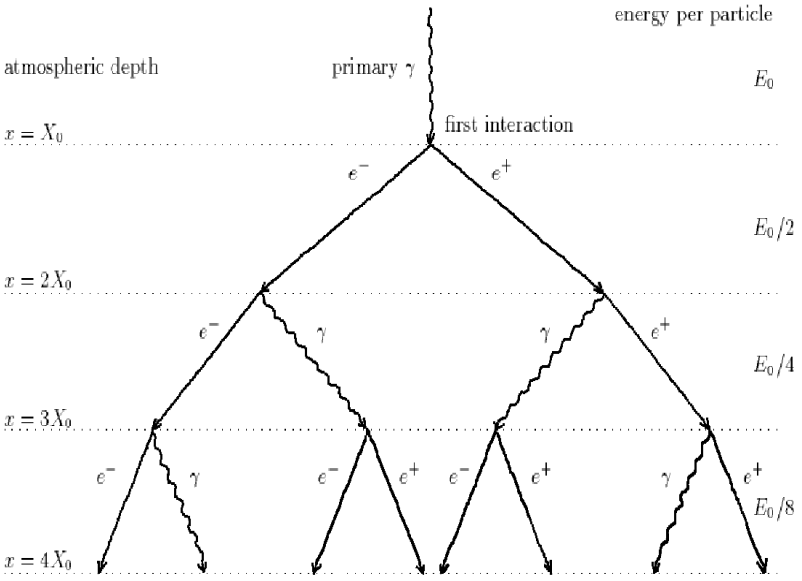

Figure 1.7: A schematic of the early stages of EAS development for a photon-initiated cascade (Not to scale.) (50).

This process continues until the energy of a given particle falls below a critical energy ϵ_c, at which the rate of energy loss to particle production (from bremsstrahlung processes) is equal to the rate of energy loss by ionisation. $\epsilon_\mathrm{c} = 84\,\mathrm{MeV}$ for electrons in air. Particles whose energies fall below the critical energy

continue to propagate towards the ground until they are either attenuated by the atmosphere or impact the ground.

In this simplified model (the 'Heitler model'), the number of particles produced in a photon initiated air shower after N interactions is $\sim 2^N$ and each particle has on average an energy $\mathrm{E} = \frac{\mathrm{E}_0}{2^\mathrm{N}}$, where E_0 is the initial energy of the incident photon (51). Using more realistic, detailed models that include quantum electrodynamics, the total number of particles in a 10^{18} eV photon initiated shower is of the order of 10^{10} particles at shower maximum.

The depth of maximum, X_{max}, is defined as the depth (in $\mathrm{g\,cm^{-2}}$) from the top of the atmosphere to the point at which, on average across all shower particles, the rate of energy loss by ionisation equals the rate of energy loss by interaction (51). This is also the depth at which the number of particles in the cascade is maximum. In this model, $\mathrm{X_{max}}$ can be approximated by:

$$X_{max} = X_0\, ln(N_{max}) = 2.3 X_0\, log_{10}(\frac{E_0}{\epsilon_c}) \tag{1.8}$$

where $\mathrm{N_{max}}$ is the number of particles at shower maximum and X_0 the radiation length.

The depth of maximum increases almost linearly with log energy, at a rate of $\simeq 85\,\mathrm{g\,cm^{-2}}$ per decade in energy, between 10^{14} and 10^{18} eV. This is illustrated by the black line in figure 1.8. Whilst the 'Heitler model' is a very simplified model to illustrate the concept of air-showers, full Monte-Carlo simulations of photon initiated air-showers using QED theory are possible and have been used to predict the elongation rate shown in figure 1.8.

Above 10^{18} eV the elongation rate (rate of change of $\mathrm{X_{max}}$ with log energy) increases rapidly until $\simeq 10^{20}$ eV due to a process known as the LPM effect. The LPM (Landau, Pomeranchuk and Migdal) effect is the suppression of the interaction cross section for both pair production and bremsstrahlung radiation due to quantum mechanical interference (52), (53), (54). Interaction cross sections describe the interaction probability, which relates directly to the interaction length. Interaction lengths of photons with energies above $\simeq 10^{19}$ eV are therefore longer than at lower energies, hence shower particles interact less frequently with the

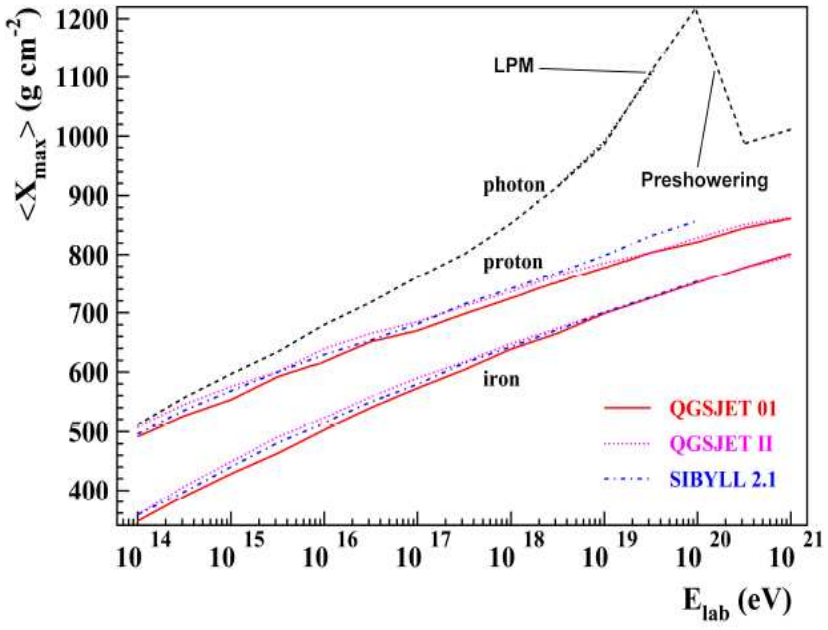

Figure 1.8: The average depth of maximum simulated for photons, protons and iron nuclei with energy. The top of the atmosphere is at $0\,\mathrm{g\,cm^{-2}}$ by convention. The LPM and pre-showering effect are also labelled for photon primaries (see text for definitions) (48).

atmosphere and so a deeper depth of maximum is achieved. This suppression of the cross section is also theoretically possible for hadronic showers (54). The energies at which the LPM effect is predicted to occur in hadronic air showers is well in excess of $10^{23}\,\mathrm{eV}$, much higher than the energy of any cosmic-ray observed to date; therefore only the LPM effect for photon initiated EAS need be considered.

At energies larger than $\sim 10^{20}\,\mathrm{eV}$ the elongation rate decreases again due to pre-showering. Pre-showering can be thought of conceptually as an air shower that begins early - well above the atmosphere. At energies above $\sim 10^{20}\,\mathrm{eV}$ an incoming photon can interact with the Earth's magnetic field before reaching the atmosphere, pair producing electrons and positrons. These electrons can then interact with the Earth's magnetic field. These two interactions can happen a number of times before the top of the atmosphere is reached. Instead of one pho-

ton of energy E_0 initiating a shower at the top of the atmosphere, N simultaneous photon and electron initiated showers each of energy $\simeq$ E/N are created. The result of pre-showering is to reduce the depth of maximum (55). Pre-showering cannot happen for hadronic primaries.

Photon initiated showers are dominated by secondary photons and electrons in the approximate ratio 10:1. The production of muons from the interaction of photons with protons in atmospheric nuclei via the creation of neutrons and charged pions is also possible:

$$p + \gamma \rightarrow n + \pi^+ \rightarrow n + \mu^+ + \bar{\nu} \tag{1.9}$$

However, this is suppressed by a factor of more than 200.

1.7.2 Hadronic Primaries

The development of hadronic showers in the atmosphere is substantially different to that of photons. A proton interacts in an inelastic collision with atmospheric nuclei, losing about half its initial energy and producing pions (see, for example, (51) for a simple introduction). On average equal numbers of all three types of pions are produced. A leading particle carrying most of the initial proton's energy is also produced, which can continue to interact with atmospheric nuclei, producing more pions. This process continues until the energy of the leading particle falls below the critical energy for pion production ($\epsilon_c = 140\,\mathrm{GeV}$). Typically for a $10^{18}\,\mathrm{eV}$ primary particle around 10^{12} secondaries are produced.

Resulting neutral pions (π^0) decay after a mean lifetime of $8.4 \times 10^{-17}\,\mathrm{s}$ times the Lorentz factor, Γ to pairs of photons which then initiate electromagnetic sub-showers as described in section 1.7.1. These sub-showers will continue to cascade until the energy losses due to ionisation exceed those due to bremsstrahlung, when particle multiplication stops and attenuation dominates. The average energy of the photons which initiate each sub-shower can be approximated by:

$$E_\gamma = \frac{\kappa E_0}{6 N_\pi} \tag{1.10}$$

where E_0 is the energy of the primary particle, N_π is the number of pions and κ is the inelasticity (51).

Charged pions can interact again with atmospheric nuclei (with an interaction length of $\lambda_{\mathrm{I}} = 120\,\mathrm{g\,cm^{-2}}$) to produce hadronic sub-showers consisting primarily of lower energy pions. Pions can also decay to muons in a mean rest-frame lifetime of $2.6 \times 10^{-8}\,\mathrm{s}$. At ground, the average ratio of photons to electrons and muons is 100:10:1 for hadronic EAS. The muonic component is thus substantially larger for hadronic than for photon initiated showers, with approximately 10% of the primary particle energy converted to muons and neutrinos whilst the remainder goes into the electromagnetic component (56).

This model for proton primaries can be extended to heavier nuclei. The development of a cascade initiated by a nucleus with A nucleons and energy E_0 can be approximated by A simultaneous proton-initiated showers of initial energy $\frac{E_0}{A}$. Using this assumption, the depth of maximum for a hadronic primary can be approximated by (51):

$$X_{max} = \lambda_I + 2.3\lambda_r log_{10}(\frac{\kappa E_0}{6AN_\pi\epsilon_c}) \tag{1.11}$$

where $\lambda_{\mathrm{I}} = 80\,\mathrm{g\,cm^{-2}}$ is the interaction length of a proton.

From equation 1.11 it can be seen that $\mathrm{X_{max}}$, and hence the elongation rate, depends upon the mass of the primary particle. Therefore a change in the elongation rate implies a change in the mass of the primary particle, assuming that the interaction cross section and particle physics does not change significantly at high energies (39). Figure 1.8 shows different model predictions for the elongation rate of both iron and proton initiated cascades. These predictions have been obtained from full Monte-Carlo simulations of hadronic EAS.

The above description for the development of hadronic air showers is a good general description but contains a number of simplifications. Detailed models, however, do not exactly match data for a number of reasons. Firstly, the proton-air interaction cross section is not known at these energies and has been extrapolated from collider data for much lower energy (proton-proton) collisions. Secondly, the pion multiplicity N_π and the inelasticity κ are not well known due

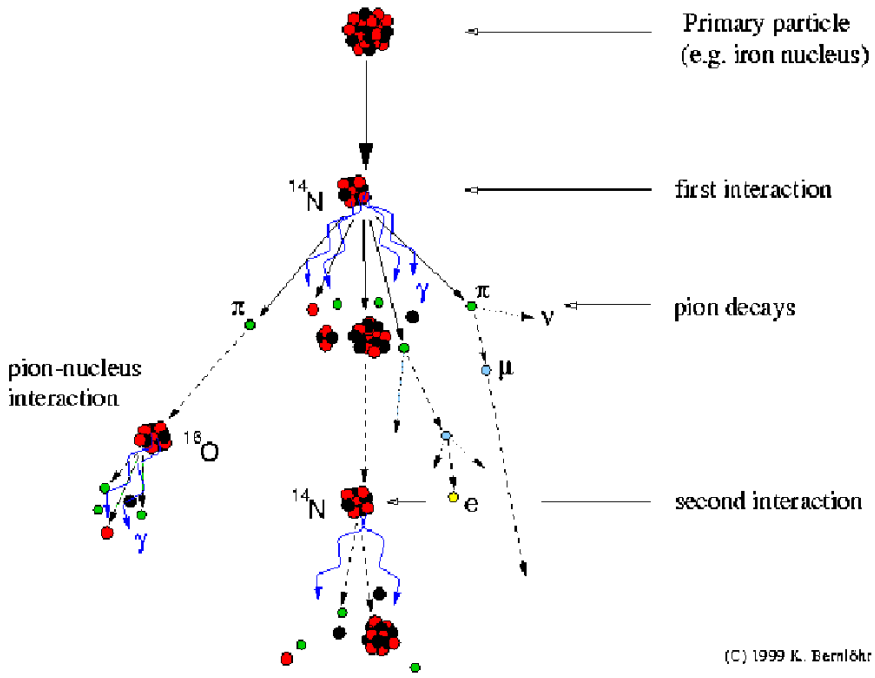

Figure 1.9: A schematic of the early stages of EAS development for a cascade initiated by an iron nucleus (Not to scale!), Image credit: Bernlöhr 1999.

to discrepancies in the fine details of hadronic interaction models. Measurements with the LHC, in particular the LHCf experiment which studies the interaction of neutral particles in the forward direction, will increase our understanding of these parameters at higher energies and constrain current interaction models at energies of order 10^{17} eV ($\sqrt{S} = 10^4$ GeV).

For both hadronic and photon-initiated showers, the different geometries of each interaction cause the shower to be spread both laterally and in time. As a result, the leading edge of the shower (the shower front) is close to spherical about the shower axis. The lateral distribution, time-spread of the shower particles and curvature of the shower-front can be measured and have been shown to be sensitive to the mass of the primary particle. Each of these observables will be discussed further in chapter 2.

1.8 Cosmic-Rays: The Unanswered Questions

The field of cosmic-ray astrophysics is varied and complex. The energy spectrum is roughly power-law in shape and covers 12 orders of magnitude. A steepening of the spectrum is observed at around 3×10^{19} eV which could indicate the coveted GZK effect (57). Concerning the highest energy cosmic-rays, the composition both at source and at Earth are uncertain, although recent results imply a mixed composition above 3×10^{18} eV, provided our current understanding of particle physics is correct (39).

Three major factors indicate that our understanding of the underlying particle physics is inadequate. Model predictions currently significantly underestimate ($\simeq$ 20%) the muon content of hadronic EAS. The energy reconstructed using (calorimetric) fluorescence detection techniques is also less than the true energy of simulated showers. Finally, recent data from the LHC indicates that our knowledge of particle production mechanisms, including interaction cross-sections, is far from complete.

If the sources of cosmic-rays lie within the nearby universe - within the GZK horizon for example - and have a primarily proton-dominated composition, then an anisotropic distribution of UHECRs is expected. A heavier composition will incur more deflections within galactic and extragalactic magnetic fields and therefore a more isotropic distribution is expected. Determination of the composition may enable the extent of the deflections in galactic and extragalactic magnetic fields to be estimated and provide better constraints on the sources of ultra-high energy cosmic-rays. The detection of a photon component above 10^{19} eV, and the determination of the photon flux will determine whether or not the GZK effect exists as predicted. Until then, limits imposed on the photon flux will constrain some of the more exotic models for their creation. The improvement of mass-sensitive parameters and the addition of a larger data set to impose new limits on the photon fraction forms the focus of this thesis.

Chapter 2

The Pierre Auger Observatory

2.1 Introduction

Located in Malargüe, Argentina, at an altitude of 1.4 km (atmospheric depth 875 g cm^{-2}), the Pierre Auger Observatory consists of 27 fluorescence telescopes (FD) at four locations overlooking an array of 1660 water-Cherenkov detectors (SD) covering an area of 3000 km^2. The Observatory also includes extensive atmospheric monitoring equipment necessary for calibration and the reduction of measurement uncertainties. The layout of the Observatory and the nearest principal town are shown in figure 2.1. Over 300 scientists from 19 countries form the Pierre Auger Collaboration.

The Pierre Auger Observatory was designed to study the flux, mass composition and arrival directions of cosmic-rays above 10^{18} eV with high statistical precision (58). Air showers detected simultaneously by both the fluorescence and surface detectors (hybrid events) can be used to obtain a high-quality data set with better core position reconstruction, energy and X_{max} than FD or SD measurements alone. Additionally, the high-statistics provided by surface array data can be used on its own. This makes the Pierre Auger Observatory a unique hybrid detector. The large area covered by the Observatory is beneficial for the detection of small fluxes of UHECRs and the accumulation of unprecedented statistics. Data taking started in January 2004 with completion of the array in June 2008.

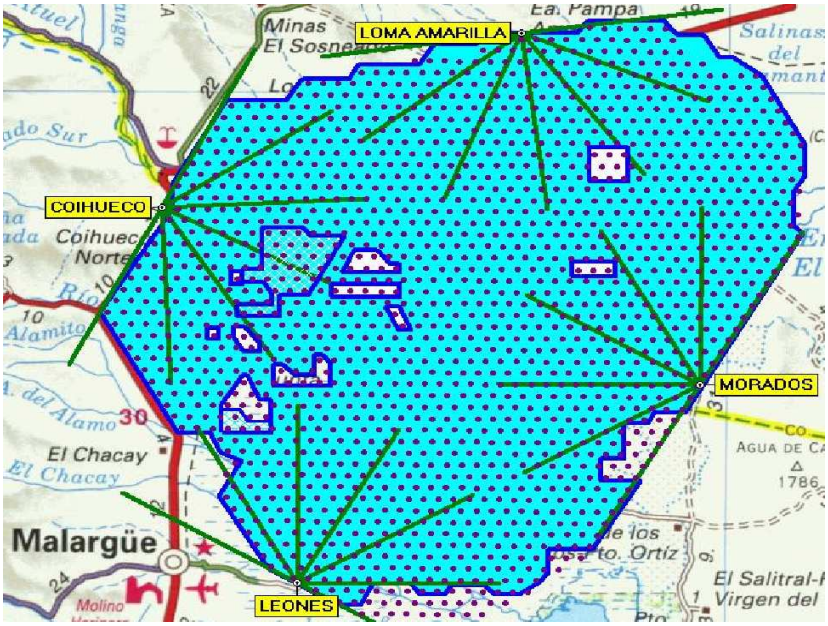

Figure 2.1: The layout of the Pierre Auger Observatory. Closed circles indicate the position of 1600 surface detectors covering an area of 3000 km^2 (shaded blue). Green lines indicate the field of view of each fluorescence telescope. The nearest principal town, Malargüe, is shown in the bottom left hand corner. Extensions to the original design (AMIGA, HEAT, AERA) and atmospheric monitoring stations are not shown.

Since 2009 a number of new components have been added to study cosmic-rays down to 10^{17} eV, including a muon scintillator and water-Cherenkov infill array (AMIGA), three high elevation fluorescence telescopes (HEAT) and an engineering radio array (AERA). These components are still in the construction and initial data taking phases (see references (59), (60) and (61) for more details). The two main components of the Pierre Auger Observatory and some important recent results are described in this chapter.

2.2 The Fluorescence Detectors

Electrons within atmospheric nitrogen molecules are excited by passing charged secondary cosmic-ray particles. The de-excitation of these electrons causes fluorescence light photons to be emitted. Nitrogen fluorescence light is emitted isotropically at a number of discrete wavelengths between 300 and 400 nm (near-UV) corresponding to the molecular band structure of nitrogen (62). Fluorescence telescopes are used to detect this light.

Each fluorescence telescope consists of a 1.7 m diameter diaphragm with a ring of Schmidt optic corrector elements attached to the outer edge. This increases the effective aperture to 2.2 m. A $300 - 400$ nm (UV) filter located behind the diaphragm blocks out unwanted ambient background light, thus increasing the signal to noise ratio. Fluorescence light is collected by a $3.5\,\text{m} \times 3.5\,\text{m}$ segmented mirror focused onto a camera containing 440 hexagonal photomultiplier tubes (PMTs). Each PMT is 45 mm in diameter and has a quantum efficiency of $\simeq 25\%$. A schematic of a fluorescence telescope is shown in figure 2.2. Each telescope is housed in an individual bay within the associated FD building and can be operated and monitored either on-site or from a control centre in Malargüe.

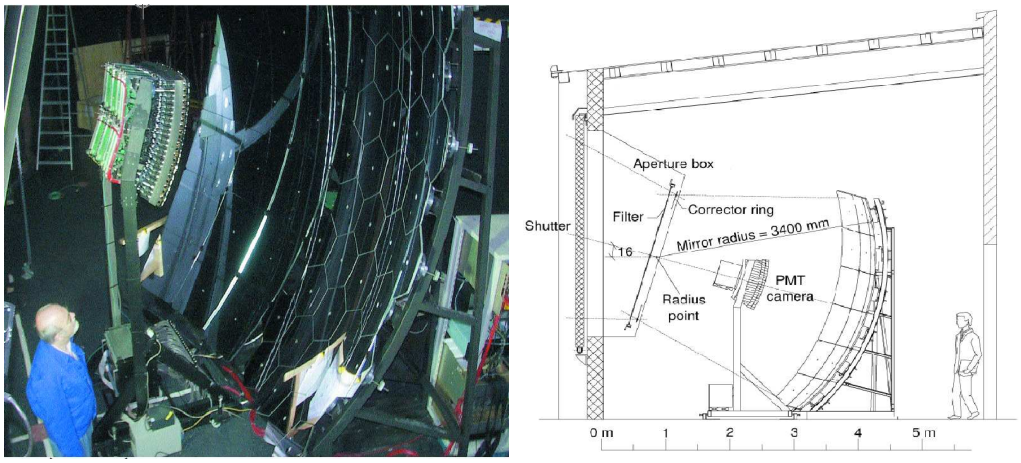

(a) (b)

Figure 2.2: Left: Photograph and Right: A schematic of a fluorescence telescope (58).

The four FD sites are located on hills between 40 and 150 m in elevation at the edge of the array. Each fluorescence telescope has a field of view of $30° \times 30°$ and an elevation of 2° above the horizontal (63). Fluorescence light signals in the PMTs are digitised using a Fast Analogue to Digital Converter (FADC) with a readout rate of 10 MHz. Prior to the energy and direction reconstruction, a second level trigger requires groups of at least 5 adjacent PMTs to be triggered in close succession. A third level trigger, T3, selects shower candidates and performs a quick preliminary reconstruction to eliminate false triggers from background objects such as stars. If the T3 reconstruction is good, the data are sent to the Central Data Acquisition System (CDAS) and stored. At this stage information from the surface array can also be included to form a hybrid event. An example of a fluorescence light profile and an image of a cosmic-ray track are given in figure 2.3.

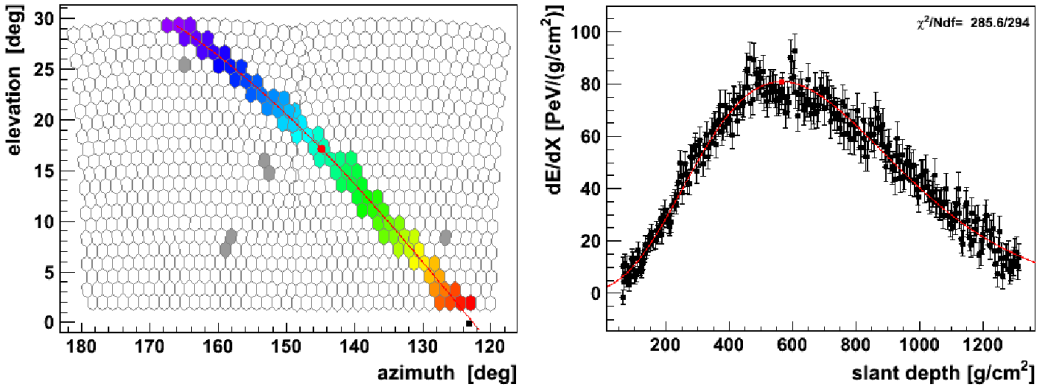

(a) (b)

Figure 2.3: Left: Image of a fluorescence light track observed by two adjacent telescopes. Colours show the time evolution of the shower across the camera from purple (early) to red (late). Right: The corresponding longitudinal profile with a Gaisser-Hillas fit (red line). The shower energy is derived from the integrated energy profile and X_{max} is given by the position of the peak. By convention, the top of the atmosphere is at $0\,\mathrm{gcm}^{-2}$

2.2.1 Fluorescence Energy and X_{max} Reconstruction

The intensity of light in each pixel as a function of time and position on the camera is used for the geometrical reconstruction of the shower and determination of the shower energy and depth of maximum. This is a two-stage process. The geometry of the shower axis with respect to the camera plane and the core location on the ground are identified from the light track across the camera. Timing information is used to determine the distance to the shower axis, R_p, the orientation of the shower axis to the camera, χ_0, and the time of closest approach to the telescope, t_0, by fitting to the function:

$$t_i = t_0 + \frac{R_p}{c} tan(\frac{\chi_0 - \chi_i}{2}) \tag{2.1}$$

where t_i is the trigger time (time of arrival of the light) and χ_i the viewing direction of the shower from the i^{th} pixel (figure 2.4) (58).

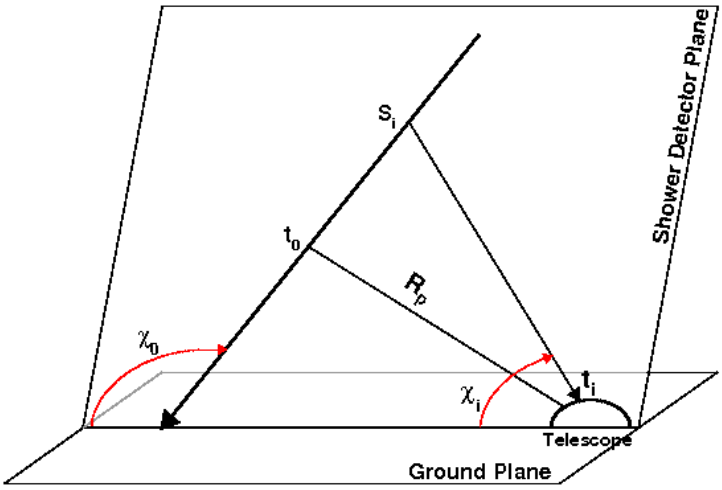

Figure 2.4: Schematic illustrating the geometrical reconstruction of an air shower observed by the fluorescence detectors (see text).

The energy deposited as a function of atmospheric depth is determined from the FADC traces for each camera pixel. Corrections are made for Cherenkov light contamination and Mie/Rayleigh scattering. These corrections depend upon the

shower geometry relative to the telescope and have a systematic uncertainty of 10%. The energy carried by neutrinos and muons must be accounted for when estimating the total shower energy. Corrections for this 'undetected energy' are estimated to be of the order of $15 \pm 5\%$ (63).

The corrected longitudinal energy deposit profile is then fitted with a Gaisser-Hillas function, the tail of which may be extrapolated for very deeply penetrating showers that reach the ground shortly after shower maximum. The shower energy is proportional to the integrated signal multiplied by the fluorescence yield and is independent of the shower development and primary type:

$$E = F_y \int S dX \tag{2.2}$$

where E is the total shower energy in eV, S is the fluorescence signal for a given depth dX and F_y is the fluorescence yield in units of photons per electron per metre.

The fluorescence yield is dependent on atmospheric conditions and the wavelength of light received and is given by:

$$F_y = \epsilon_\lambda(\rho, T) \frac{\lambda \rho_{air}}{hc} \frac{dE}{dX} \tag{2.3}$$

where $\epsilon_\lambda(\rho, T)$ is the fluorescence efficiency for a given wavelength λ as a function of atmospheric density and temperature, ρ_{air} is the density of air and $\frac{\mathrm{dE}}{\mathrm{dX}}$ is the energy deposit at a given depth (63). The fluorescence yield is of the order of 5 fluorescence photons per metre per ionising particle (64). This gives a calorimetric estimation of the shower energy. The depth of shower maximum, X_{max}, is also determined directly from the longitudinal profile and is the atmospheric depth at which the fluorescence signal (and hence the number of secondary particles) is largest.

Due to the small flux of fluorescence light, fluorescence detectors only operate during moonless nights. Minimal cloud cover is required to reduce atmospheric absorption. Given these requirements, the duty cycle of the fluorescence detectors is limited to $\sim 12\%$. The major advantages of the calorimetric energy

reconstruction, the ability to determine X_{max} directly and the calibration of the surface detector energy reconstruction using hybrid events outweighs the limited performance time.

2.2.2 Fluorescence Detector Calibration and Atmospheric Monitoring

Calibration of the fluorescence detectors is performed in two ways: a drum calibration and a sequence of dedicated telescope calibration runs. The 'drum calibration' is performed by placing a diffuse light source over each telescope diaphragm. The ratio of the detected to emitted light intensity is used as an absolute calibration to determine the detector response (signal from the PMTs) as a function of light intensity (65) and is performed only once every few years.

Prior to each night of telescope operation, three dedicated calibration runs are performed. A 375 nm wavelength light source is directed in turn from the mirror centre onto the camera (Cal. A), from the camera edges onto the mirror (Cal. B) and from behind the camera onto reflective targets on the inner shutter edges (Cal. C). The total charge detected by the camera from each of these calibration runs is compared to the drum calibration to determine the performance of the telescopes during each shift.

A detailed understanding of the atmosphere above the Observatory is critical for the accurate reconstruction of shower parameters. The development of an air shower depends on the atmospheric density and temperature, both of which evolve as a function of altitude and the time of day and year. Further, both nitrogen fluorescence and Cherenkov light undergo Mie and Rayleigh scattering, the extent of which is critical for the energy reconstruction.

Atmospheric monitoring is performed by back-scatter Light Detection and Ranging (LIDAR) stations (adjacent to each FD building) and the Central Laser Facility (CLF) to ensure that the most up-to-date information on the local atmosphere is available (66). Installed at the centre of the array, the CLF shines

laser light into the atmosphere at a predetermined sequence of zeniths and directions every hour throughout telescope operation. The reconstructed direction and energy is compared to the laser output and direction. Typically there is a discrepancy of $\simeq 15\%$ in energy due to scattering and absorption (65). CLF 'shot' timing is used to calibrate the GPS timings of the fluorescence and surface detectors.

Similarly, a beam of laser light is directed into the atmosphere from the LIDARs at periodic intervals. The intensity of the returning light collected by the LIDAR mirrors as a function of time is compared to the laser output and used to quantify optical transmission conditions in the vicinity of the fluorescence detectors (67). Infra-red cloud cameras and meteorological weather stations are also used to measure conditions at each FD site.

2.3 The Surface Array

The surface array comprises 1600 water-Cherenkov detectors spaced 1.5 km apart in a hexagonal arrangement. Much of the technology used for the surface detectors was pioneered at the Haverah Park Array which operated in the UK between 1968 and 1987 (68). Each detector consists of a cylindrical, rotationally-moulded polyethylene tank 1.5 m in height and 3.6 m in diameter, giving a surface area of $10\,\mathrm{m}^2$ for the top of the tank. Twelve tonnes of purified water are contained within each tank, inside a Tyvek liner. The purpose of the Tyvek liner is twofold: as a water-tight container to seal out external light; and to reflect and diffuse Cherenkov light created within the detector, which it does with $\simeq 98\%$ efficiency. Three 22.5 cm ($9''$) hemispherical PMTs situated at the top of the detector point down into the water to collect Cherenkov light. Signals from both the anode and the last dynode in each PMT are extracted and digitised using FADCs with a sampling rate of 40 MHz. The signal is amplified $32\times$ between the anode and last dynode (58).

Each station is equipped with its own power supply in the form of a 12 V battery recharged by two solar panels mounted on top of the tank. GPS units

at each detector establish the timing of the FADC signals with a resolution of 7.2 ns. A radio antenna transmits signals to a communications tower situated at the nearest FD site. Signals are then relayed to the Central Data Acquisition Station (CDAS). A photograph and schematic of a surface detector are given in figure 2.5.

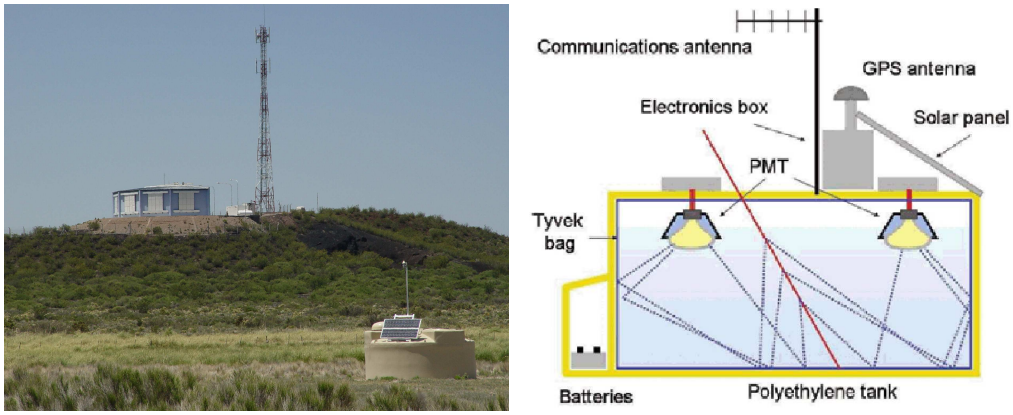

(a) (b)

Figure 2.5: Left: Photograph of a surface detector (foreground) and the Los Leones fluorescence detector building and a communications tower (background). Right: Schematic illustrating the components of a surface detector and the path of Cherenkov light within the detector.

Cherenkov light inside the surface detectors is reflected and diffused off the Tyvek walls several times prior to entering the PMTs. This spreads the signal from an individual particle in time. Signals from surface stations are converted into units of VEM. A VEM (Vertical Equivalent Muon) is defined in both 'peak' and 'charge' units. A 'Peak-VEM' is the signal deposited by a vertical muon in one time-bin of a single PMT (from the dynode signal). A 'Charge-VEM' is the integrated signal, averaged over all 3 PMTs, produced by a muon travelling vertically through the entire depth of the tank and is equivalent to 240 MeV. Unless otherwise specified, 'VEM' refers to 'Charge-VEM'.

Surface station electronics include programmable logic devices used to determine whether local trigger conditions have been passed. The trigger system for

the surface array is a five-step process and is independent of the FD trigger system. The first level, the T1 trigger condition, is local to the detector and requires that either at least 1.75 Peak-VEM is recorded in any one time-bin for all three PMTs in a tank (Single Trigger Condition, STC), or that the signal remains over 0.2 VEM in any 12 out of 120 time bins (0.3 μs in every 3 μs time window) for at least 2 PMTs (Time Over Threshold, ToT) (58). The single trigger condition results in a trigger rate of $\simeq$ 100 Hz while the ToT condition gives a rate of 1.6 Hz. All T1 ToT triggers and any T1 STC triggers over 3 VEM are promoted to the second trigger level, T2.

A 'T2' trigger is used to alert the central computer to a potential air-shower signal. On receipt of a T2 trigger, a search is made for similar triggers coincident within $\pm$25 μs from nearby stations, including adjacent and second- or third-nearest neighbours (69). If three or more time and spatially correlated triggers are received, the T3 trigger condition is passed and 20 μs of signal, including 6 μs prior to the trigger time, are sent from the stations concerned and stored by the CDAS computer (58). Two example FADC traces are shown in figure 2.6.

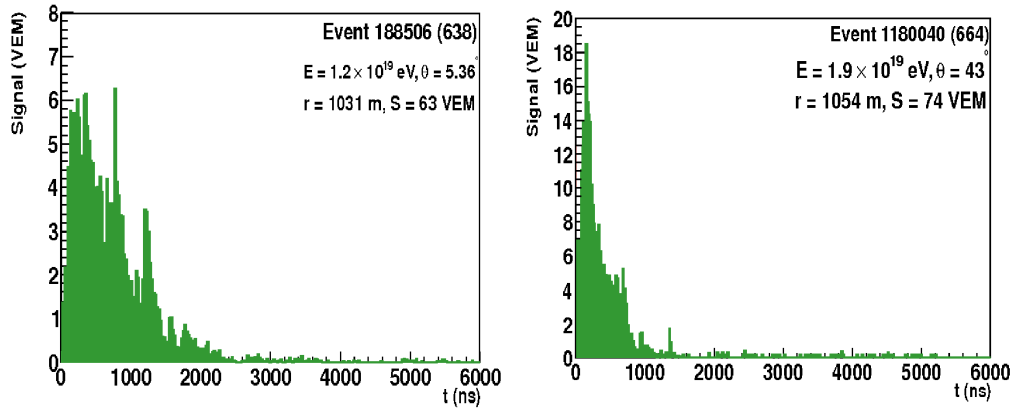

(a) (b)

Figure 2.6: Examples of typical FADC traces. Left: from an event with a zenith angle of 5° and Right: from an event with a zenith angle of 43°. Both traces are from stations approximately 1 km from the shower core and from events with similar energies.

The remaining two trigger levels are 'off-line' triggers. The T4 trigger ensures that the event geometry, core position and energy can be satisfactorily reconstructed by checking the configuration of detectors within the event. For vertical or near-vertical events, at least 3 ToT stations must be arranged in triangular configurations and not separated by un-triggered detectors. For more inclined events, this requirement increases to a minimum of 4 ToT stations. Aligned configurations (i.e. detectors in a straight line) are not flagged as T4 and hence are not used in the standard analysis, regardless of the number of triggered detectors (58). Examples of allowed trigger configurations are given in figure 2.7.

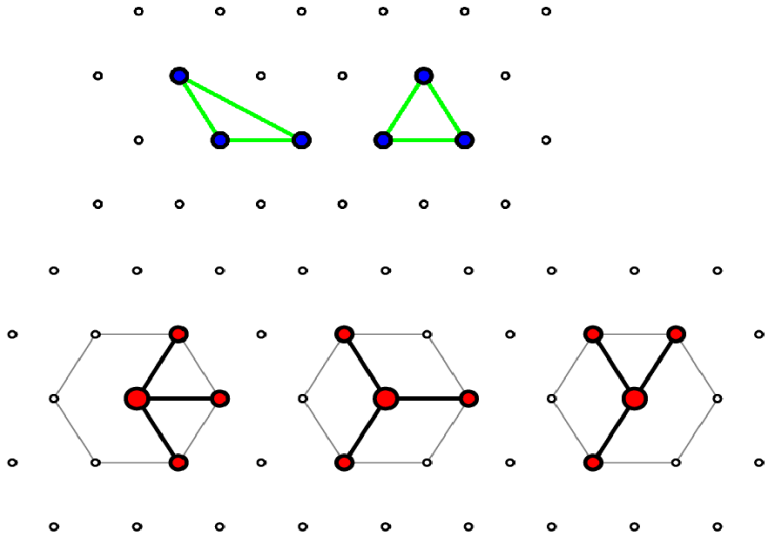

Figure 2.7: Allowed configurations of triggered detectors for the T4 trigger. Top: Configurations of 3 triggered detectors. Bottom: Configurations of 4 triggered detectors. Symmetrical transformations of these configurations are also valid.

Finally, a physics-level trigger (T5) is used to select a subset of high-quality events for further analysis. The reconstructed core position must be within the triangle created by the three stations with the largest signals, these three stations must not be on the edge of the array and the station with the largest signal must be surrounded by at least 5 fully operational neighbouring detectors at the time of the event. Stations passing this criteria are flagged 5T5 or 6T5 (58).

2.3.1 Calibration of the Surface Detectors

Atmospheric muons provide a well-understood background that can be used to calibrate stations across the entire array (70). The signal deposited by one vertical muon traversing the full depth of the detector, and the response of this in the electronic readout, is compared to that from scintillators placed centrally above and below one of the surface detectors. Coincidence measurements from the scintillators are used to select muons that traverse the full depth of the detector. The response from the PMTs inside the surface detector is then compared to the signal from the scintillators to determine the average response from a (240 MeV) vertical muon. The PMTs in each detector are gain-matched by adjusting the voltage supplied until the trigger rate above a threshold of 3 VEM is stable at 100 Hz. Evolution of the gain is monitored using deviations in the T1 (STC) rate. For individual PMTs that drift away from the expected trigger rates, the local station computer can be used to recalculate an internal PMT-specific definition of a VEM and so correct for the deviation.

The Peak-VEM (from the dynode signal) and Charge-VEM (integrated over 500 ns) are monitored and stored for all signals that just pass the T1 single trigger threshold (peak signal = 1.75 VEM). From their ratio the charge associated with 1 VEM is calculated. For signals between 8 and 20 VEM, the integrated dynode to anode ratio is calculated for cross-calibration purposes. A small number of 'twin tanks', located 11 m apart, are used to measure the GPS timing resolution and fluctuations in air-shower signals (58).

The evolution of T2 triggers with time and position is used for array monitoring (71). Unusually low or high T2 trigger rates indicate detector malfunctions, detector off-time for scheduled maintenance, communications or power failure, and computer error. Events recorded during such periods are flagged as 'bad period' events and can be discarded in off-line analysis. The growth of the array as a function of time (until June 2008) and fluctuations in the trigger rate due to weather effects can also be seen. This has to be taken into account when calculating the active array area and hence the aperture.

2.3.2 Core Position and Energy Reconstruction

The shower geometry of a surface event is reconstructed from the timing information and then the core position and shower energy estimate are calculated in an iterative procedure. A rough estimate of the core position is found within the triangle bounded by the three stations with the largest signal. An initial determination of the shower direction is made from the start-time information in each detector, approximating the leading edge of the shower as a plane front. From this, the zenith angle and direction with respect to geographic north can be determined. The core location and axis direction are then refined in an iterative manner assuming a spherical shower front. The actual shape of the shower front is not precisely known: a spherical approximation is used for the geometric reconstruction as this is more accurate than using a plane front. The angular resolution of the surface array is better than 2.2° for events with three stations and improves for larger multiplicities. The surface array is fully efficient above 3×10^{18} eV for events with incidence angles less than 60°.

The energy deposited by shower particles as a function of distance (the lateral distribution) can be found by fitting a modified NKG-type function of the form:

$$S(r) = S(r_{opt})(\frac{r}{r_{opt}})^{\beta}(\frac{r+700}{r_{opt}+700})^{\beta+\gamma} \tag{2.4}$$

to the total signal $S(r)$ in each detector as a function of distance r in the shower plane from the core position (see figure 2.8). β and γ are θ-dependent slope parameters and $S(r_{opt})$ is the signal at a given reference distance.

The reference distance, or optimum distance as it is more usually known, is the distance at which the fluctuations in the signal due to uncertainties in the slope parameter β are smallest ($\leq 5\%$). The optimum distance is primarily dependent upon the array geometry with only a minor dependence (of the order of tens of metres) on the energy and zenith of the shower and is $\simeq 1000$ m for the Pierre Auger Observatory (72), although r_{opt} can be up to several hundred metres larger for showers with saturated stations. Saturated stations (S $\geq$ 800 VEM) occur when the shower core falls very close to a detector, typically within 600 m.

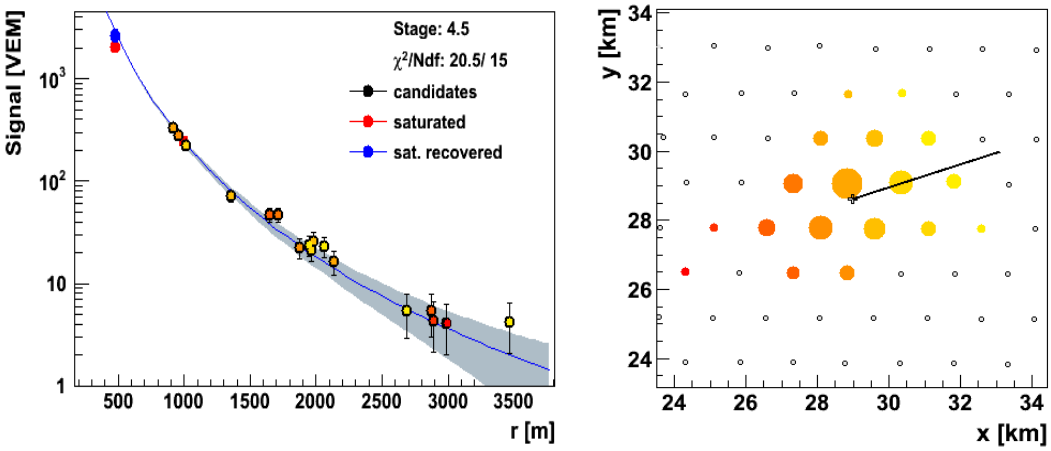

(a) (b)

Figure 2.8: Left: The lateral distribution of an inclined shower and Right: the corresponding layout of triggered detectors. The central detector in this event is saturated and has been recovered.

Algorithms have been devised for the treatment of saturated stations to improve the LDF fit and energy reconstruction. The recovered signal from a saturated station is shown in figure 2.8. Hereafter $r_{opt} = 1000\,\mathrm{m}$ and $S(r_{opt}) = S(1000)$.

Due to the number of parameters involved in the reconstruction of surface events, less than 7% can be accurately fitted with β and γ as free parameters (72). Instead a parametrisation of the form:

$$\begin{aligned} \beta = &-3.35 - 0.125\, lg(S(1000)) \\ &+ (1.33 - 0.324\, lg(S(1000))\, sec\theta \\ &- (0.191 + 0.00573\, lg(S(1000))\, sec^2\theta \\ \gamma = &\ 0 \end{aligned} \tag{2.5}$$

is used.

$S(1000)$ is then converted to a reference signal $S_{38}(1000)$ by normalising to the mean zenith angle of 38°. This is done using the constant intensity cut method (73), which involves the parametrisation of $S(1000)$ as a function of zenith angle for showers of constant intensity and accounts for attenuation in

showers of different incidence angles due to the depth of atmosphere traversed (74).

The exact slope of the lateral distribution function (LDF) is dependent on the zenith angle, energy and the mass of the primary particle as well as fluctuations in the shower development. The LDF becomes flatter for showers at larger zeniths as the shower has traversed more atmosphere (74). Less energetic showers have a flatter LDF than more energetic showers as they are more developed. Photon-initiated showers have a steeper LDF than hadronic ones, with iron-initiated showers being the flattest. In principle the mass composition could be inferred from the slope parameter β. In practice this is extremely difficult as an adequate number of signals regularly spaced over a range of several hundred metres, thereby allowing β to be fitted as a free parameter, is rarely achieved.

2.4 The Pierre Auger Observatory as a Hybrid Detector

Previous experiments using surface arrays, for example the Haverah Park and AGASA detectors, relied on air-shower simulations to estimate the shower energy from $S(r_{opt})$ (68). This leads to large uncertainties on the energy estimation due to the extrapolation of particle physics from collider measurements well below 10^{17} eV. The hybrid functionality of the Pierre Auger Observatory permits calibration via the calorimetric energies from fluorescence detector measurements using a subset of high-quality hybrid events.

Hybrid events are those observed simultaneously by both types of detectors. The estimated shower impact time and core position from the fluorescence event are used to search for spatially coincident stations triggered within $20\,\mu$s of the impact time. Signals from surface detectors that pass the T2 trigger and this additional criteria are merged with T3-triggered fluorescence events to form the hybrid event set (58). Construction of the hybrid set is performed off-line at the end of each night of FD operation.

Hybrid events are used to calibrate the shower energy reconstruction of the surface array data. Fluorescence energy estimates are compared to $S_{38}(1000)$ for well-reconstructed hybrid events with at least three triggered surface stations and fluorescence energy $E_{FD} \geq 3 \times 10^{18}$ eV (figure 2.9). This relation is well described by a power law of the form:

$$E_{FD} = aS_{38}^{b} \tag{2.6}$$

where $a = (1.68 \pm 0.05) \times 10^{17}$ eV and $b = 1.035 \pm 0.009$ and S_{38} is in VEM.

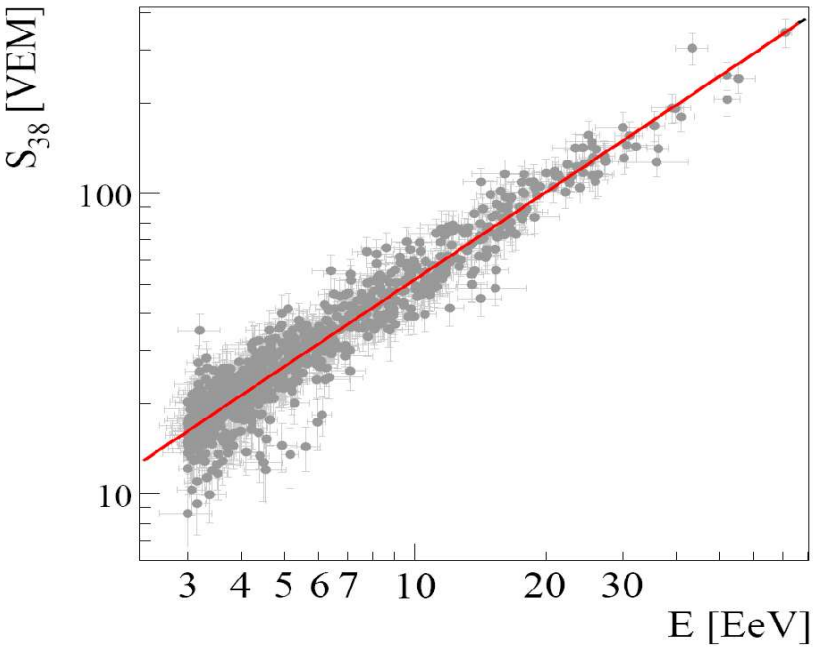

Figure 2.9: S_{38} as a function of reconstructed fluorescence energy for 839 well-reconstructed hybrid events (73). The most energetic event has an energy of approximately 75 EeV.

Determination of the shower geometry from fluorescence detector measurements alone is not trivial and leads to large uncertainties on the core position. Inclusion of a signal by at least one surface detector allows a much improved determination of the arrival direction - to better than 1° (73). The detection of a shower by fluorescence detectors at more than one site (a stereo event) will improve the core position reconstruction but does not imply hybrid status.

2.5 Review of Recent Results

2.5.1 The UHECR Energy Spectrum

The energy spectrum of events with incidence angles $\leq 60^\circ$ has been determined using hybrid events observed between November 2005 and September 2010 and for surface array data taken between January 2004 and December 2010 (24). For this period the surface array has an exposure of $20,464\,\mathrm{km}^2\,\mathrm{sr}\,\mathrm{yr}$, nearly four times that of HiRes and seven times that of AGASA.

A suppression of the flux has been observed at energies greater than $2.9 \times 10^{19}\,\mathrm{eV}$. The slope of the spectrum has been determined from a broken power-law fit to be $\alpha = 2.55 \pm 0.02$ below and $\alpha = 4.3 \pm 0.2$ above this energy (24). The 'ankle' is at $4.1 \times 10^{18}\,\mathrm{eV}$ and appears more pronounced than in an earlier HiRes result. The total systematic uncertainty in the energy reconstruction is estimated to be 22% and the energy resolution is better than 16% (73).

This spectrum is shown in figure 2.10, multiplied by E^3 to show the spectral features. While there is a clear suppression above $3 \times 10^{19}\,\mathrm{eV}$, it cannot be conclusively said that the GZK mechanism exists and is responsible for the observed suppression. It remains possible that there is simply a lack of particles accelerated to these, and higher, energies. Measurements of the anisotropy of cosmic-rays, the correlation of arrival directions with nearby extragalactic sources and the mass composition at these energies are required before further conclusions can be drawn.

2.5.2 Correlation Studies

Protons and nuclei above $3 \times 10^{19}\,\mathrm{eV}$ are expected to interact with the CMB via photo-pion or photo-disintegration processes (the GZK effect). This limits their propagation distance to within $\simeq 100\,\mathrm{Mpc}$, hence limiting the number and type of nearby sources. If the highest energy cosmic-rays are protons, they can be tracked back to their sources as deflections by magnetic fields are small. A

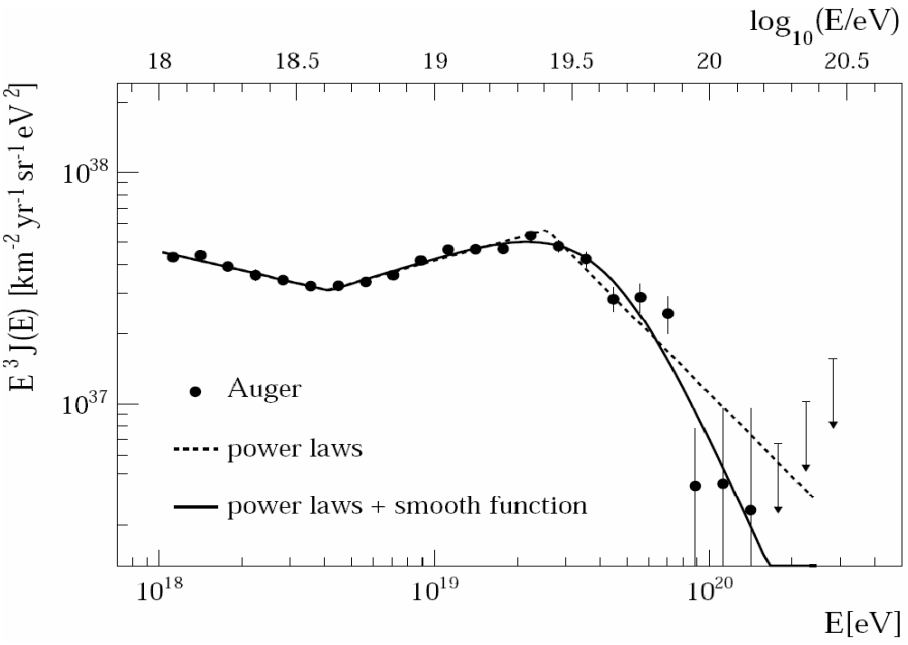

Figure 2.10: The combined hybrid and SD energy spectrum. The ankle and a suppression at 3×10^{19} eV can clearly be seen in the discontinuous slope. A broken power law fit (dashed lines) and a smooth power law fit (solid lines) are shown. Appriximately 64,000 events have been used (24).

correlation of the highest energy cosmic-rays with astrophysical objects may yield clues as to their origins.

The correlation of the arrival directions of cosmic-rays with astrophysical objects within 75 Mpc has been investigated by the Pierre Auger Collaboration. In reference (30), 14 of the highest energy events with zenith angles smaller than 60° detected prior to May 2006 (Period I) were used to perform an exploratory scan to determine the optimal search parameters for a correlation to be observed. The lower energy threshold (E_{min}), maximum distance from Earth (z_{max}) and maximum angular separation (ϕ) between an AGN position and a cosmic-ray arrival direction were determined. AGN in the 12th Veron-Cetty-Veron catalogue were used for this scan. The largest number of correlations were found for $E_{min} = 56 \times 10^{18}$ eV, $z_{max} = 0.018$ and $\phi = 3.1°$. Events used for the exploratory

scan were then excluded from further analysis and the above parameters applied, in an *a priori* manner, to a further 13 events in the period from June 2006 to August 2007 (Period II). Nine events were found to correlate, with 2.7 expected from isotropy, corresponding to a chance probability of 1.7×10^{-3}. Therefore it was concluded that AGN may be the sources of UHECRs.

An update to the correlation study, given in (75), includes a further 42 events to the end of December 2009 (Period III). Periods II and III have been combined in the updated result. Events from period I are still excluded. Using the same selection criteria found from the exploratory scan, 21/55 events now correlate with AGN, with 11.6 expected from an isotropic distribution. The degree of correlation has decreased from $69^{+10}_{-13}\%$ to $38^{+7}_{-6}\%$ with 21% expected from isotropy. Arrival directions of events from all three periods are shown in figure 2.11 with AGN from the VCV catalogue within 75 Mpc. The time-ordered correlation is shown in figure 2.12. The five highest energy UHECR do not correlate with AGN from this catalogue. None of the highest energy cosmic-rays appear to originate from the galactic disk region, implying extragalactic origins.

This result must be treated with caution. First, the VCV catalogue used is known to be incomplete and a more complete catalogue may yield a better correlation. Second, cosmic-rays may not necessarily come from AGN but from a collection of objects with a similar distribution on the sky. As the AGN in the VCV catalogue trace out the matter distribution within the universe, this is possible. Third, the mass composition and hence the degree of deflection of cosmic-rays is still unknown. Finally, re-analysis of HiRes (which observes the northern sky) data, found only 2/13 events correlated when using the same selection criteria and does not corroborate the above results.

A similar study has been conducted on the same set of events using different catalogues in an *a posteriori* manner (75). Galaxies from the 2MRS survey and AGN from the 58-month Swift-BAT catalogue were used to identify possible correlations. These catalogues also indicate the presence of anisotropy which suggests cosmic-ray sources follow the distribution of matter in the local universe

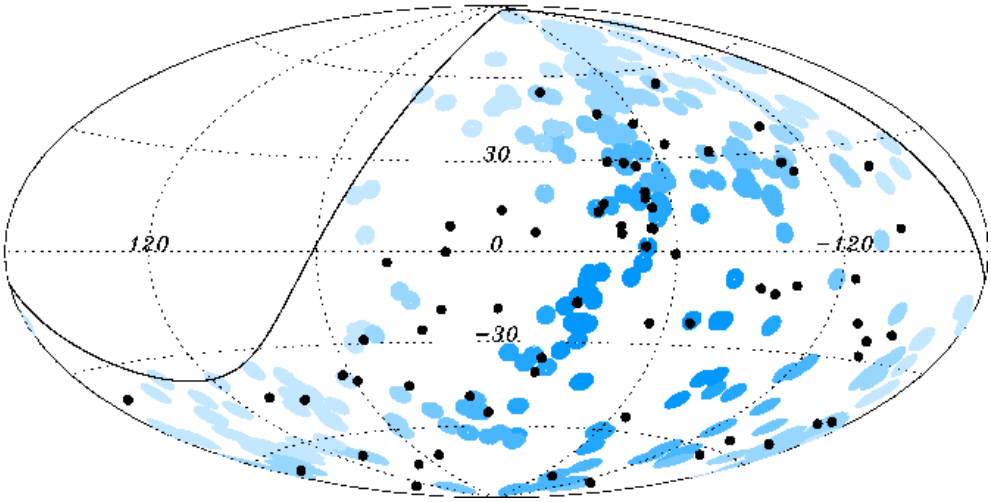

Figure 2.11: Hammer-Aitoff projection of the arrival directions (black dots) of cosmic-rays with $\theta \leq 60°$, and 318 AGN from the VCV catalogue within 75 Mpc (blue points). The solid line shows the edge of the field of view of the Pierre Auger Observatory. The blue shading indicates the relative exposure (darker = more exposure). The exposure weighted fraction of these AGN is 21% (75).

- assuming minimal deflections by magnetic fields.

The number of events as a function of angular distance from Cen A has been analysed and is shown in figure 2.13. The largest deviation from isotropy occurs for events within an 18° radius of Cen A. Of the 69 events above 56 EeV, 13 lie within 18° while 3.2 are expected from isotropy (75). Two of these events correlate within 3.1° of Cen A. This indicates that either Cen A, or a source behind Cen A such as the Centaurus cluster, may be responsible for a large fraction of UHECRs arriving at Earth.

2.5.3 Large Scale Anisotropies

The transition of galactic to extragalactic cosmic-rays may create a dipole anisotropy in the arrival directions of UHECR (76). The phase and amplitude of the first harmonic modulation in the right ascension distribution have been measured using two techniques - the East-West method and Rayleigh analysis. Well-

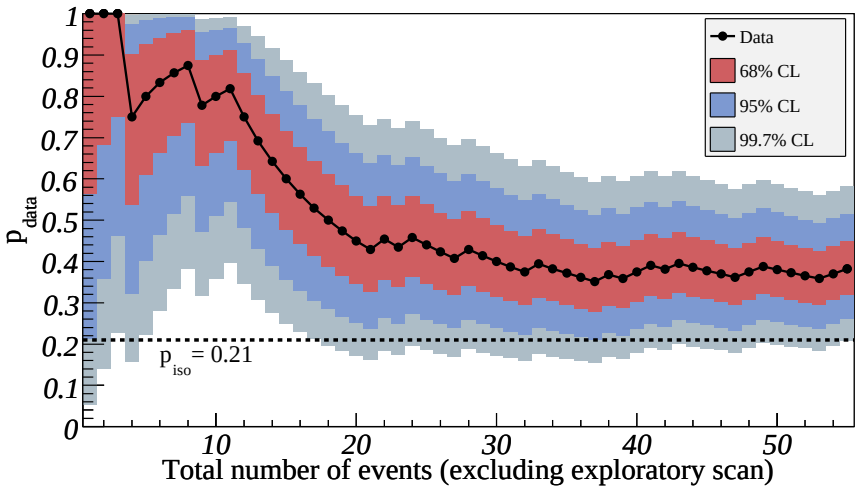

Figure 2.12: The degree of correlation (p_{data}) of data from periods II and III with AGN as a function of time. Shaded areas indicate 68.3%, 95.5% and 99.7% confidence levels. The expected correlation from isotropic sources is 0.21 (dashed line). The current correlation is 38^{+7}_{-6}% (75).

reconstructed events with zenith angles less than 60° recorded between January 2004 and December 2009 have been used. The exposure of the array for this period is $16,323\,\mathrm{km}^2\,\mathrm{sr}\,\mathrm{yr}$. Corrections for seasonal variations due to weather effects have been made before applying the Rayleigh analysis to events above $10^{18}\,\mathrm{eV}$ detected by the surface array. The differential East-West method is applied to events below $10^{18}\,\mathrm{eV}$ (76).

If dipole anisotropy is present, a modulation in the arrival distribution of UHECRs is expected with a period equal to one sidereal day. There is no evidence for anisotropy from amplitude measurements but the phase indicates interesting features as shown in figure 2.14. If the sources are isotropic, the phases should be distributed randomly. However, there is a clear smooth transition with energy. As the energy increases, the phase turns towards 90° from 270° (i.e. away from the galactic centre location) and the uncertainty on this measurement decreases. A transition in the phase could signal the transition from galactic to extragalactic cosmic-rays. However, at least twice as many events are needed to clarify this

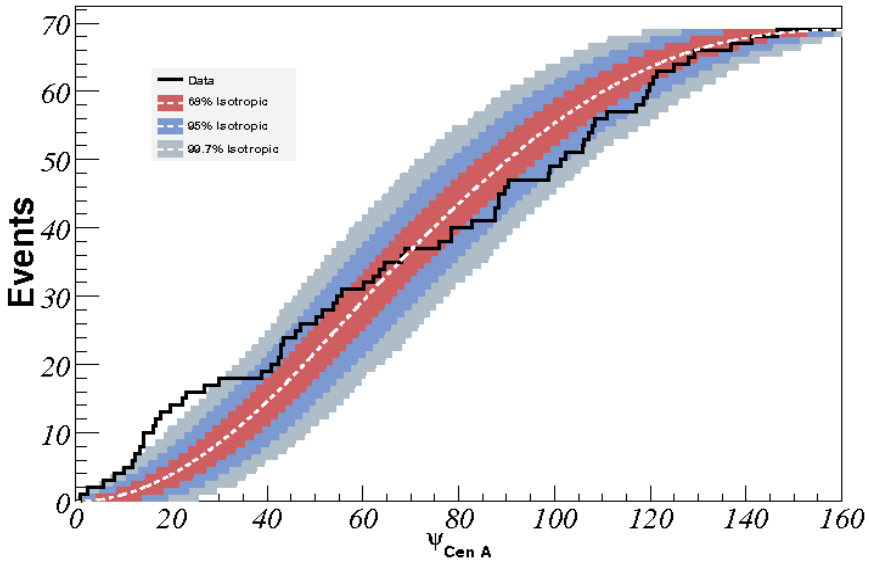

Figure 2.13: The cumulative number of events as a function of angular distance from the direction of Cen A (black line). The white dashed line shows the expected isotropic value and the coloured bands indicate 68.3%, 95.5% and 99.7% confidence levels. Thirteen events lie within 18° while 3.2 are expected from isotropy (75).

measurement at a 90% confidence level (76). The predicted Compton-Getting effect due to the movement of the solar system around the galactic centre would give lower amplitudes than currently detectable, at about 0.6% with a phase of 168°.

2.5.4 Mass Composition

The composition of ultra high energy cosmic-rays, and its evolution with energy, are important to understand the origin of cosmic-rays, their acceleration and propagation, and to clarify the origin of the ankle and cut-off. cosmic-rays could be any mixture of nuclei. Contributions from photons and neutrinos have been shown to be less than 2% at 10^{19} eV (42), (77).

The depth of maximum development is sensitive to the primary cosmic-ray composition and can be measured directly by the fluorescence detectors. Figure

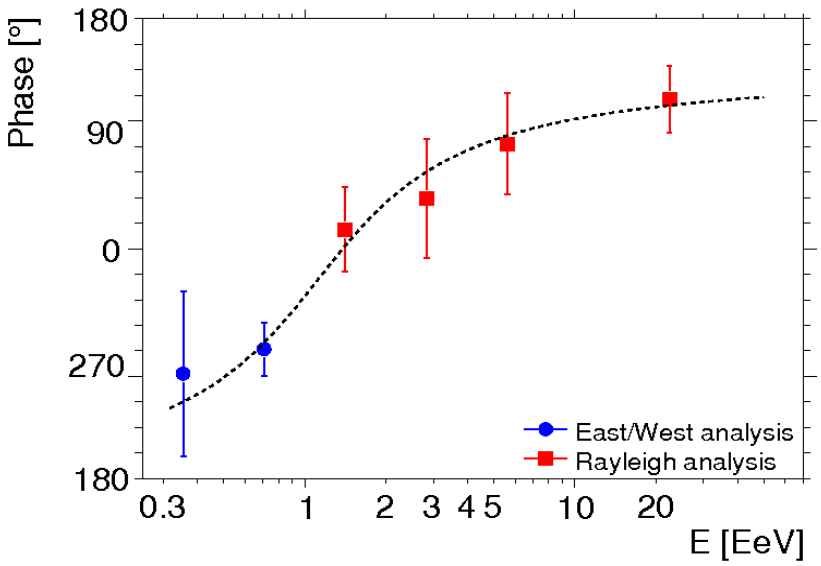

Figure 2.14: The phase of the first harmonic as a function of energy from two different analysis methods: The East-West (blue dots) and Rayleigh analysis (red dots). The dashed line is an empirical fit (76). The galactic centre is at a phase angle of 268.4°.

2.15 shows the evolution of X_{max} and its fluctuations with energy. Predictions from iron and proton simulations are shown for comparison. These results imply that the composition changes with energy from proton-dominated to iron-dominated (39). However, the models used in this work describe only a small subset of possible extrapolations from accelerator data at lower energies. These models have large uncertainties surrounding them and a change of model, for example due to an unexpected change in the interaction cross section, multiplicity or inelasticity, may yield a vastly different interpretation. These results have yet to be verified by other collaborations (for example, the Telescope Array) or using other mass-sensitive parameters deduced from surface array measurements.

2.5.5 Neutrino Limits

Neutrinos are not deflected by magnetic fields and so their arrival directions at Earth can be used as a tracer for cosmic-ray sources. UHE neutrinos are expected

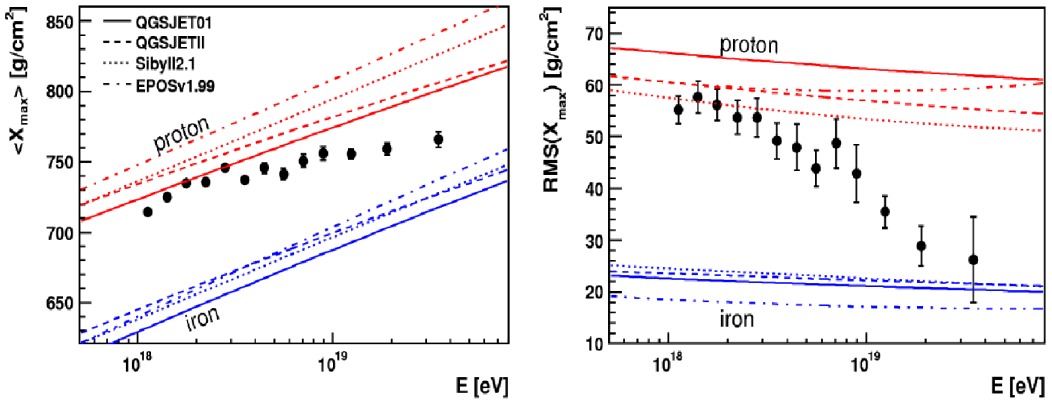

(a) (b)

Figure 2.15: Left: Average depth of shower maximum (X_{max}) and Right: Fluctuations in X_{max} as a function of energy using data from 2004 to 2009 inclusive (black points). Expectations from proton (red lines) and iron (blue lines) simulations are also shown. A transition from predominantly protons to heavier nuclei is seen in the data above 4×10^{18} eV (39).

from the decay of charged pions produced in interactions of protons with the CMB and of cosmic-rays within their source regions. Predicted neutrino fluxes are very uncertain as they depend strongly on the primary source composition but are expected to be of the order of 1% of the UHECR flux (78).

Although not a dedicated neutrino experiment, the Pierre Auger Observatory is sensitive to neutrino-initiated air showers. Neutrino-initiated EAS will be observed as very inclined ($\theta \geq 75°$), very deeply penetrating showers with a large EM component compared to proton showers at this slant depth, and caused by down-going neutrinos or by Earth-skimming (up-going) tau neutrinos. Such showers are expected to have a large electromagnetic component, large asymmetry and broad time-structure compared to very inclined hadronic showers. However, detection of neutrinos against the background of cosmic-rays is challenging. Limits have been placed on the flux of UHE tau neutrinos at $9 \times 10^{-8}\,\mathrm{GeV\,cm^{-2}\,s^{-1}\,sr^{-1}}$ (42). This limit is about an order of magnitude larger than the predictions for GZK neutrinos. No UHE neutrinos have been detected to date.

2.5.6 Photon Limits

The fraction and flux of photon-initiated cosmic-rays for both FD and SD data have been investigated using techniques that exploit the differences in photon and hadronic air shower development (see section 1.7). Measurements of X_{max} from hybrid events satisfying a selection of fiducial cuts have been compared to the predicted X_{max} from simulations. The number of well-reconstructed events whose X_{max} are larger than the median value of the photon distribution were determined for both the data and hadron simulations (77). Eight photon candidate events were found from the data in the lowest energy bin, within expectations from the hadronic background. Conservative limits to the fraction of photons in the cosmic-ray spectrum have been derived assuming these candidates are photons, yielding a photon fraction of 3.8%, 2.4%, 3.5% and 11.7% at 2, 3, 5 and 10×10^{18} eV respectively (77). These limits disfavour the possibility of a large fraction of cosmic-ray photons and hence the majority of top-down models.

Whilst these limits begin to constrain some top-down models at lower energies, the larger statistics supplied by the surface array permit more stringent limits at higher energies and exploration of the GZK region. Use of the surface array data to this end is challenging as X_{max} cannot be directly measured. Alternative mass-sensitive parameters must therefore be used. Measurements of the photon fraction using a combination of the shower risetime at 1000 m ($t_{1/2}(1000)$) and the radius of shower front curvature, both derived from SD timing information, have allowed more stringent limits to be placed above 10^{19} eV (47).

The risetime is the time taken for the signal in a given detector to increase from 10% to 50% of the total signal in that detector (79). The risetime as a function of distance from the shower core is therefore a measure of the spread in the arrival times of shower particles from a fixed segment of shower evolution. Risetimes were first shown to be a mass-sensitive variable in 1974 (79) and have since been shown to correlate with X_{max} (80). From geometric arguments, photon-initiated air showers will have a larger risetime than hadronic showers of the same energy due to their deeper development. Additionally, muons are scattered less than the

electromagnetic component and so arrive earlier (see figure 2.16). Hence risetimes from hadronic showers are expected to be shorter than those from photon-initiated showers.

In (47), the risetimes in detectors where the signal is larger than 10 VEM have been combined into one parameter describing each event - $t_{1/2}(1000)$ - using the relation:

$$t_{1/2}(r) = 40 + ar + br^2 \tag{2.7}$$

where $40\,ns$ is the smallest measurable risetime in the water-Cherenkov detectors due to the single particle response and a and b are free parameters particular to each shower. $t_{1/2}(1000)$ is then the expected risetime at 1000 m.

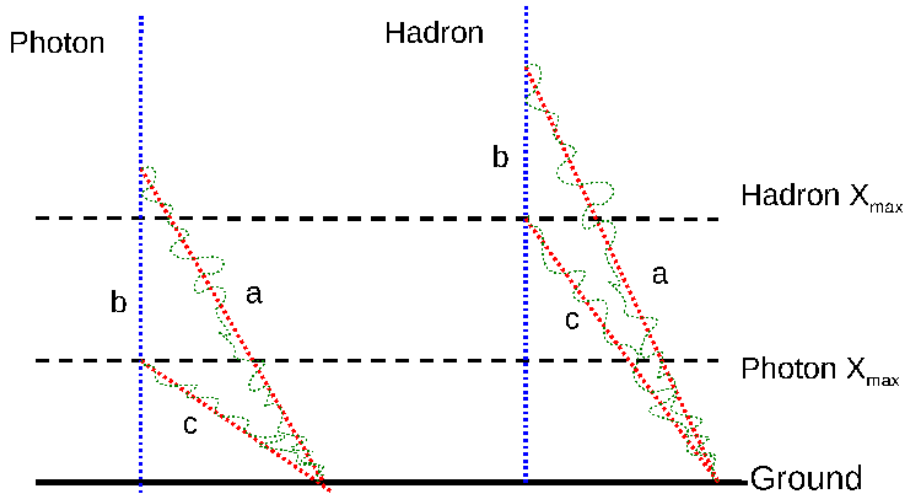

Figure 2.16: Illustration of the concept of the risetime in relation to the mass-composition. The deeper developing photon shower has a longer risetime than the hadronic shower due to the time differences along different path lengths traversed by particles at different stages of shower development ($b + c > a$). Blue lines indicate the shower axis and black dashed lines show the relative position of X_{max}. The electromagnetic component (green dotted lines) arrives later than the muonic component (red dashed lines) due to scattering.

The time residuals, t_{res}, describe the difference between the arrival times of the first shower particles and the arrival time of particles at the core of the shower

at ground level. The curvature of the shower front is thus obtained from the fit of a spherical function to the time residuals as a function of distance from the shower axis, and is strongly related to the shower geometry. Particles created in the early stages of air shower development form the leading edge of the shower, which can be approximated as an expanding spherical shell. The radius of this shell is the radius of curvature, denoted R_c, and is strongly influenced by the depths of the first few interactions and the depth of shower maximum. Like the risetimes, the curvature is sensitive to different primary particles, with photons having a smaller radius of curvature (larger curvature) than hadrons.

Combining results from two or more mass-sensitive parameters may allow different primary particles to be more easily distinguished. In (47), photon limits were derived using multi-parameter analysis techniques on the risetime and radius of curvature. No photon-like events were found and 95% confidence limits were placed at 2%, 5.1% and 31% above 10, 20 and 40 EeV, respectively. The limit at 10 EeV is ~ 6 times smaller than that achievable with current FD data due to the ~ 10 times larger statistics from the surface array and the different selection criteria used. These limits are shown in figure 2.17 for both FD and SD data, together with the predicted contribution from four top-down models and the GZK mechanism. Limits from previous experiments are also shown. Systematic uncertainties on the reconstructed cosmic-ray energy and proton-air cross-section, which would be severely affected by the presence of a substantial photon component, are also reduced by these limits (77).

An upper limit to the integral photon flux has also been derived for the first time in (47). A flux of 3.8, 2.5 and $2.2 \times 10^{-3}\,\mathrm{km^{-2}sr^{-1}yr^{-1}}$ has been found above 10, 20 and 40 EeV, respectively. These results strongly disfavour the possibility of a significant photon fraction and hence most top-down models. Only the Z-burst model and the GZK mechanism are not constrained (47).

With ~ 3.5 times more statistics available since the SD photon limits were first produced, coupled with an improved analysis technique (described in chapter 3), a significant improvement on the current limits can be made, such that the

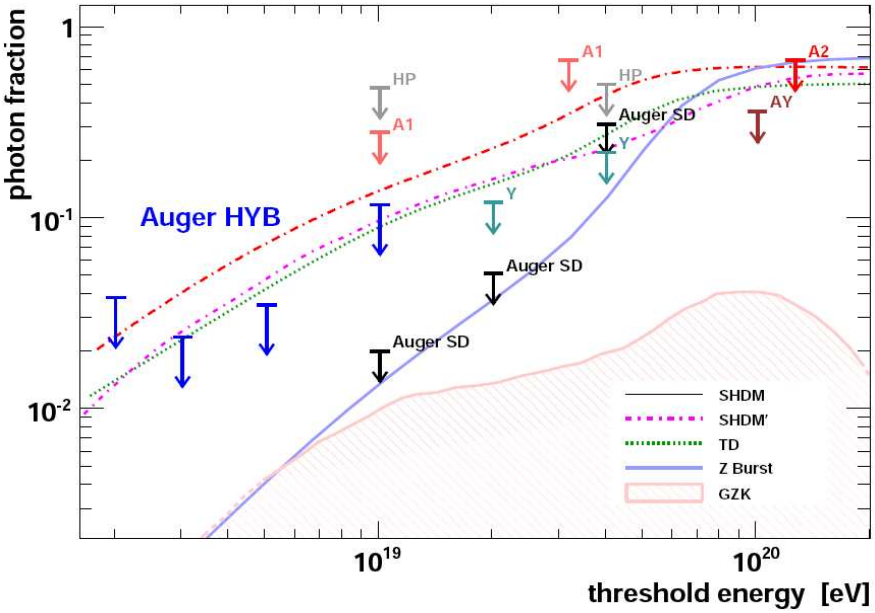

Figure 2.17: Upper limits to the photon fraction for the cosmic-ray flux above 10^{18} eV from different experiments: AGASA (A1, A2), AGASA-Yakutsk (AY), Yakutsk (Y), Haverah Park (HP), Auger SD and Auger Hybrid (HYB). The shaded region shows the expected GZK photon fraction (from (81)) and the lines indicate predictions from different top-down models. Figure and caption adapted from (77).

Z-burst model and GZK predictions can be probed.

2.6 Conclusion

The Pierre Auger Observatory has been taking data since January 2004. The surface array of 1600 water Cherenkov detectors and the 24 fluorescence telescopes were completed during 2008. This makes the Pierre Auger Observatory the largest cosmic-ray detector in operation. The array exposure is now over $20,500\,\mathrm{km}^2\,\mathrm{sr\,yr}$. World-leading results have been published on all major science goals, including mass composition and UHECR photon searches. Several extensions to the initial design are now in the construction or initial data taking phase. Future results are eagerly awaited.

Chapter 3

A Method to Use Shower Risetimes for Mass-Composition Studies

3.1 Motivation

The measurement of the composition of ultra high energy cosmic-rays is an important area of cosmic-ray research. Knowledge of the composition will aid our understanding of the origin, acceleration and propagation of UHECRs. Discrimination between photon and hadron initiated showers is easier than between different hadronic primaries due to the larger differences in shower development. Determination of the flux and fraction of UHECR photons will probe models predicting their existence - in particular the GZK model. Current limits imposed on the flux and fraction of UHECR photons already exclude many models for the composition and origin of UHECR (47), (77). The challenge is to further restrict photon flux limits such that the GZK region may be probed. A positive detection of photons would move this research to exciting new levels.

A flux of photons greater than a few percent will bias the energy reconstruction of cosmic-rays, particularly at the highest energies. Due to their steeper LDF and smaller number of secondary muons, photon-initiated showers yield a much smaller signal (by up to 75% - as will be shown in chapter 4 for photon

simulations) than hadronic primaries, thus affecting their energy reconstruction. A second motivation to determine the flux of UHECR photons is therefore to prevent the underestimation (by a factor ≥ 2) of UHE photon energies.

The direct measurement of X_{max} and its fluctuations for the purpose of composition measurements (including the study of photons) is at an advanced stage. While direct observation of X_{max} is most desirable, the small duty cycle of the FDs ($\simeq 12\%$) severely limits the available statistics, which is further reduced by the strict quality cuts necessary for good observations. A mass-sensitive parameter derived from surface detector measurements is thus required to investigate the composition of this larger data set. Ideally such a parameter will also correlate with X_{max} so that results from the two parameters can be compared.

The focus of this thesis is on the shower risetime, $t_{1/2}$, derived from surface detector measurements. As the risetime is calculated for each individual detector, a method of combining the risetime information into one parameter representing the whole shower is necessary. Two such methods exist: the aforementioned risetime at 1000 m ($t_{1/2}(1000)$), from which photon limits have been found and published (47); and the '$\langle\Delta\rangle$-method' developed in Leeds (28), (82). The $\langle\Delta\rangle$-method is designed to reflect the differences in shower development more accurately than $t_{1/2}(1000)$ via the determination of a benchmark representing the average risetime as a function of distance for a given energy and zenith angle. $\langle\Delta\rangle$ is then the average deviation of shower risetimes from this benchmark after accounting for measurement uncertainties. A complete re-analysis of the $\langle\Delta\rangle$-method has been undertaken and several substantial changes have been made to the original $\langle\Delta\rangle$-method (detailed in (28)). These changes are described in detail in this chapter, with comparison to the earlier work where appropriate.

3.1.1 Data Selection

Data from January 2004 to December 2010, which passes the 5T5 trigger condition and which is not part of a 'bad-period' (as defined in section 2.3), has been used in this work. The period from March to November 2009 has been excluded

due to a problem with the communications network across a significant portion of the site, causing information from many stations to be lost, at random, resulting in the possibility of incomplete and mis-reconstructed events (83). Only events with energies greater than 3 EeV - above which energy the array becomes fully efficient - have been used. In total, 48,324 good-quality SD events have been used in this analysis - 3.5 times more events than were used in (28) and (82).

The Pierre Auger Observatory reconstruction software, 'Offline', is used to reconstruct events as described in chapter 2. Several updates to the 'Offline' software have been implemented since the $\langle\Delta\rangle$-Method was developed. The most relevant changes affecting this work have been to the definitions of the start and stop-times of an air shower signal within the FADC trace, and to the baseline subtraction algorithm. The version of Offline used in this work is version v2r7p2.

3.1.2 Calculation of Signal Start and Stop-times

In late 2009 a problem with the calculation of the risetimes using a new version of the Offline software was observed (84). This was first observed as an unexpected decrease in the $\langle\Delta\rangle$ parameter - the average difference in the risetime, after accounting for measurement uncertainties, from a benchmark - with energy above 10^{19} eV. This was in conflict with results from earlier works (28), (82). Investigation into the cause of this decrease indicated an underlying problem with the calculation of the stop-times of shower signals and thus with the baseline, used to estimate the heights of the FADC traces. This problem particularly affected events where the low-gain FADC trace had been used due to saturation in the high-gain signal ($\sim 15\%$ of all events). This problem has since been dubbed the 'stop-time' problem and is illustrated in figures 3.1 and 3.2.

Traces affected by the stop-time problem had anomalous risetimes, caused by a miscalculation of the signal stop-time, leading to an overestimation of the baseline and hence an underestimation in the total signal. This is illustrated in figure 3.1 where it can be seen that the cumulative signal reaches maximum at

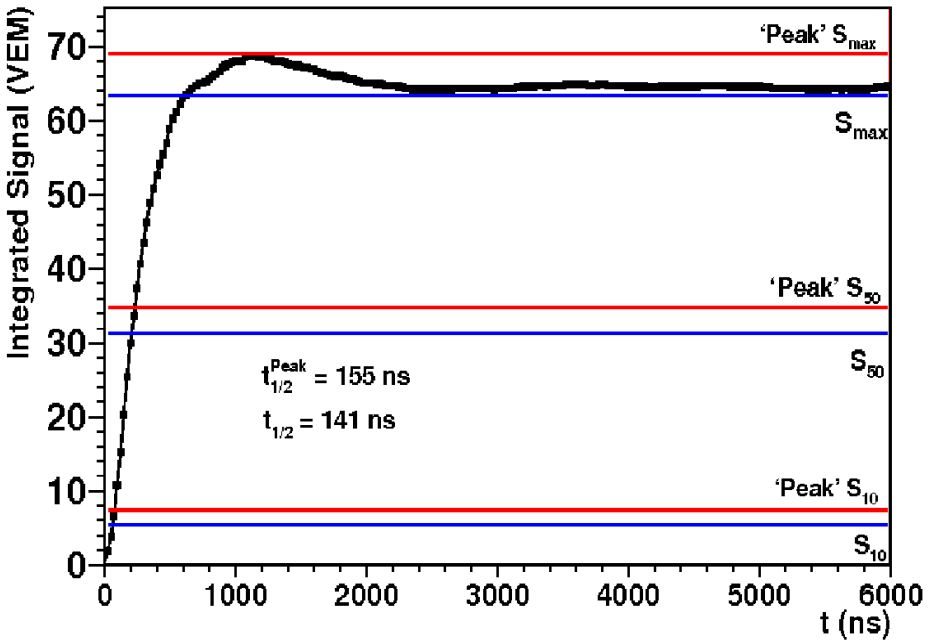

Figure 3.1: The cumulative signal in a detector affected by the stop-time problem (black points). Due to an incorrect stop-time and overestimated baselines, the signal peaks at around 1000 ns and decreases thereafter. The total signal, 50% and 10% of the total signal are marked for the peak signal (labelled 'peak') and that calculated using the incorrect stop-times are shown. A 14 ns difference is observed between the risetime calculated using the 'total signal' ('S_{max}', blue lines) and that using the maximum signal ('peak S_{max}', red lines).

$\sim 1.0\,\mu$s and then decreases thereafter. Figure 3.2(a) indicates the overestimation of the baseline in this trace.

To appreciate why the stop-times were incorrectly calculated and the solution to this problem, the way in which the start-time and baselines are calculated must first be understood. The section(s) of the FADC trace containing the shower signal are determined by systematically scanning the FADC bins searching for 'segments' and 'gaps'. A shower 'segment' is defined as a set of N_{seg} consecutive bins with signal greater than a threshold value S_{min}, separated by a 'gap' ('flat' section of trace) of N_{gap} bins with signal below S_{min}, as illustrated in figure 3.3 (85). The entire FADC trace is searched, from $\simeq$ 250 ns prior to the recorded

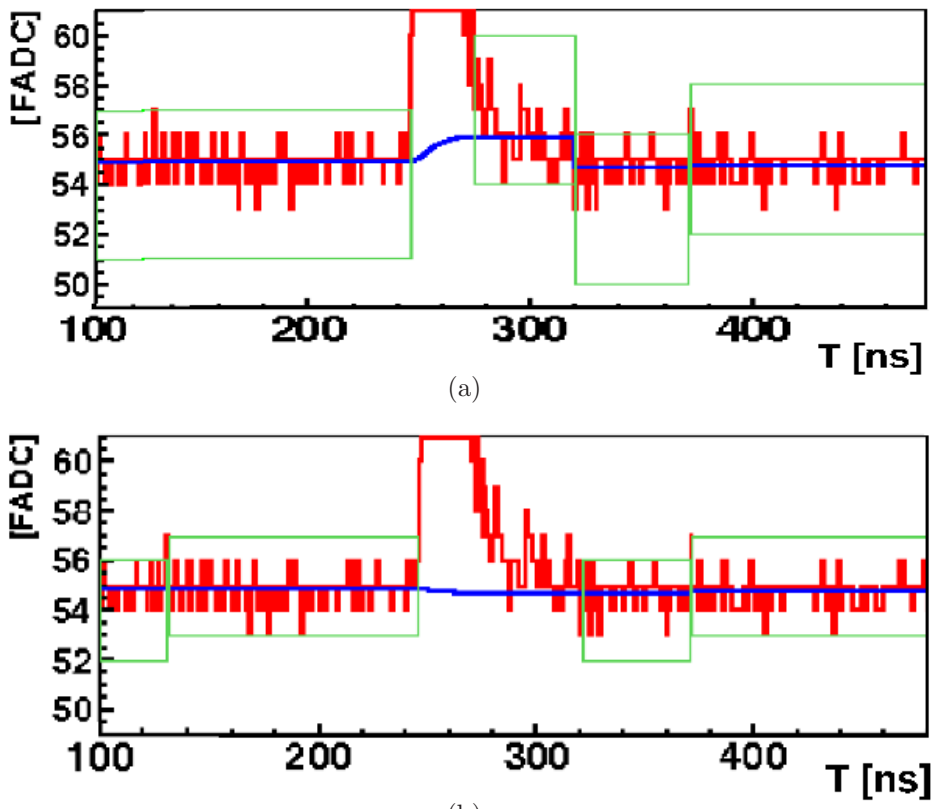

Figure 3.2: Example showing a portion of the baseline for a single PMT in one detector. The FADC signal (red line), the baseline (blue line) and the sections of signal used to calculate the baseline (green boxes) are shown. The upper and lower panels show the baseline calculated using the old and new stop-times respectively. A significant change in the baseline can be seen between $\sim 250 - 325$ ns.

trigger time to the end of the trace, $\simeq 6\,\mu$s later. The start-time is the position of the first time bin in the largest segment - the only segment for the majority of traces. The stop time is thus the end of the main segment. Secondary segments are attributed to 'accidental' signal from e.g. coincident muons. The 'gaps' (sections of 'flat' trace surrounding each segment) are used to calculate the baseline.

The baseline is that part of the FADC trace not directly attributable to the air shower signal or coincident muons. The baseline is a combination of an artificial

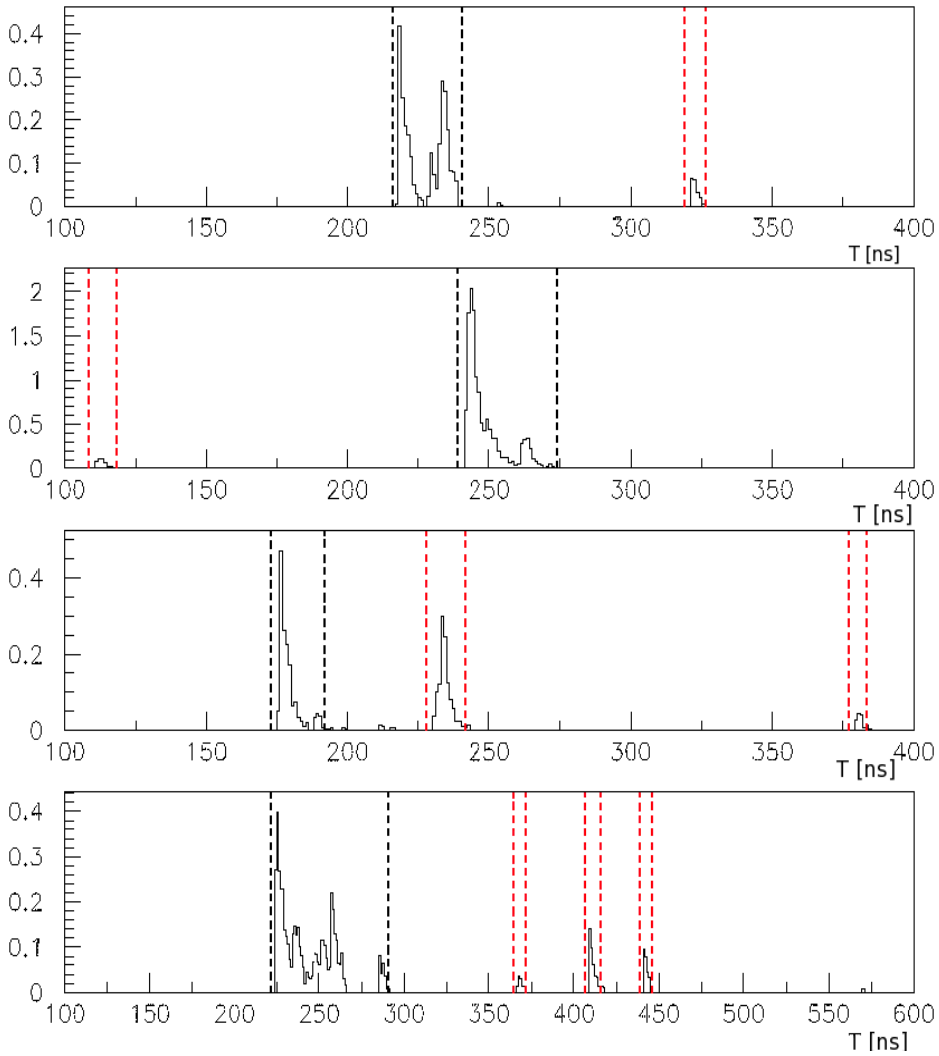

Figure 3.3: Determination of the start and stop times in an FADC trace by determination of shower 'segments'. The main shower segment in each example is marked by vertical black dashed lines, secondary segments by vertical red dashed lines. Sections of trace between segments are called 'gaps'. The y-axis scale is arbitrary in this illustration. Figure and caption taken from (85).

constant off-set from zero (thus allowing signal fluctuations to be measured), fluctuations due to electronic noise and the undershoot. The undershoot is a drop in the voltage that restores over time, is caused by high currents flowing through the PMTs, and should be corrected for in a time dependent manner.

In sections of 'flat' trace either side of a 'segment', the baseline is simply the average of the recorded signal. The baseline corresponding to each 'segment' is then an interpolation of the baseline between surrounding flat sections with a time-dynamic correction for the undershoot, as illustrated in figure 3.2. If the baseline is incorrectly calculated for one section of 'flat' trace then the interpolation of the baseline and undershoot correction for adjacent segments will also be incorrect. To correctly calculate the baseline, the correct start and stop times must be found.

In detectors where the high-gain trace is saturated, the low-gain trace is used to find the start and stop-times. Examination of such events highlighted the incorrect determination of the stop-times. The tail of the event signal had mistakenly been included as part of the next 'gap' rather than part of a 'segment' in both the low and the high-gain trace. The level of baseline to be subtracted was therefore overestimated, creating negative signals in FADC bins towards the end of the trace, thus underestimating the cumulative signal and the risetime. This is illustrated in figure 3.1. The stop-time problem predominantly affected $\simeq 15\%$ of signals in the highest energy events - where the low-gain trace had been used - typically by $\sim 3\%$ but by as much as 10% difference in signal in extreme cases (84). The change in the magnitude of the risetimes is of the order of tens of ns.

Due to the complex nature of this problem, a solution has only recently been found (84). Prior to this solution, a re-analysis of the risetime method described in (28) was performed by the author and which made use of up-to-date software but with the old stop-time and baseline algorithms. This interim work utilised all data between January 2004 and July 2010 inclusive. It was shown that the $\langle\Delta\rangle$-method and results discussed in (28) could be satisfactorily reproduced.

A solution to the stop-time problem has now been found (84). Once the end of a 'flat' section of trace is reached, the end of the previous 'segment' is checked by working backwards through the FADC bins (using a lower signal threshold) to ensure that the end of the signal has not been mistaken for part of the 'flat' trace. Where this does occur, the stop-time and the size of the 'flat' section are

recalculated to ensure the tail of the signal is included in the signal 'segment'. As a result, the baseline is no longer overestimated (e.g. figure 3.2 (bottom panel)) and the risetime can be correctly calculated. Note that the equations governing the baseline calculation and subtraction have not been altered but that the values input into this calculation have changed. Figure 3.4 indicates the effect of using the old and new stop-time algorithms on the cumulative signal.

The remainder of this chapter and the next will concentrate on new results and important updates to the $\langle\Delta\rangle$-method utilising the new baseline and stop-time algorithms.

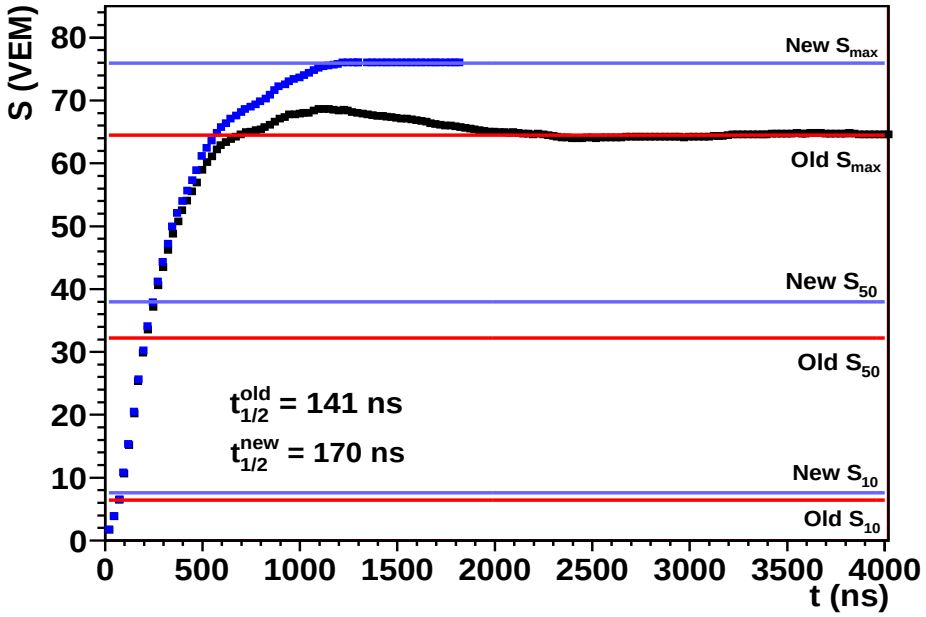

Figure 3.4: The cumulative signal found using the old (black points) and new (blue points) stop-times for one detector. The total signal, 50% and 10% of the total signal are marked for both results. A 29 ns difference is observed in the risetimes. Note that the value of the 'new S_{max}' is not the same as that labelled 'peak S_{max}' from fig. 3.1 due to the re-calculation of the baseline and undershoot correction.

3.2 The ⟨Δ⟩-Method

3.2.1 Direct Light Removal

In a number of detectors a significantly larger signal has been recorded in one or two time bins in one PMT compared to the corresponding time bins for the other two PMTs. This is known as 'direct light contamination' and is illustrated in figure 3.5(a). The reasons for direct light contamination are not fully understood. Possible reasons include the edge of the Cherenkov light cone shining directly onto a PMT (for very inclined showers), particles striking the PMT directly and causing Cherenkov emission in the glass, after-pulsing in the PMT or Cherenkov emission from electrons from the decay of muons such that the Cherenkov cone is directly incident on the PMT. Any of these effects could cause a disproportionately large energy deposit to be observed in just one or two time bins.

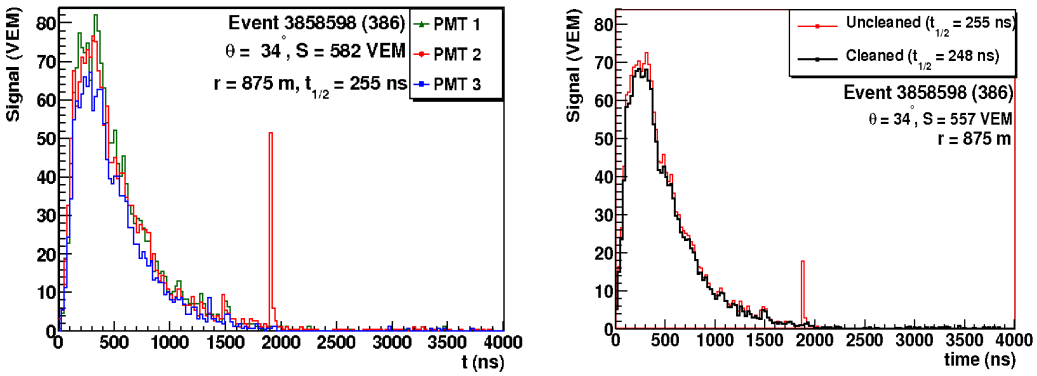

(a) (b)

Figure 3.5: An example of an FADC trace affected by direct light. Left: FADC traces from the three PMTs. A large energy deposit is observed at $\sim 1.9\,\mu$s in one PMT which is not observed in the other two. Right: The average time trace for the same detector before (red) and after (black) direct light removal. Prior to direct light removal, the total signal (averaged over all PMTs) was 582 VEM and $t_{1/2} = 255$ ns. After direct light removal this reduces to S = 557 VEM and $t_{1/2} = 248$ ns.

An algorithm was created by C. Wileman to correct for direct light effects (28). Direct light contamination is identified where the signal in a given time bin for a single PMT deviates by more than 1σ above the corresponding bin average for all three PMTs. The outlying signal in the affected time bin has been removed and a new bin average calculated from the remaining signals (see fig. 3.5(b)). Direct light is found to occur in 88% of unsaturated detectors that record a total signal S $\geq$ 15 VEM, although the change in the average signal after direct light removal is less than 5% for the majority of cases. For detectors where the change in signal is significant ($\geq$ 5%), a spike of several VEM from late in the FADC trace has been removed (e.g. fig. 3.5(a)). For a handful of these detectors ($<$ 1% of all detectors), one PMT has malfunctioned and records many times the signal of the other two detectors in nearly every time bin ('raining PMTs'). This is equivalent to having direct light in nearly every time bin. The direct light removal procedure effectively discards the malfunctioning PMT signal, allowing an accurate risetime to be calculated from the other two PMT traces. In such cases, the change in the PMT-averaged total signal can be as much as 200 VEM.

In detectors where one or two PMT traces are missing, direct light removal cannot be implemented. Therefore the average of the signals from the remaining PMTs are used. Direct light removal has been implemented throughout this analysis.

3.2.2 Deconvolution

The FADC trace is a convolution of the time-spread from particles incident on a detector with the time-smearing due to the multiple reflections of Cherenkov light on the detector walls and the responses from the PMT and associated electronics. This time-smearing is known as the single particle response (SPR) and is given by (86):

$$S(t) = A(e^{\frac{-t}{67}} - e^{\frac{-t}{13}}) \tag{3.1}$$

where t is the time in ns and $A = 1$. The width of the SPR is $\sim 60\,ns$, with a peak at $\sim 40\,ns$. The Gold Deconvolution Algorithm (GDA) was used in (28)

and (82) to unfold the smearing, using the SPR, and obtain the time distribution of the incoming particles, thus providing a more accurate determination of the risetime. An example of an FADC trace before and after deconvolution is shown in figure 3.6.

Signals close to the shower core and those for inclined events are affected most by the deconvolution as the smearing due to the SPR dominates in fast risetimes. The smearing from the SPR limits even the fastest risetimes to a minimum of $\sim 40\,\text{ns}$.

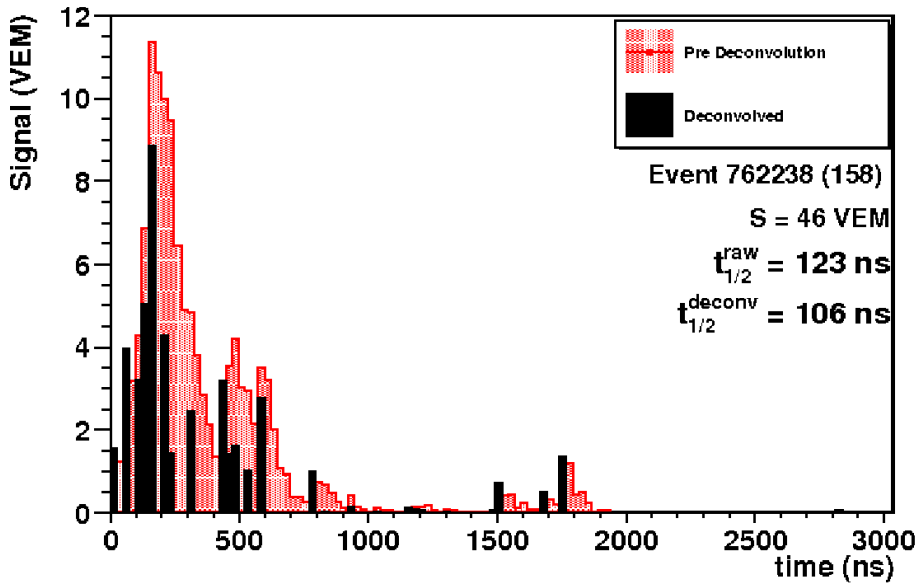

Figure 3.6: The average FADC trace from Event 762238 (158) before (red shading) and after (solid black) deconvolution.

Whilst the deconvolution stage was used in (28) and (82), concerns over the necessity and stability of the GDA have led to its exclusion from the ⟨Δ⟩-method. The GDA requires that there are no negative signals in any time bin. With the very first (pre-2008) baseline definitions - which were a simple subtraction of a constant signal, negative fluctuations of the signal in individual time bins were not possible. Due to the re-definition of the baseline to be a dynamic subtraction (post 2008, with or without correct stop-times), it is now possible for baseline-

subtracted signals to be negative in some bins due to signal fluctuations. To comply with the constraints of the GDA will therefore introduce artificial signal in some time bins, thus adversely affecting the risetimes.

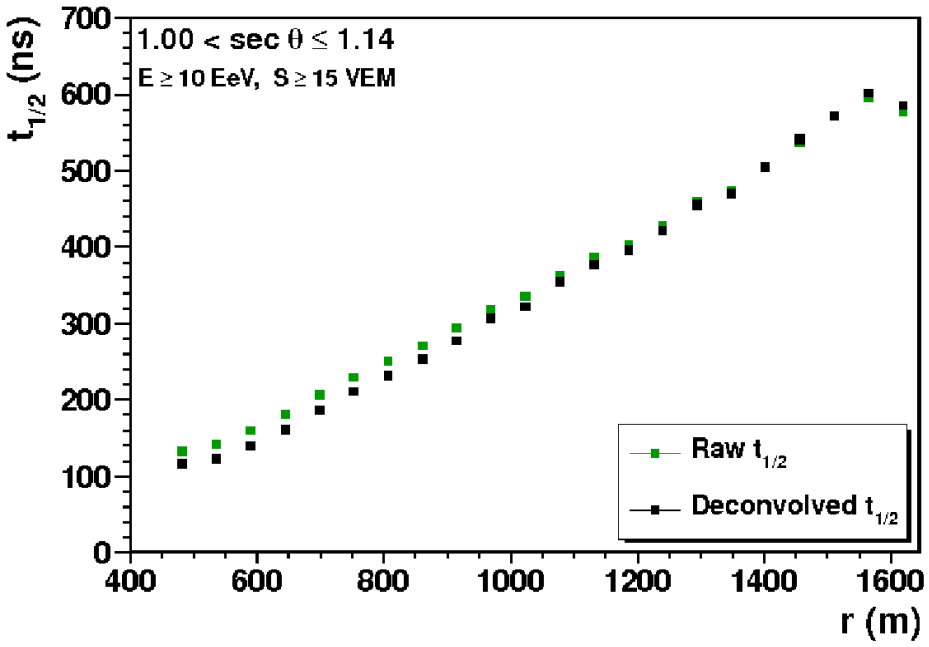

Figure 3.7: Average risetimes as a function of distance for events from 01/01/2004 to 30/06/2007 with E $\geq 10^{18}$ eV, $\theta \leq 25°$ and S $\geq$ 15 VEM. Risetimes before (green) and after deconvolution (black) are shown.

The stability of any deconvolution routine is also a concern. Although the GDA was chosen as the most stable routine, such routines are extremely sensitive to errors in measured data and to statistical fluctuations. Further, uncertainties on the SPR - a measured quantity - are not accounted for. Uncertainties due to the GDA are therefore not quantifiable.

That the deconvolution stage has a significant effect only on fast risetimes close to the shower core is clear from figure 3.7, which shows vertical events recorded between January 2004 and July 2007. These results agree with those in (28). Cuts on signals, distances and risetimes, as required by the asymmetry correction and uncertainty parameterization later in the $\langle\Delta\rangle$-method (see sections

3.2.3 and 3.2.4), virtually eliminate all risetimes for which the deconvolution plays a significant part. Given this, the deconvolution stage has been removed - with little effect on the overall analysis ($\leq 10\%$ change in $\langle\Delta\rangle$ for vertical showers). This has an additional advantage in that a dramatic speed-up to this method is achieved. A new cut on risetimes less than 40 ns (the average of the SPR) is required. This changes the number of events by less than 50 (from a set of nearly 50,000 events) compared to when a 25 ns cut (equal to the FADC bin-width) was used on the deconvolved risetimes.

3.2.3 Corrections for the Asymmetry in the Risetimes

The risetime-asymmetry is the change in the risetime as a function of azimuthal angle about the shower core. Asymmetry occurs in inclined showers due to the shower geometry relative to the ground and the development of the electromagnetic component at different slant depths (87). The azimuthal position (ζ) of a detector relative to the vertical projection of the shower axis on the ground ($\zeta = 0°$) defines whether the detector is triggered before (early detector, small azimuth) or after (late detector, large azimuth) the core hits the ground, as illustrated in figure 3.8.

The geometric component of the asymmetry is caused by the angle of the shower with respect to the ground, the layout of the array with respect to the shower core, the detector effective area seen by the shower particles and differences in the path length of particles on either side of the shower. The attenuation of the shower on different sides of the axis also gives rise to a component of asymmetry in the risetimes. Electromagnetic particles incident upon a 'late' detector will have traversed a greater depth of atmosphere than particles entering an 'early' detector. Therefore a smaller signal and risetime will be measured in the 'late' detector as more attenuation has occurred. A small geomagnetic component due to deflections of muons and electrons in the Earth's magnetic field is also present (88).

To quantify the effect of shower asymmetry on the risetime, the distribution of risetimes as a function of azimuth for different bands of distance and zenith angle have been found and fitted with a cosine function. An example of the asymmetry for one zenith angle and seven distances is shown in figure 3.9. The magnitude of the asymmetry is comparable to that in (28) for distances less than 1200 m but $\sim 10\%$ smaller at larger distances.

The amplitude of the asymmetry (g), taken from the cosine fit to the risetime with azimuth in figure 3.9, has a dependence on the distance to the shower core:

$$g = mr^2 \tag{3.2}$$

Figure 3.10 shows the asymmetry parameter m as a function of zenith angle. The maximum asymmetry, at $\sim 42°$, is comparable to that found in previous

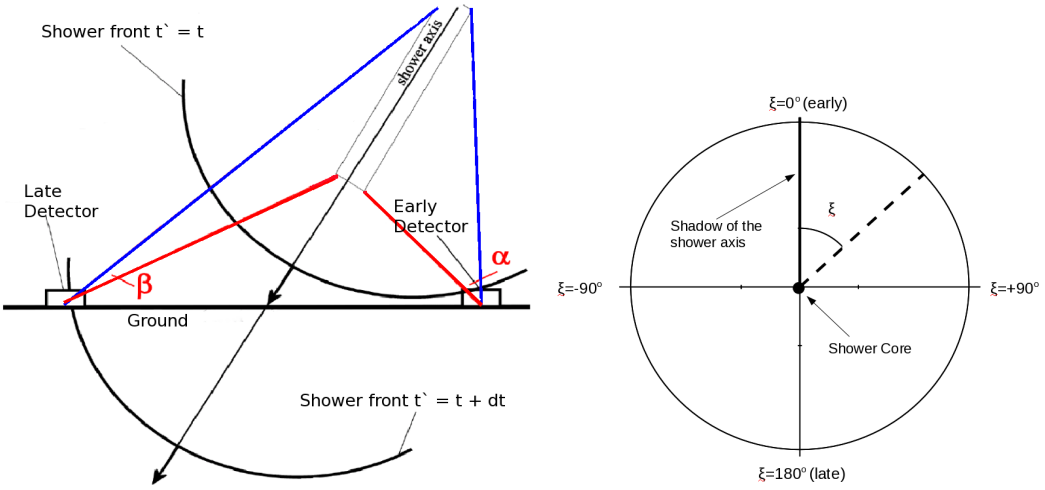

Figure 3.8: Schematic indicating the origin of the asymmetry in the risetimes of inclined showers. Left: the path of particles on either side of the shower axis from two different stages of development (red and blue lines) to detectors equidistant from the core. Due to the shower geometry, particles on the right of the axis have less far to travel and so arrive earlier than particles on the left. The angle subtended by particles entering the 'early' station (α) (and, by implication, the risetime) is larger than for particles entering the 'late' station (β). Right: top-view indicating the azimuthal angle ζ with respect to the vertical projection of the shower axis (thick line). Figures adapted from (82).

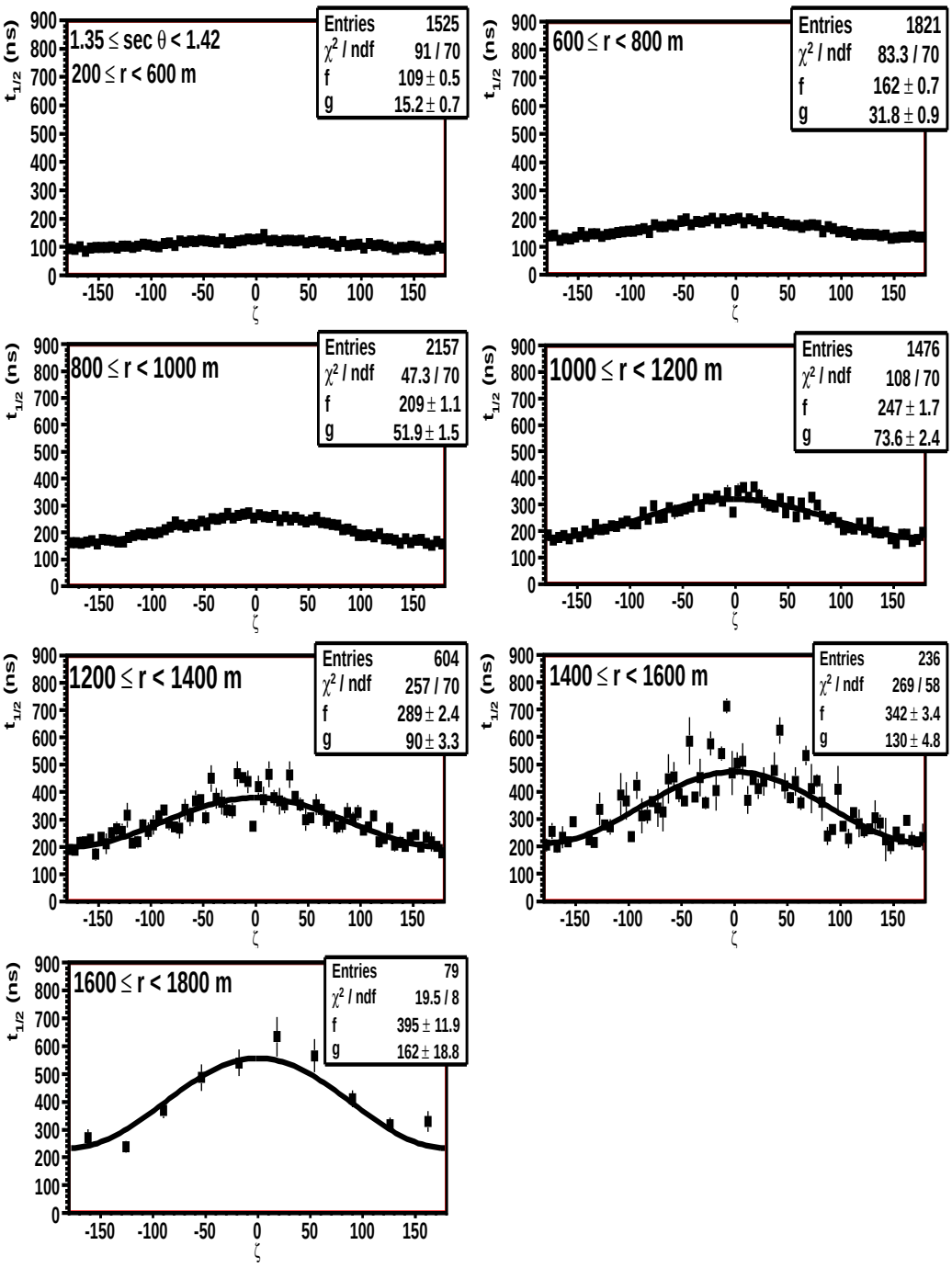

Figure 3.9: The average risetime as a function of azimuthal angle for showers at zenith angles $1.35 \leq sec\theta < 1.42$ ($42° \leq \theta < 45°$). Seven different distances are shown. Each figure has been fitted with a function of the form $t_{1/2} = f + gcos\theta$.

work (28), (89), (90). For showers inclined more than $\sim 50°$, geometric effects dominate the asymmetry as the electromagnetic part is largely attenuated.

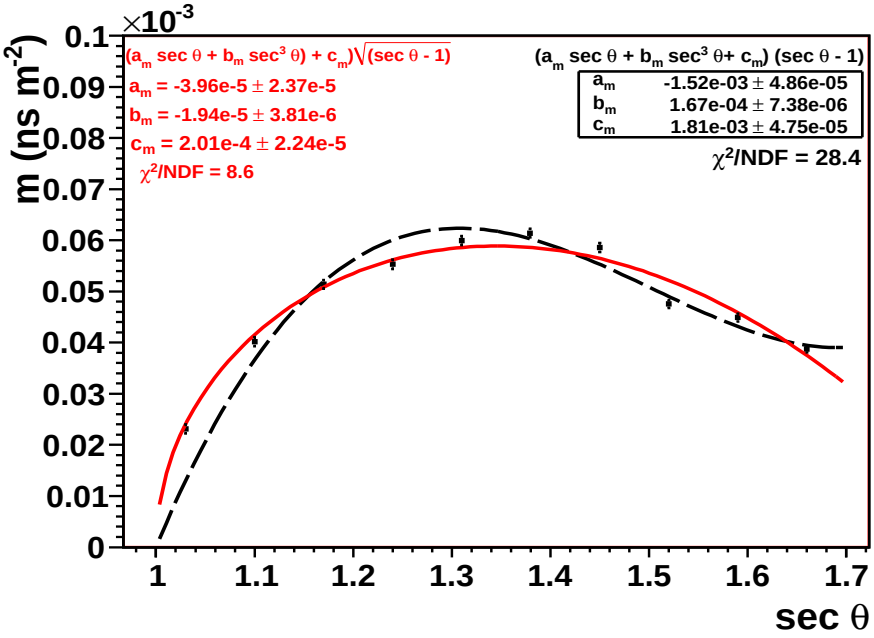

Figure 3.10: The asymmetry parameter m as a function of zenith angle (Black points). Two fit functions are shown. Black dashed line and text: That used in (28), Red solid line and text: This work (see text for details).

In (28), the parameter m was described by a function of the form:

$$m = (asec\theta + bsec^3\theta + c)(sec\theta - 1) \tag{3.3}$$

This is shown by the black line in figure 3.10. Due to a combination of new stop-times, better core positions (which caused azimuth angles and distances to change), and the removal of the deconvolution stage, equation 3.3 no longer adequately describes the asymmetry. It has been found that the inclusion of a square-root to the last term of equation 3.3 describes the asymmetry better. The

new parameterization is thus:

$$m = (asec\theta + bsec^3\theta + c)\sqrt{(sec\theta - 1)}$$

where :

$$\begin{aligned} a &= (-3.96 \pm 2.37) \times 10^{-5}\,\mathrm{ns\,m^{-2}} \\ b &= (-1.94 \pm 0.38) \times 10^{-5}\,\mathrm{ns\,m^{-2}} \\ c &= (2.01 \pm 0.22) \times 10^{-4}\,\mathrm{ns\,m^{-2}} \end{aligned} \tag{3.4}$$

and is shown by the red line in figure 3.10. The reduced χ^2s from both functions are also given, indicating that equation 3.4 gives the superior fit.

A correction to the risetimes (to $\zeta = 90°$) has been made by subtracting the expected average asymmetry as calculated using the parameterization in equation 3.4:

$$t_{1/2}^{corrected} = t_{1/2} - m(\theta)\, r^2 cos\zeta \tag{3.5}$$

The distributions of the raw and asymmetry-corrected risetimes are shown in figure 3.11 for all detectors with S $\geq$ 15 VEM and sec$\theta \leq 1.7$. There is, on average, a slight shift ($\sim 2\%$) to longer risetimes upon correction for the asymmetry for all risetimes larger than $\sim$ 50 ns. The appearance of some risetimes smaller than 40 ns is also seen due to the asymmetry correction. Asymmetry-corrected risetimes will be used for the remainder of this work. No dependence of the asymmetry on the signal size has been found for any zenith angle or distance range. This is in agreement with (28).

3.2.4 Analysis of the Uncertainty on the Risetimes

Knowledge of the uncertainty in the risetime is important if the effect of shower-to-shower fluctuations on the ability to distinguish particles of different mass is to be determined. There are three primary sources of uncertainty on the risetime measurements: sampling effects, detector electronics and digitisation procedures, and uncertainties introduced during reconstruction. The propagation of uncertainties during the asymmetry correction and direct light removal stages must also be considered.

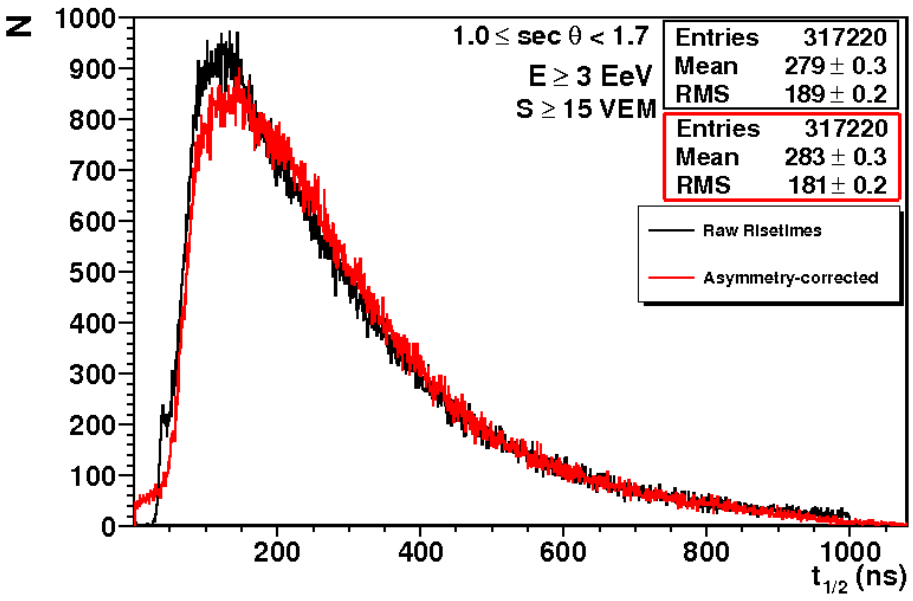

Figure 3.11: Distribution of asymmetry-corrected (red) and raw (black) risetimes for all detectors with S $\geq$ 15 VEM from events in the range $1.0 \leq \sec\theta \leq 1.7$.

It is inadvisable to use simulations to estimate the uncertainty on the data as the extrapolation of particle physics from much lower energies and the technique of thinning, where only a subset of particles are tracked to reduce the strain on computing requirements (see section 4.2), introduce more complex uncertainties which cannot be accurately quantified. Instead, the empirical uncertainty on the risetime has been parametrised by comparing the risetimes in 'pairs' of detectors. A 'pair' is defined as any two detectors in the same shower whose difference in distance to the shower core ($r_1 - r_2$) is less than 100 m, irrespective of azimuthal angle. Additionally, the total signal in each pair must differ by no more than $\pm$25% from the pair average.

The data have been divided into seven bins of zenith angle in the range $1.0 < \sec\theta < 1.7$, then subdivided into seven bins of distance (to the centre of each pair) in 200 m intervals from 400 m to 1800 m. Finally a further subdivision into ten bins of signal in steps of 10 VEM up to 100 VEM, plus a final bin with all unsaturated signals larger than 100 VEM has been made.

For events with zenith angles less than 37°, there are no pairs in the distance range $400 - 600$ m due to the array geometry. Detectors in the surface array form equilateral triangles of side length 1500 m. While the shower core may fall anywhere within such a triangle, the definition of a 'pair' restricts the midpoint of the closest pair to a distance of $\frac{1500}{2}\cos\theta$ m from the shower core. Only for zenith angles greater than 37° does the first distance bin play a part in the uncertainty estimation. In (28) it is implied (and indicated in several figures therein) that pairs have been found within 600 m of the shower core for zenith angles less than 37°. This is clearly erroneous. Further, there is a disagreement between C. Wileman (28) and B. Smith (82) over the form of the parameterization of the uncertainty and the number of pairs found. A complete re-analysis of the uncertainty has therefore been necessary. With the increased data set a total of 146,387 pairs have now been found.

The uncertainty in the risetime of each pair has been calculated using (91):

$$\sigma_{t_{1/2}^{pair}} = \frac{\sqrt{\pi}}{2}\langle|t_{1/2}^{(1)} - t_{1/2}^{(2)}|\rangle \tag{3.6}$$

where $\langle|t_{1/2}^{(1)} - t_{1/2}^{(2)}|\rangle$ is the average absolute difference between pairs of asymmetry-corrected risetimes for a given signal bin. A correction has then been made to compensate for the difference in distance between each detector in the pair, $\sigma_{\Delta r}$:

$$\sigma_{t_{1/2}} = \sigma_{t_{1/2}^{pair}} - \sigma_{\Delta r} \tag{3.7}$$

where:

$$\begin{aligned}
\sigma_{\Delta r} &= \frac{\partial}{\partial r}\langle t_{1/2}(r)\rangle \,\langle|r_1 - r_2|\rangle \\
&= \frac{\partial}{\partial r}(40 + \sqrt{(A^2 + Br^2)} - A)\,\langle|r_1 - r_2|\rangle \\
&= \frac{1}{\sqrt{(A^2 + Br^2)}}\, Br\,\langle|r_1 - r_2|\rangle
\end{aligned} \tag{3.8}$$

Where A and B are parameters from a fit to the average risetime as a function of distance, $\langle t_{1/2}(r)\rangle$ (see section 3.2.5 or (28) for details). $\langle|r_1 - r_2|\rangle$ is the absolute

average difference between the two detector-core distances and r is the average distance of the pair to the shower core.

Figure 3.12 shows the average uncertainty in risetimes between pairs of detectors for three different zenith angles, including the most vertical events. A minimum of 10 pairs in any zenith angle/distance/signal bin combination has been required to avoid large statistical fluctuations. The uncertainty increases as $1/\sqrt{S}$ for all zenith angles and distance ranges and reflects the increase in Poissonian fluctuations due to the decreasing number of particles present.

The form of the uncertainty parameterization used in either (28) or (82) is no longer satisfactory. By parametrising the uncertainty as a function of the square root of the signal (rather than simply the signal) the uncertainty is better described:

$$\sigma_{t_{1/2}} = \frac{J(r,\theta)}{\sqrt{S}} + K(r,\theta) \tag{3.9}$$

where:

$$\begin{aligned} K =& a_K(\theta) + b_K(\theta) r \\ J =& a_J(\theta) + b_J(\theta) r \end{aligned} \tag{3.10}$$

The four parameters a_K, b_K, a_J and b_J show a linear dependence with θ (figure 3.13).

The uncertainty on the risetime is now much smaller (due to the $\sqrt{S}$ term) than in (28) or (82), which will introduce a larger spread on $\langle\Delta\rangle$ than in previous works. A cut on the signal at 15 VEM is introduced to limit the impact of the fluctuations from detectors with few incident particles on the calculation of $\langle\Delta\rangle$ and has been used throughout this work.

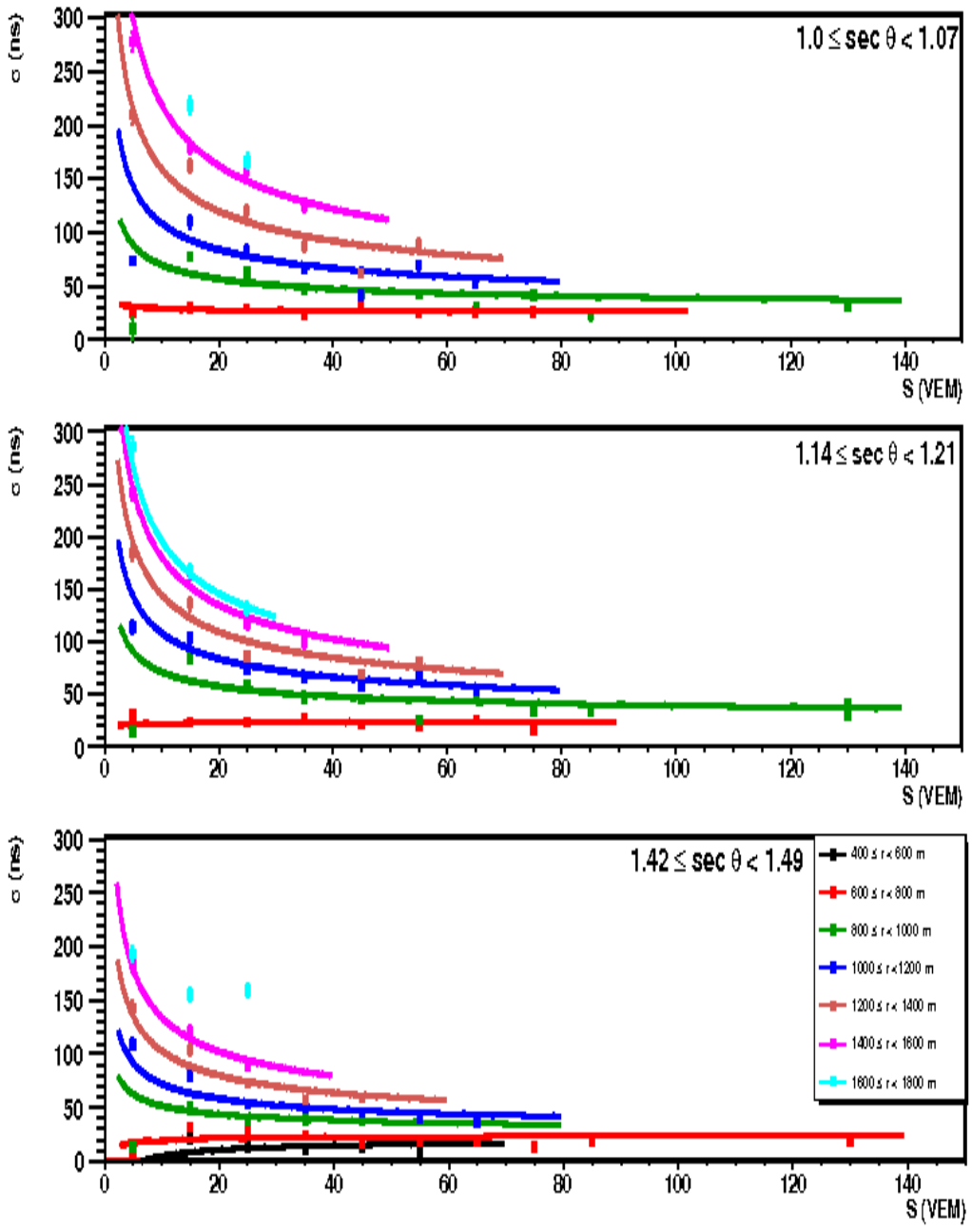

Figure 3.12: The uncertainty on the risetime as a function of signal size for three zenith angle ranges (Top panel: $0 - 20°$, Middle: $28 - 34°$, Bottom: $45 - 47°$). The uncertainties have been calculated from 'pairs' of detectors equidistant from the shower core. Each colour represents a different distance range (as indicated in the bottom panel) and each point is the average of at least 10 pairs. The fit function used is $\sigma_{t_{1/2}} = \frac{J(r,\theta)}{\sqrt{S}} + K(r,\theta)$.

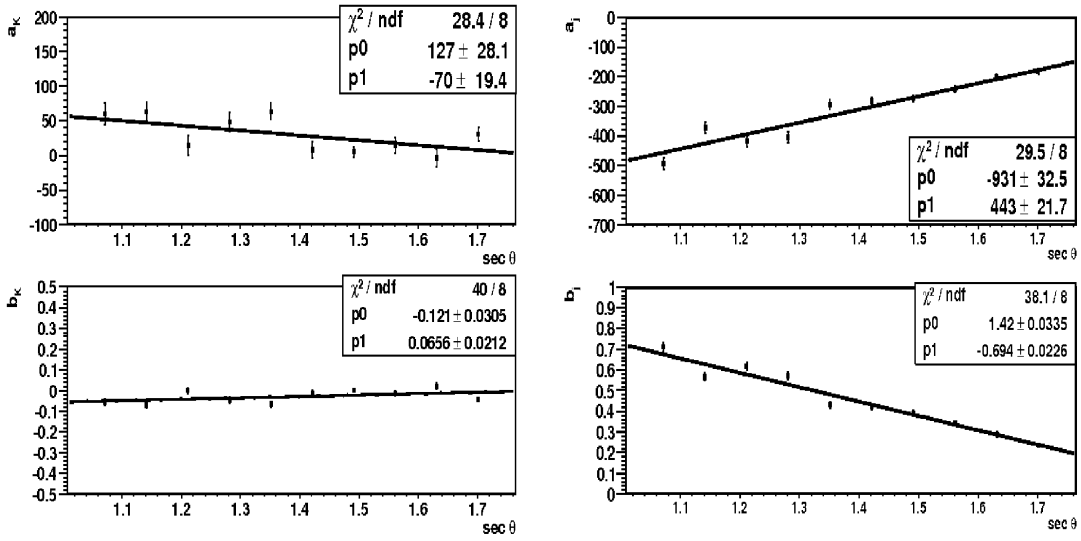

(a) (b)

Figure 3.13: Left: The uncertainty parameters a_K and b_K and Right: The uncertainty parameters a_J and b_J as a function of zenith angle.

3.2.5 Derivation of a Benchmark from the Data

The risetime is dependent upon the energy, zenith angle, signal size and distance from the shower core. A higher-energy shower produces more secondary particles, of which a larger proportion will reach ground, than a lower energy shower. A more energetic event implies a deeper shower development, on average, which in turn implies a larger risetime at a given distance due to an increase in the path-length difference traversed by particles from different stages of shower development.

The composition and lateral distribution of secondary particles plays a role in the time spread of the signal. This was first observed by Linsley and Scarsi in 1962 (92). With the exception of electrons from the decay of muons close to the observation level and the shower axis, electrons are scattered more than muons and so arrive later. The early part of the shower therefore predominantly consists of muonic signal, from which the risetimes are calculated.

A benchmark has been derived which represents the average risetime for a

given distance, zenith angle and energy. The range of zenith angles, signals and distances used to calculate the benchmark must be carefully chosen to avoid bias. Risetimes from detectors with signals less than 15 VEM have already been excluded from this analysis, as are saturated stations ($S \geq 800$ VEM) where the risetime cannot be properly ascertained.

Unsaturated signals with risetimes less than 40 ns are problematic. Such risetimes are shorter than the average time smearing introduced by the diffusion of light inside the water-Cherenkov detectors and therefore cannot be accurately measured. From figure 3.11 it can be seen that the main reason for a risetime ≤ 40 ns is due to the asymmetry correction of raw risetimes in the range $40 \leq r < 60$ ns. Such risetimes are usually from detectors with large signal sizes, small distances and large zenith angles. The risetime tends to 40 ns in showers inclined by more than $\simeq 45^\circ$ and in detectors less than 650 m from the shower core, where the uncertainty on the risetime is not properly quantified due to insufficient statistics from the pairs method. To avoid biases from very inclined showers due to this and inaccuracies in the asymmetry correction, only events with zenith angles smaller than 45° have been used.

A lower limit to the distance has been implemented at 650 m to prevent biases due to the removal of saturated stations. An upper limit on the distance has been imposed at 1400 m as the uncertainty on the risetime is poorly defined for larger distances (see figure 3.12). This is a reduction from the 1600 m cut used in (28). Whilst this upper distance cut may be more strict than necessary in the case of the data, it will be seen later that the risetimes in photon simulations at larger distances are not well-measured. To allow future, consistent, comparison to photon simulations and to err on the side of caution, the stricter cut at 1400 m has been adopted. The number of risetimes removed by each of these cuts are indicated in table 3.1.

Whilst the ⟨Δ⟩-method can in principle be used in events where only 3 detectors are triggered, in this work events with a minimum of 5 detectors are required - of which at least two must survive the cuts described above. This ensures that

Cut	Detectors Remaining	% Remaining
$E \geq 3\,\mathrm{EeV}$ & $\theta \leq 60°$	244969	100
$\theta \leq 45°$	168155	68
$S \geq 15\,\mathrm{VEM}$	81517	33
$S \leq 800\,\mathrm{VEM}$	74354	30
$r \geq 650\,\mathrm{m}$	59053	24
$r \leq 1400\,\mathrm{m}$	55231	23
$t_{1/2} \geq 40\,\mathrm{ns}$	55181	23

Table 3.1: The number and percentage of risetimes surviving each detector-level cut used in the $\langle\Delta\rangle$-method, in the order they are applied. After these cuts, a total of 10,961 events above 3 EeV (22.7%) have a calculable $\langle\Delta\rangle$.

only events with well-reconstructed core positions and energies are used and will also be necessary in future photon searches if the long-term goal of combining $\langle\Delta\rangle$ and the radius of curvature in a multi-parameter analysis are to be achieved. Of the 48,324 events with $E \geq 3\,\mathrm{EeV}$ and $\theta \leq 60°$, 10,961 events (22.7%) have a calculable $\langle\Delta\rangle$.

Events with energies $10 \leq E < 15\,\mathrm{EeV}$ have been used to create a benchmark in 10 bins of zenith angle in the range $1.0 \leq \sec\theta < 1.5$. This is well above the energy at which the surface array becomes fully efficient and contains sufficient events to calculate a robust benchmark against which all other events can be compared. Only those risetimes satisfying the above quality cuts have been used to derive the benchmark. The benchmark is derived by fitting the function:

$$t_{1/2} = 40 + \sqrt{(A(\theta)^2 + B(\theta)r^2)} - A(\theta) \tag{3.11}$$

to the asymmetry-corrected risetimes as a function of distance in each zenith angle bin (figure 3.14 top panel). Whilst the generic form of this fit remains the same as in (28), the intercept - which represents the minimum measurable risetime - has been changed from 10 to 40 ns to compensate for the removal of the deconvolution stage. Risetimes deviant by more than 2σ from this preliminary benchmark have been discarded and the remaining data binned in 15 distance

bins between 650 m and 1400 m. The benchmark function was then re-fitted to the binned data as shown in figure 3.14 (lower panel).

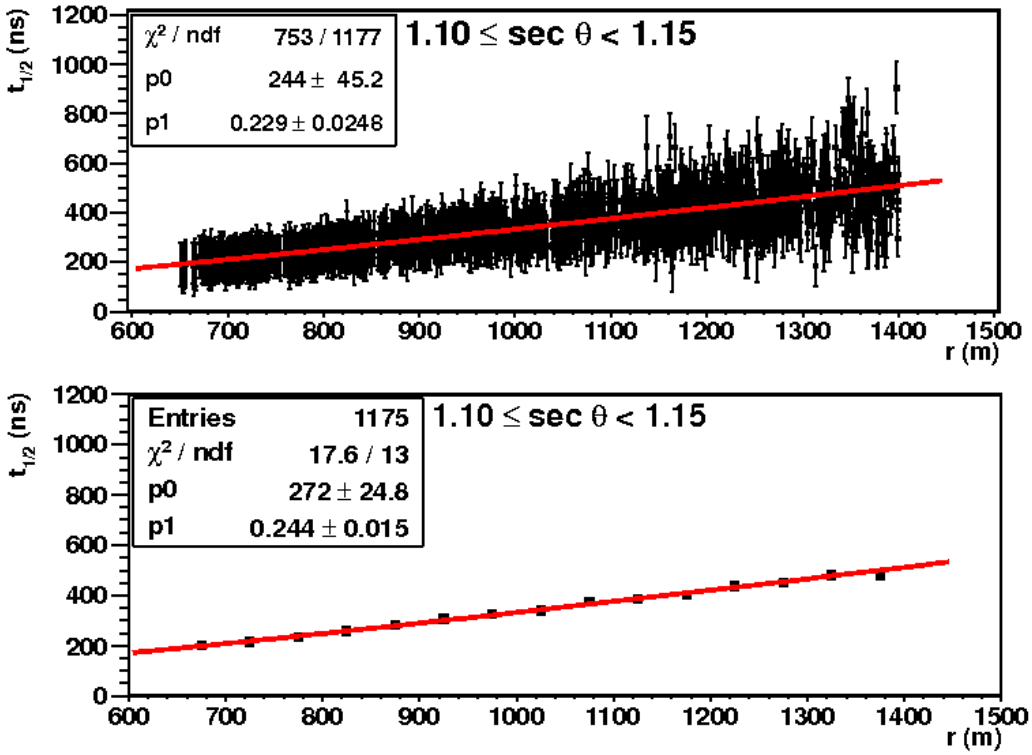

Figure 3.14: Derivation of the benchmark from the risetimes as a function of distance for the zenith angle range $1.10 \leq \sec\theta < 1.15$ and energy $10 \leq \mathrm{E} \leq 15$ EeV. Top: All risetimes passing the quality cuts (see text); Bottom: risetimes within 2σ of the benchmark derived in the top panel and in bins of 50 m. The benchmark fit is indicated by the red line in each panel.

The benchmark parameters A and B decrease exponentially with zenith angle as:

$$\begin{aligned} A &= (27.1 \pm 20.7) + (4.1 \pm 5.1) \times 10^5 \, e^{(-6.6 \pm 1.2)\, sec\theta} \\ B &= (1.9 \pm 1.1) \times 10^{-2} + (190 \pm 140) \, e^{(-6.0 \pm 0.7)\, sec\theta} \end{aligned} \tag{3.12}$$

This is illustrated in figure 3.15. These benchmarks represent the average risetime within a given zenith angle and energy band and will be used to form a ⟨Δ⟩-parameter describing the time structure of an individual shower as discussed in the next section.

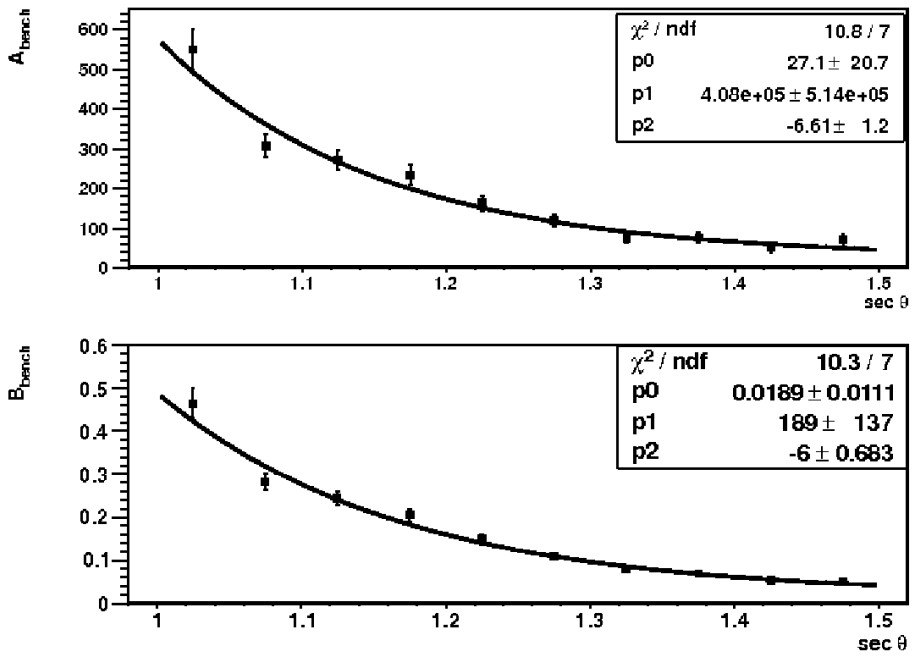

Figure 3.15: Benchmark parameters as a function of zenith angle.

3.2.6 Derivation of the $\langle\Delta\rangle$-Parameter

The aim of the $\langle\Delta\rangle$-method is to combine risetimes from individual detectors into one parameter representing a single event. $\langle\Delta\rangle$ is defined as the average deviation of risetimes within an event from the expected average risetime (the benchmark), after accounting for measurement uncertainties. The expected risetime, $t_{1/2}^{bench}$, for a particular detector at a distance r in an event with zenith angle θ is calculated using the benchmark parameterization from the previous section. The expected risetime is then subtracted from the measured risetime and divided by the measurement uncertainty, giving a δ_i for each detector. $\langle\Delta\rangle$ is then the average of all the δ_i within the same event:

$$\langle\Delta\rangle = \frac{\Sigma\delta_i}{N_i} = \frac{\Sigma(\frac{(t_{1/2}-t_{1/2}^{bench})}{\sigma_{t_{1/2}}})}{N_i} \tag{3.13}$$

The derivation of $\langle\Delta\rangle$ is illustrated in figure 3.16.

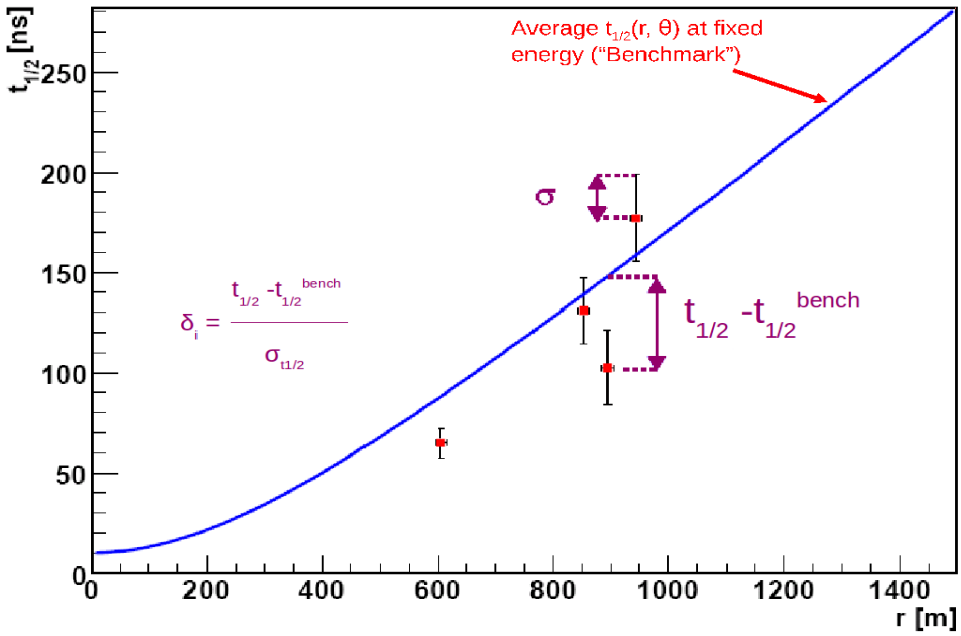

Figure 3.16: Schematic illustrating the derivation of $\langle\Delta\rangle$ from the risetimes. The expected risetime at a given distance and zenith using the benchmark function (blue line) is subtracted from the measured risetime (red points) and divided by the measurement uncertainty (black error bars). $\langle\Delta\rangle$ is then the average over all risetimes used in the event. Reproduced from (82).

Events with larger than average risetimes have a positive $\langle\Delta\rangle$. The distribution of $\langle\Delta\rangle$ for events within the benchmark energy range ($10 - 15$ EeV) is shown in figure 3.17. By definition the average, $\overline{\langle\Delta\rangle}$, for events within the benchmark energy range should be zero. For the events used in this work, $\overline{\langle\Delta\rangle}$ is 0.004 ± 0.010, consistent with expectations.

The benchmark function derived in section 3.2.5 is used to calculate $\langle\Delta\rangle$ for all events, regardless of the energy of the event studied. The distributions of $\langle\Delta\rangle$ are shown for 11 energy bins above 3×10^{18} eV in figure 3.19 and the distribution of all events above 10 EeV is given in figure 3.18. $\overline{\langle\Delta\rangle}$ shifts to larger values with increasing energy, as expected. In all cases, the distribution of $\langle\Delta\rangle$ is asymmetric about the mean with a slight skew towards positive $\langle\Delta\rangle$, and therefore larger risetimes.

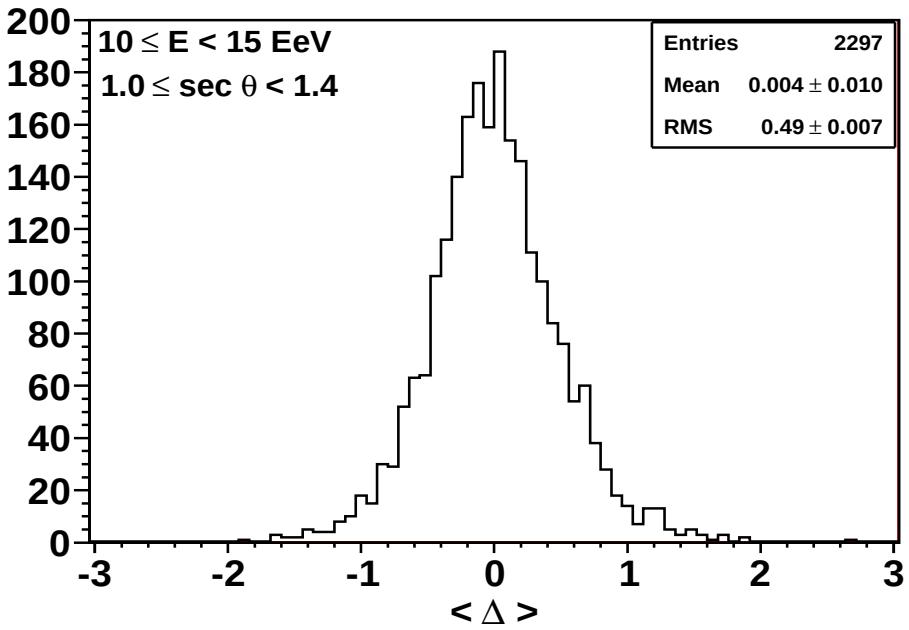

Figure 3.17: Distribution of $\langle\Delta\rangle$ for the benchmark energies $10 \leq \mathrm{E} \leq 15\,\mathrm{EeV}$ and zenith angles $\leq 45°$.

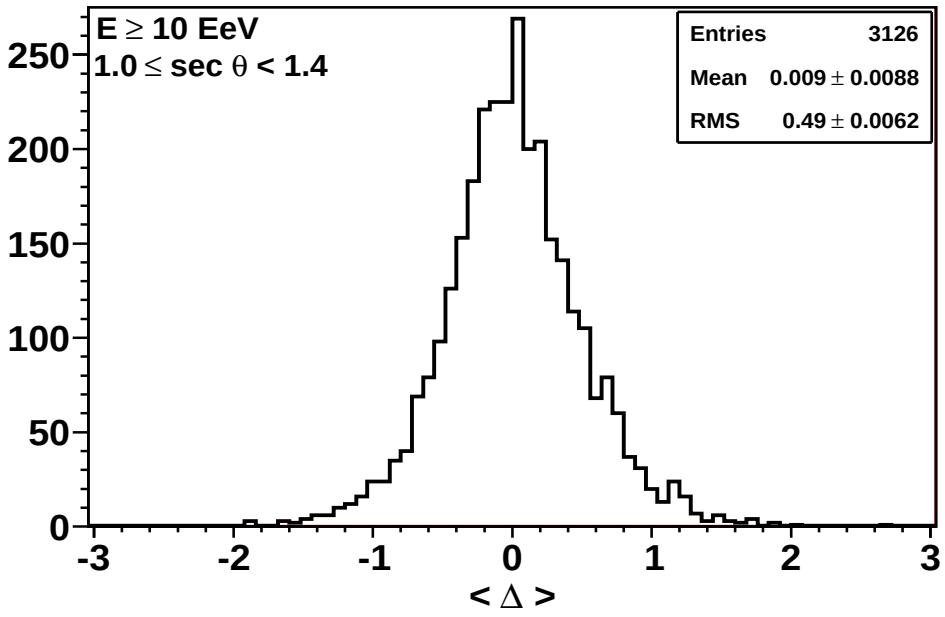

Figure 3.18: Distribution of $\langle\Delta\rangle$ for all events with $\mathrm{E} \geq 10\,\mathrm{EeV}$ and $\theta \leq 45°$.

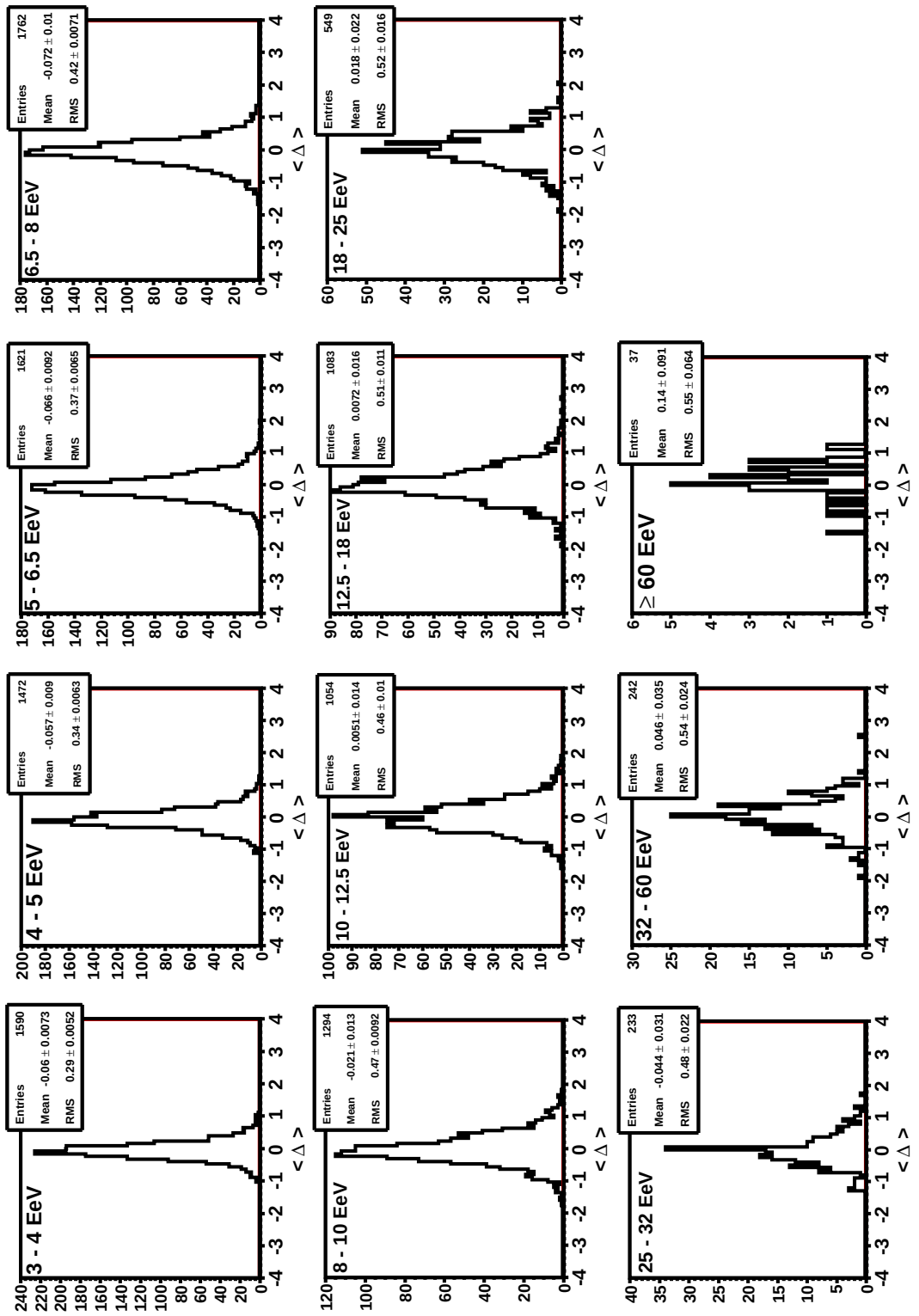

Figure 3.19: Distributions of $\langle\Delta\rangle$ for the data in 11 different energy bins above 3 EeV.

3.3 Inspection of Outliers in $\langle\Delta\rangle$

Events for which $\langle\Delta\rangle$ lies in the tails of the distribution shown in figure 3.18 have been individually inspected. Whilst care has been taken to select the highest quality events available, some anomalous events may remain that need to be dealt with appropriately. Forty-seven events with $\langle\Delta\rangle$ outside the range $-1.5 \leq \langle\Delta\rangle \leq 1.5$ and with energies $\geq 3\,\mathrm{EeV}$ have been inspected, of which 34 have energies above 10 EeV.

The ground-plan, risetimes (without correction for asymmetry) and FADC traces from a well-reconstructed event with a very large $\langle\Delta\rangle = 2.52 \pm 0.44$ are shown in figure 3.20 and 3.21. The energy of this event is $56.9 \pm 0.27\,\mathrm{EeV}$ at a zenith angle of $11.4 \pm 0.2°$. This event comprises ten triggered detectors, of which only three have been used in the calculation of $\langle\Delta\rangle$. These are shown in figure 3.21.

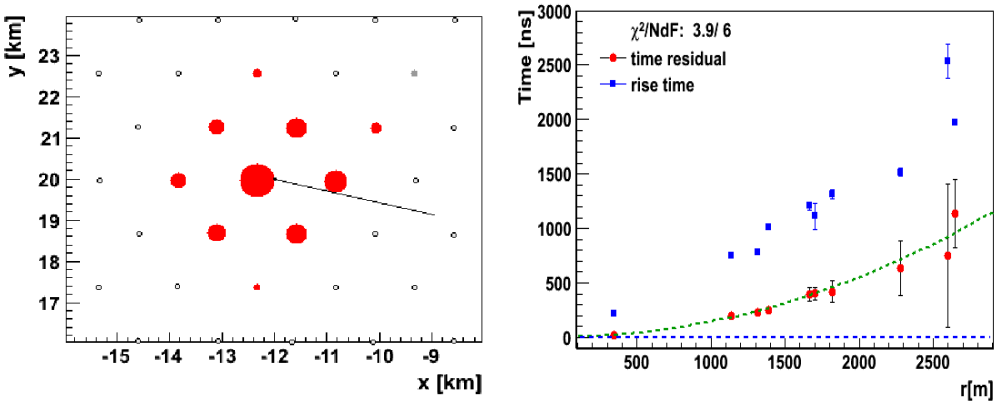

(a) (b)

Figure 3.20: Ground plan and risetimes for a well-reconstructed event (Event ID = 10612476) with a large $\langle\Delta\rangle = 2.52 \pm 0.44$. (a): Layout of triggered detectors (red dots) and direction of shower axis (black line). (b): Risetimes (prior to asymmetry-correction) (blue squares) and residuals in the start-time (red points) relative to the impact time of the shower core (blue line at t = 0) as a function of distance. The green line is a fit of a spherical function to the time-residuals.

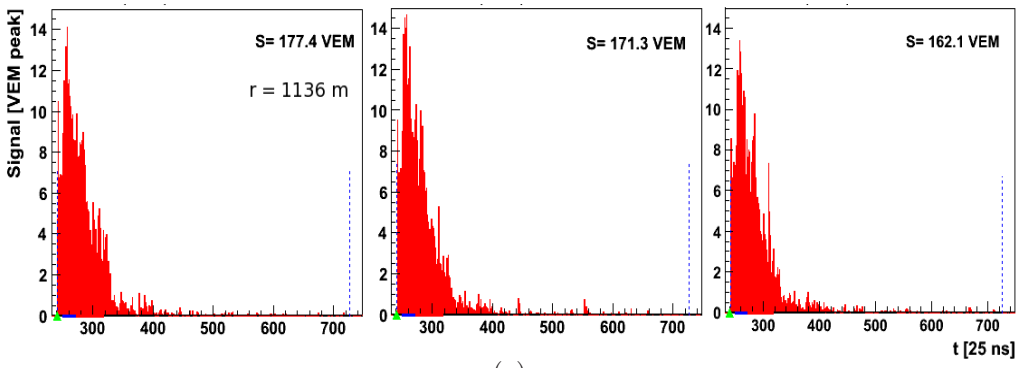

(a)

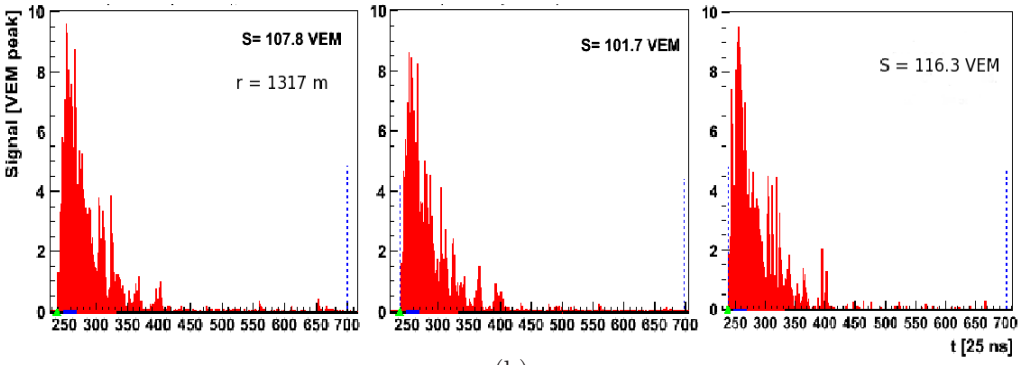

(b)

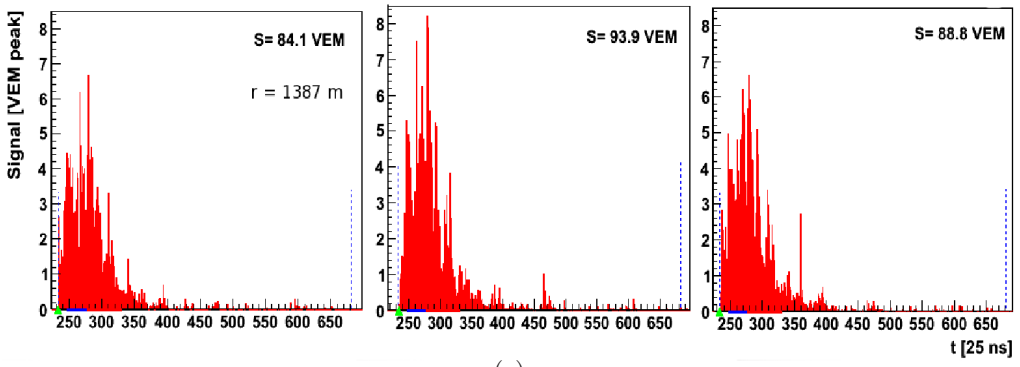

(c)

Figure 3.21: FADC traces of the detectors used to calculate $\langle\Delta\rangle$ for a well-reconstructed event (Event ID = 10612476) with a large $\langle\Delta\rangle = 2.52 \pm 0.44$ in order of increasing distance from the shower core. The distances shown are 1136, 1317 and 1387 m respectively. The detector closest to the core (not shown) is saturated and has not been used to calculate $\langle\Delta\rangle$.

Although one cannot be completely certain at this stage, it seems unlikely on visual inspection that this event is a photon due to the 'spikiness' or 'raggedness' of the traces, indicating the presence of a substantial muon component. Photons are expected to produce long, relatively smooth traces due to the electromagnetic component. By contrast, hadronic showers are expected to yield shorter traces with muon spikes evident.

A well-reconstructed event with a very small $\langle\Delta\rangle$ is shown in figures 3.22 and 3.23. This event has a $\langle\Delta\rangle$ of -1.74 ± 0.35, an energy of $\mathrm{E} = 27.7\pm1.4\,\mathrm{EeV}$ and a zenith angle of $\theta = 28.0\pm0.2°$. Nine detectors have been triggered, of which four have been used to calculate $\langle\Delta\rangle$. The detector closest to the core is saturated. It can be seen that the traces are very short in comparison to those in figure 3.21, implying a shallower shower development. However, without direct comparison to expectations from hadronic simulations it is impossible to determine the nature of the primary particle in this event.

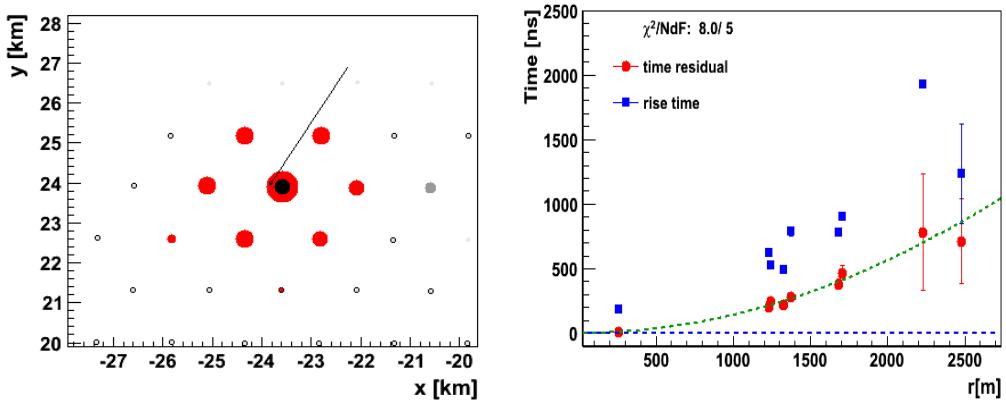

(a) (b)

Figure 3.22: Ground plan and risetimes for a well-reconstructed event (Event ID = 1682549) with a very small $\langle\Delta\rangle = -1.74 \pm 0.35$. (a): Layout of triggered detectors (red dots) and direction of shower axis (black line), (b): Risetimes (prior to asymmetry-correction) (blue squares) and residuals in the start-time (red points) relative to the impact time of the shower core (blue line at t = 0) as a function of distance. The green line is a fit of a spherical function to the time-residuals.

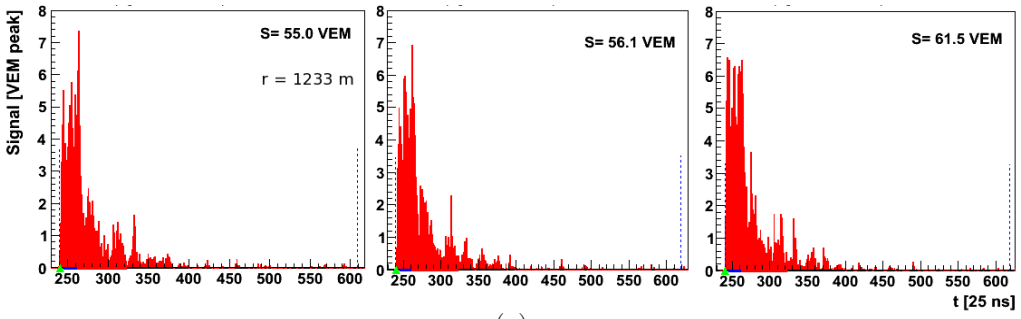

(a)

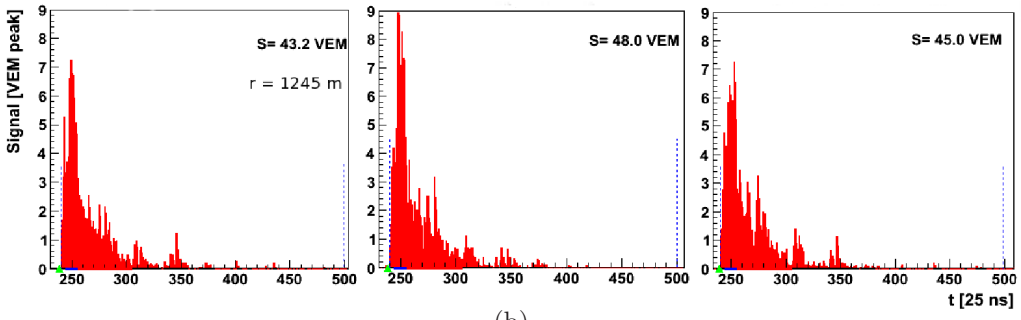

(b)

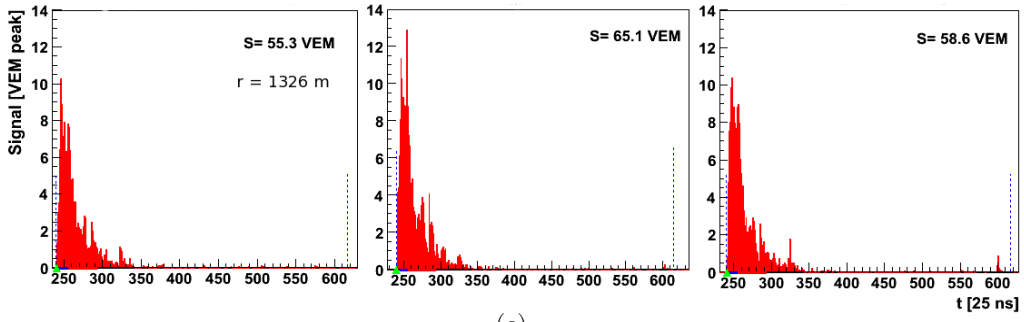

(c)

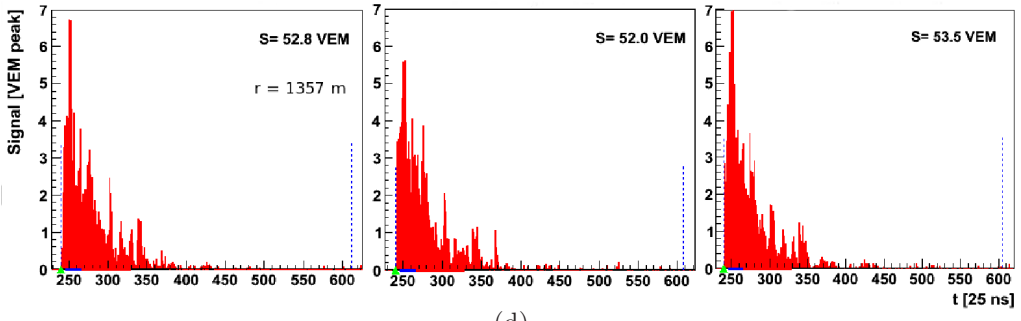

(d)

Figure 3.23: FADC traces of the detectors used to calculate $\langle\Delta\rangle$ for an event (Event ID = 1682549) with a very small $\langle\Delta\rangle = -1.74 \pm 0.35$ in order of increasing distance from the shower core. The distances shown are: 1233, 1245, 1326 and 1375 m respectively.

Nine outliers with energies above, and one with energy below 10 EeV have been identified as mis-reconstructed and removed. Reasons for considering these events for rejection include: the presence of traces with large, late energy deposits ($\geq$ 1 VEM) which yield abnormal risetimes; traces with incorrect start-times; 'raining' PMTs (where one or more PMTs in the same detector records a large signal in all time bins and the characteristic signal shape is obscured) and mis-reconstructed core positions. All events identified as mis-reconstructed in this sample have a saturated station and nearly all have a muon arriving late at ground in at least one other detector. Whilst a large number of events have saturated detectors, and more events with saturated stations than without appear in the tails of the distribution, there is no evidence of a bias of such events towards either very high or low $\langle\Delta\rangle$, as indicated in figure 3.24.

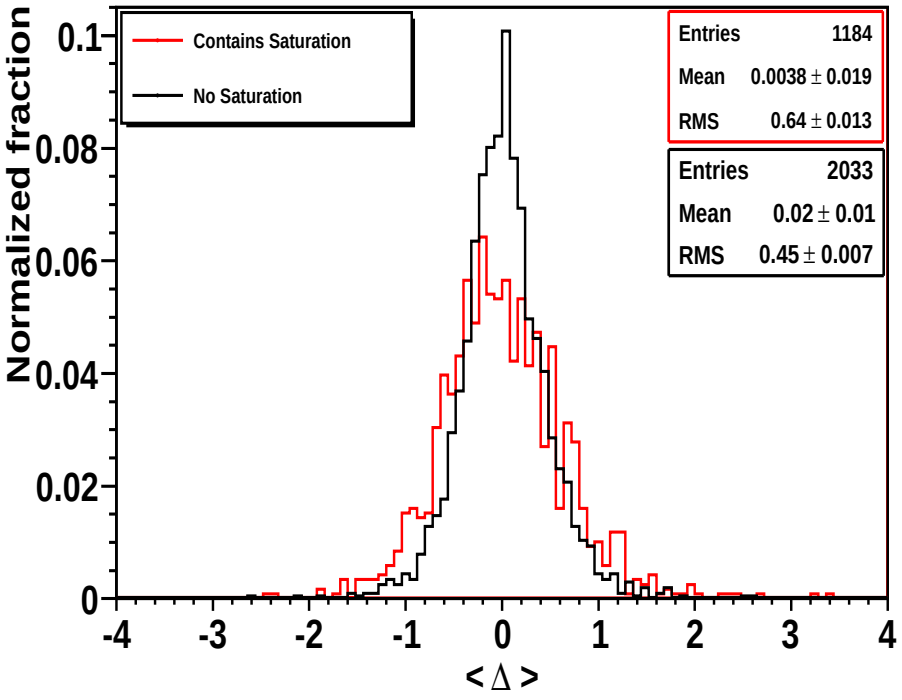

Figure 3.24: Normalised distribution of $\langle\Delta\rangle$ for events above 10 EeV with (red) and without (black) saturated stations. The risetimes from saturated stations are not used in the calculation of $\langle\Delta\rangle$.

An anomalous and thus mis-reconstructed event with a $\langle\Delta\rangle = 2.35 \pm 0.87$ is shown in figures 3.25 and 3.26. The reconstructed energy of this event is $E = 43.8 \pm 2.0\,\mathrm{EeV}$ and the zenith angle is $42.1 \pm 0.1°$. Fifteen detectors have been triggered, of which four have been used to calculate $\langle\Delta\rangle$. The detector closest to the core is saturated. This event has incorrect start-times and time-residuals in many of the detectors (as shown in figure 3.25(b)), which leads to erroneous risetimes.

Figure 3.26(a) shows a detector from this event where one PMT records a very different time to the other two, more than reasonably expected from direct light effects. This is obviously due to a PMT malfunction. Two other detectors shown are lacking a signal in at least one PMT. In itself this is not a problem as the risetime can be calculated from the existing traces, although direct light effects cannot be accounted for. Figure 3.26(c) shows a late energy deposit of $\simeq 1\,\mathrm{VEM}$ which may also be affecting the calculated $\langle\Delta\rangle$ and which is not removed via the direct light removal algorithm as one PMT in this detector has not triggered.

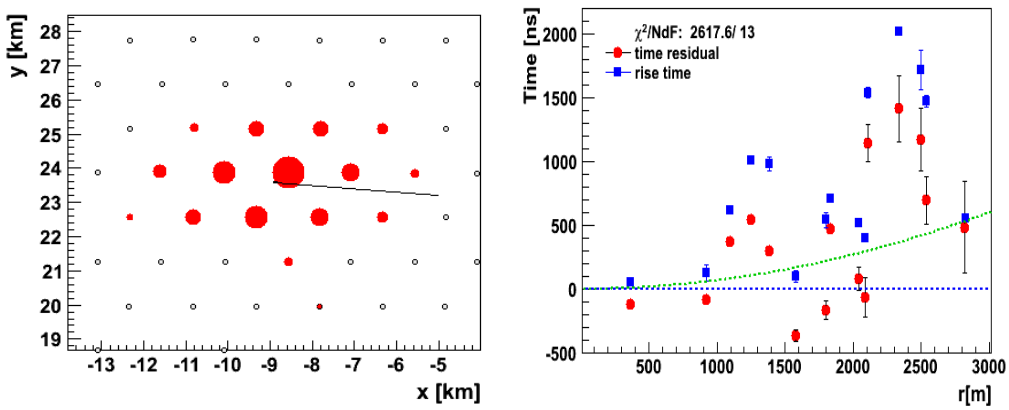

(a) (b)

Figure 3.25: Ground plan and risetimes for a mis-reconstructed event (Event ID = 10689921) with a large $\langle\Delta\rangle = 2.35 \pm 0.87$. (a): Layout of triggered detectors (red dots) and direction of shower axis (black line). The size of the red dots relates to the different signal sizes in each detector. (b): Risetimes (prior to asymmetry-correction) (blue squares) and residuals in the start-time (red points) relative to the impact time of the shower core (blue line at t = 0) as a function of distance. The green line represents a typical projection of the time-residuals as a function of distance.

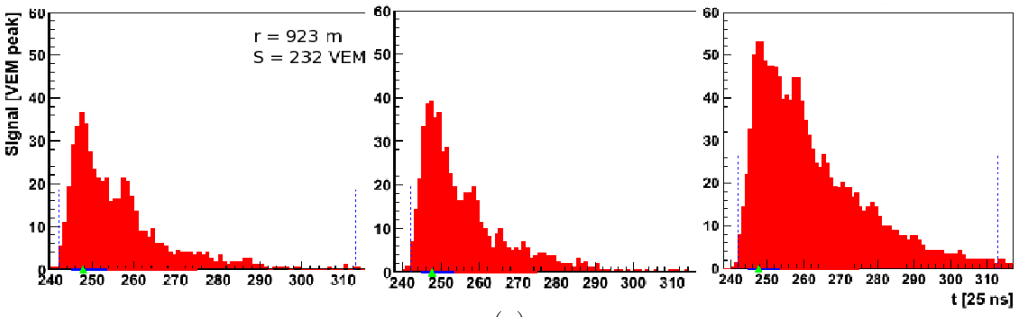

(a)

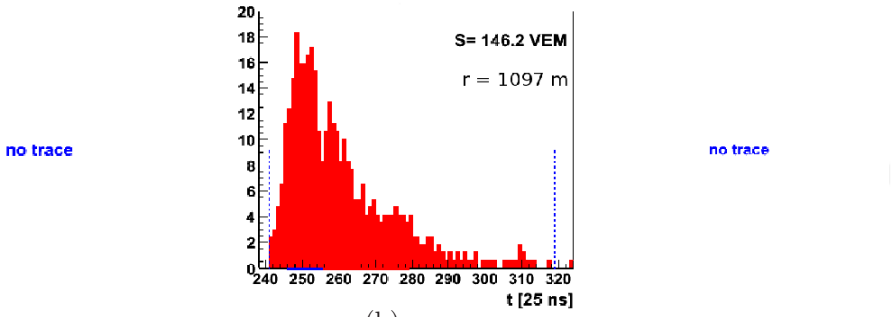

(b)

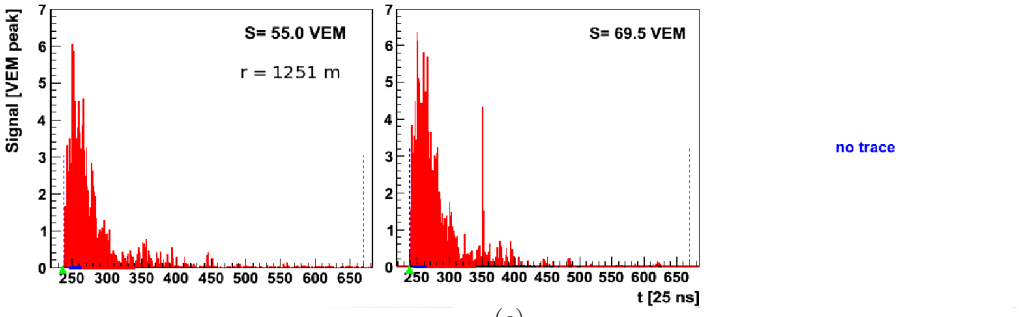

(c)

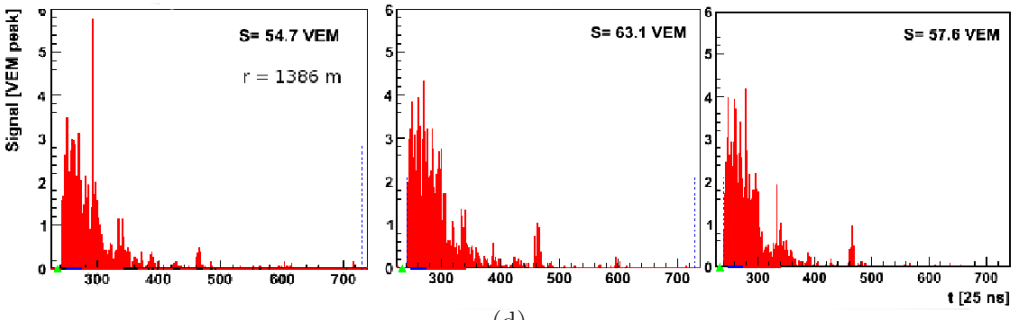

(d)

Figure 3.26: FADC traces of the detectors used to calculate $\langle\Delta\rangle$ for a misreconstructed event with a $\langle\Delta\rangle$ of 2.35 ± 0.87 in order of increasing distance from the shower core. The distances shown are 923, 1097, 1251 and 1386 m respectively.

3.4 $\langle\Delta\rangle$ as a function of Energy and X_{max}

The dependence of the average $\langle\Delta\rangle$ on the energy, zenith angle and X_{max}, has been investigated. $\overline{\langle\Delta\rangle}$ shows no dependence on zenith angle, as expected since the benchmark is defined for each zenith angle. As anticipated, $\overline{\langle\Delta\rangle}$ increases with energy above $\simeq 5\,\mathrm{EeV}$ as indicated in figure 3.27. Below 5 EeV there appears to be little or no dependence of $\langle\Delta\rangle$ on energy. Also indicated in figure 3.27 are the results from (82). The results from this work are compatible with the previous results for events above $\simeq 5\,\mathrm{EeV}$, despite the numerous changes to the method and software. Deductions on the mass composition cannot be made by studying figure 3.27 without some comparison to simulations, which will be described in chapter 4.

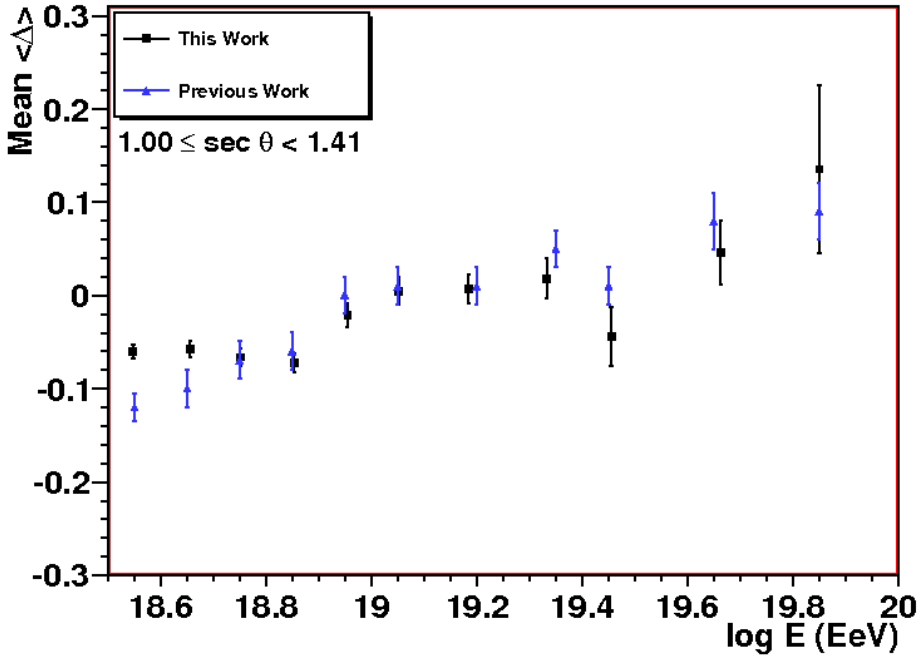

Figure 3.27: Average $\langle\Delta\rangle$ as a function of energy. Black squares: This work; Blue triangles: from (82).

The distributions of $\langle\Delta\rangle$ for each energy bin were shown in figure 3.19. A large spread in $\langle\Delta\rangle$ is observed for the 37 events above 60 EeV due to the outliers

at $\langle\Delta\rangle = -1.52$ and 1.25, both of which have been inspected. No unusual or mis-reconstructed traces were observed.

A set of high-quality hybrid events have been used to compare $\langle\Delta\rangle$ to X_{max}. These hybrid events have been selected according to the requirements of the $\langle\Delta\rangle$-method - including that the number of triggered detectors is ≥ 5. Additionally, the selection criteria from (39) has been used to ensure the FD counterpart is well-reconstructed. Events during periods of high cloud coverage and large atmospheric aerosol content have not been used. The longitudinal profile fit must have a $\chi^2/\text{NDF} \leq 2.5$ and the depth of maximum must be within the field of view of the telescopes. Fluorescence events with a large Cherenkov contamination ($\geq 20\%$) have been removed and fiducial cuts on the shower geometry have been applied. After these cuts, 508 'golden hybrid' events recorded between December 2004 and December 2010 with $\text{E} \geq 3 \times 10^{18}\,\text{eV}$ and $sec\,\theta \leq 1.41$ have been selected. A correlation can be seen in figure 3.28 between $\langle\Delta\rangle$ and X_{max}, with a correlation coefficient of 0.28. A linear fit to this data gives:

$$\langle\Delta\rangle = (-4.7 \pm 0.1) + (0.0063 \pm 0.0002) X_{max} \tag{3.14}$$

This compares to:

$$\langle\Delta\rangle = (-3.9 \pm 0.5) + (0.0053 \pm 0.0007) X_{max} \tag{3.15}$$

from the work in (82).

Equation 3.14 has been used to convert $\langle\Delta\rangle$ to X_{max} for the remainder of the surface array data, thus deriving a new parameter, $X_{max}^{\langle\Delta\rangle}$. The average $X_{max}^{\langle\Delta\rangle}$ as a function of energy for 10,961 events with zenith angles less than 45° is shown in figure 3.29 and tabulated in table 3.2. Results from hybrid events and predictions from simulations previously published in (39) are shown for comparison. There is a good agreement between the two sets of data, which appear to show an increasingly heavier composition with energy above $\simeq 3\,\text{EeV}$. It remains possible that inaccuracies in the extrapolation of particle physics from low energies introduce systematic uncertainties in the simulations and therefore a pure proton composition cannot be ruled out.

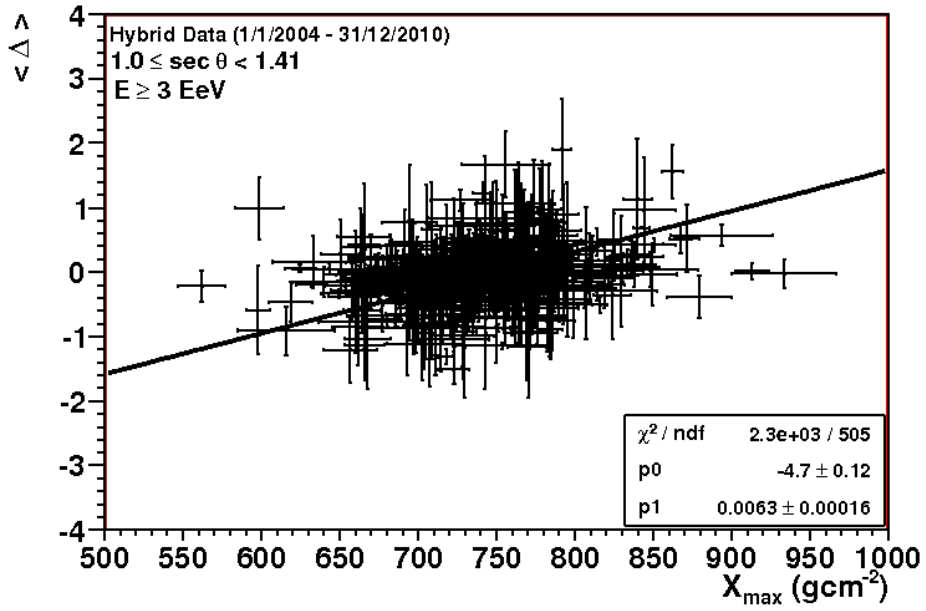

Figure 3.28: $\langle\Delta\rangle$ as a function of X_{max} for hybrid events with E $\geq$ 3 EeV and $\sec\theta \leq 1.41$ which pass a selection of fiducial cuts (see text). The correlation coefficient for this data is 0.28.

Log E (eV)	18.5	18.6	18.7	18.9	19.0	19.2	19.3	19.5	19.6	19.8
N	1513	1549	3385	1297	1669	689	522	189	126	22
$X_{max}^{\langle\Delta\rangle}$	740	741	738	746	751	752	755	759	761	775
$\sigma_{X_{max}}$	1.2	1.40	1.11	2.1	1.9	3.4	3.8	6.6	10.2	29.2

Table 3.2: Table of values of $X_{max}^{\langle\Delta\rangle}$ (in g cm^{-2}) and the associated number of events from figure 3.29.

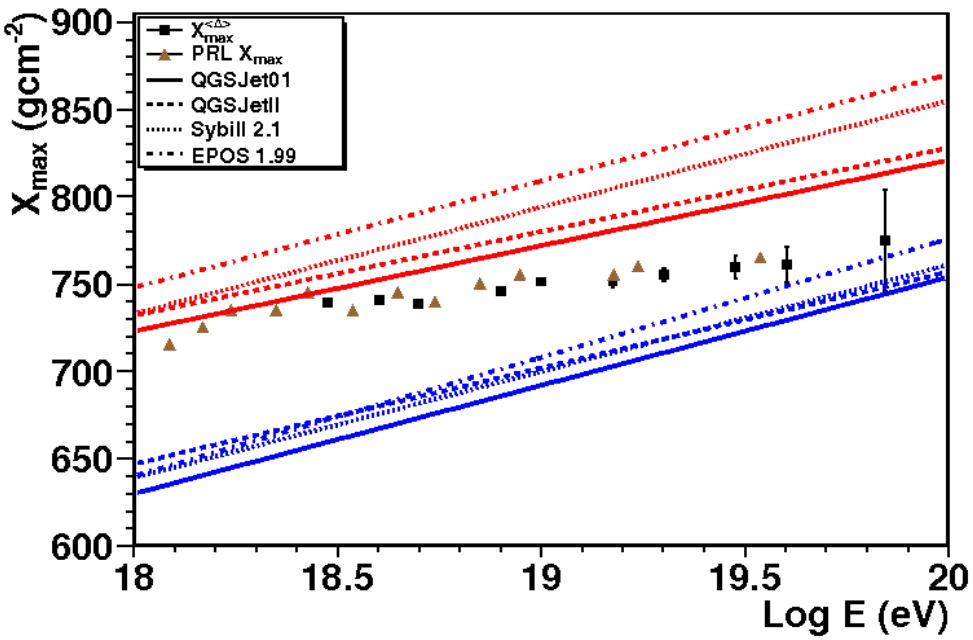

Figure 3.29: X_{max} as a function of energy from data (brown triangles) and simulations (red: Protons, blue: Iron) from (39). The average X_{max} as a function of energy from 10,961 events with zenith angles less than 45°, calculated using the $\langle\Delta\rangle$-method and the conversion given in equation 3.14 and denoted $X_{max}^{\langle\Delta\rangle}$, have been overlaid on the same axes (black squares).The number of events associated with each point are listed in table 3.2.

3.5 Conclusion

The risetime $\langle\Delta\rangle$-method first discussed in (28) and (82) has been updated using the latest Pierre Auger Observatory software. An additional 3.5 times more data recorded by the surface array has been included since the method's conception. Some long-standing problems associated with the stop-times and baselines of the FADC traces have now been resolved, allowing meaningful results using the $\langle\Delta\rangle$-method to be presented.

As a consequence of these problems and various upgrades to the analysis software, it has been necessary to re-analyse and re-parametrise each stage of the

$\langle\Delta\rangle$-method. The deconvolution procedure is no longer used and the parameterization for both the asymmetry correction and empirical uncertainties on the risetimes have been substantially altered. A new set of cuts has been imposed on the data, based on those in the original method and on physical reasoning. These alterations have been discussed in detail in this chapter.

Outliers in the distribution of this new, improved, $\langle\Delta\rangle$-parameter have been identified and inspected. Nine mis-reconstructed events have been removed from the tails of the $\langle\Delta\rangle$-distribution. Events with larger than average $\langle\Delta\rangle$ have slow risetimes and therefore a deeper development. It has been shown that $\overline{\langle\Delta\rangle}$ increases with energy in a manner similar to that in (82). A correlation of $\langle\Delta\rangle$ with X_{max} has been observed for a subset of well-reconstructed hybrid events, allowing a conversion between $\langle\Delta\rangle$ and X_{max} to be applied to the remaining SD-only events.

A comparison of $X_{max}^{\langle\Delta\rangle}$ has been made to published work that measured X_{max} directly from hybrid data. The results in this work are consistent with those in (39) and imply a mixed hadronic composition that gets heavier with energy, assuming the results from simulations are reasonable. No direct comparison of $\langle\Delta\rangle$ has yet been made to predictions from simulations. This will be described in chapter 4.

Chapter 4

Updated Photon Limits Using Shower Timing Parameters

4.1 Introduction

To determine the flux and fraction of photons, or to impose limits on these quantities, a comparison with photon simulations must be performed. The expected contamination of the photon sample from a background of hadrons is also of interest. In this chapter the predictions obtained from applying the $\langle\Delta\rangle$-Method to photon, proton and iron simulations are described. These are then compared to the data. An example of the $\langle\Delta\rangle$-distributions from the data and photon simulations are indicated in figure 4.1 for all events with $E \geq 10\,EeV$. The $\langle\Delta\rangle$s of ten events identified as most likely to be photons (the 'photon-candidates') are also marked. The steps taken to achieve this result, and those at other energies, are described in this chapter. From these results upper limits to the photon flux and fraction have been calculated and are given at the end of this chapter.

4.2 Photon Simulations

For photon-limit studies it is preferable to compare the data to photon simulations rather than hadronic simulations as the underlying physics, described by quantum electrodynamics (QED), is better understood than hadronic interactions at the

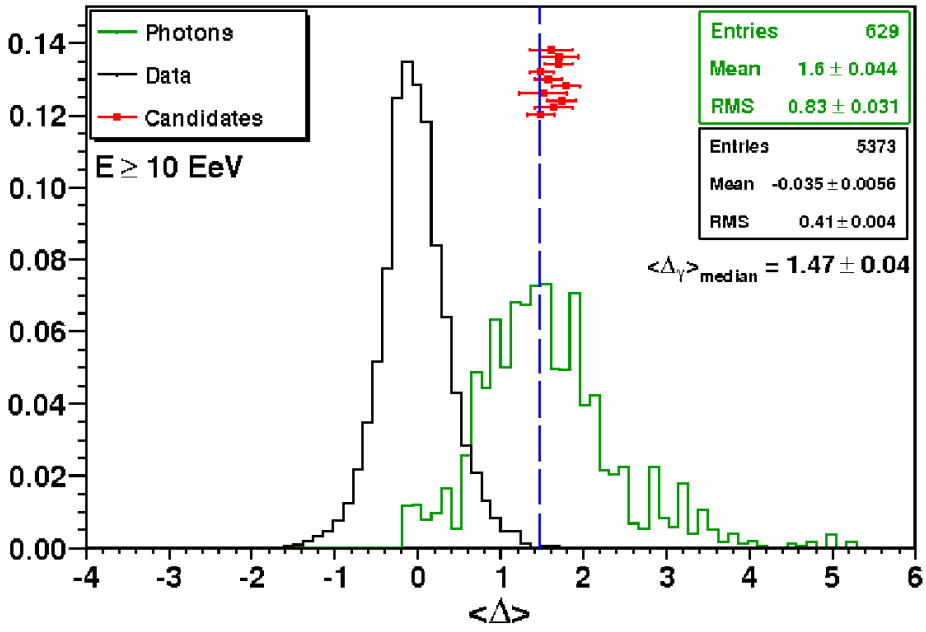

Figure 4.1: An example of the normalised distribution of $\langle\Delta\rangle$ for data and photon simulations with photon energy $E_\gamma \geq 10\,\text{EeV}$ and in the zenith angle range $30° \leq \theta < 45°$. The area under each distribution is equal to 1. The benchmarks derived from the data have been used to compare both photons and data. The $\langle\Delta\rangle$s of the ten photon-candidates are indicated (offset on the y-axis for clarity). The median of the photon distribution is at 1.47 ± 0.04 (blue dashed line).

energies concerned. Hadronic simulations suffer from large uncertainties due to the extrapolation of particle physics from much lower energies. Comparison of photon simulations to the data is therefore expected to be more reliable and so more suited to the analysis of the UHECR photon flux and fraction.

Due to their deeper development, smaller multiplicities and almost entirely electromagnetic composition, the differences between the risetimes of photon and hadron-initiated air showers are expected to be larger than between different species of hadronic primaries. On average, photons are expected to have larger risetimes (and hence a larger $\langle\Delta\rangle$) than their hadronic counterparts, with very little overlap between the two distributions of $\langle\Delta\rangle$. Where this overlap occurs, photon-initiated events in the data can be determined by inspecting events whose

$\langle\Delta\rangle$ are larger than the median of the photon distribution.

A total of 5373 photon simulations have been reconstructed in Offline. These photons were simulated using the QGSJetII hadronic interaction model and the CORSIKA (version 6.97) simulation package. A Malargüe seasonal atmospheric model has been used, providing more realistic simulations than with the US standard model (93). A continuous range of energies from 3 EeV to 300 EeV and a continuous spread of zenith angles from 0 to 60° have been simulated, the distributions of which are indicated in figure 4.2 before and after reconstruction. This represents a $\sim$ 2.5 times larger set of photons than were used in (28) and (82). Photons with pre-showering simulated have not been used.

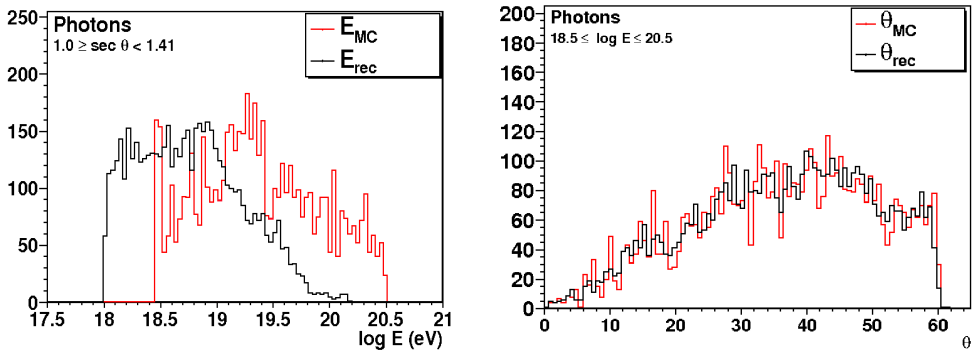

Figure 4.2: Left: Distribution of energies and Right: Distribution of zenith angles for simulated photons (Red: Monte-Carlo (MC) inputs, Black: Reconstructed using the standard reconstruction procedure).

The complete simulation of an air shower of energy greater than 10^{18} eV involves the simulation of over 10^{10} secondary particles, requiring many terabytes of disk space and taking several months to complete. To reduce the strain on computing resources and time requirements, a statistical technique called 'thinning', first introduced by Hillas (94), is applied to simulations. Air showers are simulated in full until the energy of individual particles falls below a given threshold. Below this threshold, only a representative subset of particles are tracked (95). A statistical weight is assigned to each particle in the surviving subset which accounts for the number of un-tracked particles of the same type and similar energy

within a sampling area surrounding the tracked particle. The 'surviving' particles from this process are then followed to ground level. An illustration of the concept of thinning is given in figure 4.3.

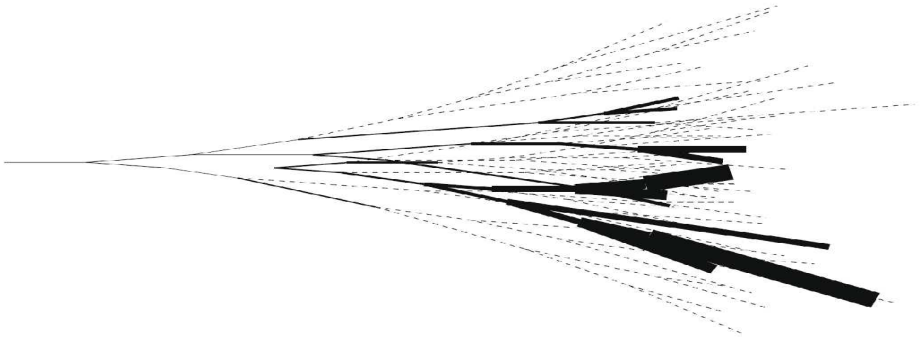

Figure 4.3: Schematic illustrating the concept of 'thinning' in simulations. The dashed lines represent particles not actually followed, the solid lines represent tracked particles, with a width proportional to the weight. Figure from (96).

Immediately prior to the simulation of detector responses, the shower is 're-sampled' by regenerating particles according to the energy, timing, position and relative weights of the particles that were tracked to ground level (96). The number of re-sampled particles is determined using a Poissonian distribution centred on the relative weight of the tracked particle. The spread of the re-sampled particles over the sampling area, which is larger than the detector area, is uniform.

Whilst shower observables are preserved on an average basis, the thinning and re-sampling procedures can introduce artificial fluctuations in individual rise-times, particularly at large distances from the core where particle densities are low (95). Further, as different particle types are thinned and re-sampled separately, correlations between them can be inadvertently modified.

The level of thinning chosen is a compromise between the computing resources available and the minimisation of artificial fluctuations introduced by the thinning and re-sampling procedures. A larger thinning level (smaller fraction of particles kept) leads to larger fluctuations in the re-sampling (95). A thinning level of 10^{-6}

is typically used for air showers with $E \geq 10^{18}$ eV and is used for all simulations in this work.

Simulation of the detector response to the photon showers is implemented using the GEANT4 package available in Offline. Simulated showers were 'dropped' at random locations on the surface array. After simulation of the detector response, the standard offline reconstruction procedure (as used for real data) has been used to reconstruct the showers. As for the data, the new stop-time and baseline algorithms have been utilised.

4.3 Construction of a Photon Energy Estimator

The distributions of Monte-Carlo (MC) and reconstructed energies for photon simulations were shown in figure 4.2, where it can be seen that the standard energy reconstruction underestimates the energy of photon-initiated air showers by up to 75%. A photon-initiated shower will produce a smaller signal in a given detector than a hadron-initiated shower of the same energy due to the steeper LDF and smaller muon content. The response of the surface detectors therefore differs for photon and hadron-initiated showers. Whilst the FD energy provides a calorimetric estimate, the calibration used to convert between $S_{38}(1000)$ and E_{FD} (figure 2.9) will systematically under-estimate the energy of photon-initiated showers recorded by the surface array. Any photon-initiated air shower existing in the data will also have an incorrectly reconstructed energy, which may cause the event to be rejected by the energy cuts used to find the photon limits, thereby remaining undiscovered.

A method for estimating photon energies has been derived to combat these problems. This method was first discussed in (97) and was incorporated into previous photon studies. Updated parameterizations have since been provided which describe photon showers more accurately and which use the reconstructed S(1000) rather than the Monte-Carlo S(1000) (98). This updated method can therefore be applied to both data and simulations.

To determine the photon energy, the stage of development attained by a photon shower reaching the detectors must be considered. This depends upon the slant depth: $\mathrm{X} = \frac{\mathrm{X_{Auger}}}{\cos\theta}$, where $\mathrm{X_{Auger}} = 875\,\mathrm{g\,cm^{-2}}$ is the vertical depth from the top of the atmosphere to the detectors. From photon simulations, the average $X_{max} = 1000\,\mathrm{g\,cm^{-2}}$ at $10^{19}\,\mathrm{eV}$. Photons with zenith angles less than $\theta = cos^{-1}(875/1000) = 29°$ will thus reach the observation level before their depth of maximum is reached. In the following search for photons, only events with a zenith angle greater than 30° are used to prevent a biased $\langle\Delta\rangle$ distribution caused by showers that have not yet reached their maximum.

The photon energy estimation is calculated in an iterative manner starting with twice the standard reconstructed energy ($\mathrm{E_{prim}}[0] = 2\mathrm{E_{rec}}$ (EeV)) (98). An approximation to the depth of maximum is then calculated using:

$$X_{max} = 847 + 131\,log_{10}(E_{prim}) \tag{4.1}$$

It should be noted that the value of X_{max} derived in this method is not suitable for mass composition measurements (98). The difference, ΔX, between X_{max} and the slant depth corresponding to the zenith angle of the shower under consideration is then found:

$$\Delta X = \frac{X_{Auger}}{cos\theta} - X_{max} \tag{4.2}$$

Finally the photon energy is found using:

$$\frac{S(1000)}{E_{prim}[i]} = 1.99 \times \frac{1 + \frac{\Delta X - 100}{1846}}{1 + (\frac{\Delta X - 100}{335})^2} \tag{4.3}$$

in units of VEM/EeV (98). $S(1000)$ and θ are taken from the standard reconstruction procedure.

This procedure is iterated until the photon energies converge, typically within 3 - 5 iterations. Events where $\Delta\mathrm{X} \leq -50\,\mathrm{g\,cm^{-2}}$, or where the photon energies have not converged within 10 iterations are considered to have an incalculable photon energy and discarded. Using the above method, the energy resolution is 18% for photon simulations whose photon energy converges (98).

For the determination of the number of photon-candidates, photon energies are calculated for both the data and simulations. Hereafter, the photon energy will be denoted E_γ to avoid confusion with the standard reconstruction E_{rec} or the Monte-Carlo energy E_{MC}. Any event in the data considered a photon-candidate (see section 4.5) will retain its photon energy estimate, E_γ, whilst all non-candidates will be re-assigned their original energy, E_{rec}, as determined from the standard offline reconstruction procedure.

4.4 Application of the $\langle\Delta\rangle$-method to Photon Simulations

4.4.1 Asymmetry in the Risetimes of Photon Simulations

It was first shown in (28) that there exists a significant asymmetry in the risetimes of simulated photon showers. In a manner similar to that described in section 3.2.3, the risetime as a function of azimuth for events in bins of zenith angle and distance has been fitted with a cosine function of the form $t_{1/2} = f + g\,cos\zeta$.

The magnitude of the asymmetry in photon simulations is much larger than for the data, as illustrated in figure 4.4, where the amplitude of the asymmetry in photon showers with zenith angles of $40-45^\circ$ at a distance of 1 km from the shower axis is approximately twice that of the data. The amplitude of the asymmetry, g, has been parametrised as a function of distance and zenith angle. Unlike the data, it is found that g varies with the cube of the distance: $g = m(\theta)\,r^3$, whereas the data show a quadratic dependence.

The result in (28) claimed that the asymmetry parameter m as a function of zenith angle for simulated photon showers was best described by a quadratic function for zenith angles greater than 25° and a linear function for smaller zenith angles. Using this larger set of photons, it is found that the function used to describe the data in section 3.2.3 will also adequately describe the photon simu-

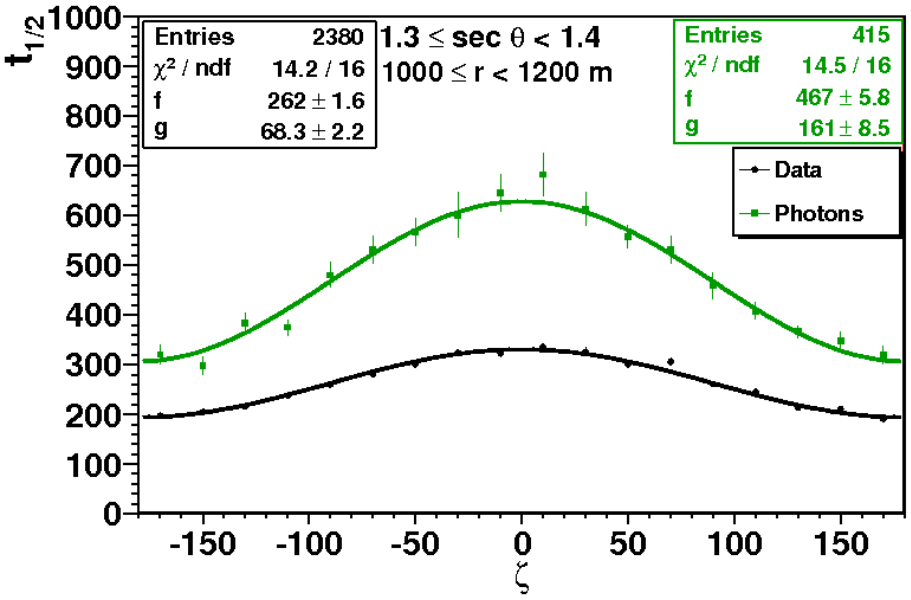

Figure 4.4: Comparison of the asymmetry in the risetimes for the data (black) and photon simulations (green) for zenith angles $1.3 \leq sec\theta < 1.4$ $(40 - 45°)$ and distances of $1000 \leq \mathrm{r} < 1200\,\mathrm{m}$. The fit-function is of the form $t_{1/2} = f + g\,cos\zeta$.

lations, namely:

$$m = (asec\theta + bsec^3\theta + c)\sqrt{(sec\theta - 1)}$$

where, forphotonsimulations :

$$\begin{aligned} a &= (3.0 \pm 0.9) \times 10^{-7}\,\mathrm{ns\,m^{-3}} \\ b &= (-7.7 \pm 0.2) \times 10^{-8}\,\mathrm{ns\,m^{-3}} \\ c &= (-2.7 \pm 0.9) \times 10^{-8}\,\mathrm{ns\,m^{-3}} \end{aligned} \tag{4.4}$$

This is illustrated in figure 4.5. Using this fit, the angle at which the asymmetry is largest is at 46°, compared to 42° for the data (see figure 3.10 for comparison).

An asymmetry correction to azimuths of $\zeta = 90°$ of the form:

$$t_{1/2}^{Corrected} = t_{1/2} - mr^3 cos\zeta \tag{4.5}$$

using the above parameterization of m has been applied to the photon risetimes. The asymmetry corrected risetimes are used for the remainder of this work.

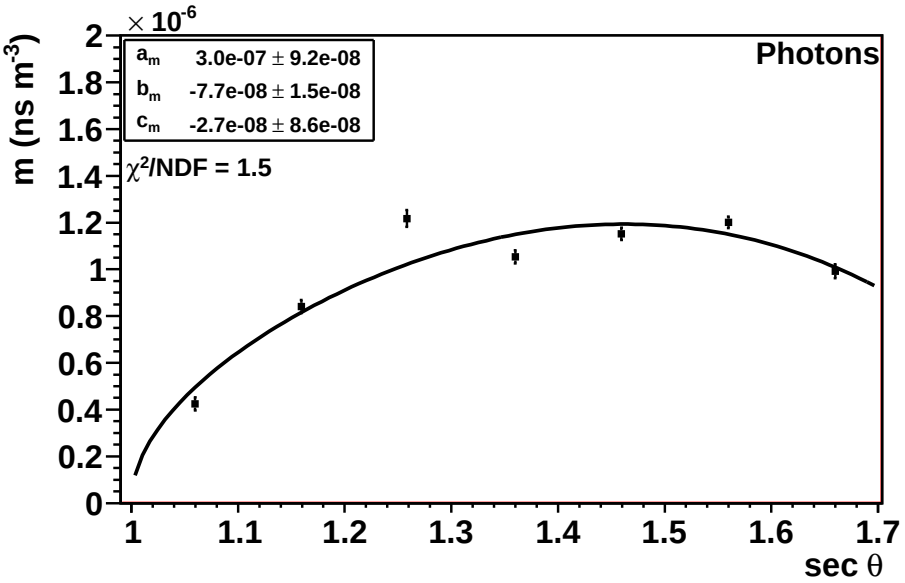

Figure 4.5: The asymmetry parameter m as a function of zenith angle for photon simulations. The fitted function is of the form: $m = (a\,sec\theta + b\,sec^3\theta + c)\sqrt{(sec\theta - 1)}$.

4.4.2 Uncertainty on the Risetimes from Photon Simulations

The uncertainty on the risetimes of photon simulations has also been updated and re-parametrised. Following the method described in section 3.2.4, the uncertainty on the photon risetimes has been parametrised as a function of zenith angle, distance and signal size using 'pairs' of detectors located within concentric rings of 100 m separation. Over 2600 pairs have been found. The uncertainty as a function of signal size for three different zenith angles and a range of distances are shown in figure 4.6. Due to the requirement that at least 10 pairs are used per zenith angle/distance/signal combination, not all bins have a calculated average uncertainty. For those that do, the uncertainty is $\sim 1.5 - 2$ times larger than for the equivalent point in the data. This is most likely due to larger fluctuations in the signals between pairs of detectors caused by the thinning and re-sampling procedures during the shower simulation. Limitations from statistics may also

play a role.

For each distance where three or more signal bins have an average uncertainty from more than 10 pairs of risetimes, a function of the form $\sigma_{t_{1/2}} = \frac{J(\theta)}{\sqrt{S}} + K(\theta)$ has been fitted. The parameters J and K as a function of zenith angle are:

$$\begin{aligned} K &= a_K(\theta) + b_K(\theta) r \\ J &= a_J(\theta) + b_J(\theta) r \end{aligned} \tag{4.6}$$

where:

$$\begin{aligned} a_K &= (2.4 \pm 0.4) \times 10^3 + (-1.9 \pm 0.3) \times 10^3 \, sec\theta \\ b_K &= (-2.6 \pm 0.4) + (2.2 \pm 0.3) \, sec\theta \\ a_J &= (-1.03 \pm 0.04) \times 10^4 + (7.7 \pm 0.3) \times 10^3 \, sec\theta \\ b_J &= (-12.3 \pm 0.3) + (-9.3 \pm 0.3) \, sec\theta \end{aligned} \tag{4.7}$$

As for the data, only risetimes from detectors with signal S $\geq$ 15 VEM are used in the rest of this analysis to reduce the effect of fluctuations on the analysis.

4.4.3 The Photon Benchmark and $\langle \Delta_\gamma \rangle$

A set of benchmarks of the form:

$$t_{1/2} = 40 + \sqrt{A(\theta)^2 + B(\theta)\, r^2} - A(\theta) \tag{4.8}$$

corresponding to the average risetime for the photon simulations, have been produced. The parameterization of the photon-benchmark parameters A and B as a function of zenith angle differs from that of the data. Whilst an exponential function was used for the data, here a quadratic function is found to describe the photons better. This is likely to be a consequence of the number of simulations used rather than a more fundamental reason associated with the physics of photon-initiated EAS. Figure 4.7 shows the parameterization of the photon benchmark parameters A and B with zenith angle.

The photon benchmarks for each zenith angle are shown in figure 4.8 together with those from the data for comparison. It is clear from this figure that both the average risetime for the photons and the corresponding uncertainty as a function

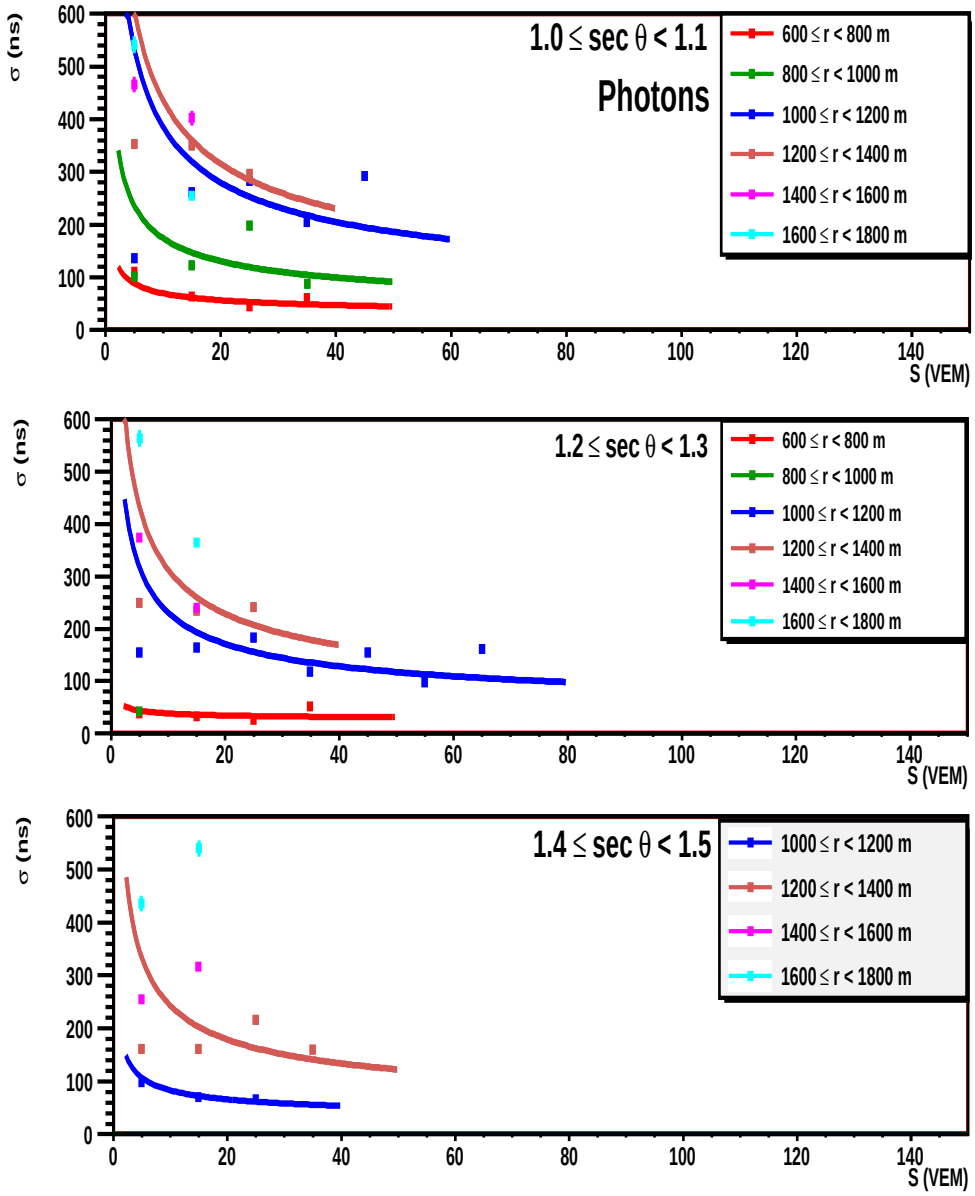

Figure 4.6: The uncertainty on the risetime as a function of signal size for photon simulations at three zenith angles for different distance ranges. Each colour represents a different distance. A fit of the form $\sigma_{t_{1/2}} = \frac{J}{\sqrt{S}} + K$ has been applied to each distance range where three or more signal bins have an average uncertainty from more than 10 pairs of risetimes.

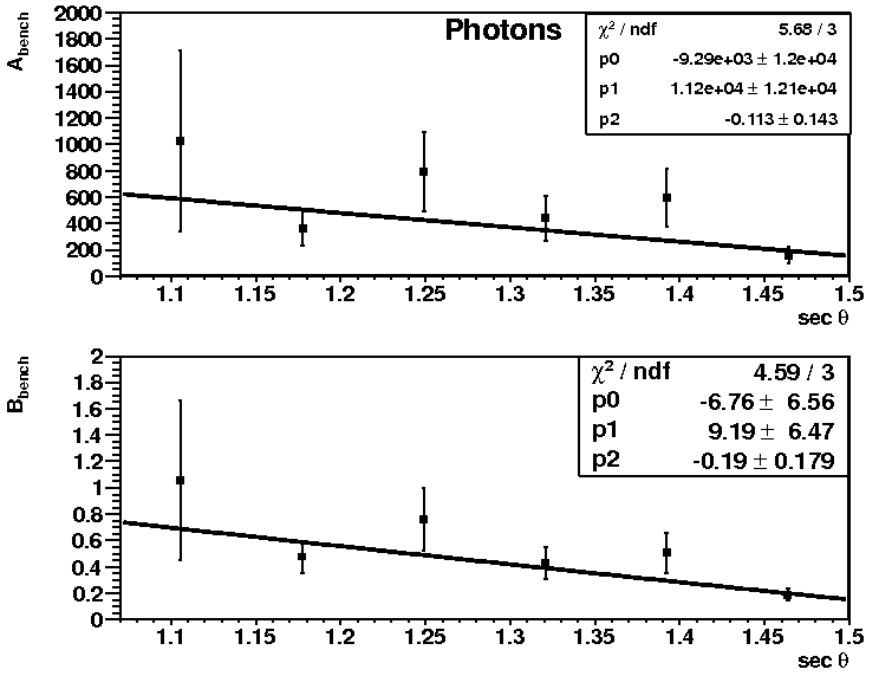

Figure 4.7: The benchmark parameters A and B as a function of zenith angle for photon simulations.

of distance are larger than that for the data. The difference between the two benchmarks increases for larger distances and zenith angles. To give clarity to later work, the notation $\langle\Delta_\gamma\rangle$ indicates use of the photon-benchmark whereas the notation $\langle\Delta\rangle$ indicates use of the benchmark derived from the data.

The photon benchmark has been used to calculate $\langle\Delta_\gamma\rangle$ for the photon simulations using equation 3.13. This gives an average $\langle\Delta_\gamma\rangle$ of -0.23 ± 0.09 for the energy range $10 \leq \mathrm{E}_\gamma < 20\,\mathrm{EeV}$ - lower than expected for the benchmark energy as it should be zero by construction. The average $\langle\Delta_\gamma\rangle$ shows no dependence on zenith angle and increases with energy (figure 4.10). The distribution of $\langle\Delta_\gamma\rangle$ for each energy bin is shown in figure 4.9.

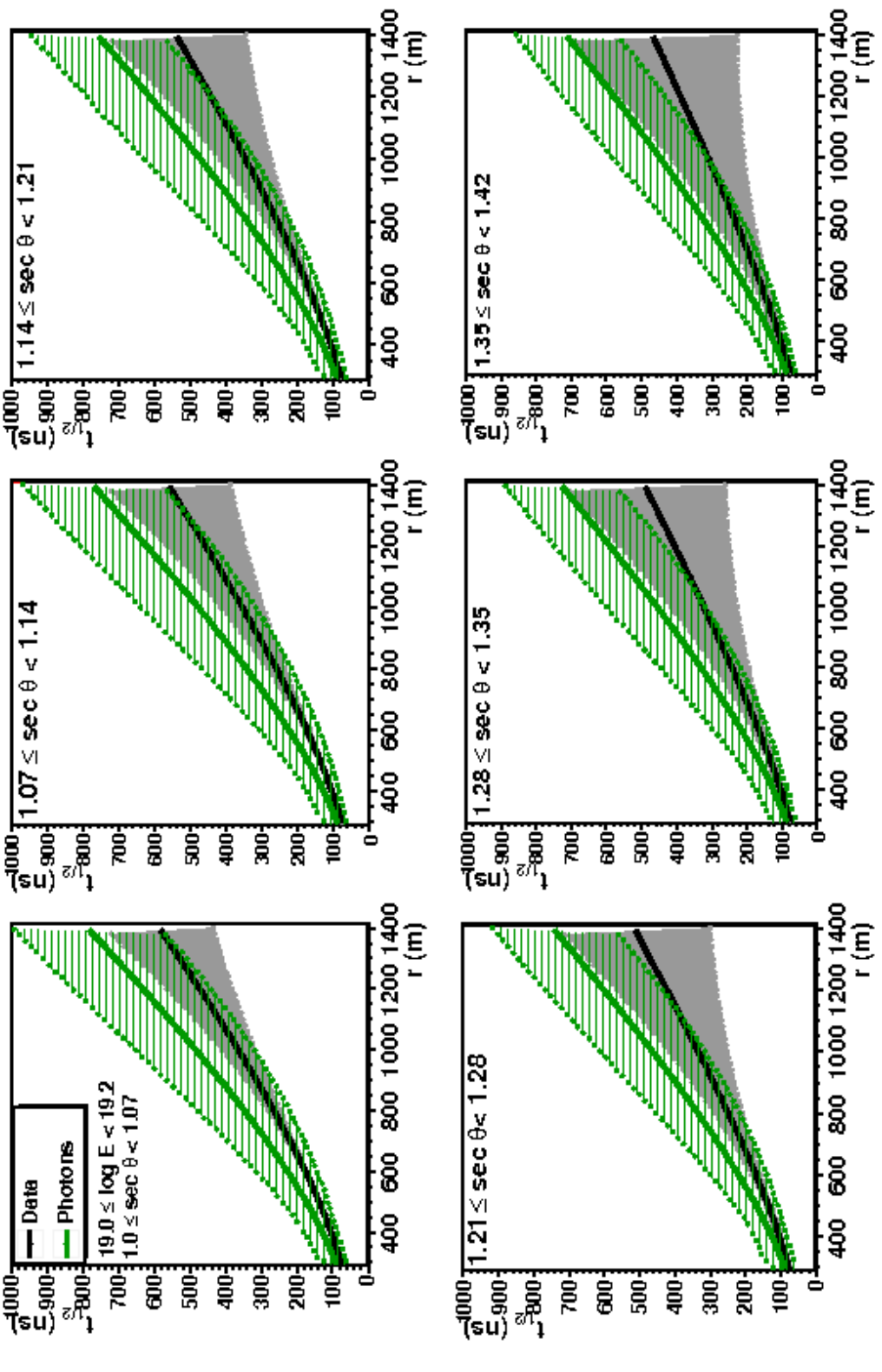

Figure 4.8: A comparison of the benchmark function (average risetime as a function of distance) in different zenith angle bands for simulated photons (green) and the data (black). The shading indicates the uncertainty on the benchmarks.

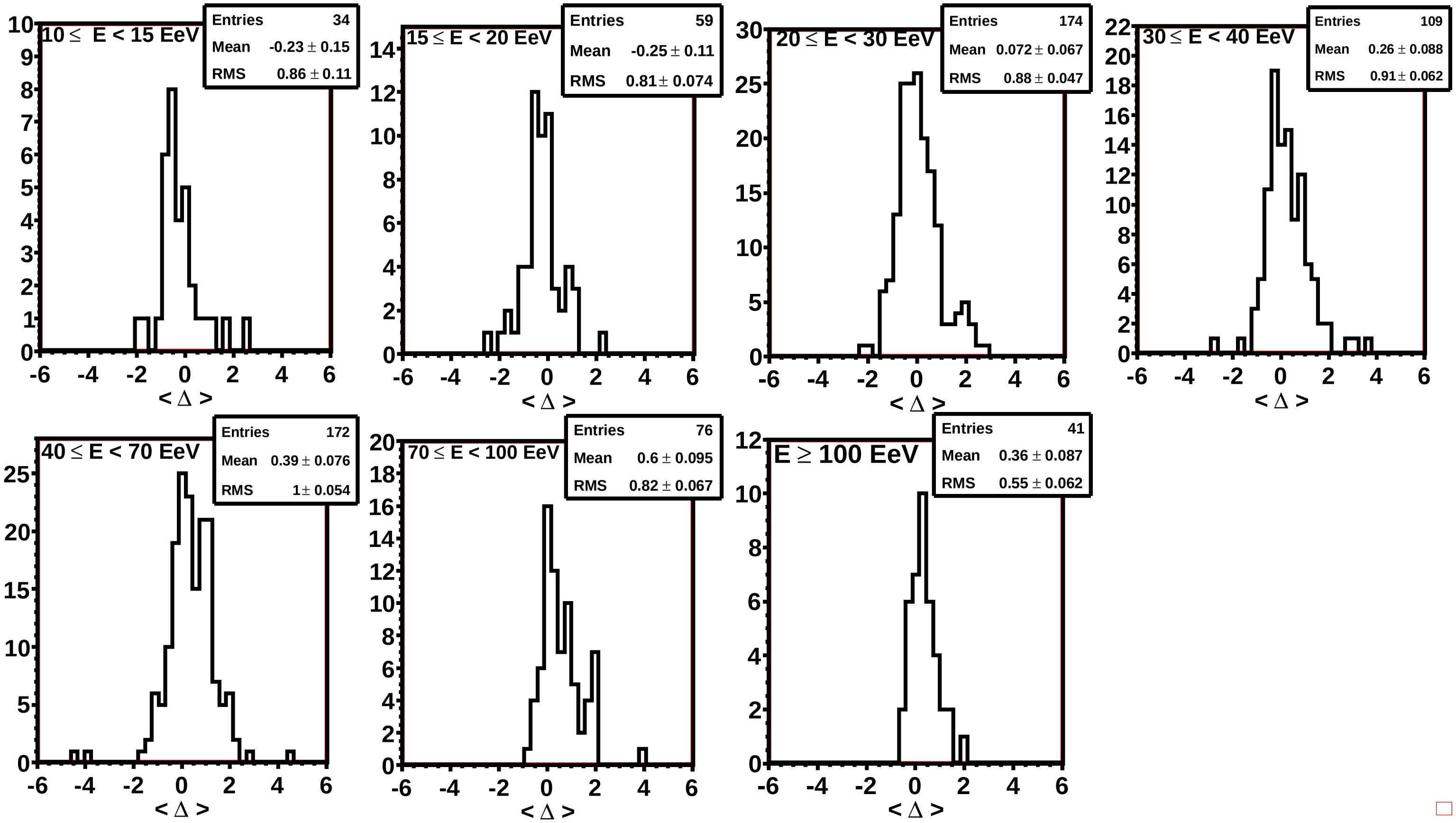

Figure 4.9: Distribution of $\langle \Delta_\gamma \rangle$ for photon simulations in each (photon) energy bin indicated in figure 4.10. The photon benchmark has been used for this calculation.

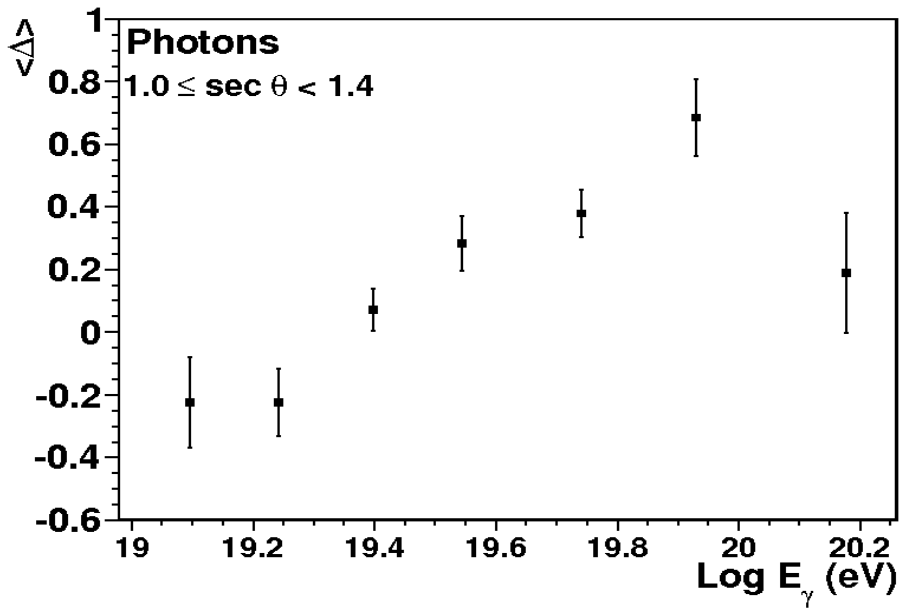

Figure 4.10: Average $\langle\Delta_\gamma\rangle$ as a function of energy, E_γ, for photon simulations.

4.4.4 Outliers in the Photon $\langle\Delta_\gamma\rangle$ Distribution

Due to the nature of simulated events, mis-reconstructed photons are not expected, unlike in the data. However, outliers in $\langle\Delta_\gamma\rangle$ distribution have been inspected such that the differences between photons with very large and very small $\langle\Delta_\gamma\rangle$ may be understood. Such differences are primarily due to differences in the development of showers of different primary energies. Random fluctuations due to the simulation procedure - including the thinning and re-sampling of the showers may also be present. The FADC traces, layout of triggered detectors and risetimes with distance for a photon with a very large $\langle\Delta_\gamma\rangle$, and one with a very small $\langle\Delta_\gamma\rangle$ are illustrated in figures 4.11 to 4.13.

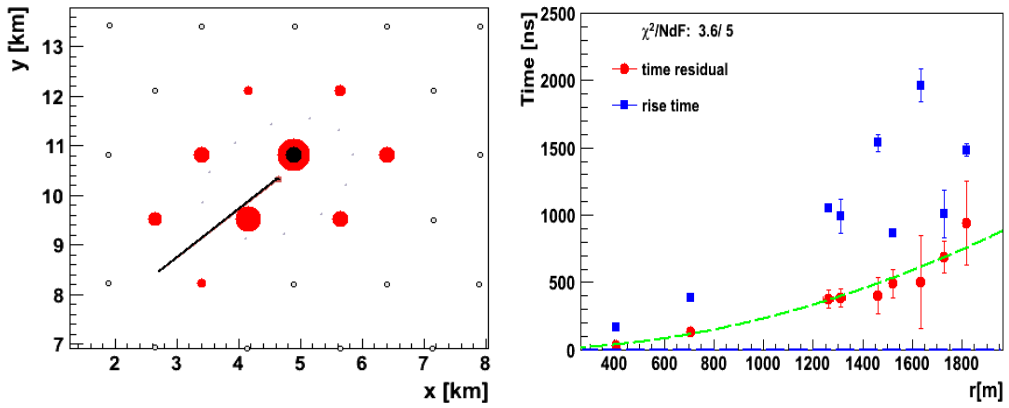

(a) (b)

Figure 4.11: (a): Layout of triggered detectors and (b): uncorrected risetimes (blue) and residuals in the start-time (red) as a function of distance for a simulated photon with a small $\langle\Delta_\gamma\rangle = -4.36 \pm 2.41$. The (MC) energy of this event is 5.9×10^{19} eV at a zenith angle of 44.1°. The corresponding FADC signals from the detectors used to calculate $\langle\Delta_\gamma\rangle$ are shown in figure 4.12.

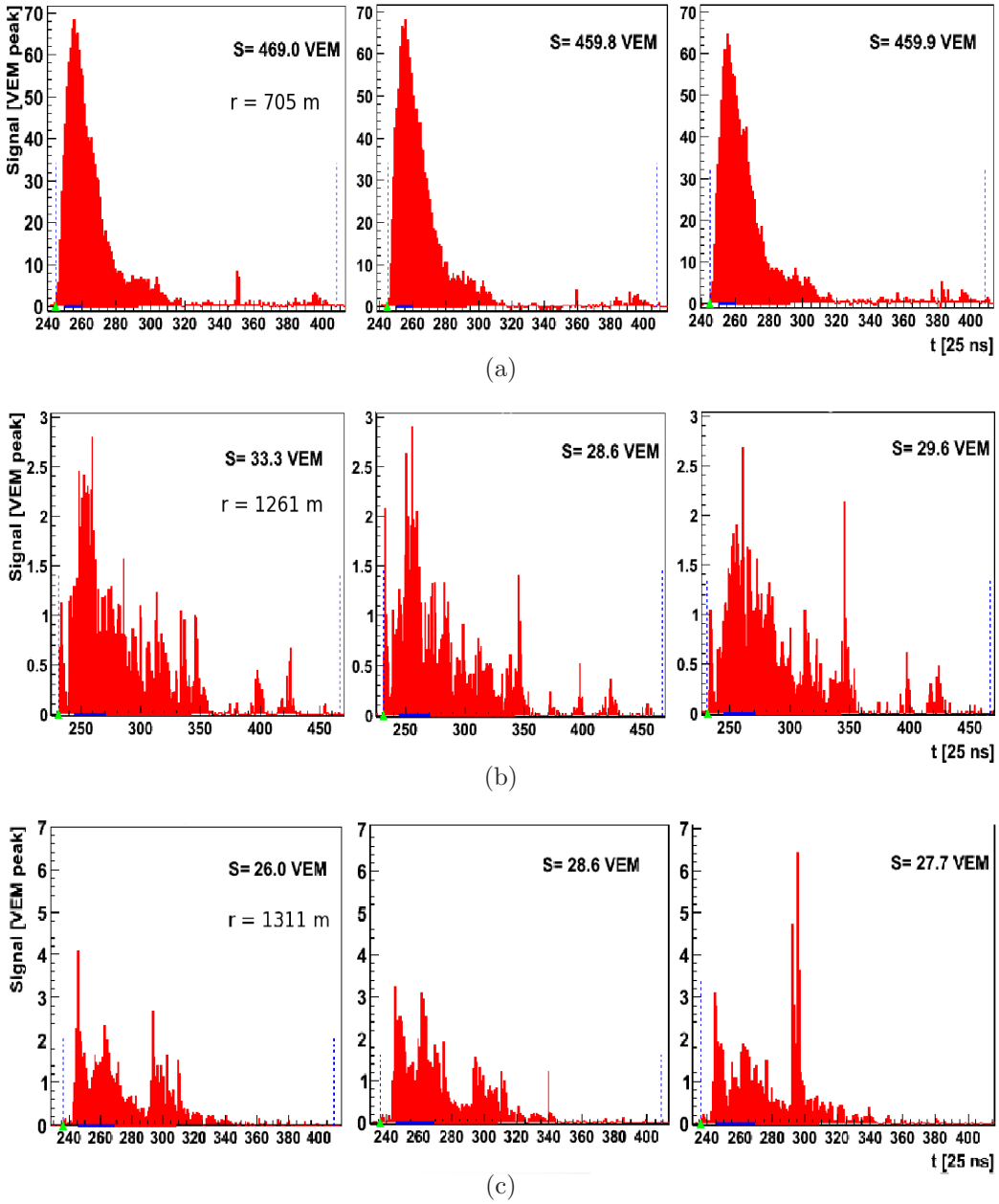

Figure 4.12: FADC traces of the detectors used to calculate $\langle \Delta_\gamma \rangle$ for a photon with a small $\langle \Delta_\gamma \rangle = -4.36 \pm 2.41$. The distances shown are (from top to bottom): 705, 1261 and 1311 m. The station closest to the core (not shown) is saturated.

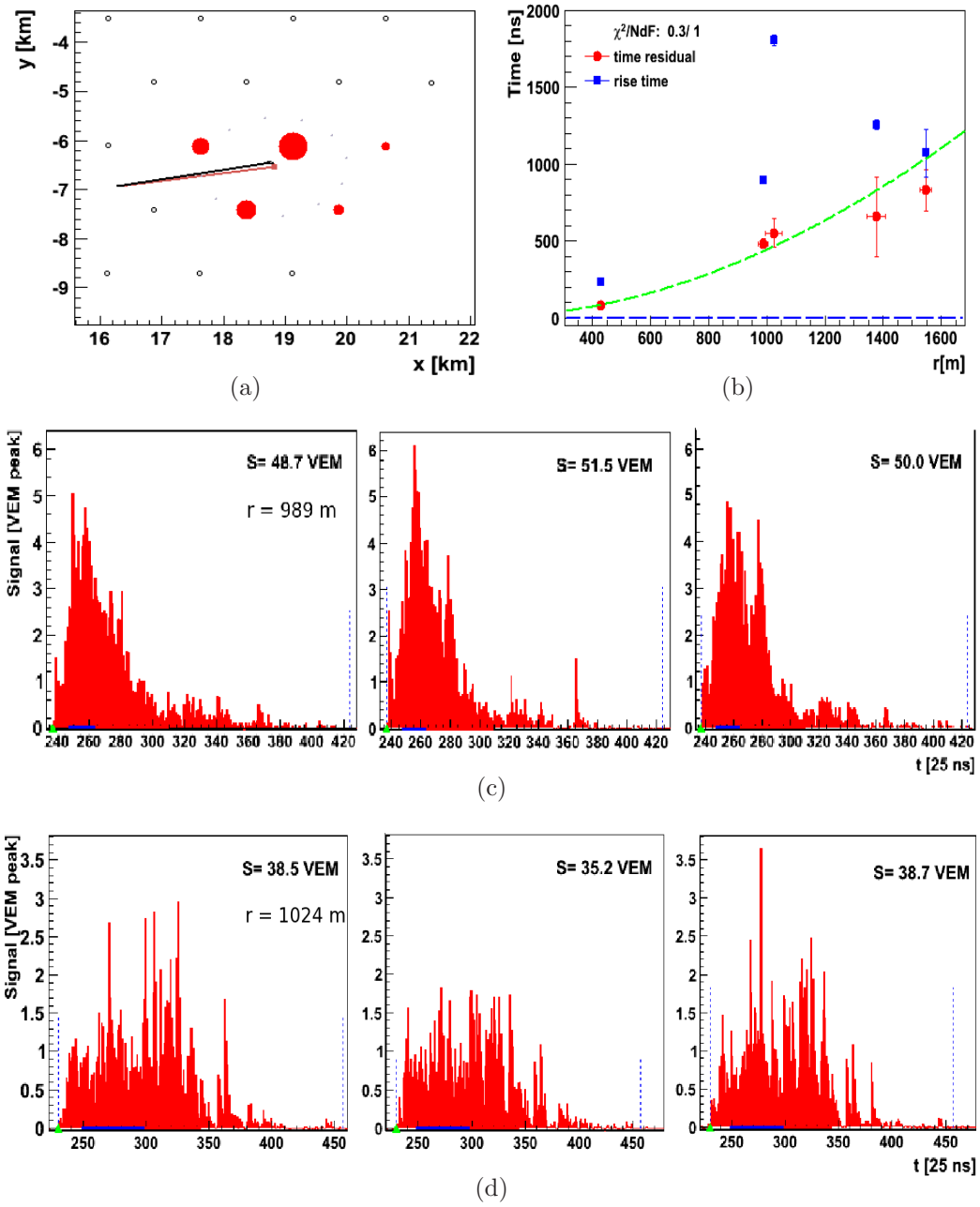

Figure 4.13: (a): Layout of triggered detectors and (b): uncorrected risetimes (blue) and residuals in the start-time (red) as a function of distance for a simulated photon with a large $\langle \Delta_\gamma \rangle = 2.83 \pm 0.85$. The (MC) energy of this event is 4.8×10^{19} eV at a zenith angle of 35.5°. The FADC traces of the two detectors used to calculate $\langle \Delta_\gamma \rangle$ are given in panels (c) and (d). The distances shown are 989 and 1024 m.

Twelve photon simulations have been discovered that exhibit strange "double-peaks" in one or more detectors. These events all have $\langle\Delta_\gamma\rangle \geq 2.0$. The size of the second peak and its position relative to the first peak varies from event to event, with some traces having a clear double-peak and others having a large energy deposit or 'bump' where the signal is expected to be in decline. An example of such an event is given in figures 4.14 and 4.15.

These double-peaks generally occur in the 2^{nd} or 3^{rd} detector closest to the core, with the exception of the event shown where a double-peak is also seen in the fourth-furthest detector (panel 4.15(c)). No particular trend in the distance or signal size of the affected traces is observed and all except two of the affected photon events have $\text{E}_{\text{MC}} \geq 10^{20}\,\text{eV}$. This is worrying as photon simulations are believed to be the most reliable of all simulated primary types and are assumed to closely match reality.

It is not currently known whether this anomalous behaviour is due to, say, the thinning and re-sampling procedure or some more fundamental problem with the simulation of either the showers or the simulated detector responses. In an attempt to find the cause of this problem, the affected simulated events have been 'dropped' ten times each at random locations on the array and the resulting time-traces inspected visually. On average, 26% of the 'drops' produce double-peaks or anomalous large, late energy deposits. That this behaviour is not seen in every drop indicates that the cause of the problem may be either due to or exacerbated by the re-sampling procedure and detector simulation procedures. A smaller level of thinning would retain more shower particles and thus be less prone to fluctuations and unwanted effects during the re-sampling stage, which may resolve this problem. In future, consideration could be given to the effect of thinning on photon simulations with regard to the risetimes and $\langle\Delta\rangle$. Thorough investigation into the cause of these 'double-peaks' would be an interesting area of further study. This double-peaked behaviour is not seen in the data, nor in the set of proton and iron simulations used later in this work (section 4.6).

The number of photons found with this strange behaviour is small and limited to the very largest energies, above those seen in the data. An inspection of a random sub-sample of ~ 50 simulated photons at different energies, zenith angles and $\langle \Delta_\gamma \rangle$ s has not uncovered any more such events. Therefore it has been decided to simply exclude these 12 simulations from further analysis. The median of the photon distribution does not show a significant change and the number of photon-candidates found in the data (see section 4.5) remains unchanged regardless whether these 12 events are included or excluded. However, the remainder of this analysis must be treated with some caution until such time as follow-up studies to determine the cause of these double-peaks have been performed.

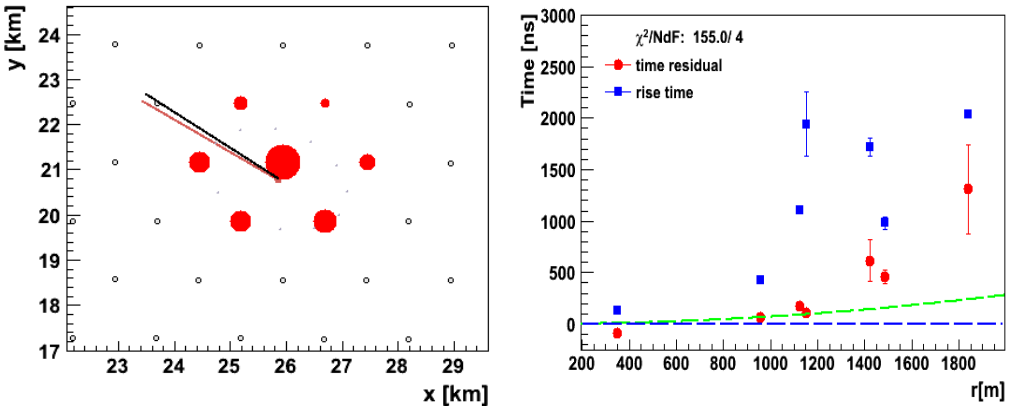

(a) (b)

Figure 4.14: (a): Layout of triggered detectors and (b) uncorrected risetimes (blue) and residuals in the start-time (red) as a function of distance for a simulated photon where double-peaks are observed. This simulated event has (MC) energy 1.7×10^{20} eV, zenith angle 43.4° and $\langle \Delta_\gamma \rangle = 3.70 \pm 1.09$. The corresponding FADC signals from the detectors used to calculate $\langle \Delta_\gamma \rangle$ are shown in figure 4.15.

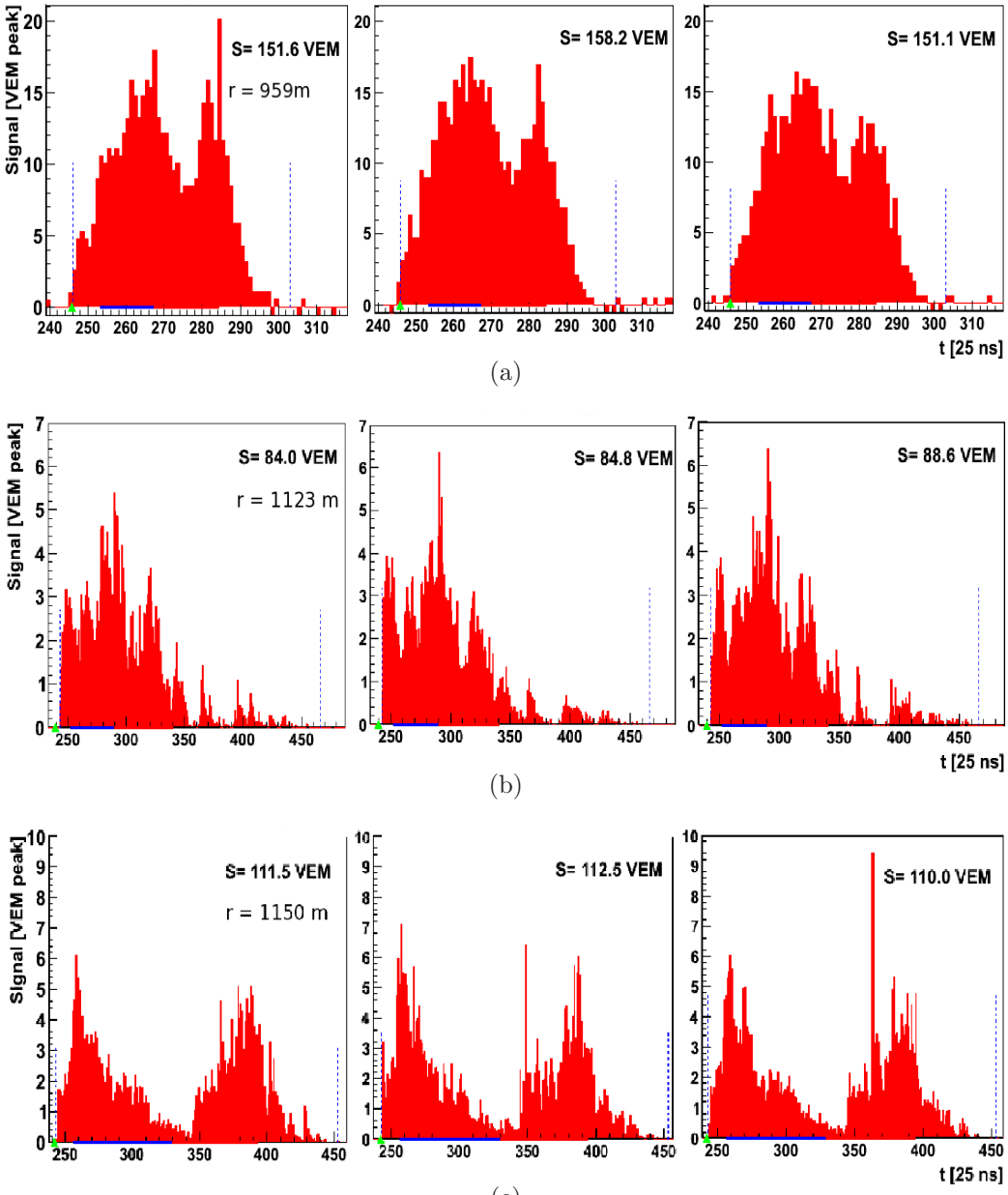

Figure 4.15: FADC traces of the detectors used to calculate $\langle \Delta_\gamma \rangle = 3.70 \pm 1.09$ for a photon where double-peaks are observed. The distances shown are (from top to bottom): 959, 1123 and 1150 m. The traces in panels (a) and (c) clearly show a double-peak due to the late arrival of a portion of the electromagnetic component. The detector closest to the shower core is saturated and not shown here.

4.5 Comparison of Photon Simulations to the Data using $\langle\Delta\rangle$

To determine the number of events in the data which could be from photon primaries, the data and photon simulations must be compared against a single set of criteria. For this comparison, the same benchmark must be used for both sets of risetimes. It is believed that the data benchmark is more robust than the photon benchmark due to the larger number of risetimes involved in its creation, and smaller uncertainties - as shown in figure 4.8. Thus the formulation:

$$\langle\Delta\rangle = \frac{\Sigma(\frac{t_{1/2}-t_{1/2}^{data\,bench}}{\sigma_{t_{1/2}}})}{N} \tag{4.9}$$

where $t_{1/2}^{data\,bench}$ is the expected risetime from the data benchmark using the benchmark parameters given in section 3.2.5 is now applied to both the data and photon simulations.

The normalised distributions of $\langle\Delta\rangle$ for the data and photons for four different energy thresholds are displayed in figure 4.16. It can be seen that the overlap between the data and photon $\langle\Delta\rangle$ distributions is small, indicating that the majority of the data are not photon-initiated. The photon energies, E_γ, as defined in section 4.3 have been used for both data and simulations. To make the comparisons shown here, the photon energy spectrum has been re-scaled to that of a power-law spectrum with index $\alpha = -2$ by re-weighting the simulated spectrum. The true photon energy spectrum is unknown but it is likely to be a steeply falling power-law spectrum. Only events with zenith angles in the range $30 - 45^\circ$ have been used. The $\langle\Delta\rangle$-method is not well-defined for larger zenith angles due to large uncertainties in the asymmetry correction and uncertainty parameterization, especially for photon simulations. For zenith angles smaller than 30°, the slant depth from the top of the atmosphere to the observation level is less than the average X_{max} expected for photons and may bias results.

To determine the number of photon-candidates in the data above a given energy threshold, a cut has been placed at the median value of the corresponding

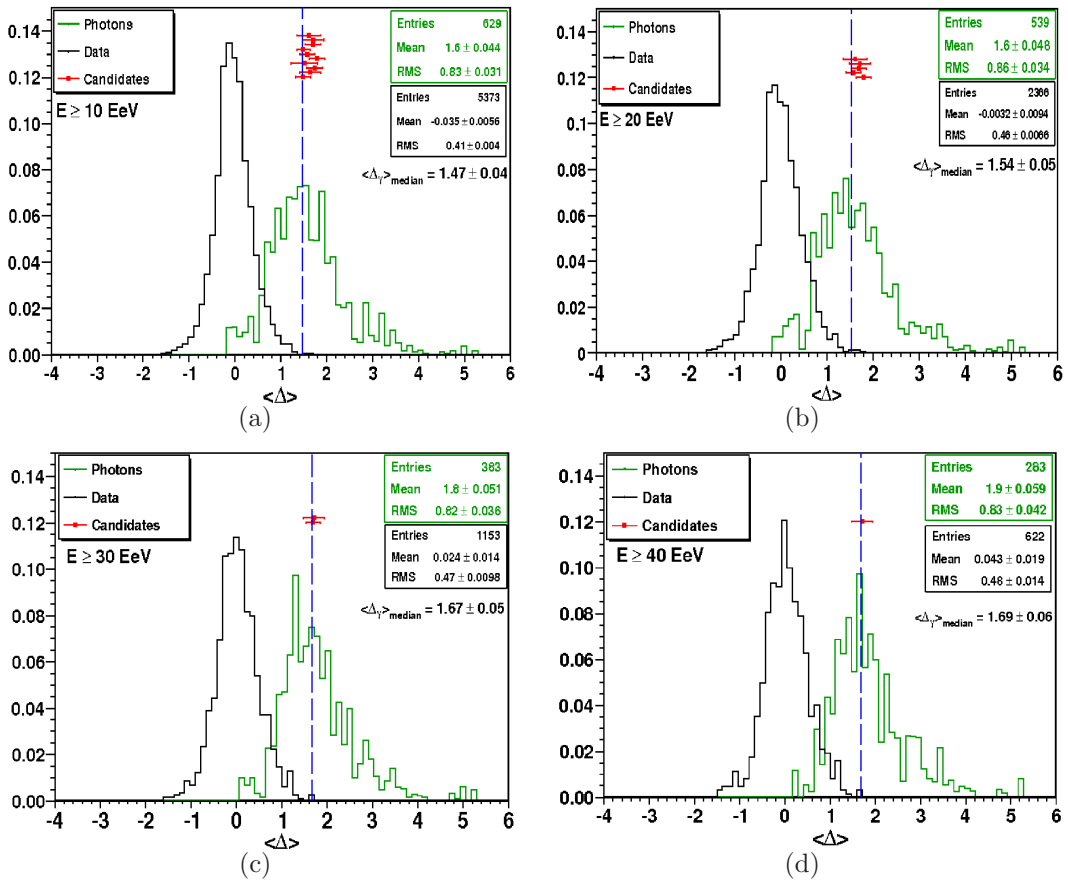

Figure 4.16: Normalised distributions of $\langle\Delta\rangle$ for data and photon simulations above four different energy thresholds and in the zenith angle range $30° \leq \theta < 45°$. The benchmarks derived from the data have been used here and the photons have been adjusted to an E^{-2} spectrum. The $\langle\Delta\rangle$s of the photon-candidates above each energy threshold (red points, offset on the y-axis for clarity) and the corresponding photon-median (blue lines) are indicated.

photon $\langle\Delta\rangle$-distribution - represented by the vertical dashed line in each panel of figure 4.16. The photon median changes depending on the energy threshold used: at $E_\gamma \geq 10\,\text{EeV}$, $\Delta_{med} = 1.47 \pm 0.04$. The efficiency of finding photons using the median value as a threshold is 0.5.

Ten, five, two and one candidates have been found above 10, 20, 30 and 40 EeV respectively. The $\langle\Delta\rangle$ of these candidates are marked in the corresponding panels

of figure 4.16. The uncertainty on $\langle\Delta\rangle$ has been fully calculated by propagating the uncertainties on each stage of the $\langle\Delta\rangle$-method. A scatter-plot showing the $\langle\Delta\rangle$s for the data and photon simulations as a function of energy is shown in figure 4.17, the $\langle\Delta\rangle$s of the photon-candidates are also highlighted in that figure. Details of the photon-candidates are given in table 4.1.

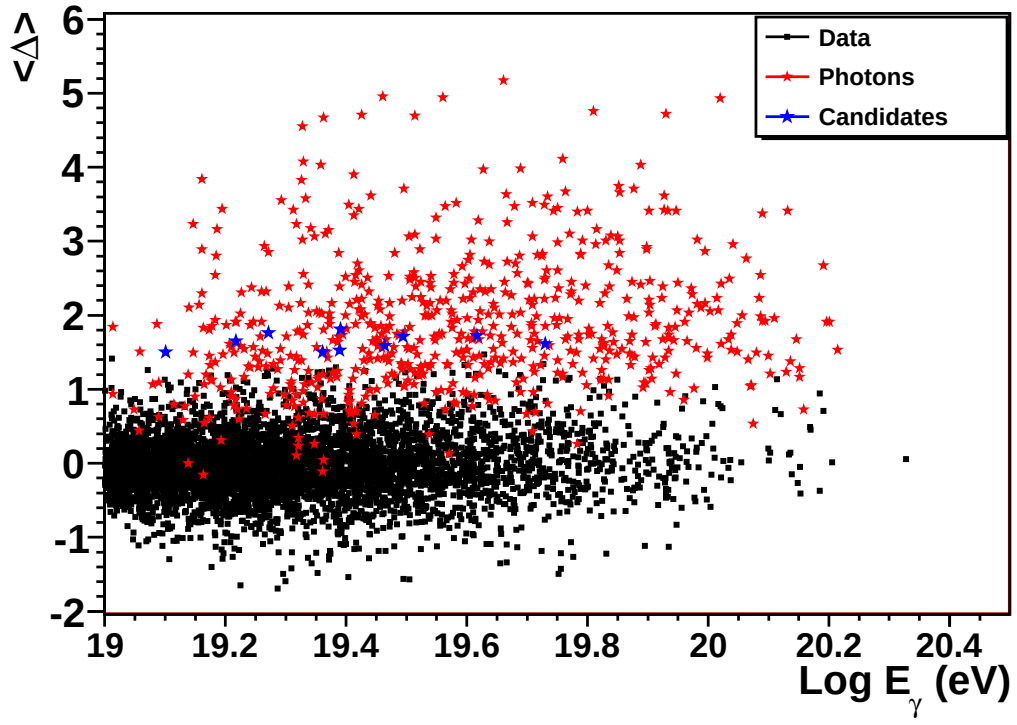

Figure 4.17: $\langle\Delta\rangle$ as a function of E_γ for the data (black points) and photon simulations (red stars). The 10 photon-candidates above 10 EeV (where $\langle\Delta\rangle_{median} = 1.47$) found in this work are also marked (blue stars).

The photon-candidates have been inspected visually. All of these candidates have between 5 and 10 detectors, of which an average of 3 detectors have been used to determine $\langle\Delta\rangle$. Four candidates have a saturated detector. Most of the FADC traces have a spiky appearance more typical of the rest of the data than of the traces observed from the photon simulations. That all these candidates lie in a narrow range of $\langle\Delta\rangle$ close to the threshold suggests they may be from the tail of a hadronic distribution where fluctuations in the shower development have led

ID	θ	Log E_{rec} (eV)	Log E_γ (eV)	N_{total}	N_{used}	$\langle\Delta\rangle$
9333599	43.0	18.7	19.10	6	2	1.49 ± 0.17
1768669	40.2	18.9	19.27	7	2	1.74 ± 0.17
1998796	34.1	19.3	19.27	9	2	1.65 ± 0.23
6784159	44.0	19.0	19.36	5	3	1.49 ± 0.15
1813111	38.9	19.0	19.39	6	4	1.79 ± 0.17
3343182	35.2	19.0	19.39	8	2	1.52 ± 0.29
6637103	40.0	19.1	19.46	8	3	1.57 ± 0.17
2248206	43.6	19.2	19.50	10	3	1.70 ± 0.16
8938022	32.1	19.1	19.62	10	3	1.71 ± 0.23
10450239	38.5	19.3	19.73	9	3	1.61 ± 0.25

Table 4.1: Table of photon-candidates found using the $\langle\Delta\rangle$-method for events with $E_\gamma \geq 10, EeV$ and $30^\circ \leq \theta < 45^\circ$. N_{total} is the total number of detectors in that event and N_{used} is the number of detectors used to calculate $\langle\Delta\rangle$. The energies from the standard reconstruction have also been included for reference.

to the large risetimes observed. If these were all photons, then a larger spread of $\langle\Delta\rangle$ would be expected. An attempt to quantify this statement using hadronic simulations is given in section 4.6.2.

In the event that the true $\langle\Delta\rangle$ of each of these photon-candidates fluctuates to the extreme left hand-end of the associated error bar (i.e. $\langle\Delta\rangle - \sigma_{\langle\Delta\rangle}$), only 4, 2, 0, 0 events would pass the photon-median above energy thresholds of 10, 20, 30 and 40 EeV respectively. However, the possibility that all of these candidate events are photons cannot be ruled out.

The most photon-like of these candidates (the one with the largest $\langle\Delta\rangle$) is event 1813111 with $\langle\Delta\rangle = 1.79 \pm 0.17$. The $\langle\Delta\rangle$ of this event is larger than the photon median at all energy thresholds considered in this work. The risetimes as a function of distance and the FADC traces from this event are shown in figures 4.18 and 4.19.

Five of the photon-candidates are from the period originally investigated in (28), where no photon-candidates were found, indicating that the separation be-

tween the data and photon distributions is not as large as originally presented in (28). This is due to the following reasons. Firstly, the new stop-time and baseline calculations have a small but significant effect on every FADC trace (see section 3.1.2) which acts non-trivially to increase the signals and risetimes. Secondly, the asymmetry correction and the uncertainty parameterizations have changed substantially, which may widen both the data and photon distributions. Thirdly, the number of simulated photons, the simulation package used and the range of photon energies and zenith angles considered are completely different to those used in (28). This could decrease the photon median, with the consequence of candidates now being observed where there were none before. The parameterizations used to calculate the photon energies have also changed since the original work on $\langle\Delta\rangle$ (98).

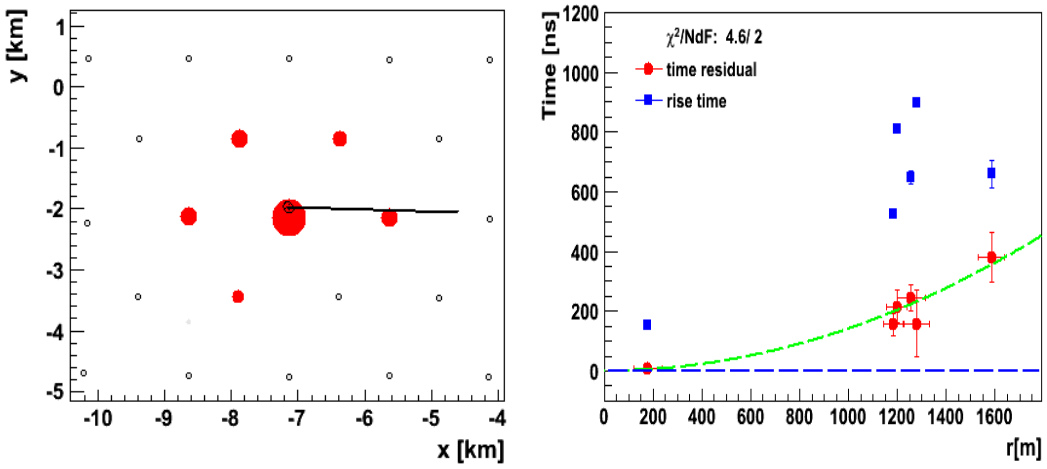

(a) (b)

Figure 4.18: Layout of triggered detectors and risetimes with distance for the most photon-like event in the data (i.e. with the largest $\langle\Delta\rangle$). This event is inclined at 39° and has a photon energy $E_\gamma = 24.5\,\mathrm{EeV}$ ($E_{rec} = 9.7\,\mathrm{EeV}$) and $\langle\Delta\rangle = 1.79 \pm 0.17$. The FADC traces corresponding to this event are shown in figure 4.19.

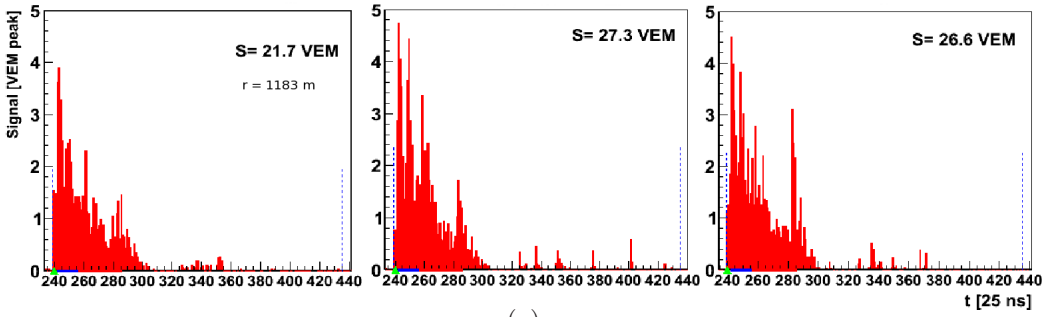

(a)

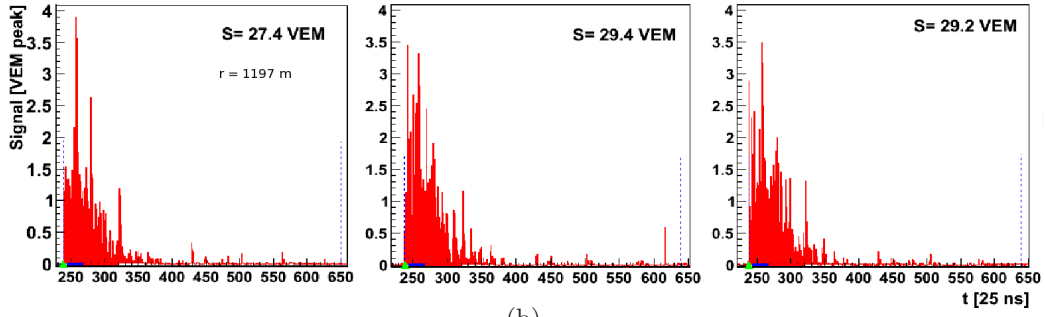

(b)

(c)

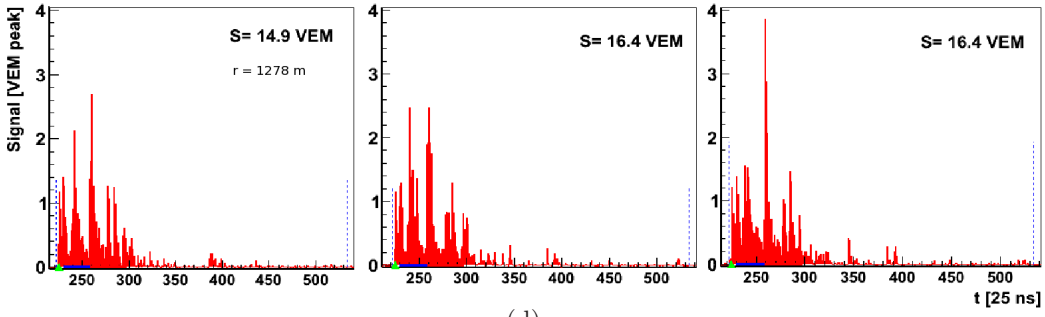

(d)

Figure 4.19: FADC traces of the detectors used to calculate $\langle\Delta\rangle$ for the photon-candidate with the largest $\langle\Delta\rangle$. The distances shown are (from top to bottom): 1183, 1197, 1256 and 1278 m. The station closest to the core (not shown) is saturated.

Given that the set of photons used in (28) were at a few discrete energies and not a continuous spectrum, it would have been inadvisable to convert the simulated spectrum to a more realistic one - for example to an E^{-2} spectrum as performed here - as such a conversion would introduce large uncertainties into the analysis. The photon median will therefore have been larger in that work, reducing the likelihood of finding photon candidates. If an un-weighted (i.e. 'flat') spectrum of photons is used for this work, the photon median is much larger, at $\langle\Delta\rangle = 1.63 \pm 0.04$ and only 5 candidates are found above 10 EeV. In contrast, use of a steeper photon spectrum, for example $\alpha = -2.5$, decreases the photon median and increases the number of photon candidates by (1,1,1,0) above $10, 20, 30$ and 40 EeV respectively.

4.6 $\langle\Delta\rangle$ From Hadronic Simulations

To determine whether the photon-candidates found in the data are really photons, or simply the tail of a hadronic distribution, the number of candidates expected from proton and iron simulations are desirable. Additionally, the ability of the $\langle\Delta\rangle$-method to distinguish protons from iron nuclei - even on an average basis - has not yet been tested.

A set of 7900 protons and 8200 iron showers with energies between 3 and 300 EeV and a continuous distribution of zenith angles $\leq 55^\circ$ have been simulated using CORSIKA 6.97 and QGSJetII, with a 10^{-6} thinning level and the Malargüe atmospheric model (93), and processed in Offline. The Monte-Carlo and reconstructed energies and zenith angles are indicated in figure 4.20. The standard energy reconstruction (as used for the data) gives energies $\sim 20 - 25\%$ lower than the original Monte-Carlo energy. This discrepancy in energy may be due to a deficiency of muons in hadronic simulations.

Analysis of each stage of the $\langle\Delta\rangle$-method reveals that the asymmetry, uncertainty and benchmark functions needed for the hadronic simulations are of the same form as those used for the data. The asymmetry in both the iron and proton simulations is of a similar order of magnitude to that of the data as can be

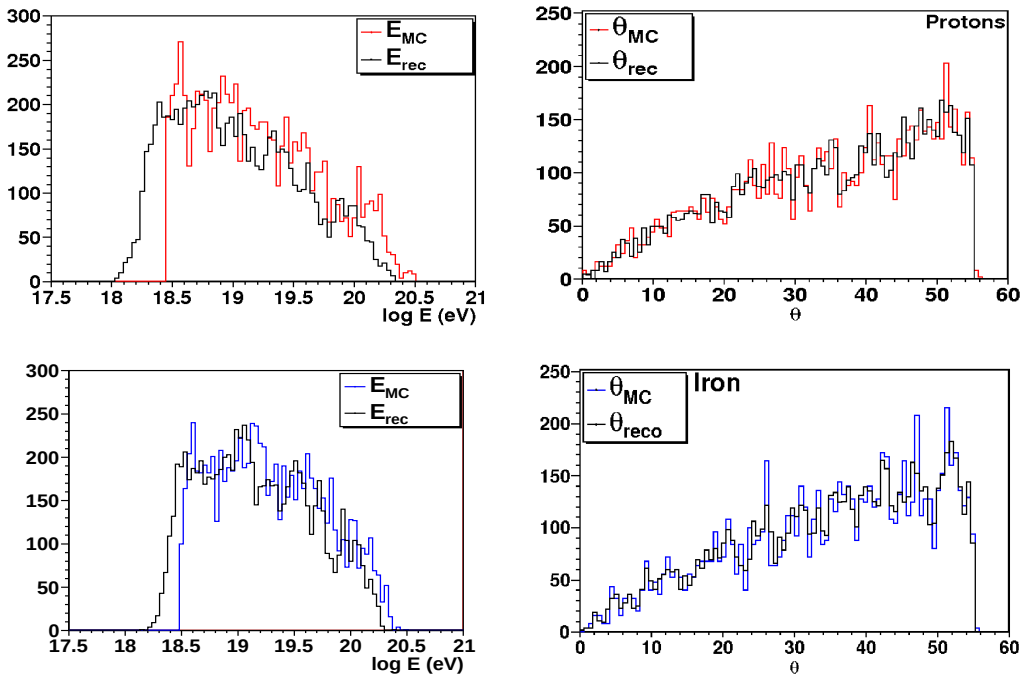

Figure 4.20: Left: Distribution of energies and Right: Distribution of zenith angles for proton (top panels) and iron (lower panels) simulations (Red: Proton MC inputs, Blue: Iron MC inputs, Black: from the standard reconstruction).

seen from figures 4.21 and 4.22, indicating that the data is more akin to hadronic showers than photons (see figs. 4.4 and 4.5 for comparison). The amplitude of the asymmetry parameter m from the photon simulations is many orders of magnitude smaller than for the data and hadronic simulations.

Both the proton and iron simulations have a larger amplitude to the asymmetry as a function of zenith angle than seen in the data - as shown in figure 4.22, which may be due to thinning and re-sampling effects. The position of maximum asymmetry increases with decreasing mass composition from $\sim 41°$ for iron nuclei, through $\sim 44°$ for protons to $\sim 46°$ for the photon simulations. This compares to $\sim 42°$ from the data and is broadly consistent with the results in (89), where the asymmetry is used to study the mass composition at different energies. A more comprehensive study of the asymmetry as a potential parameter for mass-composition measurements is given in chapter 6.

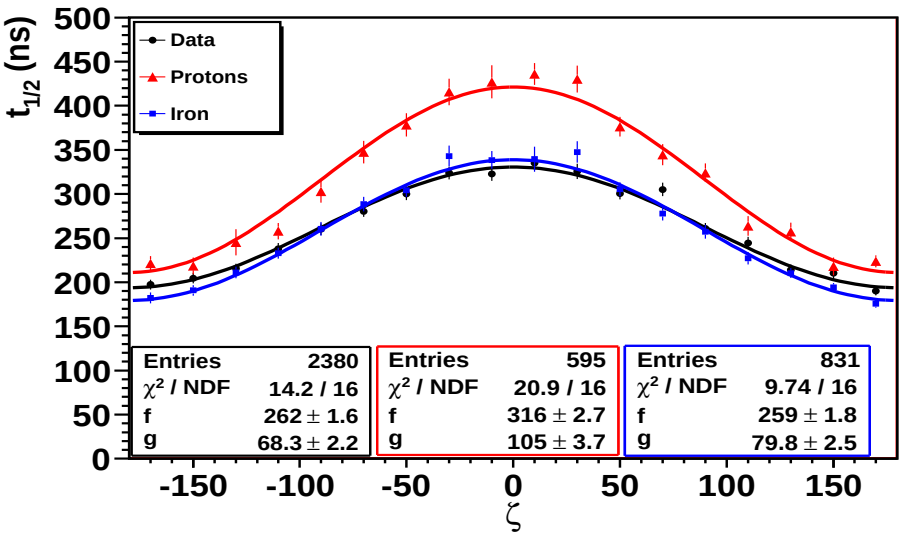

Figure 4.21: Comparison of the asymmetry in the risetimes of proton (red) and iron (blue) simulations and the data (black) for zenith angles $1.3 \leq sec\theta < 1.4$ ($40° - 45°$) and distances of $800 \leq$ r < 1000 m. The fitted function has the form $t_{1/2} = f + gcos\zeta$.

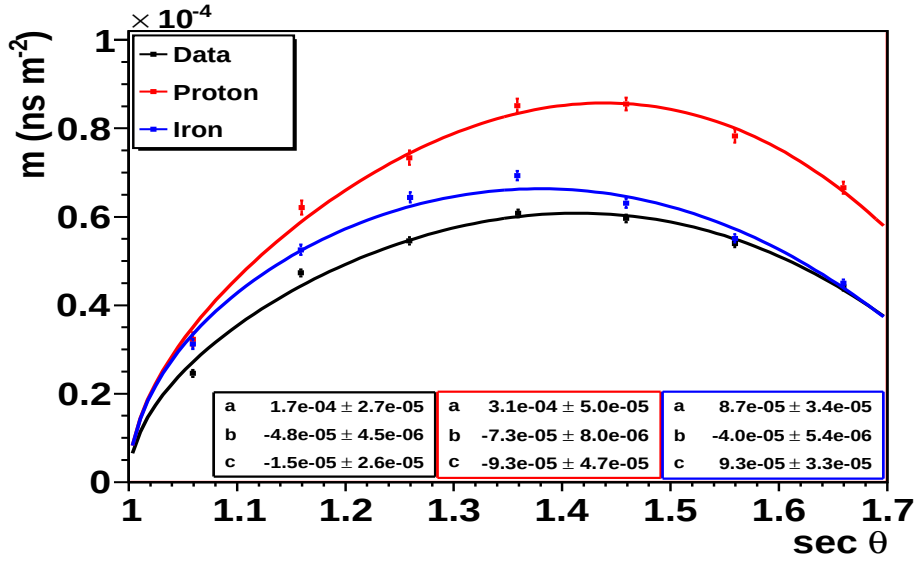

Figure 4.22: The asymmetry parameter m as a function of zenith angle for protons (red), iron (blue) and the data (black). The fitted function is of the form: $m = (a\, sec\theta + b\, sec^3\theta + c)\sqrt{(sec\theta - 1)}$.

The uncertainty on the hadronic simulations has been compared to that of the data and photons and is found to decrease with increasing signal size according to $\sigma_{t_{1/2}} = J/\sqrt{S} + K$, where J and K are functions of distance and zenith angle. Due to the thinning and re-sampling procedures it was expected that the uncertainty would be larger for protons and iron than for the data. However, this is not the case - indicating that the thinning and re-sampling procedures may have little effect on the uncertainty on the risetime. The uncertainty on the hadronic simulations is comparable to that for the data for signal sizes between $\sim 40-90$ VEM, whilst at lower signals the uncertainty is smaller. This is illustrated in figure 4.23 for one zenith angle and distance. The uncertainty on the photon simulations is much larger than that for either the hadronic simulations or the data.

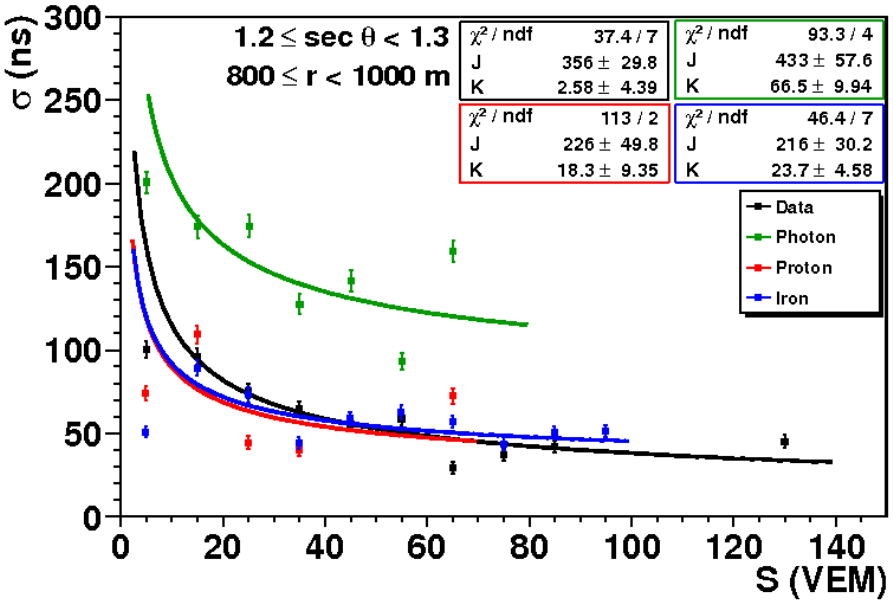

Figure 4.23: Comparison of the uncertainty on the risetime for simulations and the data at $800 < \mathrm{r} < 1000\,\mathrm{m}$ and $1.2 \leq sec\theta < 1.3$ ($34 \leq \theta < 40°$). The fit-function applied to each set of points is of the form $\sigma_{t_{1/2}} = \frac{J}{\sqrt{S}} + K$.

A rigorous study of the uncertainty on the risetimes of different primaries could provide an estimate of the effect of the thinning and re-sampling procedures

by comparison to un-thinned showers or showers with different thinning levels. As the uncertainty on the risetimes of hadronic simulations is similar to that of the data, the effect of thinning and re-sampling will be small. Due to the limitations of statistics provided by the simulations used here, many signal bins do not contain adequate numbers of events, therefore such a study is not possible at this time.

The benchmarks for iron and proton simulations with reconstructed energies $10 \leq \mathrm{E_{rec}} \leq 15\,\mathrm{EeV}$ have been found and compared to that from the data (figure 4.24). The form of the benchmark function is the same as that used for the data, namely $t_{1/2} = 40 + \sqrt{A(\theta)^2 + B(\theta)r^2} - A(\theta)$. The benchmark for the data falls between that of the proton and iron simulations at all zenith angles. No conclusive statement from figure 4.24 can be made regarding the mass-composition of individual events, although a mixed average composition can be tentatively suggested.

The benchmark parameters A and B as a function of zenith angle for the proton simulations are:

$$\begin{aligned} A =& (-516 \pm 2370) + (3.68 \pm 8.21) \times 10^3\, exp[(-1.29 \pm 4.4)\, sec\theta] \\ B =& (-0.17 \pm 0.19) + (6.8 \pm 7.8)\, exp[(-2.33 \pm 1.34)\, sec\theta] \end{aligned} \tag{4.10}$$

and for the iron simulations they are:

$$\begin{aligned} A =& (2.41 \pm 20.1) + (2.0 \pm 2.9) \times 10^5\, exp[(-6.2 \pm 1.4)\, sec\theta] \\ B =& (5.3 \pm 11.2) \times 10^{-3} + (79.1 \pm 63.1)\, exp[(-5.43 \pm 0.76)\, sec\theta] \end{aligned} \tag{4.11}$$

The distributions of $\langle\Delta\rangle$ for proton and iron simulations found using their respective benchmarks are shown for different bins in energy in figures 4.25 and 4.26. The symbol $\langle\Delta_P\rangle$ represents calculations using the proton-benchmark and $\langle\Delta_{Fe}\rangle$ represents calculations using the iron-benchmark. As expected, no reconstruction problems or anomalies have been found on inspection of simulated events in the tails of these distributions.

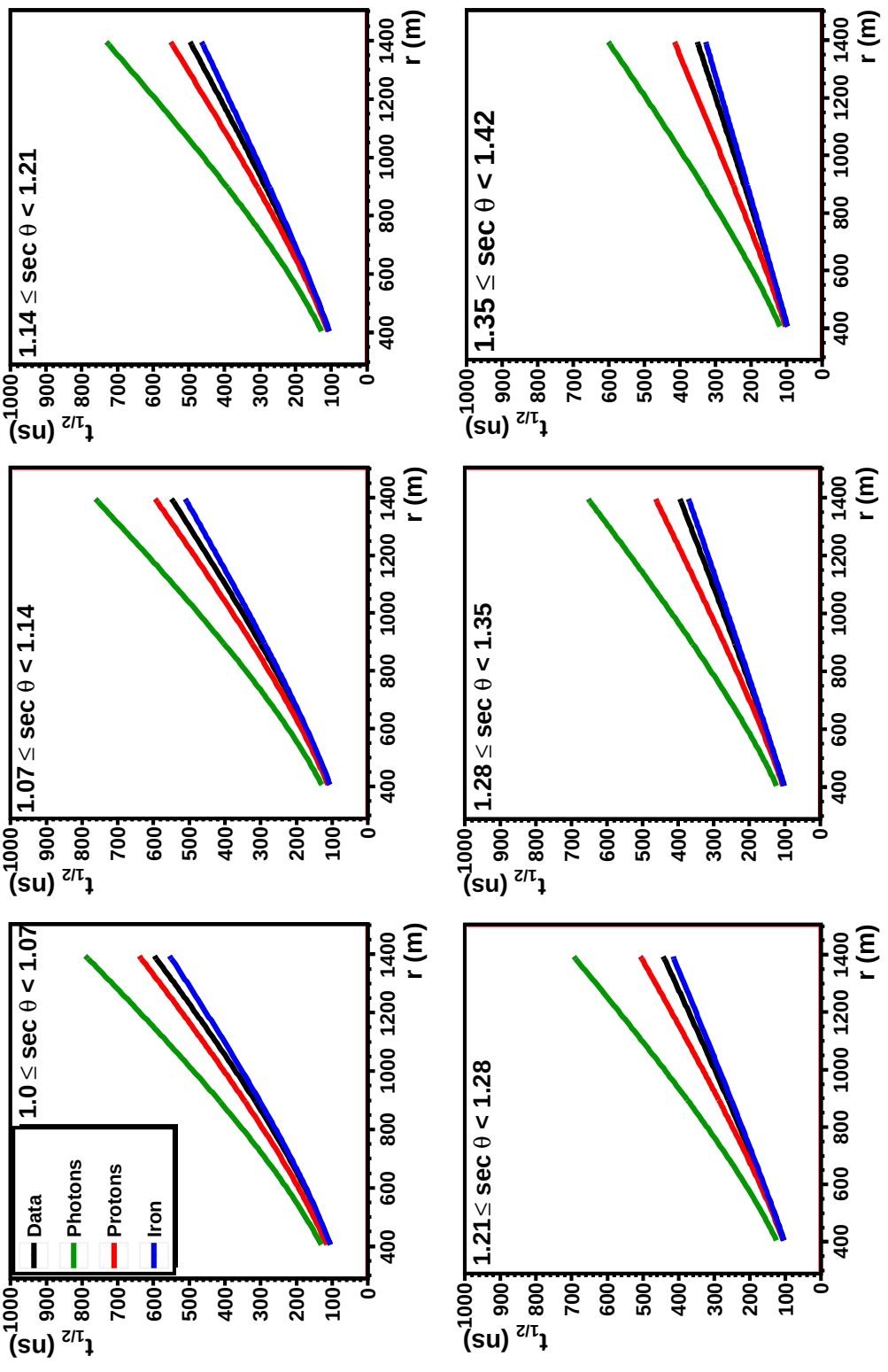

Figure 4.24: Benchmarks for proton, photon and iron simulations and the data for 6 different zenith angles at $10 \leq E_{rec} < 15\,\mathrm{EeV}$.

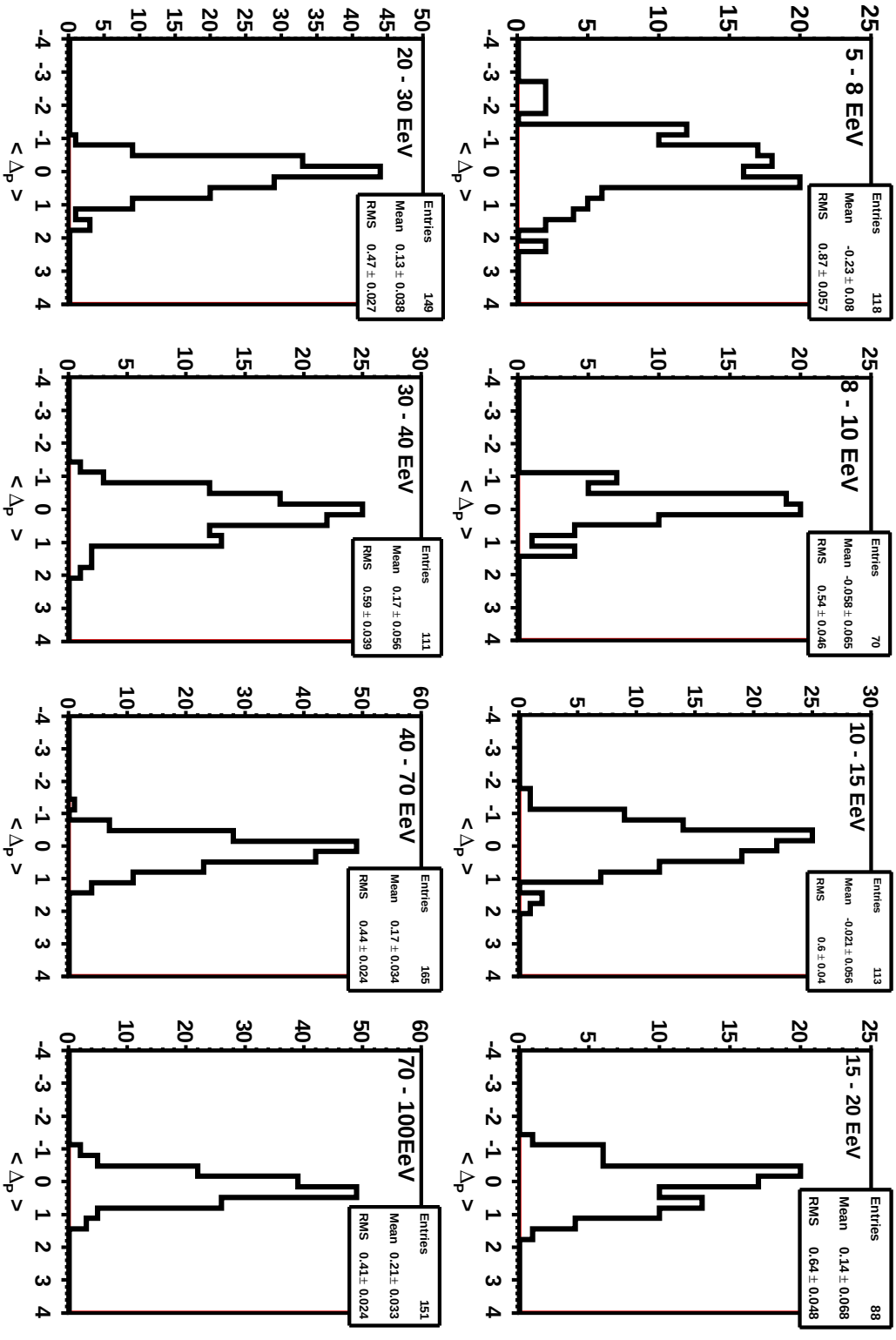

Figure 4.25: Distribution of $\langle \Delta_P \rangle$ for proton simulations of different energies E_{rec}.

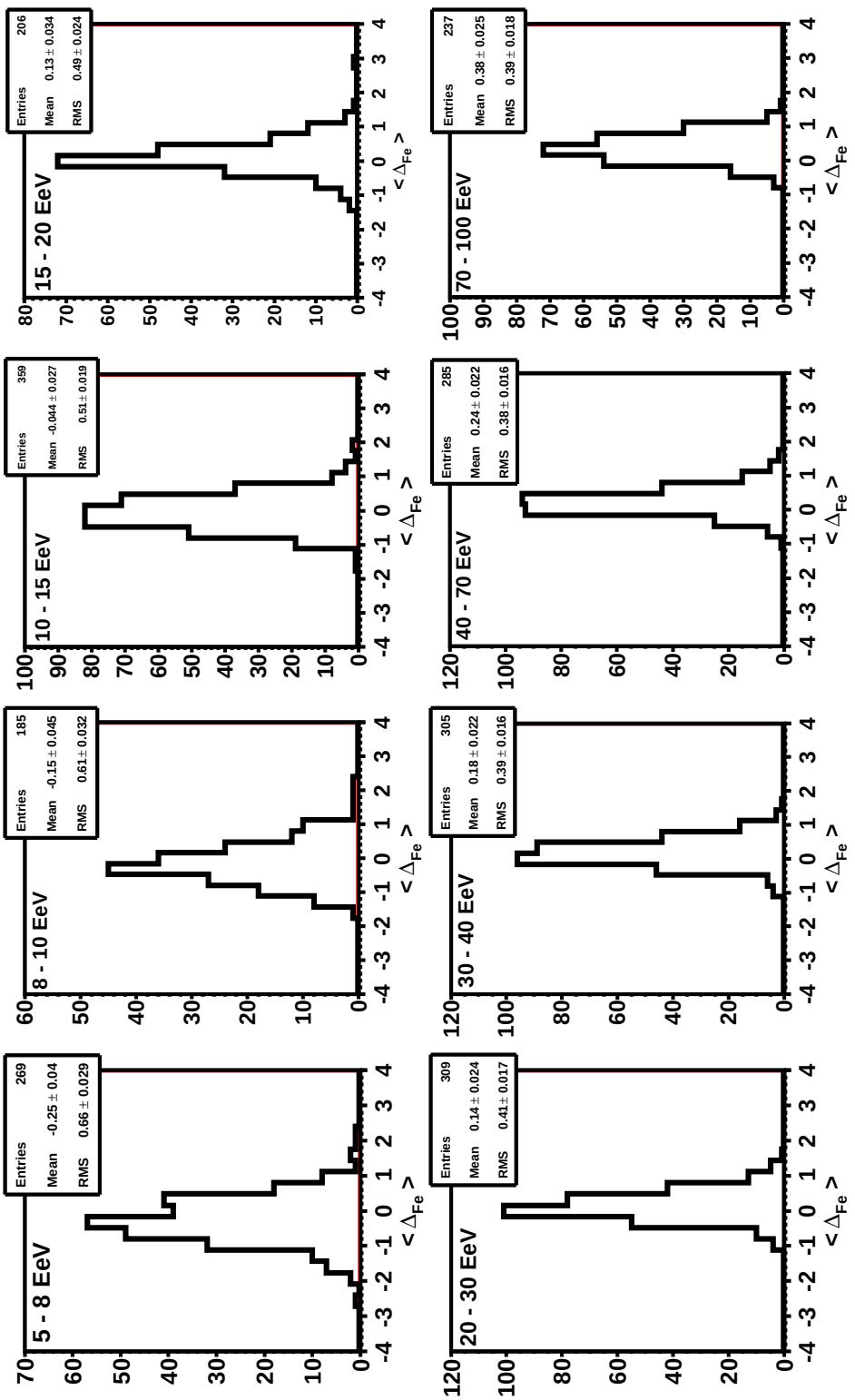

Figure 4.26: Distribution of $\langle\Delta_{Fe}\rangle$ for iron simulations of different energies E_{rec}.

4.6.1 Comparison of Simulations and Data Using $\langle\Delta\rangle$

The average $\langle\Delta\rangle$s as a function of energy for the data and simulations have been compared using the benchmarks derived from the data in section 3.2.5. As shown in figure 4.27, the average $\langle\Delta\rangle$s for the iron simulations do not increase linearly with energy - instead appearing to flatten off above $\sim 1.6 \times 10^{19}$ eV ($\log \mathrm{E} = 19.2\,\mathrm{eV}$). The highest-energy bin for the photon simulations contains only 5 entries and has fluctuated to lower $\langle\Delta\rangle$. The data lies between the expectations for protons and iron nuclei at all energies and tends towards heavier compositions above $\sim 1.6 \times 10^{19}$ eV.

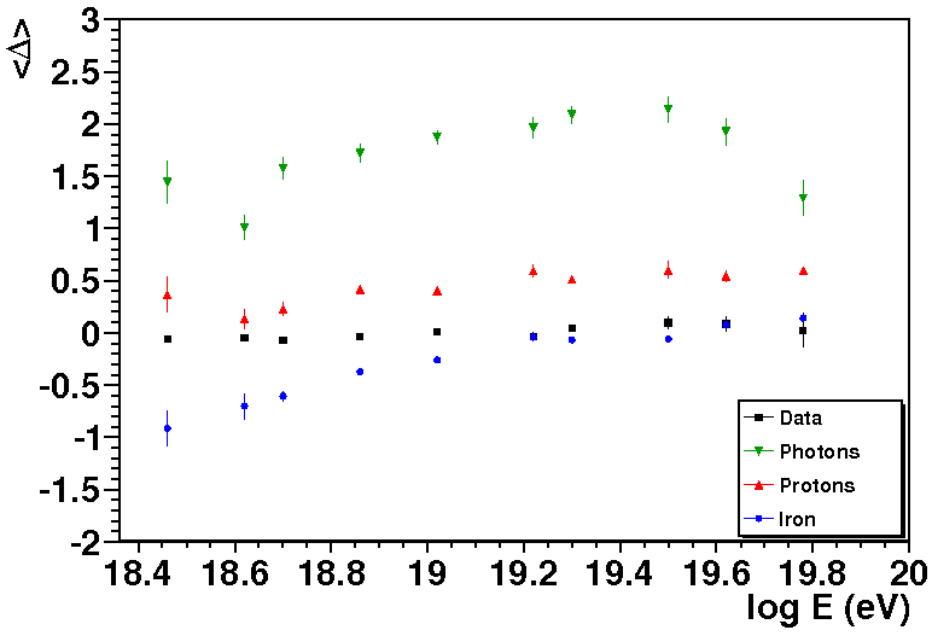

Figure 4.27: Comparison of $\langle\Delta\rangle$ with energy for the data and simulations. The standard energy reconstruction, E_{rec}, has been used for all three simulated primary types and the data. The highest-energy bin for the photon simulations contains only 5 entries and has fluctuated to lower $\langle\Delta\rangle$.

A conversion has been made between $\langle\Delta\rangle$ and $X_{max}^{\langle\Delta\rangle}$ for both the data and simulations using the parameterization derived in section 3.4 from hybrid events. The results are shown in figure 4.28, top panel. The lower panel of this figure

shows the X_{max} result from (39) for comparison. The proton $X_{max}^{\langle\Delta\rangle}$ is at consistently larger values than the direct X_{max} result for the same interaction model (QGSJETII) but agrees remarkably well with the direct X_{max} result from the EPOS interaction model. The iron $X_{max}^{\langle\Delta\rangle}$ do not agree with the direct X_{max} result from any interaction model. Both figures appear to indicate an increasing mass-composition, although this appears more extreme from the $X_{max}^{\langle\Delta\rangle}$ result. Due to the poor separation between proton and iron primaries, and the uncertainties surrounding hadronic simulations, an in-depth study of the mass-composition for individual events is not possible with the $\langle\Delta\rangle$-method.

4.6.2 Estimation of the Number of Photon-Candidates Expected from Hadronic Simulations

The number of photon-candidates expected from proton and iron primaries has been determined. This provides an indication of whether the photon-candidates found in the data are really photons or simply some contamination from the tail of a set of hadron-initiated showers. The distributions of $\langle\Delta\rangle$ for proton and iron have been compared to that of the photons and are shown in figure 4.29. Both the iron and the protons have been re-weighted and normalised from their simulated spectra to match the flux measured for the data. As for the data, a photon energy, E_γ, has been calculated for each simulated event. The number of candidates is then the number of simulated events above a given (photon) energy threshold with $\langle\Delta\rangle$ larger than the median of the photon distribution.

The number of photon-candidates found above four different energy thresholds from proton and iron simulations are listed in table 4.2, along with the number found from the data. The number of candidates from the data is well within the number expected from a pure proton composition in the first two energy bins but larger (by 1 or 2 events) in the two highest energy bins. The number of candidates from the data is larger than the number expected from a pure iron composition at all energies.

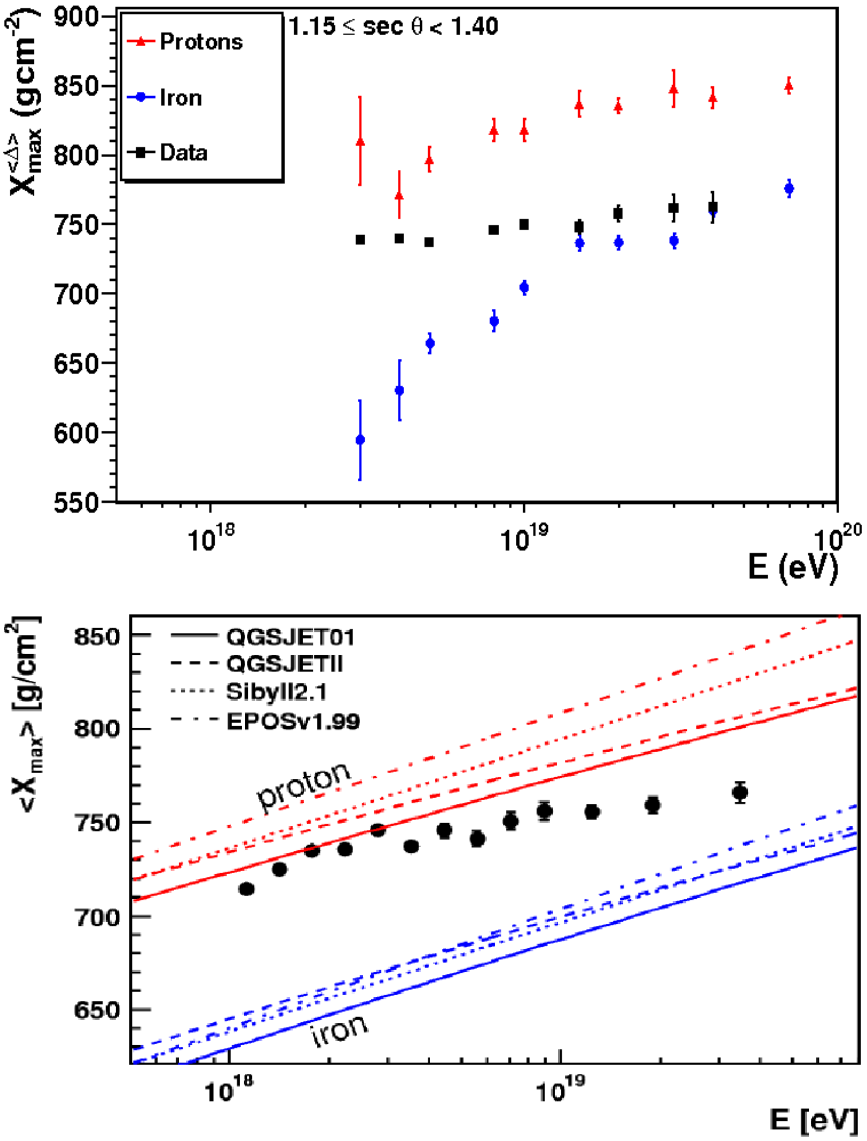

Figure 4.28: Top: Average $X_{max}^{\langle\Delta\rangle}$ and Bottom: the average X_{max}^{FD} from (39), as a function of energy from the data and simulations. $\langle\Delta\rangle$ has been converted to $X_{max}^{\langle\Delta\rangle}$ for the data and all simulations using the conversion given in section 3.4.

The effect of shifting the threshold for finding photon-candidates by minus (plus) the uncertainty on the median of the photon distribution increases (decreases) the number of photon-candidates from the data by 1, 2, 0, 0 (2, 2, 2, 1) events above 10, 20, 30 and 40 EeV respectively.

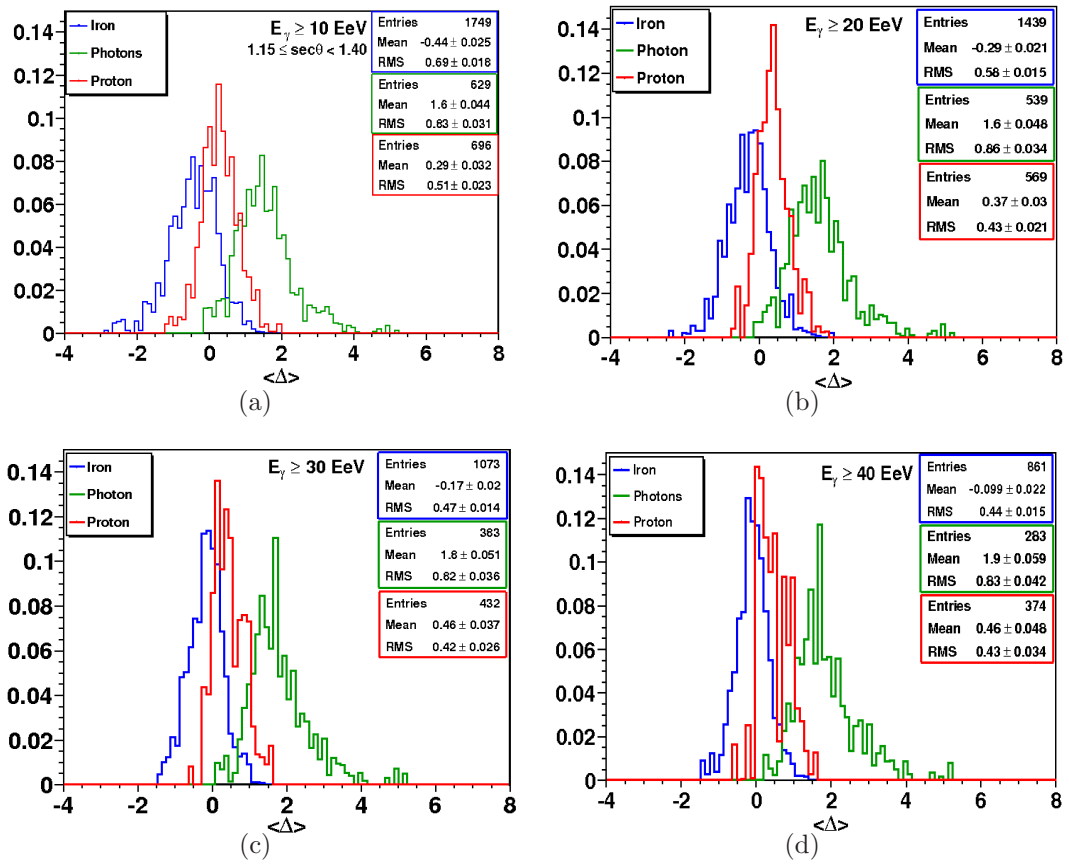

Figure 4.29: The normalised distributions of $\langle\Delta\rangle$ for iron, proton and photon simulations for four different energy thresholds. The proton and iron have been weighted such that their energy spectra matches that of the data. The photon simulations have been weighted to an E^{-2} spectrum. The benchmarks derived from the data have been used to calculate $\langle\Delta\rangle$ in all cases.

$E_{threshold}$	Photon Median	N_{data}^{total}	N_{data}^{cand}	N_{proton}^{cand}	N_{iron}^{cand}
10	1.47 ± 0.04	5373	10	19	2
20	1.54 ± 0.05	2366	5	6	2
30	1.67 ± 0.05	1153	2	0	0
40	1.69 ± 0.06	622	1	0	0

Table 4.2: The number of photon-candidates found from the data, proton and iron simulations. The total number of events from the data above $E_\gamma = E_{threshold}$ and the median of the photon distribution are also shown.

The effect of changing the simulated photon spectrum has also been investigated. For an $E^{-2.5}$ photon spectrum, the photon median is shifted to smaller $\langle\Delta\rangle$, increasing the number of photon-candidates in the data by (1,1,1,0) events. A similar increase is observed for the proton and iron simulations in all cases.

4.7 Photon Limits

Recent new constraints on the proton-proton cross-section from the LHC (99) and the proton-air cross-section from the Pierre Auger Observatory (100) indicate modifications to the QGSJetII interaction model are needed to accurately describe UHECR air showers. This may resolve the discrepancy between the simulated and reconstructed energies in hadronic simulations (see, for example, figure 4.20) and increase the muon multiplicity in simulated showers. Comparisons to hadronic simulations in this work can therefore only be considered a useful indication of the current situation and cannot be used to confirm or refute the number of events believed to be photon-candidates. Nor is a study of the composition of individual events possible. Robust upper limits to the photon flux and fraction are still achievable with current models as the physics behind photon-initiated EAS is well-known.

Conservative integral upper limits have been placed on the flux and fraction of UHECR photons assuming all 10 candidates found here are photons. All non-candidate events are assumed to be hadronic in composition. Photon-candidate events will retain their photon energies, E_γ whilst all non-candidates are reassigned their energies from the standard energy reconstruction, E_{rec}. The number of events above each energy threshold is listed in table 4.3.

The integral upper limit to the flux of photons is given by:

$$\Phi = \frac{\Lambda_\gamma^{95}}{\epsilon\epsilon_\gamma f T} \tag{4.12}$$

and the integral upper limit to the fraction of photons in the data is:

$$\Gamma = \frac{\Lambda_\gamma^{95}}{\epsilon\epsilon_\gamma f N_{total}(E \geq E_{lim})} \tag{4.13}$$

where: f is the photon-candidate cut efficiency (0.5 by construction), $N_{total}(E \geq E_{lim})$ is the total number of events, including photon-candidates, above a given energy threshold E_{lim} and $\theta \leq 60^{\circ}$. The efficiency of the $\langle\Delta\rangle$-method for the zenith angles and energies considered here is denoted by ϵ and the integral photon reconstruction efficiency by ϵ_{γ}. The array exposure, T, is $6083\,\mathrm{km}^2\,\mathrm{sr}\,\mathrm{yr}$.

The expected number of photons at a 95% confidence level, Λ_{γ}^{95}, given N_{cand} candidates has been found by considering the Poissonian tail of a distribution where n events have been studied. The values of Λ_{γ}^{95} corresponding to the number of photon candidates found in this work are given in table 4.3 for each energy threshold. Had a firm detection of photons been made, a definite flux could have been obtained. In this case Λ_{γ}^{95} would be replaced by N_{cand} in equations 4.12 and 4.13.

E_{lim}(EeV)	N_{total}	n	N_{cand}	ϵ	ϵ_{γ}	Λ_{γ}^{95}	$\Phi\,(\mathrm{km}^{-2}\mathrm{sr}^{-1}\mathrm{yr}^{-1})$	$\Gamma(\%)$
10	3542	1669	10	0.96	0.67	17.0	0.0087	1.5
20	898	462	5	0.95	0.77	10.5	0.0047	3.2
30	348	184	2	0.90	0.81	6.3	0.0028	4.9
40	154	81	1	0.82	0.82	4.7	0.0023	9.1

Table 4.3: Integral upper limits to the flux (Φ) and fraction (Γ) of UHE photons for four different energy thresholds. N_{total} is the total number of events with $E_{rec} \geq E_{lim}$ and $\theta \leq 60^{\circ}$ before cuts, n is the number of events with $E_{rec} \geq E_{lim}$ which pass all the $\langle\Delta\rangle$-method cuts and N_{cand} is the number of photon-candidates above the same energy threshold. For the explanation of other values, see text.

The differential photon reconstruction efficiency is shown in figure 4.30. At 10^{19} eV, the average photon efficiency is 0.20 ± 0.02. For the calculation of integral photon limits, the integral photon efficiencies (ϵ_{γ}) must be used and have been calculated from figure 4.30. These are given in table 4.3 for the corresponding energy thresholds.

Using the formula given in equations 4.12 and 4.13, new upper limits to the photon flux and fraction have been calculated and are given in table 4.3. These

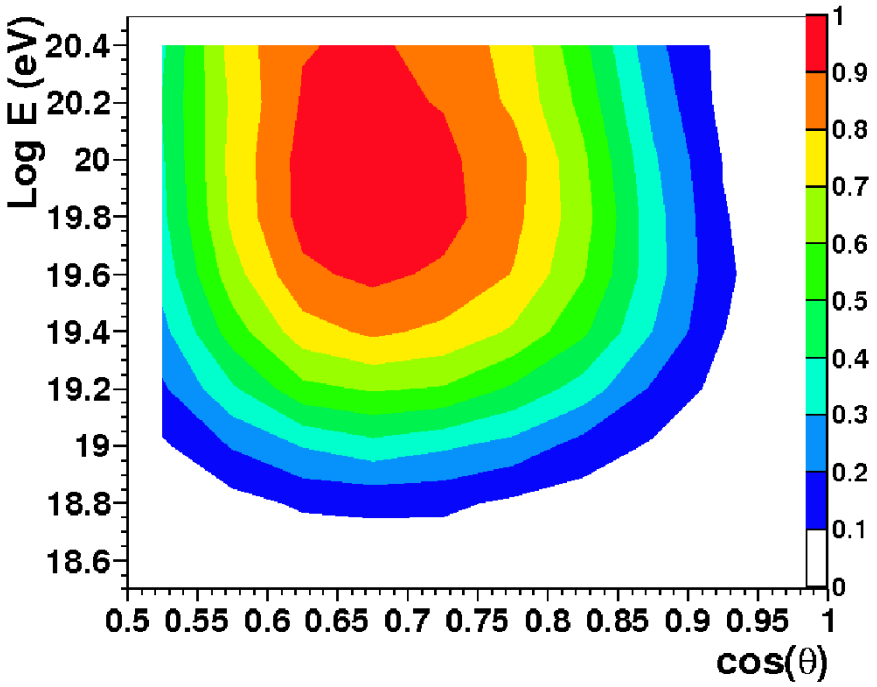

Figure 4.30: Differential photon selection efficiencies corresponding to the set of photons and cuts described in this work. Warmer colours indicate higher efficiencies.

limits are shown in figures 4.31 and 4.32, together with a selection of model predictions and previous results from the Pierre Auger Observatory.

The new limits to the photon fraction, shown in figure 4.32, indicate a significant improvement over previous limits at all energies. Only at 10 EeV does this limit remain above the prediction for the Z-burst model. None of these limits probes the predicted GZK region.

Larger flux limits above 10 and 20 EeV have been found compared to those presented in (47). This does not indicate a failure of the $\langle\Delta\rangle$-method as the work in (47) utilised a combination of the risetime ($t_{1/2}(1000)$) and the radius of curvature in a multi-parameter study, whereas this work does not. The analysis in (47) was conducted to give a preliminary idea of the performance of a multi-parameter analysis technique given limited statistics. The $\langle\Delta\rangle$-method was developed to give a more rigorous analysis using only a single parameter. A sim-

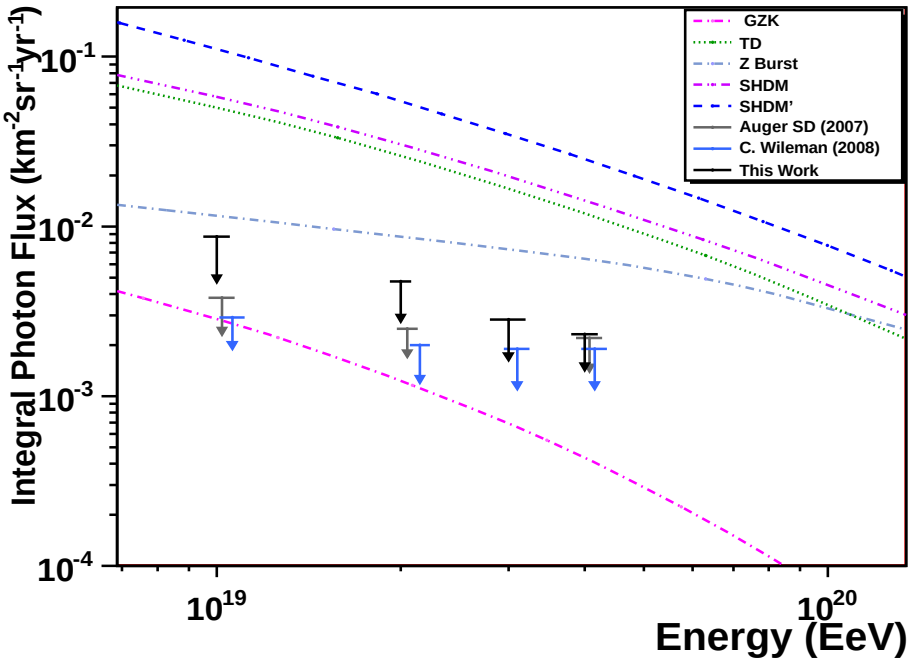

Figure 4.31: Integral upper limits to the flux of UHECR photons found in this work (black arrows). Previous limits made by the Pierre Auger Observatory (grey arrows) (47) and from (28) (blue arrows) (offset slightly on the x-axis for clarity) and model predictions from the GZK mechanism (pink line - upper limit), Top-down (green line), SHDM (magenta and blue lines) and Z-Burst (mauve) models are also shown.

ilar, rigorous analysis has not been conducted on the radius of curvature which currently has very poor discrimination power between primary types.

Significant doubt has also been cast on the limits presented in (47). A recent re-analysis of this earlier work has not managed to successfully reproduce the published limits (101) - instead achieving significantly larger limits ($\Phi = 8.1 \times 10^{-3}\,\mathrm{km^{-2}s^{-1}yr^{-1}}$ at 10 EeV for the same period). An incorrect calculation of the photon efficiencies is cited as a primary cause of this discrepancy. A re-analysis of the $t_{1/2}$(1000)-Curvature method is ongoing (101).

Calculation of the flux of photons (rather than the upper-limits) for the number of candidate events found in this work gives $\Phi = (5.1 \pm 0.5) \times 10^{-3}$,

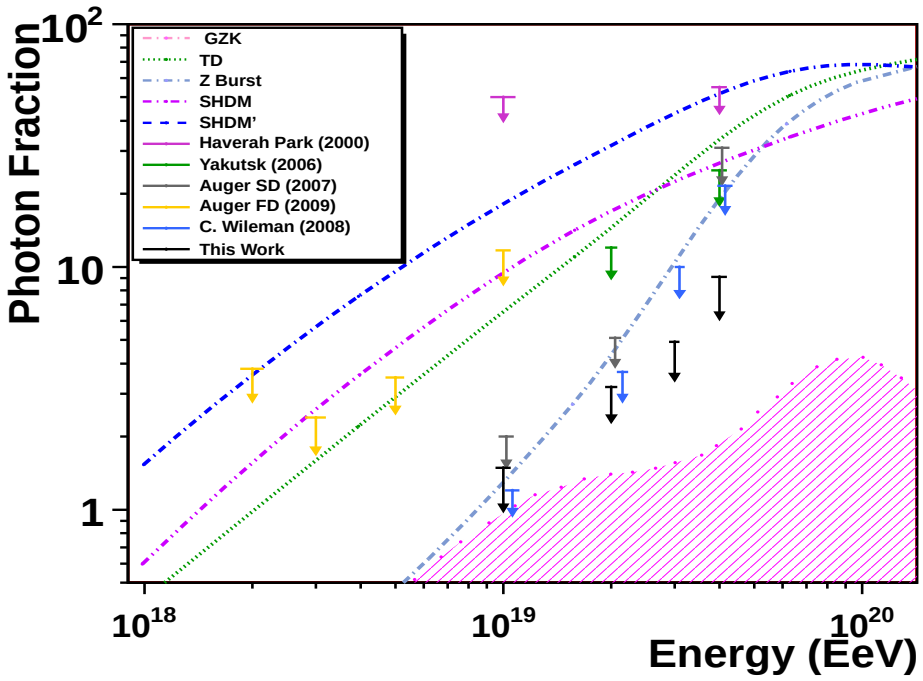

Figure 4.32: Integral upper limits to the fraction of UHECR photons found in this work (black arrows). Previous limits made by the Pierre Auger Observatory (grey and orange arrows) (47), (48) and from (28) (blue arrows) (offset slightly on the x-axis for clarity) and model predictions for the GZK mechanism (pink shading), Top-down (green line), SHDM (magenta and blue lines) and Z-Burst models (mauve line) are also shown.

$(2.3 \pm 0.1) \times 10^{-3}$, $(0.90 \pm 0.08) \times 10^{-3}$ and $(0.48 \pm 0.02) \times 10^{-3}$ above 10, 20, 30 and 40 EeV respectively. The fraction of photons above these energies is $(0.88 \pm 0.08)\%$, $(1.52 \pm 0.08)\%$, $(1.56 \pm 0.13)\%$ and $(1.92 \pm 0.08)\%$ respectively. All these numbers are tantalisingly close to the GZK region shown in figures 4.31 and 4.32 and are smaller-valued than limits from previous works. However, in the absence of a positive detection of photons, the 95% confidence upper limits to the flux and fraction must be used.

4.8 Conclusion

In this work a large set of photon simulations with a continuous distribution of energies and zenith angles were analysed using the $\langle\Delta\rangle$-method described in chapter 3. Previously, only a much smaller set ($\sim 1/3$ of the current number) of photons at discrete energies and zenith angles had been studied. Additionally, for the first time, the $\langle\Delta\rangle$-method has been applied to a large number of proton and iron simulations, also with a continuous energy and zenith angle distribution.

Using the benchmark derived from the data, the distribution of $\langle\Delta\rangle$ from photon simulations has been compared to the data. An E^{-2} energy spectrum has been assumed for the photons. The number of photon-candidates has been determined by examining events with a $\langle\Delta\rangle$ larger than the median of the photon distribution. Ten, five, two and one photon-candidates have been found above 10, 20, 30 and 40 EeV respectively.

The number of photon-candidates expected from a pure proton and pure iron composition, with the same flux spectrum as the data, has been determined. Whilst the number of photon-candidates from the data is well within the number expected from protons, these candidate events cannot conclusively be dismissed as part of a hadronic tail in the data. This is predominantly due to uncertainties surrounding the simulation of hadronic showers. With this in mind, new 95%-confidence level upper limits to the integral flux and fraction of UHE photons above 10, 20, 30 and 40 EeV have been calculated assuming that the observed candidate events are photons. This gives flux limits of 8.7×10^{-3}, 4.7×10^{-3}, 2.8×10^{-3} and $2.3\times10^{-3}\,\mathrm{km^{-2}\,sr^{-1}\,yr^{-1}}$ above 10, 20, 30 and 40 EeV respectively. The corresponding limits to the fractions of photons are 1.5%, 3.2%, 4.9% and 9.1%. For the photon fraction this represents a significant improvement to the photon limits, ruling out the Z-burst model at all energies except 10 EeV. Examination of the average $\langle\Delta\rangle$ as a function of energy from hadronic simulations and the data indicates an increase in mass with increasing energy - provided hadronic interaction models are correct.

Future attempts to determine limits to the photon flux and fraction will achieve better separation between photons and hadrons by using multi-parameter analysis techniques - for example, combining the $\langle\Delta\rangle$-method and the radius of shower front curvature. This will push limits down into the GZK region and determine whether the observed candidates are truly photons or just a tail to a hadronic distribution. Better discrimination between proton and iron primaries may also be achieved, allowing the mass-composition of UHECR to be probed. An increase in statistics from both the data and simulations will also aid this goal, thereby allowing uncertainties to be reduced.

Chapter 5

Application of the $\langle\Delta\rangle$-Method to the Search for UHECR Sources

5.1 Introduction

In this chapter the results of the $\langle\Delta\rangle$-method are applied to the search for UHECR sources. Firstly, the position on the sky of the photon candidate events found in chapter 4 are determined and compared to the positions of 318 AGN from the VCV catalogue. Secondly, the difference in $\langle\Delta\rangle$ for the highest energy events that correlate or do not correlate with AGN from the VCV catalogue used in (75) is investigated. Similarly, the distribution of $\langle\Delta\rangle$ for the highest energy events originating from within an 18° region centred on Cen A are also investigated and compared to events with larger angular separations.

5.2 A Search for the Sources of the Photon-Candidate Events

Photons are not deflected by magnetic fields and can therefore be traced back to their source locations. A correlation of photon-initiated air showers with sources from a given catalogue could give an indication of the nature of the accelerators capable of producing ultra high energy cosmic-rays. The arrival directions of the photon-candidates found using the $\langle\Delta\rangle$-method in chapter 4 are indicated

in figure 5.1, together with the positions of 318 AGN with red-shifts closer than $z = 0.018$ ($r \leq 75\,\mathrm{Mpc}$), taken from the VCV catalogue used in (75). The arrival directions of these events are determined from the zenith and azimuthal angles, GPS timing of the event and the location of the shower core on the array. The angular resolution of the arrival directions is defined as the region around the real arrival direction in which 98% of the reconstructed shower directions fall and is better than 0.9° for SD events with at least 6 triggered detectors (75). From these arrival directions, the right ascension (α) and declination (δ) of each event has been calculated and then converted into to the galactic coordinate system (l, b) and plotted using a Hammer-Aitoff projection (figure 5.1). All coordinate transformations correspond to the J2000 epoch. The galactic coordinates and $\langle\Delta\rangle$s of the photon-candidate events are listed in table 5.1. The position of 106 cosmic rays with energy $E \geq 55\,\mathrm{EeV}$ and $\theta \leq 60°$ recorded between 1/1/2004 and 31/11/2011 are also shown in figure 5.1.

ID	**l**	**b**	$\mathrm{Log}\,E_\gamma\,(\mathrm{eV})$	$\langle\Delta\rangle$
9333599	-170.2	-63.3	19.10	1.49 ± 0.17
6784159	-137.9	-12.0	19.36	1.49 ± 0.15
1813111	-137.1	-58.1	19.39	1.79 ± 0.17
8938022	-138.8	-30.4	19.62	1.71 ± 0.23
2248206	-62.1	-39.3	19.50	1.70 ± 0.16
6637103	-35.1	-38.7	19.46	1.57 ± 0.17
1768669	-20.2	-10.4	19.27	1.74 ± 0.17
1998796	-26.4	-9.2	19.27	1.65 ± 0.23
3343182	27.6	6.6	19.39	1.52 ± 0.29
10450239	156.3	-54.9	19.73	1.61 ± 0.25

Table 5.1: Positions of the photon-candidate events in galactic coordinates in order of increasing longitude. The corresponding $\langle\Delta\rangle$ and photon-energies are also given.

None of the photon candidates found in this work appear within the 18° region around Centaurus A, indicating that Cen A is not a source of the observed photon-

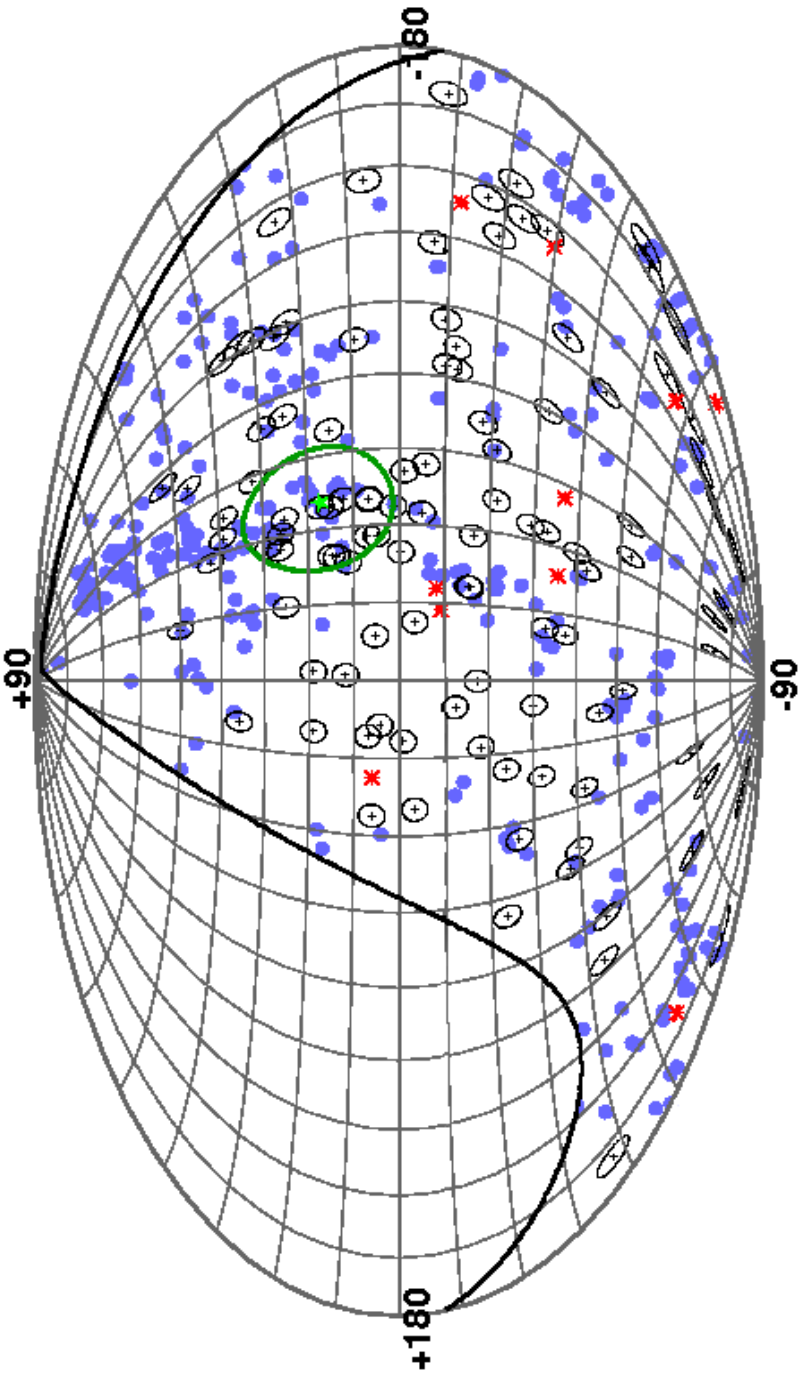

Figure 5.1: Hammer-Aitoff projection of the arrival directions of the photon-candidates (red stars). Also shown are the positions of AGN from the VCV catalogue (blue circles) within the Auger field of view (thick black line), the arrival directions of the 106 highest energy events (with $E \geq 55\,\mathrm{EeV}$) used in the correlation study in (75) (black crosses), Centaurus A (green star) and an 18° region around Cen A (green circle). The black circles mark a 3° region surrounding each of the highest energy events (75). The angular resolution is better than 1° for all the events shown here.

candidates. Only one photon candidate event (event 3343182) is at latitudes greater than 0°, indicating a possible lack of sources of UHECR in this region that give rise to GZK-protons, such that photons may be observed at Earth. Similarly, only one other photon-candidate event is observed at positive galactic longitudes. That these events are not grouped in one region of the sky indicates that the photon-candidate events do not all originate from the same source, if these events are indeed photons. If these events were proton primaries rather than photons, the observed distribution on the sky still indicates more than one source is present, given current knowledge of intergalactic and galactic magnetic fields.

Two photon candidates appear close together on the sky - at (20.2, -10.4) and (26.4, -9.2) and are within 3° of AGN from the VCV catalogue. If photons, these two events could potentially come from the same source, or from sources within a few degrees on the sky. The event at (156.3, -54.9) also lies close to an AGN from this catalogue. Three other photon candidates appear within 20° of small, sparse 'clusters' of the highest energy events - in the regions surrounding (-140, -30) and (-140, -60) respectively, However, neither of these regions contain AGN within 75 Mpc from the VCV catalogue. The remainder of the photon-candidates do not have arrival directions close to those of the highest energy cosmic-rays or AGN within redshift $z = 0.018$ from the VCV catalogue.

The arrival directions of the photon-candidate events have also been compared to the positions of 373 AGN within 200 Mpc from the Swift-BAT catalogue used in (75). Using this catalogue, the events at (-138.8, -30.3) and (-137.1, -58.1) have an AGN within 3° of their respective locations. No other photon-candidate events have arrival directions close to nearby AGN from the Swift-BAT catalogue.

The lack of correlation with AGN from the VCV or Swift-BAT catalogues indicate that either the photon-candidate events found in chapter 4 are not photons and therefore are deflected from their sources by a significant amount or that the sources of UHECR are not the AGN listed in these catalogues. The lack of apparent correlation between the highest energy events, where deflections

should be minimal, and the photon-candidate events implies either that these candidate events are not photons, or that the highest energy events are strongly deflected by magnetic fields. In the case of the highest energy events, this could be due to the presence of iron primaries, or that the extragalactic magnetic field is much stronger than previously believed, causing the highest energy events to be deflected more than hitherto assumed. Comparison of the photon candidates to hadronic simulations in chapter 4 indicated the possibility that these photon-candidates might actually be from the tail of a hadronic distribution. The results in this section add to that argument, although the possibility of a proportion of these events being photon primaries cannot be eliminated. The sources of these events therefore remain unknown.

5.3 The Risetimes of the Highest Energy Events

The highest energy events have previously been investigated for correlations with nearby extragalactic objects (30), (75). In the latter of these two works, only 29/69 events (42%) with $E \geq 55\,\mathrm{EeV}$ and $\theta \leq 60^\circ$ were observed to correlate with AGN within 3° (including those used in the initial prescription) (75). Further, the six events with the highest energies do not appear to correlate with AGN. An additional 37 events with $E \geq 55\,\mathrm{EeV}$ have been recorded since, bringing the total to 106 events as of 31/11/2011. The arrival directions of these events are indicated in figure 5.1. Using this updated set of events, the total number that correlate with AGN is now 36/106 (34%) - including those from the initial prescription.

Recent work on the composition using X_{max} (39), which finds a steadily increasing average mass-composition with energy, raises the possibility that events uncorrelated with AGN may be heavy primaries that have suffered large deflections from their original direction. If those events that do not correlate with AGN have a much heavier composition than those that do, their lack of correlation could be explained by large deflections in galactic magnetic fields, thus AGN could still be sources of UHECR. If, on the other hand, the events that correlate

with AGN are from heavier primaries, then those events correlate by chance and other types of object must be considered as the sources of UHECR.

The correlation study in (75) used the first 14 events (those recorded prior to 26/05/06, 'Period I') in an exploratory scan to determine the maximum separation between arrival directions and AGN that minimised chance correlations. These events were then discarded and future events (Periods II and III) were used to determine the degree of correlation of cosmic rays and AGN. In the following sections the events from period I have not been discarded in this *a posteriori* analysis.

5.3.1 Events That Correlate With AGN

The highest energy events that correlate with AGN have been compared to those that do not using the ⟨Δ⟩-parameter. ⟨Δ⟩ is calculated as described in chapter 3 for all events with $\theta \leq 45°$. The cut on events with $\theta \leq 30°$ used for the photon searches in chapter 4 has been relaxed for this analysis. Twenty-nine events which do, and 41 events which do not correlate with AGN, have an available ⟨Δ⟩. The distribution of ⟨Δ⟩ for these events are shown in the top panel of figure 5.2. A larger value of ⟨Δ⟩ indicates a deeper developing shower (larger X_{max}) or a lighter composition. Ten of these events are hybrid events with a reliable X_{max}, of which 2 that do and 5 that do not correlate with AGN have a calculable ⟨Δ⟩. Of the remaining 36 events with no available ⟨Δ⟩, 24 have a zenith angle larger than $\theta \leq 45°$ and 12 events do not have at least two detectors which pass the cuts on distance, signal and risetime.

It can be seen from figure 5.2 that the average ⟨Δ⟩ appears to be the same, within uncertainties, for events that correlate with AGN and for those that do not correlate. If the outlier at $\langle\Delta\rangle = -2.6 \pm 2.9$ is removed, the mean values of these two distributions differ by only 0.02. The distribution of zenith angles and energies of those events which do and do not correlate with AGN and which survive the ⟨Δ⟩-method cuts are also the same within uncertainties. The outlying event at $\langle\Delta\rangle = -2.6 \pm 2.9$ has been inspected and, with the exception of short

traces as indicated by its value of $\langle\Delta\rangle$, no unusual features are observed. The values of $\langle\Delta\rangle$ with energy for these events are shown in the lower panel of figure 5.2. No difference in the $\langle\Delta\rangle$ of each set of events as a function of energy is observed.

The composition of any of these highest energy events cannot be precisely determined due to the large overlap between the $\langle\Delta\rangle$-distributions of proton and iron simulations, except to note that, at first glance, the average $\langle\Delta\rangle$ is larger than expectations from iron simulations but smaller than for proton simulations above the same energy, as seen from figure 5.2. None of these events are photon-candidates.

5.3.2 Events Within the Centaurus A Region

As the closest radio galaxy potentially capable of accelerating UHECR, and being well within the GZK region at a distance of 3.5 Mpc, Centaurus A (Cen A or NGC 5128) is obviously of some interest. In (75), the most significant departure from isotropy for the cumulative number of events with $E \geq 55\,\mathrm{EeV}$ as a function of angular distance from Cen A was found to be 18°. In this section a comparison of the $\langle\Delta\rangle$s of events within 18° of Cen A and those outside this region is discussed. $\langle\Delta\rangle$ has been found for 13/15 of the highest energy events that lie within and 57/91 events outside this this 18° region. As stated in the previous section, 24 events - of which all are outside the 18° region - have zenith angles larger than 45°, where $\langle\Delta\rangle$ is undefined. A further 12 events do not have at least two detectors which pass the selection criteria from the $\langle\Delta\rangle$-method.

The two distributions of $\langle\Delta\rangle$ are shown in figure 5.3, where it can be seen that the average $\langle\Delta\rangle$ of those events within the Cen A region is smaller than that of events which lie further afield (-0.25 ± 0.24 compared to 0.18 ± 0.08). Since these means are not the same, a two-tailed students t-test has been performed to determine the likelihood that these two samples are drawn from the same population. The student's t value given by :

$$t = \frac{|\mu_A - \mu_B|}{S\sqrt{1/N_A + 1/N_B}} \tag{5.1}$$

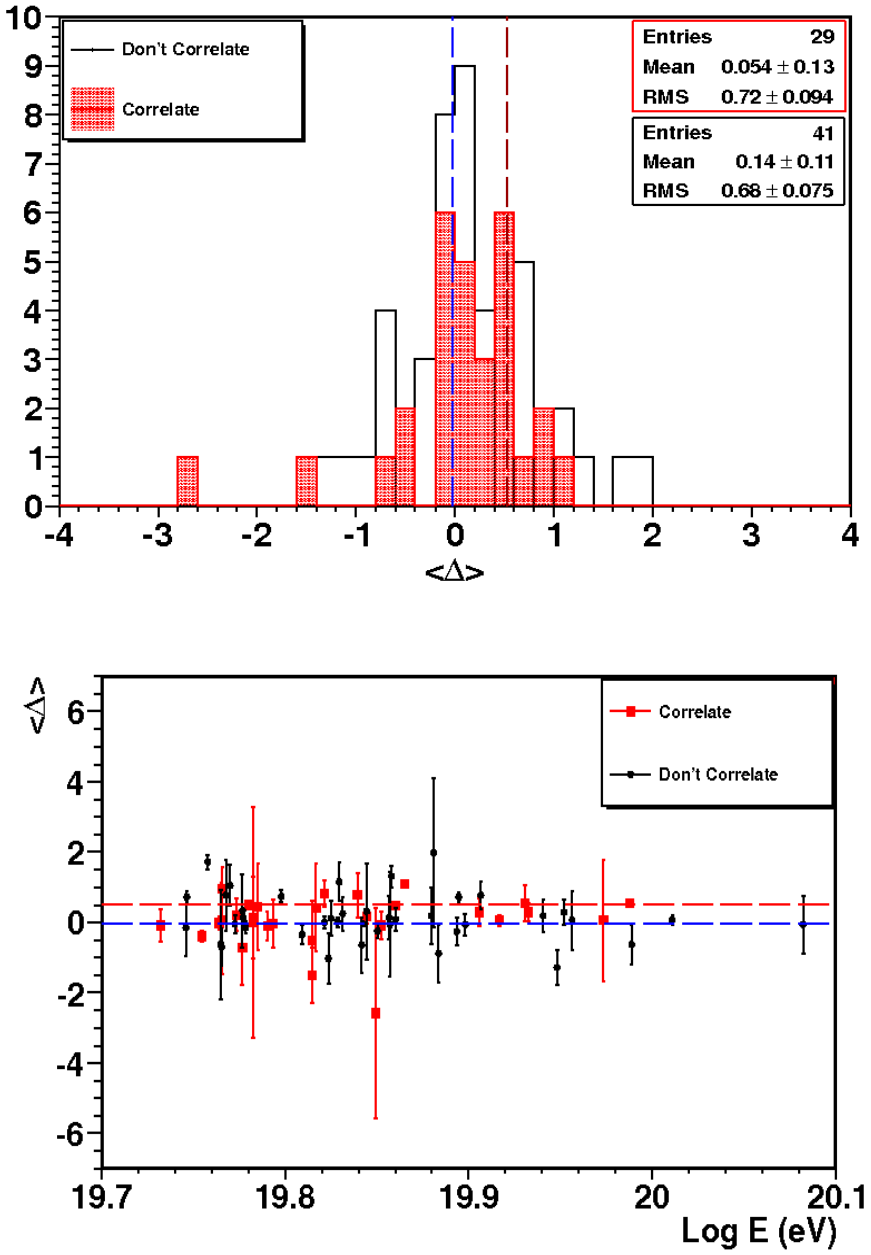

Figure 5.2: Top: Distribution of $\langle\Delta\rangle$ for events which do (shaded red) and do not (black) correlate with AGN. Bottom: $\langle\Delta\rangle$ as a function of energy for events which do (red) and do not (black) correlate with AGN. The average $\langle\Delta\rangle$ from proton (red dashed line) and iron (blue dashed line) simulations with energies above 55 EeV are also indicated in both figures at 0.53 ± 0.05 and -0.03 ± 0.01, respectively. A larger $\langle\Delta\rangle$ implies a deeper development and lighter composition.

where the sample variance, S, is:

$$S = \sqrt{\frac{(N_A - 1)\,\sigma_A^2 + (N_B - 1)\,\sigma_B^2}{N_A + N_B - 2}} \tag{5.2}$$

and N_A and N_B are the number of events with a calculable $\langle\Delta\rangle$ within and outside 18° respectively. σ_A and σ_B are the corresponding uncertainties on the means, μ_A and μ_B. The value for t has been found to be 11.7, indicating that these two distributions are the same at the 95% confidence level. In other words, there is no significant difference between the $\langle\Delta\rangle$ distribution for events within the Cen A region and for those events with larger angular separations. The distribution of $\langle\Delta\rangle$ as a function of energy for these events is given in figure 5.4, where it can be seen that there is no bias in the distributions of $\langle\Delta\rangle$ as a function of energy. The average $\langle\Delta\rangle$ expected from proton and iron simulations with E $\geq$ 55 EeV are also shown. As in the previous section, no deductions about the mass-composition of these events can be given.

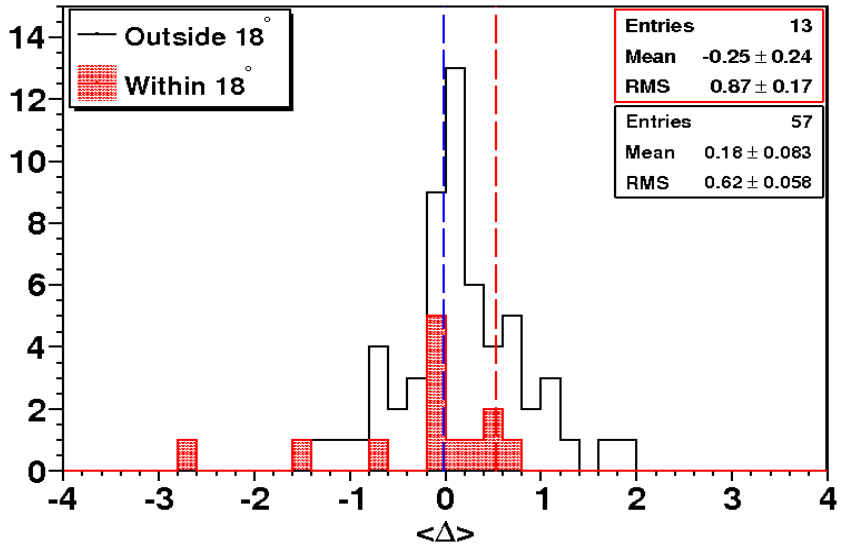

Figure 5.3: Distribution of $\langle\Delta\rangle$ for events that lie within an 18° region around Cen A (red, shaded) compared to those that do not (black). The average $\langle\Delta\rangle$ from proton (dark red dashed line) and iron (blue dashed line) simulations with energies above 55 EeV are also indicated at 0.53 ± 0.05 and -0.03 ± 0.01, respectively.

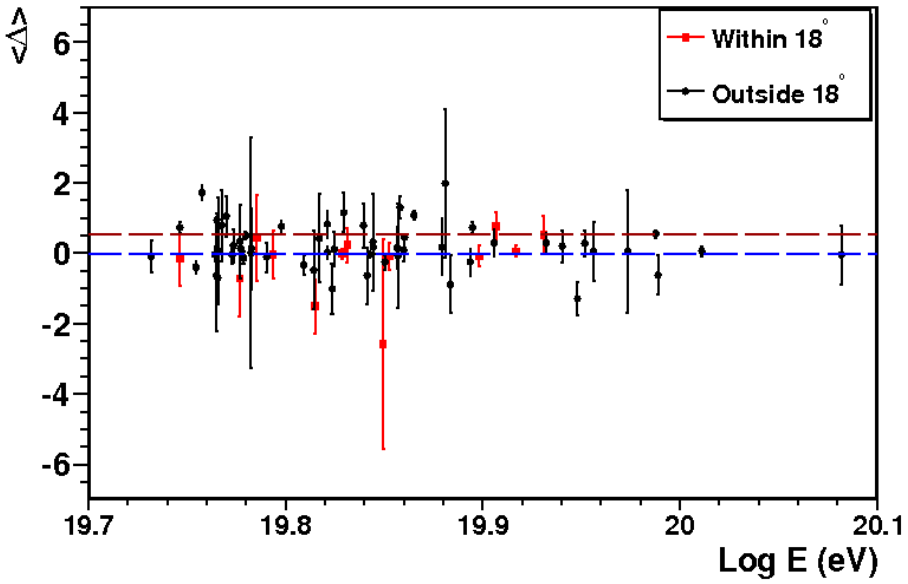

Figure 5.4: ⟨Δ⟩ as a function of energy for events that lie within an 18° region around Cen A compared to those that do not. The average ⟨Δ⟩ from proton (red dashed line) and iron (blue dashed line) simulations with energies above 55 EeV are also indicated at 0.53 ± 0.05 and -0.03 ± 0.01, respectively.

If Cen A were to be the sole source of UHECR arriving at Earth, then an increase in mass-composition with increasing angular distance is necessary to explain the observed distribution of arrival directions. This requires that ⟨Δ⟩ shows a decrease with increasing angular distance from Cen A, modified perhaps by the increase of ⟨Δ⟩ with energy and fluctuations due to the development of air showers in the atmosphere. A plot of ⟨Δ⟩ as a function of angular distance from Cen A is shown in figure 5.5. The average ⟨Δ⟩ from proton and iron simulations are also shown. The data are consistent with there being no dependence of ⟨Δ⟩ on angular distance (as shown by fitting a linear function to the data). Thus, no trend towards a shallower shower development and hence heavier composition with increasing distance from Cen A exists in the data for the very highest energy events. This strongly implies that UHECR come from more than one nearby source, of which Cen A may be the closest.

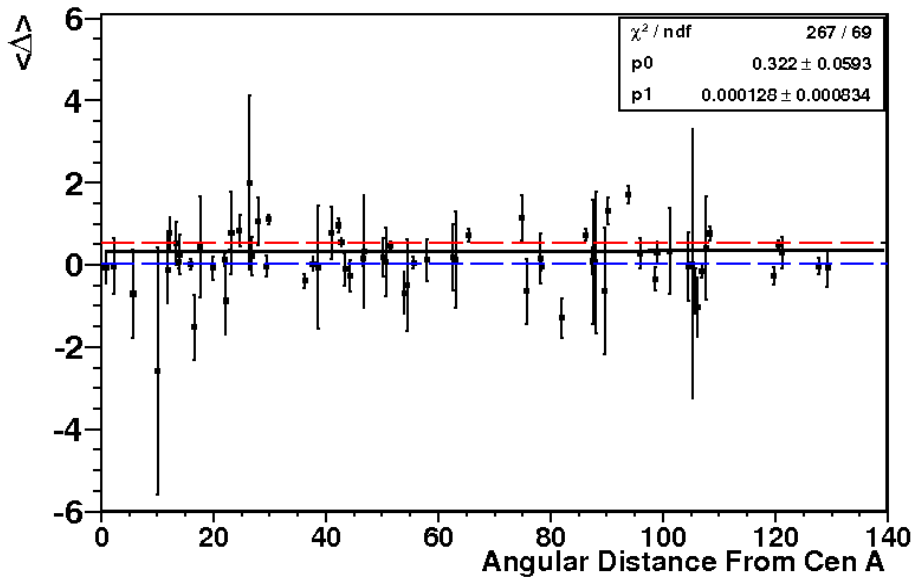

Figure 5.5: $\langle\Delta\rangle$ as a function of angular distance from Cen A for the highest energy events. The solid black line is a linear fit to the data. The average $\langle\Delta\rangle$ from proton (red dashed line) and iron (blue dashed line) simulations with energies above 55 EeV are also indicated at 0.53 ± 0.05 and -0.03 ± 0.01, respectively.

5.4 Conclusion

The arrival directions of the photon candidates found in chapter 4 have been compared to the positions of 318 AGN within a distance of 75 Mpc from the VCV catalogue, to the positions of 373 AGN within 200 Mpc from the Swift-BAT catalogue and to the updated set of highest energy events (now numbering 106 events to the end of November 2011) using the prescriptions from previous correlation studies. No photon candidates lie in the vicinity of Cen A or correlate with the AGN from this catalogue. Two photon candidates lie within 20° of sparse 'clusters' of the highest energy events in areas well away from AGN from the VCV catalogue, although a possible correlation with an AGN from the Swift-BAT catalogue is found in either case. That the photon candidates are distributed across all galactic latitudes below +10° indicates more than one source is responsible for the observed flux of UHECRs. The possibility that these events are not photons

still remains. The lack of correlation with the highest energy events implies either that these candidate events are not photons, or that the highest energy events are strongly deflected by magnetic fields. The possible sources of these events remain unknown.

The average $\langle\Delta\rangle$ for the updated set of high energy events has been investigated in two ways. The average $\langle\Delta\rangle$ of 29 events which correlate with AGN from the VCV catalogue has been compared to the average of 41 events that do not correlate with AGN and are the same within uncertainties. Similarly, the average $\langle\Delta\rangle$s of 13 events within an 18° radius around Centaurus A have been compared to 57 events outside this region. Again, no statistically significant difference between the two distributions has been found. The possibility of a gradual change in $\langle\Delta\rangle$ as a function of angular distance from Cen A has also been investigated. However, no such change has been found, thereby implying no systematic change of mass composition. Thus Cen A is unlikely to be the sole source of UHECR.

Due to the extreme overlap of $\langle\Delta\rangle$ from proton and iron simulations it has not been possible to determine the individual mass-composition of the highest energy events. However, in all four distributions investigated above, the average of the $\langle\Delta\rangle$-distribution has fallen between the values expected from proton and iron simulations of energy greater than 55 EeV. None of the 106 highest energy events are photon-candidates.

Chapter 6

The Asymmetry on the Risetimes as a Mass-Sensitive Parameter

6.1 Introduction

As discussed in chapter 3, the timing parameters of inclined showers are subject to asymmetry effects due to the geometry of the shower with respect to the ground and the development of the electromagnetic component at different slant depths. The asymmetry in the risetime as a function of distance and zenith angle was parametrised for the data (for all energies above $E \geq 3\,EeV$) in chapter 3.2.3 such that a correction for the asymmetry effect could be made to the risetimes to obtain a reliable and unbiased $\langle\Delta\rangle$-parameter. The zenith angle at which the maximum asymmetry occurs was found to be $\sim 42^\circ$ for events with $E \geq 3\,EeV$. This compared to $\sim 41^\circ$ for iron simulations, $\sim 44^\circ$ for protons and $\sim 46^\circ$ for photon simulations, thus indicating a possible mass-sensitivity in the value of maximum asymmetry from which the average mass-composition of UHECR might be determined.

A recent study, described in (90) and (89) attempted to utilise the asymmetry in the risetimes as a mass-sensitive variable. Several concerns have arisen over the reliability of this method and the interpretation of the results, including some of their basic assumptions, which are being reviewed by the Pierre Auger

collaboration. This chapter reviews the method in (89) and (90), and examines a potential alternative.

6.2 Summary of Previous work

The average asymmetry on the risetime as a function of energy and zenith angle was studied in (89) and (90) using data recorded between January 2004 and December 2009. This analysis has been updated to include events to the end of December 2010. Risetimes from events with $E \geq 3\,EeV$ and $\theta \leq 65°$ and from detectors with signals and distances in the range $10 \leq S \leq 800\,VEM$ and $500 \leq r < 2000\,m$ were used. After these cuts nearly 10^5 risetimes from 19051 events are available. In (89) and (90) the old (pre-2011) stop-times and baseline subtractions were utilised. Their method has been re-examined using the new stop-times and baseline subtraction (as described in section 3.1.2), which accounts for slight variations from the results of the original work.

In (89) and (90) it is argued that as the risetime increases linearly with distance from the shower core within the range of distances studied, the asymmetry in the risetime must also follow this relationship, allowing the parameter $t_{1/2}/r$ (risetime divided by the distance from the shower core) to be created in an attempt to eliminate the dependence of the distance on the risetimes. The data have been subdivided into bins of energy and zenith angle and the average $\frac{t_{1/2}}{r}$ plotted as a function of azimuthal angle (the angle the detector makes to the vertical projection of the shower axis on the ground at the shower core) and fitted with a cosine function:

$$\langle \frac{t_{1/2}}{r} \rangle = a + bcos\zeta \tag{6.1}$$

Example results are shown in figure 6.1 and table 6.1 for events at four different zenith angle ranges in the energy range $19.2 \leq \log E < 19.5$. These results are in reasonable agreement to those in (89), despite the implementation of new stop-times and baseline corrections.

The quantity $\frac{b}{a}$ is used to describe the amplitude of the asymmetry. The variation of $\frac{b}{a}$ with $ln(sec\theta)$ has been studied and is symmetric about a maximum

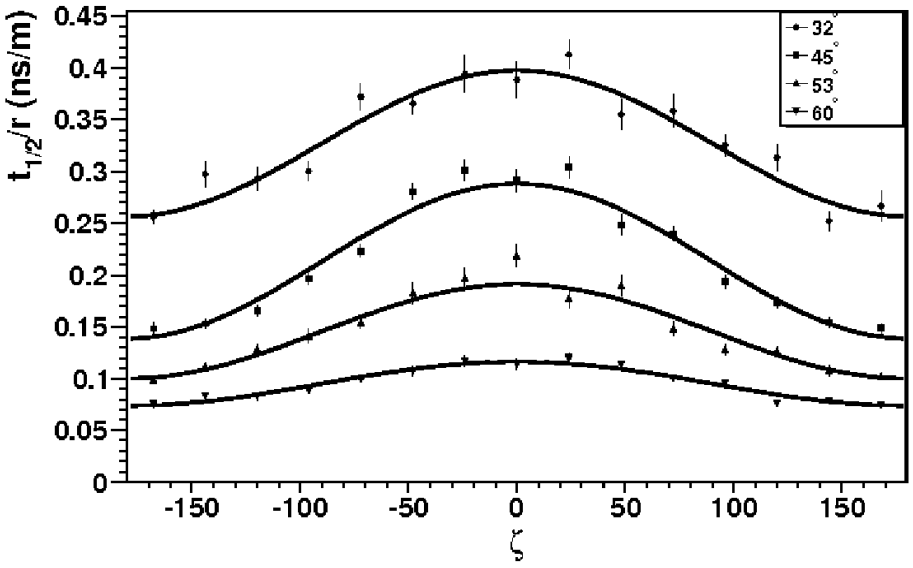

Figure 6.1: $\langle \frac{t_{1/2}}{r} \rangle$ as a function of azimuthal angle for detectors in showers at four different zenith angles in the energy range $19.2 \leq \log E < 19.5$. Reproduced using the method from (89) and the new stop-time algorithms (section 3.1.2).

Zenith Angle	from (89)		This Work	
	a ($ns\,m^{-1}$)	b($ns\,m^{-1}$)	a ($ns\,m^{-1}$)	b ($ns\,m^{-1}$)
32	0.30 ± 0.003	0.084 ± 0.004	0.32 ± 0.002	0.066 ± 0.002
45	0.20 ± 0.003	0.082 ± 0.003	0.24 ± 0.002	0.073 ± 0.003
53	0.13 ± 0.002	0.050 ± 0.003	0.14 ± 0.002	0.043 ± 0.003
60	0.08 ± 0.002	0.026 ± 0.002	0.10 ± 0.001	0.021 ± 0.002

Table 6.1: Comparison of a and b from figure 6.1 (where the new baseline and stop-time parameterizations discussed in section 3.1.2 have been utilised) and from (89) for four zenith angles and in the energy range $19.2 \leq \log E < 19.5$.

value for each energy bin and is well-described by a Gaussian function. The parameter A_{max} is defined as the maximum value of $\frac{b}{a}$ from this Gaussian function, and the zenith angle at which this occurs is $(\sec\theta)_{\max}$. These two parameters describe the maximum asymmetry for a given energy (see figure 6.2 and table 6.2). Both A_{max} and $(\sec\theta)_{\max}$ were investigated in (89) for different proton/iron fractions in steps of 10% and found to be dependent upon the mass composition.

The width of the Gaussian distributions were also studied but no sensitivity of this parameter to different primaries has been found. In (89), $(\sec\theta)_{\max}$ was found to increase linearly with X_{max}.

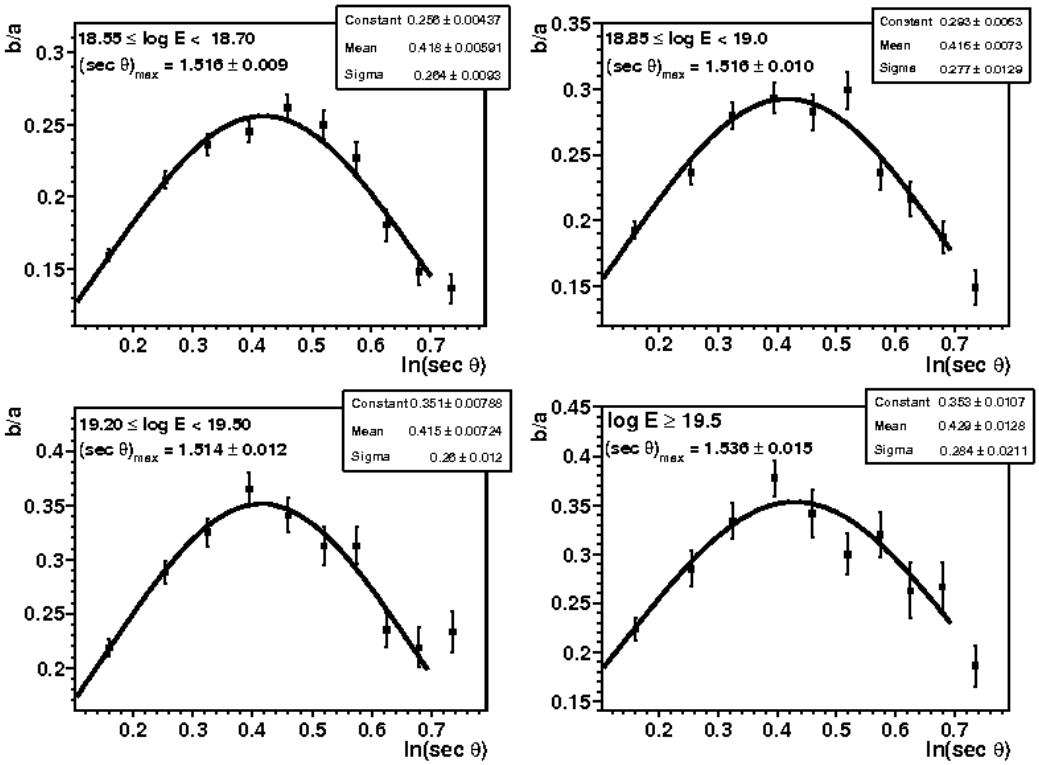

Figure 6.2: The asymmetry parameter $\frac{b}{a}$ as a function of $ln(sec\theta)$ for four different energies, reproduced using the method from (89). The angle of maximum asymmetry, $(\sec\theta)_{\max}$ is given in each case. The new stop-time algorithms (section 3.1.2) have been applied here.

Due to the nature of this method, it is not possible to use the asymmetry of the shower for photon-limit studies, or for detailed event-by-event mass-composition work as it is not possible to analyse the asymmetry on the risetimes on an event-by-event basis. The study of the asymmetry can therefore only provide an indication of the average mass-composition as a function of energy or X_{max}.

Whilst this method is advantageous for its simplicity, aspects of this study are contentious for several reasons. The argument that as the risetime is approxi-

Energy	from (89)		This Work	
	$(sec\theta)_{max}$	A_{max}	$(sec\theta)_{max}$	A_{max}
18.55	1.532 ± 0.008	0.27 ± 0.02	1.516 ± 0.009	0.25 ± 0.004
18.70	1.540 ± 0.008	0.28 ± 0.02	1.542 ± 0.010	0.27 ± 0.005
18.85	1.538 ± 0.009	0.30 ± 0.02	1.516 ± 0.011	0.29 ± 0.006
19.00	1.530 ± 0.010	0.31 ± 0.02	1.527 ± 0.010	0.31 ± 0.006
19.20	1.514 ± 0.012	0.32 ± 0.02	1.514 ± 0.011	0.35 ± 0.007
19.50	1.527 ± 0.019	0.34 ± 0.02	1.536 ± 0.015	0.35 ± 0.01

Table 6.2: $(sec\theta)_{max}$ and A_{max} for each energy. Values from (89) are given for reference.

mately linear with distance (for the range of distances considered), the asymmetry must also be linear (89) is viewed as one of the more contentious aspects. No evidence has been presented in (89) (or references therein) to support this theory. It does not neccessarily follow that the asymmetry will have the same relationship as the risetime with distance. In fact, there is plenty of evidence that the two parameters do not have the same relationship with distance. This can be seen by comparing the function used to describe the average risetime with distance and the correction applied to the risetimes to compensate for the asymmetry in each of the different risetime studies given in references (28), (47), (82), (102) and chapter 3 of this thesis. In all these works the amplitude of the asymmetry has an r^2 dependence:

$$\begin{aligned} t_{1/2} =& f + g cos\zeta \\ \text{where :} \qquad \text{g} =& n(\theta) + m(\theta) r^2 \end{aligned} \tag{6.2}$$

for both the data and hadronic simulations ($n(\theta) = 0$ in the $\langle\Delta\rangle$-method). Moreover, in the $\langle\Delta\rangle$-method the amplitude of the asymmetry for photon simulations was found to have a cubic dependence on distance (see section 4.4.1).

Additional proof that the use of $\langle\frac{t_{1/2}}{r}\rangle$ for asymmetry studies does not remove all dependence on distance can easily be found by plotting $\langle\frac{t_{1/2}}{r}\rangle$ and the asymmetry parameter $\frac{b}{a}$ as a function of r. This is shown in figures 6.3 and 6.4 for several different zenith angles. In both figures it can be seen that the respec-

tive parameters are not independent of distance, as implied in reference (89). This is particularly evident in figure 6.4. In figure 6.3, it can be seen that $\langle\frac{t_{1/2}}{r}\rangle$ increases with r for $ln(sec\theta) \leq 0.29$ ($\theta \leq 41°$) and decreases with r for larger zenith angles. This is true even when the data are subdivided into different bins in energy, although the scatter on the points is larger due to a smaller number of times per bin. This change of the dependence of $\langle\frac{t_{1/2}}{r}\rangle$ vs r with increasing zenith angle could be due to the assumption that $t_{1/2} = p(\theta)r$ when, in fact, from the $\langle\Delta\rangle$-method, the risetime depends on distance in a more complex fashion: $t_{1/2} = 40 + \sqrt{p^2 + qr^2} - p$, where p and q are both functions of zenith angle.

The zenith angle at which the maximum asymmetry occurs for each individual distance shown in figure 6.4 has been investigated. The data have been divided into four energy bins, of which two are shown in figure 6.5. Due to the limitations of statistics it has been necessary to halve the number of distance bins used. Figure 6.5 indicates that both A_{max} and $(sec\theta)_{max}$ vary with distance. This is better illustrated in figure 6.6, where all four energy bins are shown. A clear increase in A_{max} and decrease in $(sec\theta)_{max}$ with distance can be seen for each energy, indicating these parameters are still dependent on distance.

In (89) strong arguments are also presented suggesting that the cause of the asymmetry in the risetimes for zenith angles larger than $\sim 30°$ is solely due to the attenuation of the shower and that there exists no geometric component above this zenith angle. These arguments have been re-examined and found to be inaccurate and therefore misleading (103). Whilst it is true that the attenuation plays a significant part in the asymmetry and that the magnitude of the asymmetry should decrease at zenith angles where the electromagnetic component is fully attenuated, it has also been shown that the geometry of the shower with respect to the ground and the detectors are important (if not the predominant effect) at all zenith angles (104), (105). This is illustrated in figure 6.7 where two showers of different zenith angles but similar energy have been chosen such that the atmospheric overburden for the 'late' particles in the more vertical shower is the same as for the 'early' particles in the more inclined shower at the same

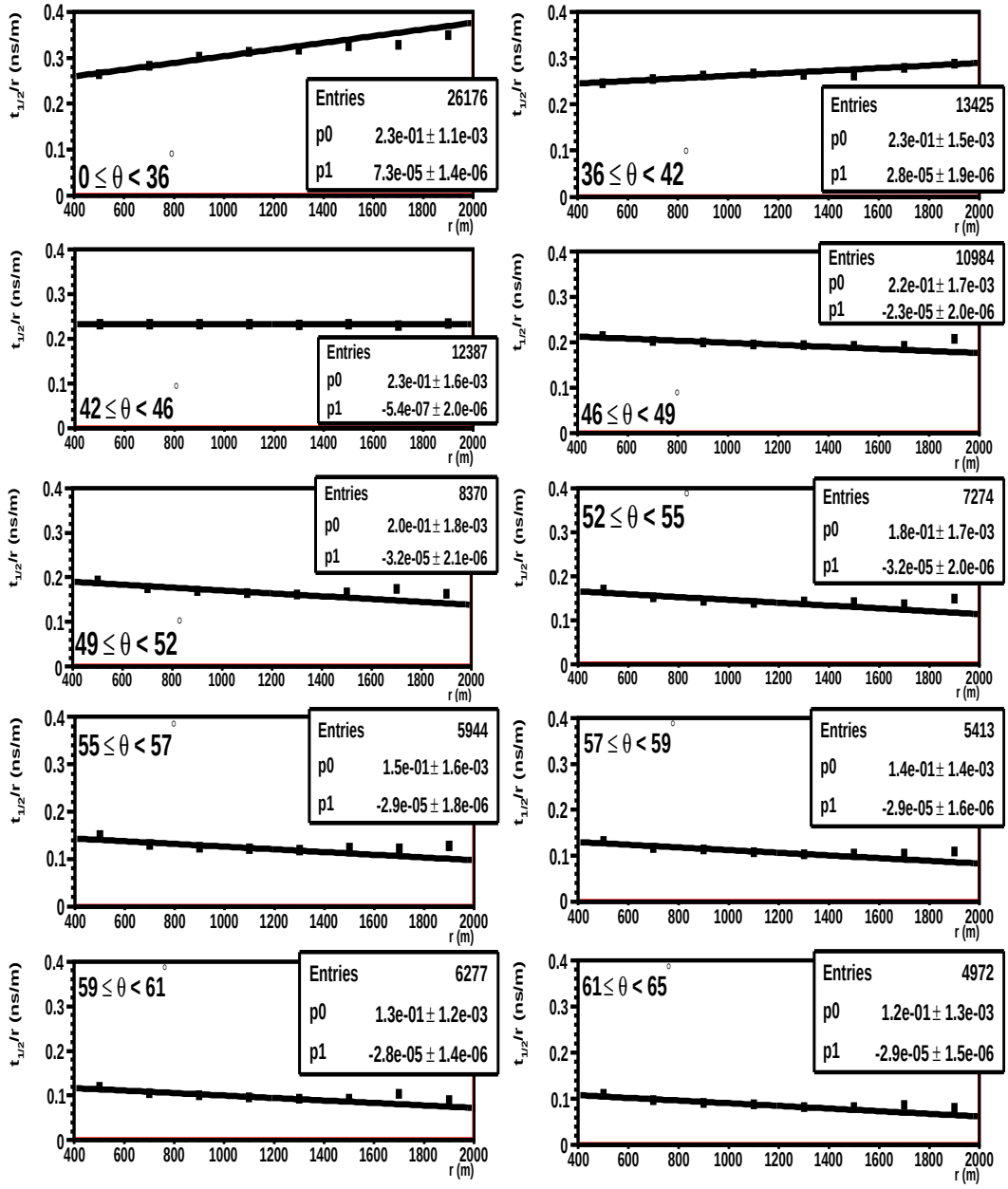

Figure 6.3: $\langle \frac{t_{1/2}}{r} \rangle$ as a function of distance for 10 different zenith angles and energy $E \geq 3\,\mathrm{EeV}$. The same θ binning as in figure 6.2 is used.

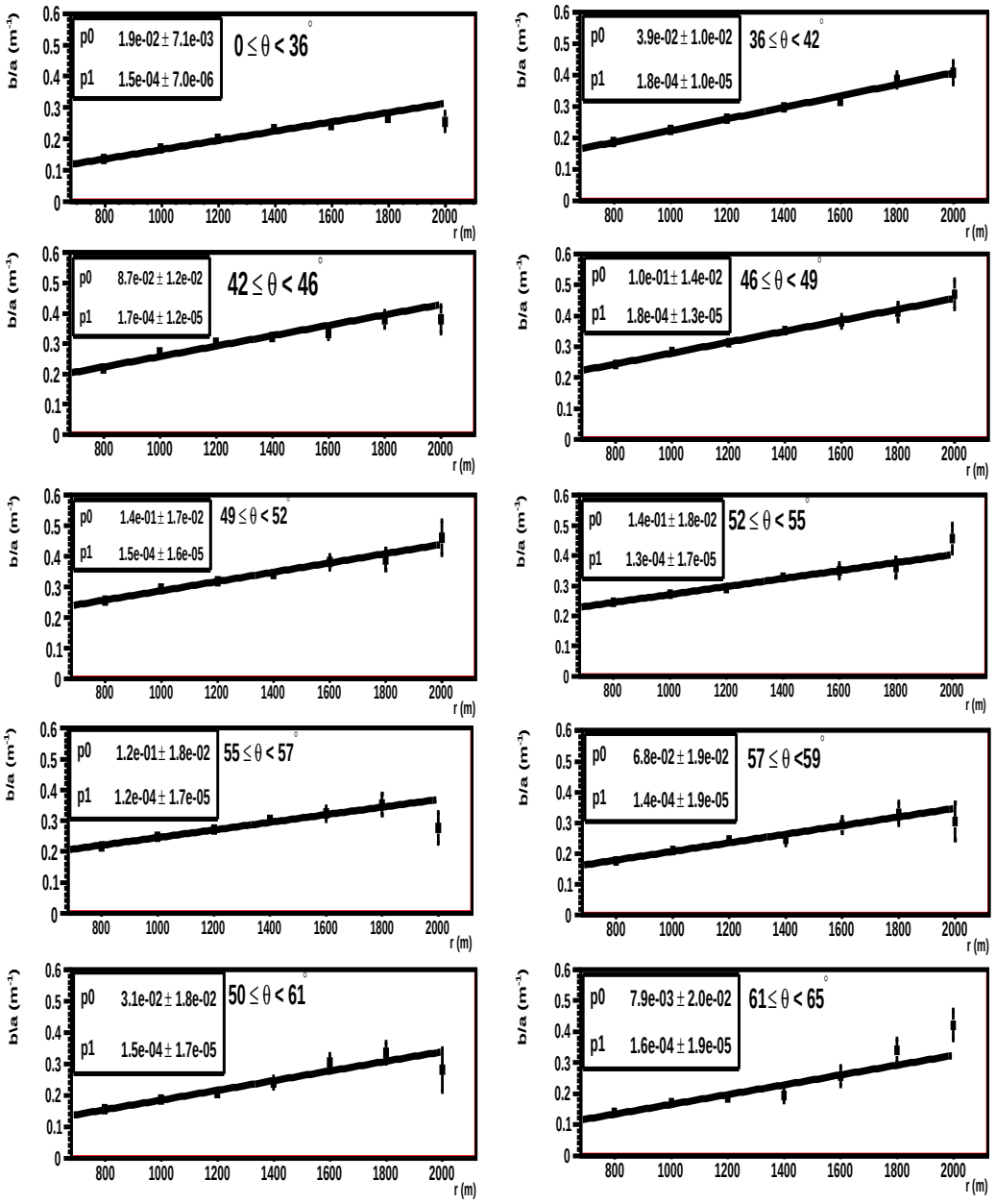

Figure 6.4: Asymmetry parameter $\frac{b}{a}$ as a function of distance for 10 different zenith angles and energy $E \geq 3\,\mathrm{EeV}$. The same θ binning as in figure 6.2 is used.

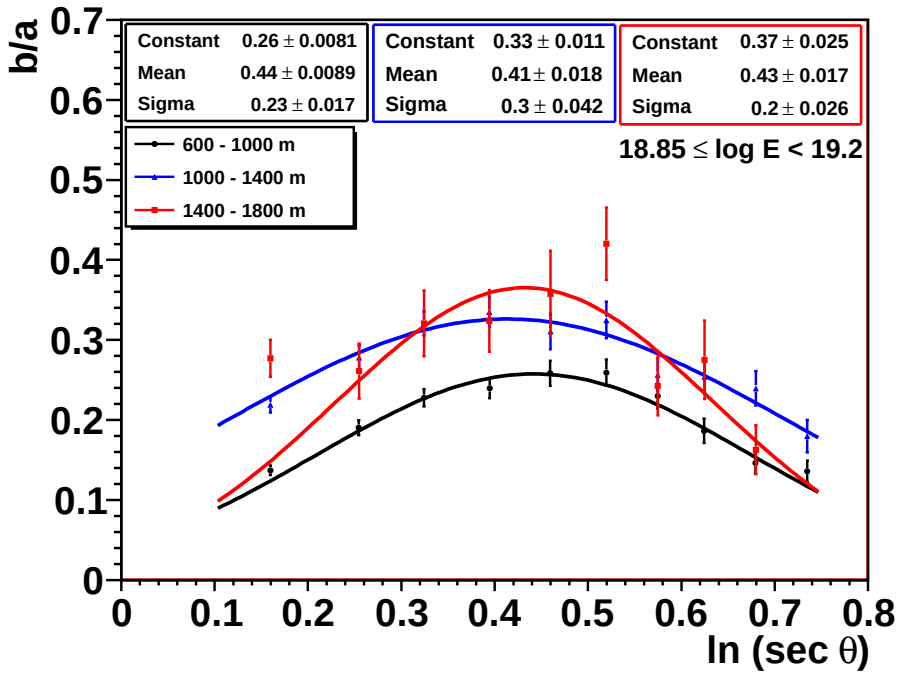

(a)

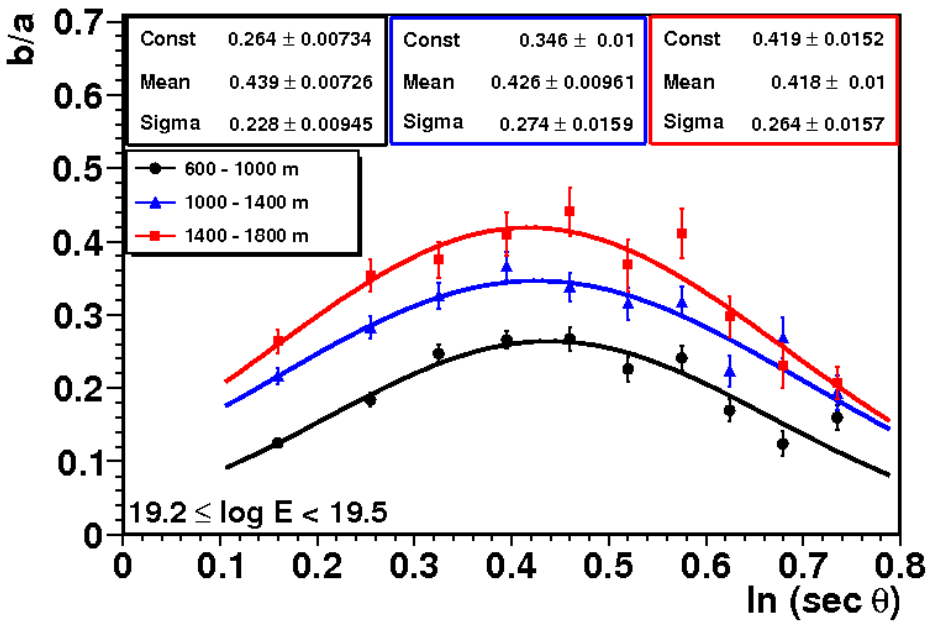

(b)

Figure 6.5: Asymmetry parameter $\frac{b}{a}$ as a function of zenith angle for 3 different distances and two energies.

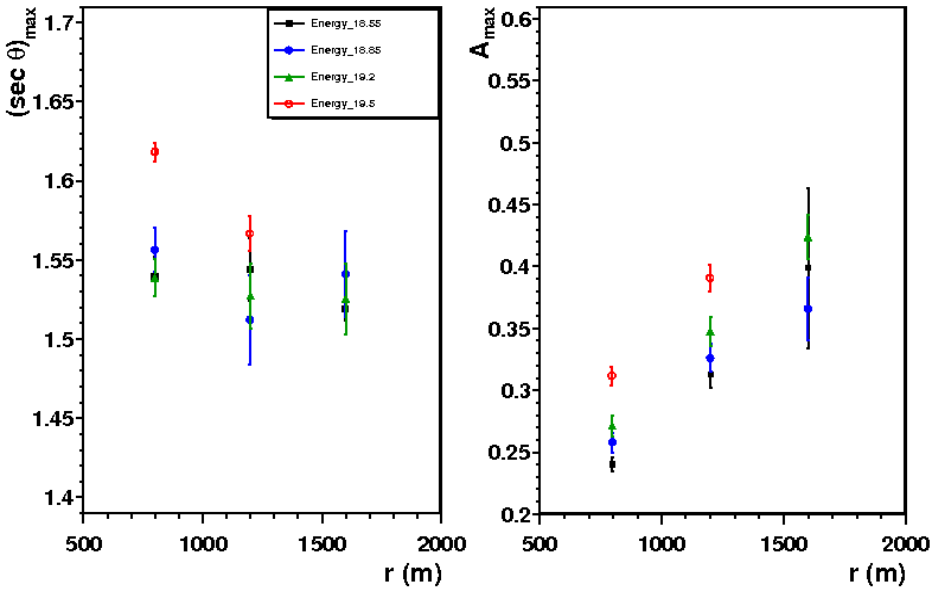

Figure 6.6: $(sec\theta)_{max}$ and A_{max} as a function of distance for four different energies.

distance from the shower axis. The signals from each are clearly different - with the early signal having a much longer tail and hence a larger risetime (by ~ 90 ns). If the asymmetry were solely due to attenuation, these risetimes should be the same within uncertainties.

An unthinned proton shower at 45° has been studied to determine the incidence angles of particles onto detectors either side of the shower axis (103). For both the early and late detectors, the majority of particles incident on the detector do so at angles between $30 - 60°$. However, in the early detector a significant contribution of late particles incident on the detector between angles of $0 - 30°$ and a smaller contribution from even later particles incident at -30 – 0° are also present, thus lengthening the risetime. The asymmetry is, therefore, due to a combination of the geometry of the shower in relation to the detectors, the solid angle from which the detectors can receive shower particles and the attenuation of the electromagnetic component for showers at all zenith angles.

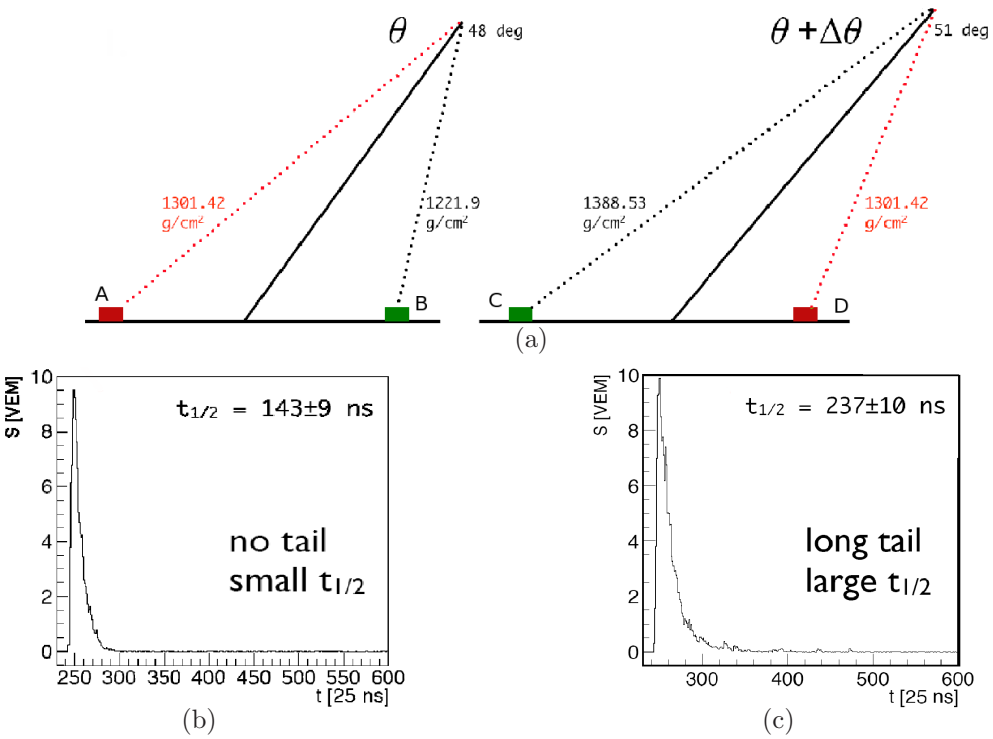

Figure 6.7: Illustration of the geometric component of the asymmetry for two inclined showers. Top: Two inclined showers of similar energy but different zenith angles have been chosen such that the atmospheric depth is the same (red dotted lines). Bottom: The time traces from the two stations shown in red (Left: Detector A (late), Right: Detector D (early)). The $\sim 90\,\mathrm{ns}$ difference in the two risetimes is due to geometric effects, not attenuation. Adapted from (103).

6.3 Exploration of an Alternative Method to Determine the Asymmetry for Mass-Composition Studies

Given the concerns raised in the previous section over the reliability of the asymmetry parameters calculated in (89), and recognising that there still exists a potential for the asymmetry to be used in mass-composition measurements, a new method for its calculation has been investigated. This method is based on the asymmetry parameterization discussed in chapter 3.2.3, adapted to determine

the angle and amplitude of maximum asymmetry as a function of energy. In this method, no *a priori* assumptions concerning the parameterization of the risetime with distance have been made.

Events with energies $\geq 3\,\mathrm{EeV}$ and zenith angles $\leq 60^\circ$ have been used. A cut on the signal and distance of individual detectors has been made to ensure the robust calculation of the risetimes. Unsaturated signals with a minimum of 15 VEM have been used in this study. This cut is larger than in the previous asymmetry work but has been chosen to reduce the effect of fluctuations on the risetime in detectors with small signals. A cut at $t_{1/2} = 40\,\mathrm{ns}$ has also been imposed to eliminate risetimes less than the average of the single particle response and which cannot have been properly measured. Detectors in the distance range $250 \leq r \leq 1650\,\mathrm{m}$ have been selected to reduce the potential for biases from the signal cut. Insufficient detectors exist at larger distances for robust analysis. A total of 95753 detectors meet these criteria. Direct light removal and trace cleaning procedures have been implemented on all traces as described in chapter 3.2.1.

The data have been divided into 8 bins in energy and then subdivided into 10 equal bins of $\sec\theta$. Next, the data have been subdivided into 6 distance bins, with the first bin covering the range $250 \leq r < 650\,\mathrm{m}$ and then in bins of 200 m width up to 1650 m. For each energy/zenith angle/distance combination containing more than 20 entries, the risetime has been plotted as a function of azimuthal angle and fitted with a cosine function of the form:

$$t_{1/2} = f + g cos\zeta \tag{6.3}$$

An example of typical results for one energy and zenith angle bin is shown in figure 6.8 for each distance bin.

The parameter g has been plotted as a function of distance. This is fitted with a quadratic function of the form $g = M(\theta, E)r^2$. An example for one energy and zenith angle range is given in figure 6.9.

Next, the parameter M has been plotted as a function of zenith angle for each energy band, as illustrated in figure 6.10 for four different energies, and fitted with

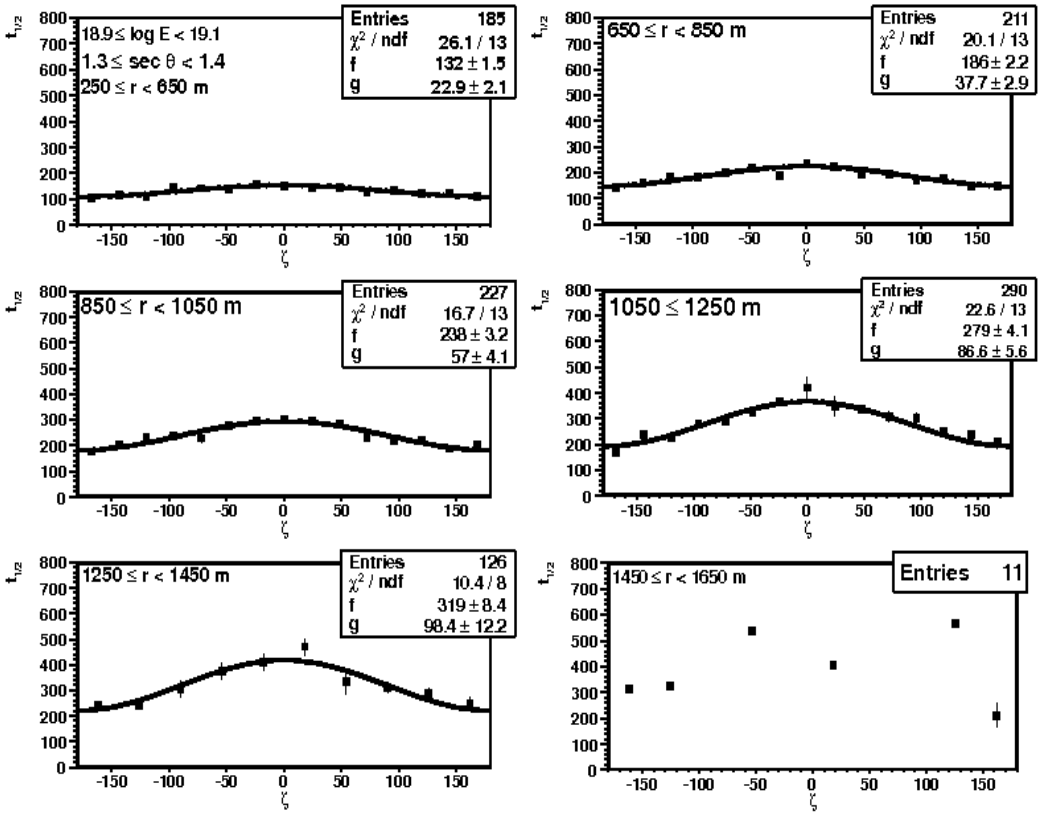

Figure 6.8: The risetime as a function of azimuth for six distances in the energy range $18.9 \leq \log(\mathrm{E}) < 19.1$ and zenith angle range $1.3 \leq sec\theta < 1.4$. The fit-function is $t_{1/2} = f + g\,cos(\zeta)$ in each case. No fit can be reliably performed for the largest distance shown and thusit is excluded from further analysis.

a function of the form:

$$M = (asec\theta + bsec^3\theta + c)\sqrt{(sec\theta - 1)} \tag{6.4}$$

in the range $1.0 \leq sec\theta < 1.8$.

The zenith angle (in terms of $sec\theta$) at which the parameter M is maximum, denoted $(\mathrm{sec}\theta)_{\mathrm{max}}$, has been found for each energy range. The maximum amplitude is denoted M_{max}. These values are plotted as a function of energy in figure 6.11. There seems to be little dependence of $(\mathrm{sec}\theta)_{\mathrm{max}}$ on energy while $\mathrm{M_{max}}$ increases with energy.

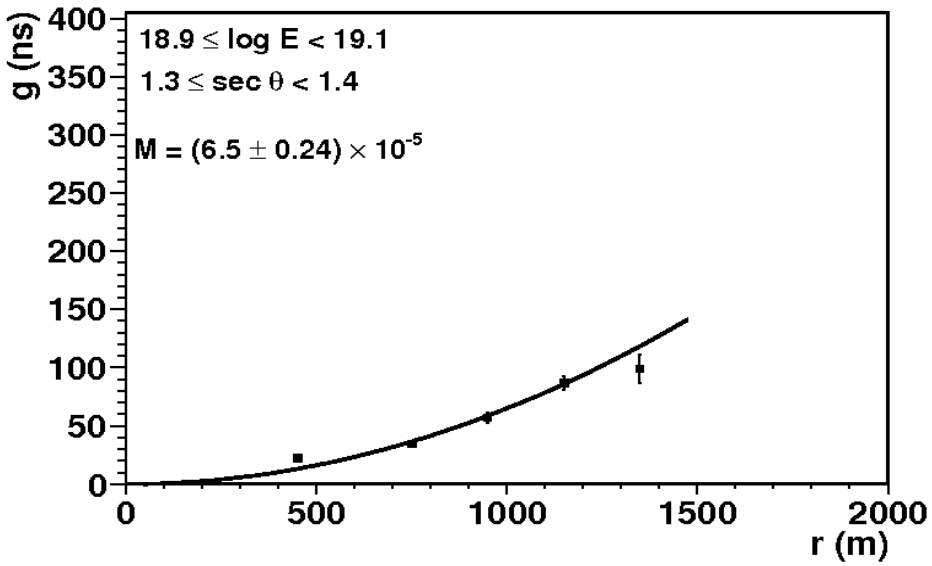

Figure 6.9: Asymmetry parameter g as a function of distance in the energy range $18.9 \leq logE < 19.1$ and zenith angle range $1.3 \leq sec\theta < 1.4$. The fit-function is $g = Mr^2$.

If these new parameters are to be used for mass-composition studies, it is desirable for a correlation with X_{max} to be present. This has been attempted using the set of high-quality hybrid events recorded between December 2004 and December 2010. Hybrid events have been selected according to the requirements of the above asymmetry method. Additional criteria have been applied to ensure the FD counterpart is well-reconstructed, following the selection criteria in (39). Events during periods of high cloud coverage and large atmospheric aerosol content have not been used. The longitudinal profile fit must have a $\chi^2/NDF \leq 2.5$ and the depth of maximum must be within the field of view of the telescopes. Fluorescence events with a large Cherenkov contamination ($\geq 20\%$) have been removed and fiducial cuts on the shower geometry have been applied. After these cuts, 4388 risetimes from around 1000 'golden hybrid' events have been obtained.

The data have been split into seven bins in X_{max} rather than in energy. A finer binning is not possible due to the limitations of statistics. The angle and amplitude of maximum asymmetry as a function of X_{max}, are shown in figure

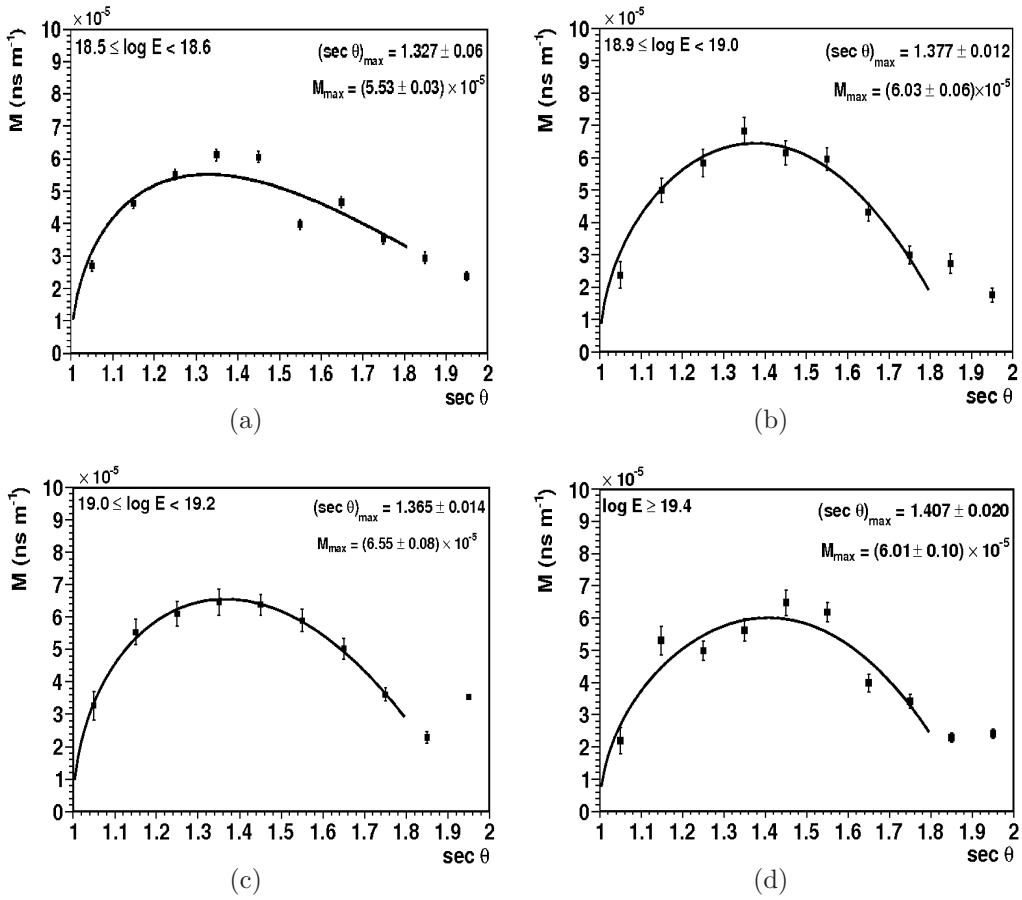

Figure 6.10: Asymmetry parameter m as a function of zenith angle for four different energies. The fit-function is $M = (asec\theta + bsec^3\theta + c)\sqrt{(sec\theta - 1)}$ in each case. The value of M where the fitted curves reach their maximum is the maximum amplitude M_{max}. The zenith angle at which this occurs is $(sec\theta)_{max}$.

6.12. A weak, positive correlation is evident in both plots.

In principle, the maximum angle and amplitude of the asymmetry can be converted to new parameters, denoted $X_{max}^{(sec\theta)}$ and X_{max}^{M}, from the correlation with X_{max} (figure 6.12). These new parameters would be another way of representing the longitudinal development of showers measured using the surface array. In practice, the correlation between either $(sec\theta)_{max}$ or M_{max} and X_{max} is very weak, with a large variations in the points. This implies little or no X_{max} sensitivity and will thus lead to unacceptably large uncertainties on $X_{max}^{(sec\theta)}$ and X_{max}^{M}.

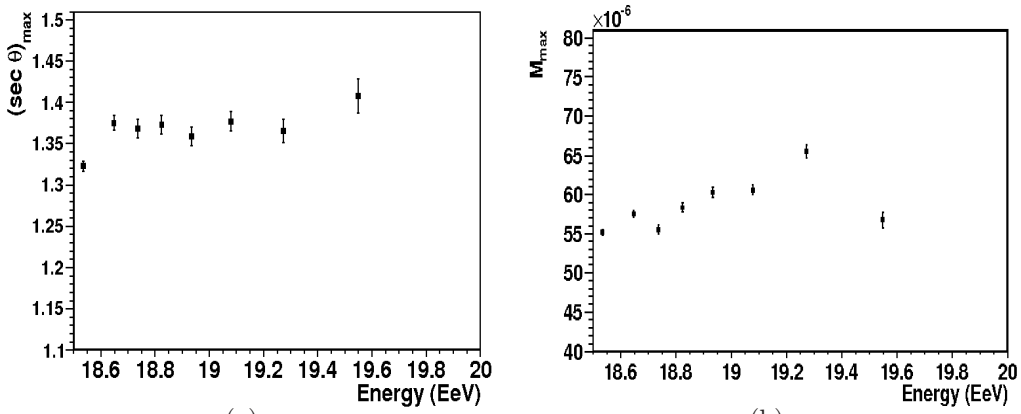

(a) (b)

Figure 6.11: Left: $(\sec\theta)_{\max}$ and Right: $M_{\max}$, as a function of energy for the data.

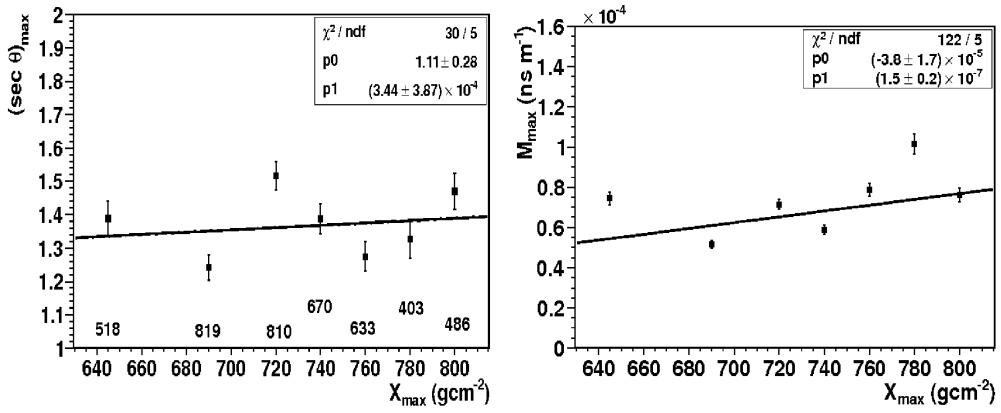

(a) (b)

Figure 6.12: Left: $(\sec\theta)_{\max}$ and Right: $M_{\max}$ as a function of $X_{\max}$ for the data. Numbers below each point in the left hand figure indicate the number of risetimes in that X_{max} bin.

To comment on the composition, the data must be compared to proton and iron simulations. This has been done and is shown in figure 6.13. Values of $(\sec\theta)_{\max}$ lie the range $1.3 \leq sec\theta < 1.45$ $(40^\circ - 46^\circ)$ for the data, much smaller and with a larger spread than in (89), where $(\sec\theta)_{\max}$ values lay between 1.45 and 1.55 $(46^\circ - 49^\circ)$. For the simulations, $(\sec\theta)_{\max}$ decreases with energy whilst

little change is seen in the data, contrary to the results from (89). It was expected that the asymmetry should increase with energy for events incident at the same zenith angle because the difference in path lengths travelled by particles from different stages in the shower development (and hence risetime) increases with energy. Further, in more inclined events the difference in the attenuation of shower particles on either side of the shower axis will be more significant in more energetic events due to their deeper development. Lower energy events are more likely to have attenuated out most of their electromagnetic component. Therefore the angle at which the component of the asymmetry due to the attenuation of shower particles tends to zero (i.e. all the particles attenuate out) should increase with increasing energy.

A significant scatter in $(\sec\theta)_{\max}$ from the proton simulations is observed, possibly due to a lack of sufficient statistics in individual energy/zenith angle/distance bins causing poor fits in M vs $sec\theta$ and thus a poor determination of the true position and amplitude of maximum asymmetry. Examination of the risetime with azimuth, g with distance and m with $sec\theta$ for the simulations supports this theory, particularly at the highest energies. From the upper panel of figure 6.13, no conclusions concerning the mass-composition of the data can currently be made.

The amplitude of maximum asymmetry may, however, be usable for mass-composition studies. The lower panel in figure 6.13 shows a clear separation between proton and iron simulations. Further, the amplitudes for the data appear to lie along the fit to the iron simulations at all energies. This is interesting for the mass-composition as it does not agree with results from X_{max} where the composition slowly changes from proton to iron. As X_{max} is measured directly from fluorescence detector information, this implies that the sensitivity of this method to the mass-composition may be very poor. This asymmetry analysis has been applied to photon simulations, however no maximum is found for several energy bins therefore no sensible deductions can be made.

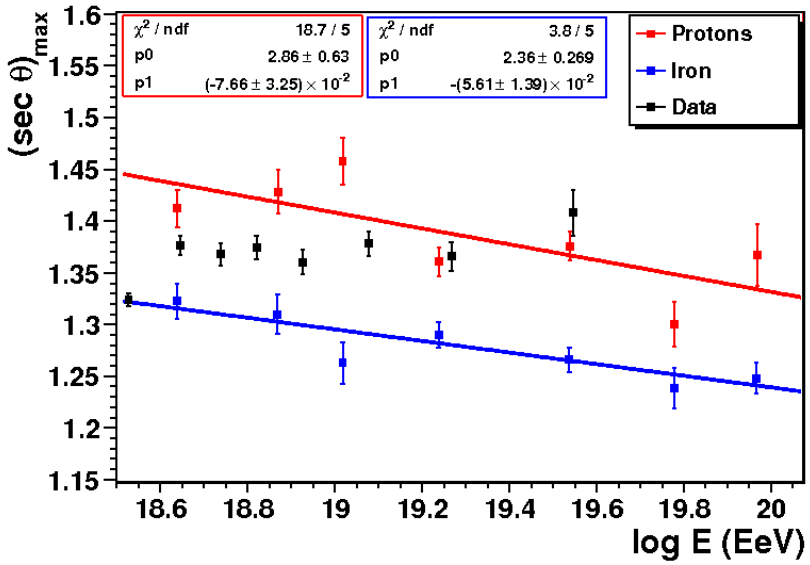

(a)

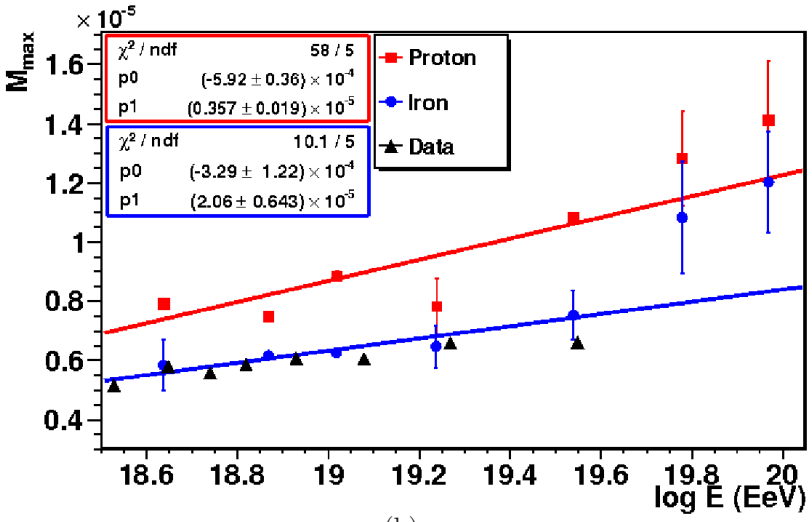

(b)

Figure 6.13: Top: $(\sec\theta)_{max}$ and Bottom: M_{max}, as a function of energy for the data (black triangles), proton (red squares) and iron (blue dots) simulations.

In an attempt to test the sensitivity of the maximum asymmetry as a function of energy to different methods, the asymmetry parameter M (from figure 6.9) has been plotted as a function of $ln(sec\theta)$ for each energy bin and fitted with a Gaussian, giving a more symmetric distribution about $(sec\theta)_{max}$. The results from these fits are shown in figure 6.14 and the corresponding angle of maximum asymmetry as a function of energy for data and simulations is shown in figure 6.15. The value of $(sec\theta)_{max}$ is noticably larger in each energy bin compared to those shown in figure 6.13, particularly for the simulations at the highest energies. Both the proton simulations and the data now show very little dependence on energy, whilst $(sec\theta)_{max}$ for the iron simulations decreases with energy less rapidly than in figure 6.13. The values of M_{max} are also larger in the lower panel of figure 6.15 than in figure 6.13, although the difference is less pronounced. Such a change illustrates a significant sensitivity to the chosen model and hence large uncertainties - much more than the 0.1%-level systematics quoted in (89). The $(sec\theta)_{max}$ values are still much smaller than the results in (89).

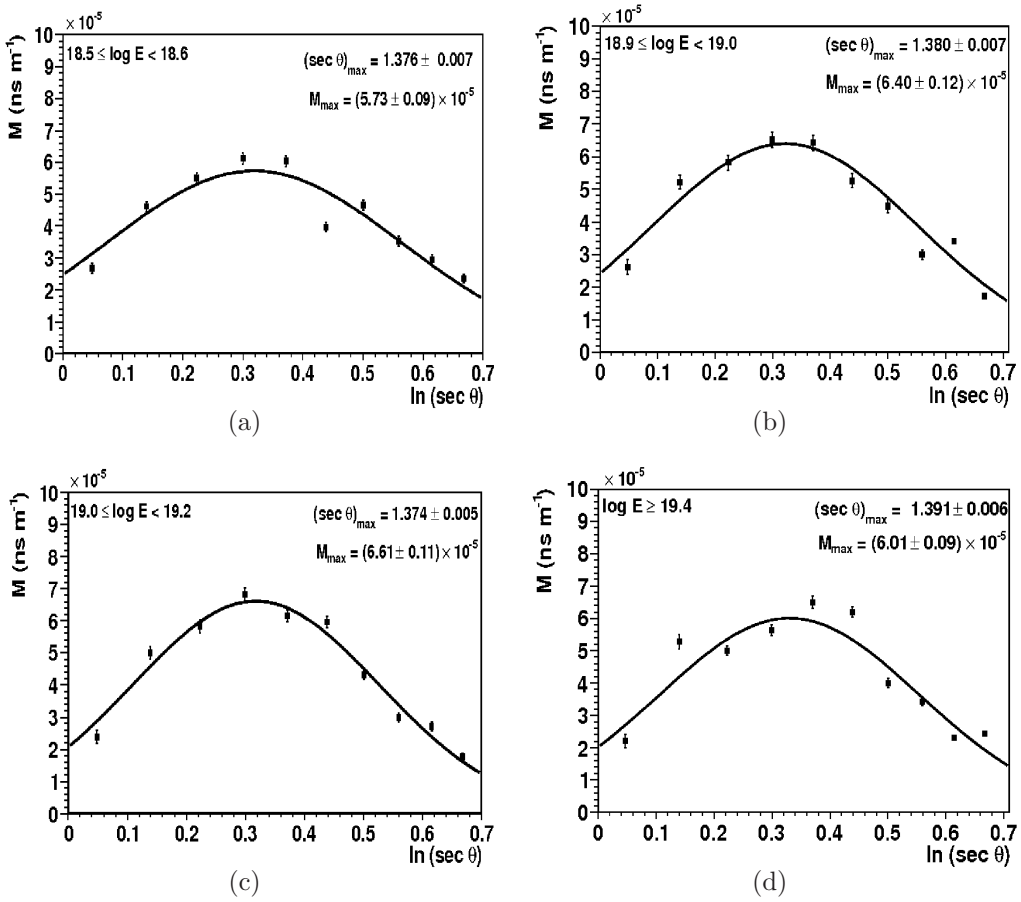

Figure 6.14: Asymmetry parameter m as a function of $ln(sec\theta)$ for four different energies. A Gaussian function has been fitted in each case. The value of M where the fitted curves reach their maximum is the maximum amplitude M_{max}. The zenith angle at which this occurs is $(sec\theta)_{max}$.

6.4 Conclusion

The asymmetry on the risetimes has been studied as a mass-sensitive parameter and results from previous works critically assessed. It has been determined that the asymmetry does not follow the same trend with distance as the risetime, therefore to attempt to eliminate the distance dependence (by dividing by r) in some previous works is not a valid approach. An alternative method to calculate the angle and amplitude at which the maximum asymmetry occurs as a function

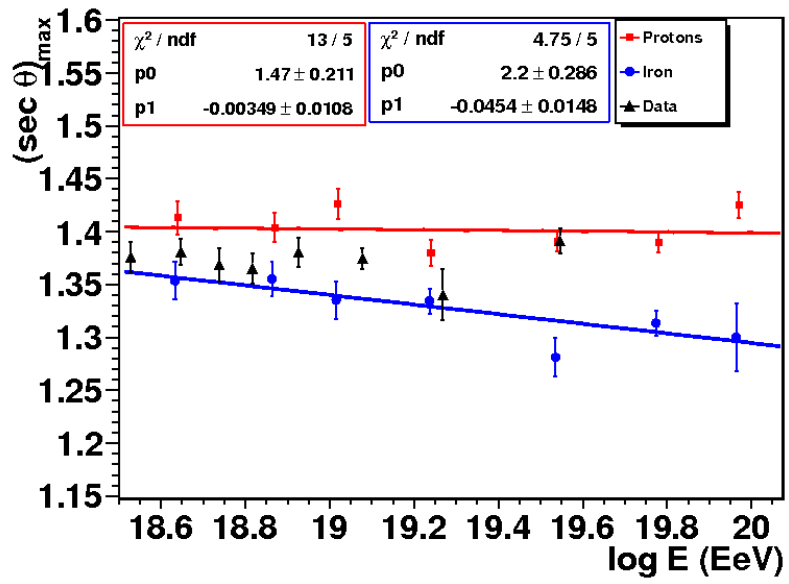

(a)

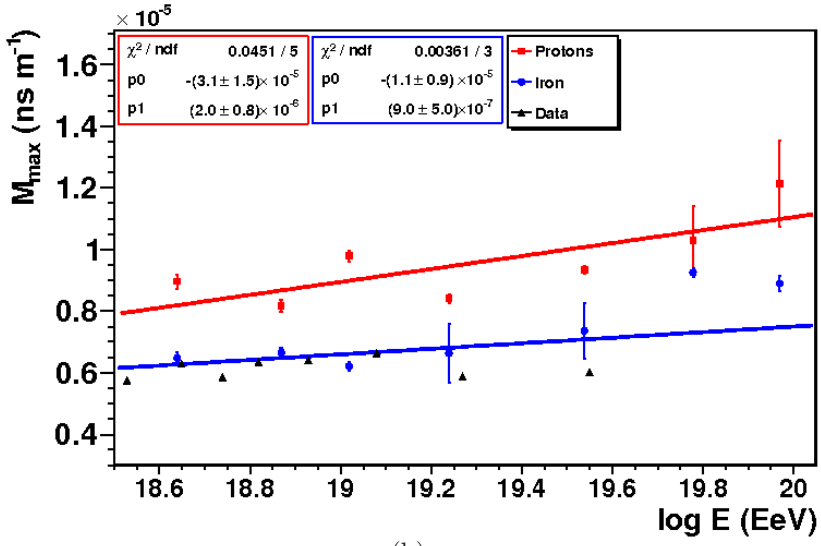

(b)

Figure 6.15: Results from the Gaussian fits to m vs $ln(sec\theta)$. Top: $(\sec\theta)_{\max}$ and Bottom: $M_{\max}$, as a function of energy for the data (black triangles), proton (red squares) and iron (blue dots) simulations.

of energy has been discussed. This method is based on the asymmetry correction first seen in chapter 3. With these new parameters, denoted $(sec\theta)_{max}$ and M_{max}, a weak linear correlation with X_{max} is observed for a set of good-quality hybrid

events. Large fluctuations in these parameters as a function of X_{max} make a conversion between either $(sec\theta)_{max}$ or M_{max} and X_{max} difficult without imposing large uncertainties. Little dependence is seen on $(sec\theta)_{max}$ with energy for the data whilst M_{max} increases with energy. Unexpectedly, $(sec\theta)_{max}$ decreases rapidly with increasing shower energy for hadronic simulations, although large fluctuations are present.

Given the large systematic uncertainties presented above, the poor correlation with X_{max}, the resulting inability to create a robust X_{max}^{SD} from $(sec\theta)_{max}$, and the poor separation between proton and iron simulations, this new $(sec\theta)_{max}$ is not currently in a form where reliable estimations of the mass composition may be made. Use of the maximum amplitude of the asymmetry, M_{max}, is more promising and could be investigated in more depth and for different proton/iron fractions and a larger set of simulations. However, the usefulness of a method where all information about individual events is lost is questionable. There are no means by which the asymmetry can be used on an event-by-event basis, unlike parameters such as X_{max} and $\langle\Delta\rangle$ - the rigorous analysis of which should be of high priority for mass-composition and photon studies.

Chapter 7

Summary and Conclusions

The Pierre Auger Observatory has been taking data since January 2004. The surface array of 1600 water Cherenkov detectors and the 24 fluorescence telescopes were completed during 2008. The total array exposure (to 31st December 2010) is now over $20,500\,\mathrm{km^2\,sr\,yr}$, making the Pierre Auger Observatory the largest cosmic-ray detector in operation. World-leading results have been published on all major science goals, including the mass-composition and UHE photon searches. The mass-composition of UHECR is still unknown. Recent measurements of the depth of maximum development (X_{max}) of air showers suggest, on average, an increasingly heavier composition above $\sim 3 \times 10^{18}\,\mathrm{eV}$.

UHE photons are predicted to originate from the interaction of UHECR protons with the cosmic microwave background via the Δ^+ resonance - one channel of the GZK mechanism:

$$p + \gamma_{\mathrm{CMB}} \rightarrow \Delta^+ \rightarrow p + \pi^0 \rightarrow p + 2\,\gamma \tag{7.1}$$

If the UHECR flux is dominated by heavier nuclei, for example iron nuclei, then a photon component is not expected. Previous limits to the photon fraction are of the order of a few % above $10^{19}\,\mathrm{eV}$. This is close to, but still above, the fraction of photons predicted from the GZK mechanism. Most top-down models for the origins of UHECR predict much larger fractions of photons and have already been excluded.

7.1 Update to the $\langle\Delta\rangle$-method for Mass-Composition Studies

7.1.1 Application to Data

An update of a pre-existing method (called the $\langle\Delta\rangle$-method) to determine the mass-composition of UHECR using the risetime has been performed. An additional 3.5 years worth of surface array data has been included since the $\langle\Delta\rangle$-method's conception. The $\langle\Delta\rangle$-method combines the risetimes from individual detectors triggered by an air shower into one mass-sensitive parameter describing the whole event. This parameter, $\langle\Delta\rangle$, represents the average deviation of the risetimes within an event from a benchmark (the average risetime as a function of distance and zenith angle), after accounting for the uncertainty on individual risetimes:

$$\langle\Delta\rangle = \frac{\Sigma\delta_i}{N_i} = \frac{\Sigma(\frac{(t_{1/2}-t_{1/2}^{bench})}{\sigma_{t_{1/2}}})}{N_i} \tag{7.2}$$

Accurate determination of the risetime is critical for the $\langle\Delta\rangle$-method. Whilst the essence of this method is not new, substantial changes have been made to yield a more robust mass-sensitive parameter suitable for use in photon-limit and mass-composition studies.

Robust determination of the risetimes was affected by a number of problems caused by the incorrect determination of signal stop-times in the FADC traces from surface detectors. This resulted in the overestimation of the baseline, the underestimation of the total signal and hence incorrect risetimes. This was most obvious in detectors where the low-gain trace had been used to determine the signal start and stop-times. These problems have now been resolved, enabling a robust re-analysis of the $\langle\Delta\rangle$-method. Subsequent concerns over the reliability, stability and necessity of one stage of the $\langle\Delta\rangle$-method - the deconvolution procedure - have led to its removal. This also achieves a significant speed-up to the analysis. Given these substantial changes, it has been necessary to conduct a thorough re-analysis and re-parametrisation of all stages of the $\langle\Delta\rangle$-method. New

cuts have been imposed, based on those in the original method and on physical reasoning, to minimise measurement inaccuracies and biases. These alterations were discussed in detail in Chapter 3. After implementation of these new cuts, 10,961 events above 3 EeV (23% of the original data set) have an available $\langle\Delta\rangle$.

Showers with a deeper development in the atmosphere have slower risetimes and therefore a larger than average $\langle\Delta\rangle$. It has been shown that $\overline{\langle\Delta\rangle}$ increases with energy and correlates with the depth of shower maximum, X_{max}. This correlation with X_{max} has permitted a conversion between $\langle\Delta\rangle$ and X_{max} to form a new parameter, $X_{max}^{\langle\Delta\rangle}$. A comparison of $X_{max}^{\langle\Delta\rangle}$ has been made to previous work that measured X_{max} directly from hybrid data (39). The results in this thesis are consistent with that work and indicate a mixed hadronic composition that gets heavier with energy, assuming that predictions from simulations are reasonably correct.

7.1.2 Photon Limits

Results from the application of this improved $\langle\Delta\rangle$-method to the data have been compared to predictions from simulations. More than 5000 CORSIKA photons were simulated over a continuous range of energies and zenith angles. Ten, five, two and one events above 10, 20, 30 and 40 EeV respectively have been found whose $\langle\Delta\rangle$s are larger than the corresponding median of the $\langle\Delta\rangle$ distribution for photon simulations. However, upon closer examination of these individual events it is likely that they may actually be from the tail of a distribution of hadronic primaries, although this cannot be completely confirmed.

The ability of the $\langle\Delta\rangle$-method to distinguish between photons and a pure proton and pure iron composition has been investigated for the first time using over 7500 proton and 8000 iron simulations with QGSJetII as the hadronic interaction model. It is found that, on an average basis, there exists a clear separation in the average $\langle\Delta\rangle$ as a function of energy between hadronic and photon primaries. Comparison with the data indicates an increasing average mass-composition with energy, provided that hadronic interaction models are correct. The number of

photon-candidates found in the data are well within the number expected from a pure proton composition and larger than the number expected from a pure iron composition. Uncertainties in the underlying physics of hadronic air showers do not permit these photon-candidates to be conclusively dismissed as the tail of a hadronic distribution.

New, more robust, 95% confidence-level upper limits to the integral flux and fraction of UHE photons above 10, 20, 30 and 40 EeV have been calculated assuming that the observed candidate events are photons. This gives fluxes of 8.7×10^{-3}, 4.7×10^{-3}, 2.8×10^{-3} and $2.3 \times 10^{-3}\,\mathrm{km^{-2}\,sr^{-1}\,yr^{-1}}$ above 10, 20, 30 and 40 EeV respectively. The corresponding upper limits to the photon-fraction are 1.5%, 3.2%, 4.9% and 9.1%. This represents a significant improvement to the photon limits, ruling out the Z-burst model at all energies except 10 EeV. Other 'top-down' models predicting larger fractions and fluxes of photons have already been excluded. These results are not yet sufficiently small as to probe the region of GZK predictions. Due to a large overlap between the distributions of $\langle\Delta\rangle$ for protons and iron, it is not possible to perform an event-by-event study of the mass-composition of UHECR.

Examination of the position of the photon-candidates found in this thesis in relation to the positions of 318 AGN within 75 Mpc from the VCV catalogue, to 373 AGN within 200 Mpc from the Swift-BAT catalogue and to the 106 highest energy events (above 55 EeV and used in correlation studies) has been performed. The angular resolution on these arrival directions is better than 1°. No photon candidates lie close to Centaurus A or correlate with AGN from these catalogues. Two photon-candidates lie within 20° of a sparse 'cluster' of the highest energy events. The possibility that these events are lower energy protons that have suffered large deflections may be a reason for the lack of correlation. The sources of these events therefore remains a mystery. The observed distribution of these photon-candidates indicates either that more than one nearby source is responsible for UHECR and/or that these events are not photons but very deeply-developing proton-initiated events.

7.1.3 Examination of the Highest Energy Events Using $\langle\Delta\rangle$

The $\langle\Delta\rangle$-method has been used to comment on the differences between those events with $E \geq 55\,EeV$ that correlate with AGN or lie within 18° of Centaurus A to those events found to not correlate, or which lie outside this region, respectively. After cuts, $\langle\Delta\rangle$ has been determined for 70 of the 106 events above 55 EeV. No significant difference has been found between the average $\langle\Delta\rangle$ for events that correlate with AGN and those that do not correlate. This indicates that events in this energy range are either all from the same type of primary particle or that a good mixture of primaries exists and that the sources of UHECR may not be AGN from the two catalogues studied here. There is also no statistically significant difference in $\overline{\langle\Delta\rangle}$ for events within 18° of Cen A and those outside this region, nor is any systematic change in $\langle\Delta\rangle$ observed as a function of angular distance from Cen A. This implies that Cen A is not the only source of UHECR, although it may still be a source. No clues to the exact mass-composition of these events are possible due to the extreme overlap from proton and iron simulations and the low statistics in this sample.

7.2 Other Mass-Sensitive Parameters

Finally, the azimuthal asymmetry on the risetimes has been reviewed as a potential mass-sensitive parameter in relation to previous works. Following a critical review of the method and results in references (89) and (90) regarding the use of the asymmetry on the risetimes as a mass-sensitive parameter, an attempt has been made to adapt the asymmetry analysis from the $\langle\Delta\rangle$-method to create a new mass-sensitive parameter, capable of determining the mass-composition of UHECR on an average basis.

It has been proven that the asymmetry on the risetime of both the data and hadronic simulations has a clear quadratic dependence on the distance from the shower core that must be accounted for. Assumptions that the asymmetry

in the risetime will follow the same or similar dependence on distance as the risetime itself are therefore incorrect. Thus dividing the risetime by the distance to eliminate the distance dependence on the asymmetry, as performed in previous works, is not a valid approach.

The asymmetry in the risetimes as a function of distance and zenith angle has been studied and the angle, $(sec\theta)_{max}$, and amplitude, $(A)_{max}$, of maximum asymmetry have been analysed using both the data and hadronic simulations. Due to the nature of its construction, it is not possible to use these two parameters for photon studies, nor for the determination of the mass-composition of individual cosmic-rays. This is a significant drawback to the long-term future of these parameters. However, both the angle and amplitude of maximum asymmetry on the risetimes can potentially be used to determine the average mass-composition of UHECR.

This new method appears to indicate little or no dependence of the angle and amplitude of maximum asymmetry from the data on either energy or X_{max}. Further, a decrease in the angle of maximum asymmetry with increasing energy for both data and hadronic simulations is observed. This result is not currently understood. Given large systematic uncertainties and the inability of the asymmetry parameters to describe the development of individual showers, the future of these asymmetry parameters as mass-sensitive variables remains uncertain.

7.3 Outlook

The ability to positively identify photons in the data, and to probe the GZK region is on the horizon and creeping ever closer. Analysis of the risetimes as a mass-sensitive parameter, and as a surrogate to X_{max}, is at an advanced stage. Future attempts to determine limits to the flux and fraction of photons will achieve better separation between photons and hadrons through the use of multi-parameter analysis techniques, for example combining $\langle\Delta\rangle$ and the radius of shower front curvature, R_c. However, accurate determination of R_c is not trivial and substantial work is required before this can be used as a robust mass-sensitive

parameter. A plethora of other mass-sensitive variables such as the slope of the LDF and muon counting methods are also being refined.

What is now needed for the future of the $\langle\Delta\rangle$-method is a rigorous, detailed Monte-Carlo study of photon and hadronic simulations such that systematics and statistical uncertainties may be understood or reduced. The behaviour of the $\langle\Delta\rangle$-parameter using different interaction models, such as EPOS or Sybill, and with different primary compositions (e.g. a 50/50 proton/iron mix) needs to be performed and will prove an interesting line of future investigation. It is also hoped that this updated $\langle\Delta\rangle$-method will, now that many problems have been resolved, be included as an analysis module into the Offline reconstruction software to complement the existing $t_{1/2}(1000)$ module, thus allowing future comparisons of these two methods and speedy updates to include more data.

A century on from the discovery of cosmic-rays, and nearly 50 years since the prediction of the GZK mechanism, the sources and composition of UHECR remain elusive. Future improvements to techniques for mass-composition measurements will assist greatly in the determination of possible source locations, by constraining the size of the deflections experienced by UHECR as they propagate to Earth. The gradual accumulation of data will assist with the reduction of uncertainties on such techniques and push photon limits down into the GZK region. A number of enhancements to the Pierre Auger Observatory will enable the study of UHECR down to $10^{17}\,\mathrm{eV}$ (HEAT and AMIGA), allow measurement of the muon component of showers (AMIGA), and use the detection of radio signals to provide innovative and complimentary techniques to established methods for the study of UHECR (AERA). These new components are already being built at the Pierre Auger Observatory or in the early stages of data taking. It is hoped that the mass-composition of UHECR and hence their origins will be determined in the near future. New results and discoveries are eagerly awaited.

References

[1] Rossi B. *Cosmic Rays* (Allen & Unwin (London), 1966).

[2] Hess V. *Über Beobachtungen der durchdringenden Strahlung bei sieben Freiballonfahrten*. Physikalische Zeitschrift, vol. 13 (1912): p. 1084.

[3] Alvarez L. and Compton A.H. *A Positively Charged Component of Cosmic Rays*. Phys. Rev., vol. 43 (1933): p. 835.

[4] Clay J. *Penetrating Radiation*. Proc. Roy. Acad. Amsterdam, vol. 30 (1927): p. 1115.

[5] Longair M. *High Energy Astrophysics*, vol. 1 (Cambridge University Press, 1992).

[6] Compton A.H. and Getting I.A. *An Apparent Effect of Galactic Rotation on the Intensity of Cosmic Rays*. Physical Review, vol. 47 (1935): p. 817.

[7] Bennett R.D., Stearns J.C. and Compton A.H. *Diurnal Variation of Cosmic Rays*. Physical Review, vol. 41 (1932): p. 119.

[8] Auger P., Ehrenfest P., Maze R., Daudin J. and Fréon R.A. *Extensive Cosmic-Ray Showers*. Rev. Mod. Phys., vol. 11 (1939): p. 288.

[9] Babha H. and Heitler W. *The Passage of Fast Electrons and the Theory of Cosmic Showers*. Proceedings of the Royal Society of London. Series A: Mathematical and Physical Sciences (1937): p. 432.

[10] Penzias A.A. and Wilson R.W. *A Measurement of Excess Antenna Temperature at 4080 Mc/s.* Astrophysical Journal, vol. 142 (1965): p. 419.

[11] Greisen K. *End to the Cosmic-Ray Spectrum?* Phys. Rev. Lett., vol. 16 (1966): p. 748.

[12] AGASA Collaboration. *Energy Spectrum Above* 3×10^{18} *eV observed with AGASA*. In *International Cosmic Ray Conference*, vol. 3 of *International Cosmic Ray Conference* (1999), p. 252.

[13] Nagano M. and Watson A.A. *Observations and Implications of the Ultra-High-Energy Cosmic Rays*. Reviews of Modern Physics, vol. 72 (2000): p. 689.

[14] Uchiyama Y., Aharonian F.A., Tanaka T., Takahashi T. and Maeda Y. *Extremely Fast Acceleration of Cosmic Rays in a Supernova Remnant*. Nature, vol. 449 (2007): p. 576.

[15] Cantoni E., Apel W.D. et al. *The Measurement of the Cosmic Ray Primary Energy Spectrum at* $10^{16} - 10^{18}$ eV *with the KASCADE-Grande Experiment*. Nuclear Physics B - Proceedings Supplements, vol. 212 (2011): p. 212.

[16] Eriksen K.A., Hughes J.P. et al. *Evidence for Particle Acceleration to the Knee of the Cosmic Ray Spectrum in Tycho's Supernova Remnant*. Astrophysical Journal, vol. 728 (2011): p. L28.

[17] Apel W.D., Arteaga-Velázquez J.C. et al. *Kneelike Structure in the Spectrum of the Heavy Component of Cosmic Rays Observed with KASCADE-Grande*. Physical Review Letters, vol. 107 (2011): 171104.

[18] Hillas A.M. *The Energy Spectrum of Cosmic Rays in an Evolving Universe*. Physics Letters A, vol. 24 (1967).

[19] Aloisio R., Berezinsky V., Blasi P., Gazizov A., Grigorieva S. and Hnatyk B. *A Dip in the UHECR Spectrum and the Transition from Galactic to Extragalactic Cosmic Rays*. Astroparticle Physics, vol. 27 (2007): p. 76.

[20] Greisen K. *Highlights in Air Shower Studies, 1965*. In *International Cosmic Ray Conference*, vol. 2 of *International Cosmic Ray Conference* (1965), p. 609.

[21] Romero G.E., Combi J.A., Perez Bergliaffa S.E. and Anchordoqui L.A. *Centaurus A as a Source of Extragalactic Cosmic Rays with Arrival Energies Well Beyond the GZK Cutoff*. Astroparticle Physics, vol. 5 (1996): p. 279.

[22] Calvez A., Kusenko A. and Nagataki S. *Role of Galactic Sources and Magnetic Fields in Forming the Observed Energy-Dependent Composition of Ultrahigh-Energy Cosmic Rays*. Physical Review Letters, vol. 105 (2010): p. 091101.

[23] Pierre Auger Collaboration, Abraham J. et al. *Measurement of the Energy Spectrum of Cosmic Rays Above* 10^{18} eV *Using the Pierre Auger Observatory*. Physics Letters B, vol. 685 (2010): p. 239.

[24] F. Salamida for the Pierre Auger Collaboration. *Update on the Measurement of the CR Energy Spectrum Above* 10^{18} eV *Made Using the Pierre Auger Observatory*. In *International Cosmic Ray Conference Proceedings*, International Cosmic Ray Conference Proceedings, Beijing (2011).

[25] Axford W.I., Leer E. and Skadron G. *The Acceleration of Cosmic Rays by Shock Waves*. In *International Cosmic Ray Conference*, vol. 11 of *International Cosmic Ray Conference* (1977), p. 132.

[26] Biermann P.L. *Galactic Cosmic Rays*. Journal of Physics Conference Series, vol. 47 (2006): p. 78.

[27] Hillas A.M. *The Origin of Ultra-High-Energy Cosmic Rays.* Annual Review of Astronomy and Astrophysics, vol. 22 (1984): p. 425.

[28] Wileman C. *The Spread in the Arrival Times of Particles in Air-Showers for Photon and Anisotropy Searches Above 10 EeV.* Ph.D. thesis, University of Leeds (2008).

[29] Rieger F.M. and Aharonian F.A. *Centaurus A as TeV γ-ray and Possible UHE Cosmic-Ray Source.* Astronomy and Astrophysics, vol. 506 (2009): p. L41.

[30] The Pierre Auger Collaboration. *Correlation of the Highest-Energy Cosmic Rays with Nearby Extragalactic Objects.* Science, vol. 318 (2007): p. 938.

[31] Kachelrieß M., Ostapchenko S. and Tomàs R. *High Energy Radiation from Centaurus A.* New Journal of Physics, vol. 11 (2009): p. 065017.

[32] Fermi Collaboration, Falcone A., Hase H., Pagoni C. and Ploetz C. *Fermi Large Area Telescope View of the Core of the Radio Galaxy Centaurus A.* Astrophysical Journal (2010): p. 1433.

[33] Kachelrieß M., Ostapchenko S. and Tomàs R. *Multi-Messenger Astronomy with Centaurus A.* International Journal of Modern Physics D, vol. 18 (2009): p. 1591.

[34] Dermer C.D. *On Gamma Ray Burst and Blazar AGN Origins of the Ultra-High Energy Cosmic Rays in Light of First Results from Auger.* ArXiv e-prints (2007).

[35] Waxman E. *Cosmological Gamma-Ray Bursts and the Highest Energy Cosmic Rays.* Phys. Rev. Lett., vol. 75 (1995): p. 386.

[36] Han J.L. *Magnetic Fields in Our Galaxy: How Much Do We Know? III. Progress in the Last Decade.* Chinese Journal of Astronomy and Astrophysics Supplement, vol. 6 (2006): p. 211.

[37] de Angelis A., Persic M. and Roncadelli M. *Constraints on Large-Scale Magnetic Fields from the Auger Results.* Modern Physics Letters A, vol. 23 (2008): pp. 315.

[38] Taylor A.M. and Aharonian F.A. *Spectral Shape and Photon Fraction as Signatures of the Greisen-Zatsepin-Kuzmin Cutoff.* Physical Review D, vol. 79 (2009): p. 083010.

[39] Pierre Auger Collaboration. *Measurement of the Depth of Maximum of Extensive Air Showers above* 10^{18} eV. Physical Review Letters, vol. 104 (2010): p. 091101.

[40] Aharonian F. *Very High Energy Gamma Radiation* (World Scientific Publishing Company, 2003).

[41] Allard D., Ave M. et al. *Cosmogenic neutrinos from the propagation of ultrahigh energy nuclei.* Journal of Cosmology and Astroparticle Physics, vol. 9 (2006): p. 5.

[42] Abraham J., Abreu P. et al. *Limit on the Diffuse Flux of Ultra-High Energy Tau Neutrinos with the Surface Detector of the Pierre Auger Observatory.* Physical Review D, vol. 79 (2009): p. 102001.

[43] Takeda M., Sakaki N. et al. *Energy determination in the Akeno Giant Air Shower Array experiment.* Astroparticle Physics, vol. 19 (2003): pp. 447.

[44] Sarkar S. *Ultra-High Energy Cosmic Rays and New Physics.* International Workshop on Particle Physics and the Early Universe (2002).

[45] Ave M., Hinton J.A., Vázquez R.A., Watson A.A. and Zas E. *New Constraints from Haverah Park Data on the Photon and Iron Fluxes of Ultra-High Energy Cosmic Rays.* Phys. Rev. Lett., vol. 85 (2000): pp. 2244.

[46] Stanev T. *High Energy Cosmic Rays* (Praxis Publishing LTD, 2004).

[47] Pierre Auger Collaboration. *Upper Limit to the Cosmic-Ray Photon Flux Above* 10^{19} eV *Using the Surface Detector of the Pierre Auger Observatory.* Astroparticle Physics, vol. 29 (2008): pp. 243.

[48] Pierre Auger Collaboration. *An Upper Limit to the Photon Fraction of Cosmic Rays Above* 10^{19} eV *From the Pierre Auger Observatory.* Astroparticle Physics, vol. 27 (2007): pp. 155.

[49] Weiler T.J. *Cosmic-ray Neutrino Annihilation on Relic Neutrinos Revisited: A Mechanism for Generating Air Showers Above the Greisen-Zatsepin-Kuzmin Cutoff.* Astroparticle Physics, vol. 11 (1999): p. 303.

[50] Ohm S. *Development of an Advanced γ/Hadron Separation Technique and Application to Particular γ-ray Sources with H.E.S.S.* Ph.D. thesis, Ruperto-Carola University of Heidelberg, Germany (2010).

[51] Matthews J. *A Heitler Model of Extensive Air Showers.* Astroparticle Physics, vol. 22 (2005): p. 387.

[52] Landau L. and Pomeranchuk I.Y. . Dokl. Akad. Nauk. SSSR, vol. 92 (1953): p. 535.

[53] Migdal A.B. *Bremsstrahlung and Pair Production in Condensed Media at High Energies.* Phys. Rev., vol. 103 (1956): p. 1811.

[54] Baier V.N. and Katkov V.M. *Theory of the Landau-Pomeranchuk-Migdal effect.* Physical Review D, vol. 57 (1998): p. 3146.

[55] Mc Breen B. and Lambert C.J. *Pair Production by High Energy ($E \geq 5\times10^{19}$ eV) Photons in the Earth's Magnetic Field.* In *International Cosmic Ray Conference*, vol. 6 of *International Cosmic Ray Conference* (1981), p. 70.

[56] Roulet E. *Latest Results From the Pierre Auger Observatory.* Proceedings of Science (2011).

[57] Berezinsky V., Aloisio R. and Gazizov A. *Ultra High Energy Cosmic Rays: The Disappointing Model*. Astroparticle Physics, vol. 34 (2009): p. 620.

[58] Abraham J. Abreu P., Aglietta M. and et al. *Properties and Performance of the Prototype Instrument for the Pierre Auger Observatory*. Nuclear Instruments and Methods in Physics Research A, vol. 523 (2004): p. 50.

[59] T. Mathes for the Pierre Auger Collaboration. *The HEAT Telescopes of the Pierre Auger Observatory. Status and First Data*. In *International Cosmic Ray Conference Proceedings*, International Cosmic Ray Conference Proceedings, Beijing (2011).

[60] F. Sanchez for the Pierre Auger Collaboration. *The AMIGA Detector of the Pierre Auger Observatory: An Overview*. In *International Cosmic Ray Conference Proceedings*, International Cosmic Ray Conference Proceedings, Beijing (2011).

[61] J. Kelley for the Pierre Auger Collaboration. *AERA: The Auger Engineering Radio Array*. In *International Cosmic Ray Conference Proceedings*, vol. 1 of *International Cosmic Ray Conference Proceedings, Beijing* (2011).

[62] Waldenmaier T., Blümer J. and Klages H. *Spectral Resolved Measurement of the Nitrogen Fluorescence Emissions in Air Induced by Electrons*. Astroparticle Physics, vol. 29 (2008): pp. 205.

[63] Keilhauer B. *The Fluorescence Detector of the Pierre Auger Observatory - a Calorimeter for UHECR*. In S.R. Magill and R. Yoshida (eds.), *Calorimetry in High Energy Physics: XII*, vol. 867 of *American Institute of Physics Conference Series* (2006), pp. 175–182.

[64] Monasor M., Vazquez J., Garcia-Pinto D. and Arqueros F. *The Impact of the Fluorescence Yield on the Reconstructed Shower Parameters of Ultra High Energy Cosmic Rays*. Astroparticle Physics, vol. 34 (2010): p. 467.

[65] The Pierre Auger Collaboration, Abraham J. et al. *The Fluorescence Detector of the Pierre Auger Observatory*. Nuclear Instruments and Methods in Physics Research A, vol. 620 (2010): p. 227.

[66] Mostafa M.A. and for the Pierre Auger Collaboration. *Atmospheric Monitoring for the Pierre Auger Fluorescence Detector*. In *International Cosmic Ray Conference* (2003), p. 465.

[67] Wiencke L. and for the Pierre Auger Collaboration. *Atmospheric Calorimetry Above* 10^{19} eV*: Shooting Lasers at the Pierre Auger Cosmic-Ray Observatory*. Journal of Physics Conference Series, vol. 160 (2009): p. 012037.

[68] Lawrence M.A., Reid R.J.O. and Watson A.A. *The Cosmic Ray Energy Spectrum Above* 4×10^{17} eV *As Measured by the Haverah Park Array*. Journal of Physics G Nuclear Physics, vol. 17 (1991): pp. 733.

[69] Abraham J., Abreu P. et al. *Trigger and aperture of the surface detector array of the Pierre Auger Observatory*. Nuclear Instruments and Methods in Physics Research A, vol. 613 (2010): pp. 29.

[70] The Pierre Auger Collaboration. *Calibration of the Surface Array of the Pierre Auger Observatory*. In *International Cosmic Ray Conference Proceedings*, International Cosmic Ray Conference Proceedings (2005), p. 101.

[71] The Pierre Auger Collaboration. *Performance of the Pierre Auger Observatory Surface Array*. In *International Cosmic Ray Conference Proceedings*, International Cosmic Ray Conference Proceedings (2005), p. 101.

[72] Newton D. *Measuring the Lateral Distribution of Extensive Air Showers to Characterise Properties of Cosmic Rays Above 1 EeV*. Ph.D. thesis, University of Leeds (2005).

[73] R. Pesce for the Pierre Auger Collaboration. *Energy Calibration of Data Recorded With the Surface Detector of the Pierre Auger Observatory: An Update*. In *International Cosmic Ray Conference Proceedings*, International Cosmic Ray Conference Proceedings, Beijing (2011).

[74] Hersil J., Escobar I., Scott D., Clark G. and Olbert S. *Observations of Extensive Air Showers Near the Maximum of Their Longitudinal Development*. Phys. Rev. Lett., vol. 6 (1961): pp. 22.

[75] The Pierre AUGER Collaboration, Abreu P. et al. *Update on the Correlation of the Highest Energy Cosmic Rays with Nearby Extragalactic Matter*. Astroparticle Physics, vol. 34 (2010): pp. 314.

[76] The Pierre Auger Collaboration. *Search For First Harmonic Modulation in the Right Ascension Distribution of Cosmic Rays Detected at the Pierre Auger Observatory*. Astroparticle Physics, vol. 34 (2011): pp. 627.

[77] The Pierre Auger Collaboration. *Upper Limit on the Cosmic-ray Photon Fraction at EeV Energies From the Pierre Auger Observatory*. Astroparticle Physics, vol. 31 (2009): pp. 399.

[78] Gora for the Pierre Auger Collaboration. *UHE neutrino signatures in the surface detector of the Pierre Auger Observatory*. In *International Cosmic Ray Conference Proceedings*, International Cosmic Ray Conference Proceedings (2009).

[79] Watson A.A. and Wilson J.G. *Fluctuation Studies of Large Air Showers: The Composition of Primary Cosmic Ray Particles of Energy* $\mathrm{E_p} \simeq 10^{18}$ eV. J. Phys. A:, vol. 7 (1974): p. 1199.

[80] Walker R. and Watson A.A. *A measurement of the elongation rate from 2 X 10 to the 17th to 10 to the 20th eV*. In *International Cosmic Ray Conference*, vol. 6 of *International Cosmic Ray Conference* (1981), pp. 31–34.

[81] Gelmini G.B., Kalashev O.E. and Semikoz D.V. *GZK Photons as Ultra-High Energy Cosmic Rays*. Soviet Journal of Experimental and Theoretical Physics, vol. 106 (2008): p. 1061.

[82] Smith B. *The Mass Composition of Cosmic Rays Above 1 EeV Using the Spread in Arrival Times of Air Shower Particles*. Ph.D. thesis, University of Leeds (2008).

[83] Lhenry-Yvon I. and Ghia P. *The "Communications Crisis" in 2009: Proposal for Handling Data Between June and November*. Pierre Auger Observatory Internal Note 2010-020 (2010).

[84] Bruijn R. *Modifications to the Treatment of FADC Traces*. Pierre Auger Observatory Internal Presentation (2011).

[85] Billoir P. *FADC Trace Cleaning In Surface Detectors Through A Segmentation Procedure*. Tech. rep., Pierre Auger Observatory Internal Note 2005-074 (2005).

[86] Creusot A. and Verberic D. *Time Structure of the Vertical Muon Signal*. Pierre Auger Observatory Internal Note 2008-010 (2008).

[87] Baxter A.J. *Properties of Extensive Air Showers Deduced from the Structure of Shower Fronts*. Ph.D. thesis, University of Leeds (1967).

[88] Arganda E., Arqueros F. et al. *Azimuthal Asymmetry in the Risetime as an Estimator of the Mass Composition of UHECRs*. Pierre Auger Observatory Internal Note 2010-069 (2010).

[89] Dova M.T., Manceñido M.E., Mariazzi A.G., Wahlberg H., Arqueros F. and García-Pinto D. *Time asymmetries in extensive air showers: A novel method to identify UHECR species*. Astroparticle Physics, vol. 31 (2009): pp. 312.

[90] Garcia-Pinto D. *Time Asymmetry in Cosmic Ray Showers. Mass Composition Studies in the Pierre Auger Observatory*. Ph.D. thesis, Universidad Complutense de Madrid (2009).

[91] Pugh E. and Winslow G. *The Analysis of Physical Measurements*, vol. 1 (Reading, Mass., Addison-Wesley, 1966).

[92] Linsley J. and Scarsi L. *Cosmic-Ray Composition At* $10^{17}-10^{18}$ eV. Physical Review Letters, vol. 9 (1962): p. 123.

[93] Keilhauer B., Engel R., Wilczynska B., Wilczynski H. and Will M. *New Malargüe Monthly Models*. Pierre Auger Observatory Internal Note 2009-037 (2009).

[94] Hillas A.M. *Two interesting techniques for Monte-Carlo simulation of very high energy hadron cascades*. In *International Cosmic Ray Conference*, vol. 8 of *International Cosmic Ray Conference* (1981), pp. 193–196.

[95] Bruijn R., Schmidt F., Ilee J. and Knapp J. *Study of Statistical Thinning with Fully Simulated Air Showers at Ultra High Energies*. In *International Cosmic Ray Conference Proceedings*, International Cosmic Ray Conference Proceedings, Lodz (2009).

[96] Billoir P. *A sampling procedure to regenerate particles in a ground detector from a 'thinned' air shower simulation output.* Astroparticle Physics, vol. 30 (2008): pp. 270.

[97] Billoir P., Roucelle C. and Hamilton J. *Evaluation of the Primary Energy of UHE Photon-induced Atmospheric Showers from Ground Array Measurements.* ArXiv Astrophysics e-prints (2007).

[98] Ros G., Gustavo A., Medina-Tanco G., Supanitsky D., del Peral L. and Rodrigues-Frias M. *Reconstruction of the Primary Energy of UHE Photon Induced Showers From Auger SD.* Pierre Auger Observatory Internal Note 2010-047 (2010).

[99] The Atlas Collaboration, Aad G. et al. *Measurement of the inelastic proton-proton cross-section at $\sqrt{s} = 7$ TeV with the ATLAS detector.* Nature Communications, vol. 2 (2011).

[100] R. Ulrich for the Pierre Auger Collaboration. *Estimate of the Proton-Air Cross Section With the Pierre Auger Observatory.* In *International Cosmic Ray Conference Proceedings*, International Cosmic Ray Conference Proceedings, Beijing (2011).

[101] Bleve C. and Krohm N. *Status of the "Standard" SD Photon Search Using $t_{1/2}(1000)$.* Pierre Auger Observatory Internal Presentation (2011).

[102] Salome Caballero Mora K. *Composition Studies of Ultra High Energy Cosmic Rays Using Data of the Pierre Auger Observatory.* Ph.D. thesis, Karlsruher Institut Für Technologie (2010).

[103] Bruijn R. and Knapp J. *The Origin of the Risetime Asymmetry.* Pierre Auger Observatory Internal Presentation (2011).

[104] Billoir P., Da Silva P. and Bertou X. *Checking the Origin of the Asymmetry of the Surface Detector Signals.* Pierre Auger Observatory Internal Note 2002-074 (2002).

[105] Pryke C. *Auger Project Technical Note: Asymmetry of Air Showers at Ground Level.* Pierre Auger Observatory Internal Note 1998-034 (1998).